Daya Bay Project

Conceptual Design Report

April 2, 2007

Daya Bay Collaboration

Beijing Normal University
Xinheng Guo, Naiyan Wang, Rong Wang

Brookhaven National Laboratory
Mary Bishai, Ralph L. Brown, Milind Diwan, Jim Frank, Richard Hahn, Kelvin Li, Laurence Littenberg, David E. Jaffe, Steve Kettell, Nathaniel Tagg, Brett Viren, Yuping Williamson, Minfang Yeh, Kin Yip, Kevin Zhang

California Institute of Technology
Christopher Jillings, Jianglai Liu, Christopher Mauger, Robert McKeown

Charles University
Zdenek Dolezal, Rupert Leitner, Viktor Pec, Vit Vorobel

Chengdu University of Technology
Liangquan Ge, Haijing Jiang, Wanchang Lai, Yanchang Lin

China Guangdong Nuclear Power Holding Company
Jiliang Sun, Yixin Zhang

China Institute of Atomic Energy
Long Hou, Xichao Ruan, Zhaohui Wang, Biao Xin, Zuying Zhou

Chinese University of Hong Kong
Ming-Chung Chu, Joseph Hor, Kin Keung Kwan, Antony Luk

Dongguan University of Technology
Li Kang, Yi Li, Yue Song, Ning Wang, Donghe Xu, Lei Yang, Huaqiang Yuan

George Mason University
Phil Rubin

Illinois Institute of Technology
Christopher White

Institute of High Energy Physics
Jun Cao, Hesheng Chen, Mingjun Chen, Yayun Ding, Jinyu Fu, Mengyun Guan, Jin Li, Weidong Li, Xiaonan Li, Jinchang Liu, Xuan Liu, Haoqi Lu, Yusheng Lu, Xinhua Ma, Yuqian Ma, Xiangchen Meng, Huayi Sheng, Gongxin Sun, Yaxuan Sun, Xinchun Tian, Ruiguang Wang, Yifang Wang, Zheng Wang, Zhimin Wang, Liangjian Wen, Zhizhong Xing, Changgen Yang, Liang Zhan, Jiawen Zhang, Qingmin Zhang, Zhiyong Zhang, Yubing Zhao, Weili Zhong, Kejun Zhu, Honglin Zhuang

Iowa State University
Kerry Whisnant, Bing-Lin Young

Joint Institute for Nuclear Research
Yuri A. Gornushkin, Dmitri Naumov, Igor Nemchenok, Alexander Olshevski

Kurchatov Institute
Vladimir N. Vyrodov

Lawrence Berkeley National Laboratory and University of California at Berkeley
Bill Edwards, Kelly Jordan, Dawei Liu, Kam-Biu Luk, Craig Tull

Nanjing University
Shenjian Chen, Tingyang Chen, Guobin Gong, Ming Qi

Nankai University
Shengpeng Jiang, Xuqian Li, Ye Xu

National Chiao-Tung University
Feng-Shiuh Lee, Guey-Lin Lin, Yung-Shun Yeh

National Taiwan University
Yee B. Hsiung

National United University
Simon Blyth, Yun Chang, Ming-Huey Afred Huang, Chung-Hsiang Wang

Princeton University
Changguo Lu, Kirk T. McDonald

Rensselaer Polytechnic Institute
John Cummings, Johnny Goett, Jim Napolitano, Paul Stoler

Shenzhen Univeristy
Yu Chen, Hanben Niu, Lihong Niu

Sun Yat-Sen (Zhongshan) University
Zhibing Li

Tsinghua University
Shaomin Chen, Hui Gong, Guanghua Gong, Li Liang, Beibei Shao, Qiong Su, Tao Xue, Ming Zhong

University of California at Los Angeles
Vahe Ghazikhanian, Huan Z. Huang, Charles A. Whitten, Stephan Trentalange

University of Hong Kong,
K.S. Cheng, Talent T.N. Kwok, Maggie K.P. Lee, John K.C. Leung, Jason C.S. Pun, Raymond H.M. Tsang, Heymans H.C. Wong

University of Houston
Michael Ispiryan, Kwong Lau, Logan Lebanowski, Bill Mayes, Lawrence Pinsky, Guanghua Xu

University of Illinois at Urbana-Champaign
S. Ryland Ely, Wah-Kai Ngai, Jen-Chieh Peng

University of Science and Technology of China
Qi An, Yi Jiang, Hao Liang, Shubin Liu, Wengan Ma, Xiaolian Wang, Jian Wu, Ziping Zhang, Yongzhao Zhou

University of Wisconsin and Physical Sciences Laboratory
A. Baha Balantekin, Farshid Feyzi, Lee Greenler, Karsten M. Heeger, Bryce Littlejohn, Michael McFarlane, Daniel Passmore, Thomas S. Wise

Virginia Polytechnic Institute and State University
Jonathan Link, Leo Piilonen

Executive Summary

This document describes the design of the Daya Bay reactor neutrino experiment to be constructed at the Daya Bay nuclear power complex in Shenzhen, China. This is an international project with collaborating institutions from China, the United States, Russia, and Czech Republic. This experiment will precisely determine the last unknown neutrino mixing angle θ_{13} with a sensitivity of 0.01 or better in $\sin^2 2\theta_{13}$ at the 90% confidence level through a measurement of the relative rates and energy spectra of reactor antineutrinos at different baselines.

Experimental Site

The Day Bay nuclear power complex is one of the most prolific sources of antineutrinos in the world. Currently the two pairs of reactor cores (Daya Bay and Ling Ao, separated by about 1.1 km) generate 11.6 $\mathrm{GW_{th}}$ of thermal power; this will increase to 17.4 $\mathrm{GW_{th}}$ by early 2011 when a third pair of reactor cores (Ling Ao II) is put into operation and Daya Bay will be among the five most powerful reactor complexes in the world.

The site is located adjacent to mountainous terrain, ideal for siting underground detectors that are well shielded from cosmogenic backgrounds. The basic experimental layout of Daya Bay consists of three underground experimental halls, one far and two near, linked by horizontal tunnels as shown in Fig. 0.1.

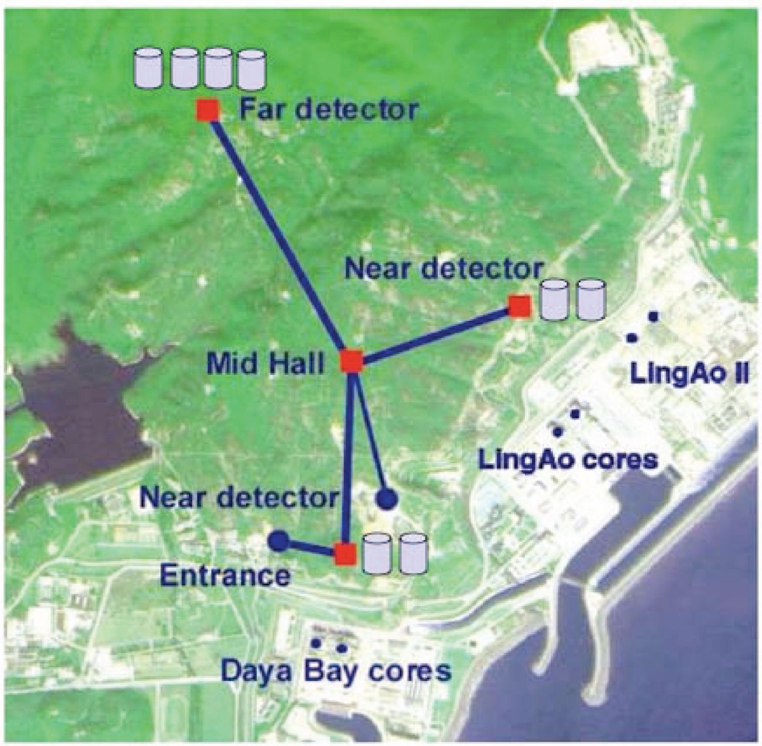

Fig. 0.1. Default configuration of the Daya Bay experiment, optimized for best sensitivity in $\sin^2 2\theta_{13}$. Four detector modules are deployed at the far site and two each at each of the near sites.

Experimental Setup

Figure 0.1 shows the detector deployment in the underground halls. Eight identical cylindrical detectors, each consisting of three nested cylindrical zones contained within a stainless steel tank, will be deployed to detect antineutrinos via the inverse beta-decay reaction. To maximize the experimental sensitivity four detectors are deployed in the far hall at the first oscillation maximum. The rate and energy distribution of antineutrinos from the reactors are monitored with two detectors in each near hall at relatively short baselines from their respective reactor cores, reducing the systematic uncertainty in $\sin^2 2\theta_{13}$ due to uncertainties in the reactor power levels to about 0.1%. This configuration significantly improves the statistical precision over previous experiments (0.2% in three years of running) and enables cross-calibration to verify that the detectors are identical. Each detector will have 20 metric tons of 0.1% Gd-doped liquid scintillator in the inner-most, antineutrino target zone. A second zone, separated from the target and outer buffer zones by transparent acrylic vessels, will be filled with undoped liquid scintillator for capturing γ rays that escape from the target thereby improving the antineutrino detection efficiency. A total of 192 photomultiplier tubes are arranged along the circumference of the stainless steel tank in the outer-most zone, which contains mineral oil to attenuate γ rays from trace radioactivity in the photomultiplier tube glass and nearby materials including the outer tank. The detector dimensions are summarized in Table 0.1.

Dimensions	Inner Acrylic	Outer Acrylic	Stainless Steel
Diameter (mm)	3100	3970	4976
Height (mm)	3100	3970	4976
Wall thickness (mm)	10	15	12
Vessel Weight (ton)	0.6	1.4	20
Liquid Weight (ton)	$\sim$20	$\sim$20	$\sim$40

Table 0.1. Summary of antineutrino detector properties. The dimensions are for the inner diameters. The liquid weights are for the mass of liquid contained only within that zone.

With reflective surfaces at the top and bottom of the detector the energy resolution of the detector is about 12% at 1 MeV.

The mountainous terrain provides sufficient overburden to suppress cosmic muon induced backgrounds to less than 1% of the antineutrino signal. The detectors in each experimental hall are shielded by 2.5 m of water against radioactivity and spallation neutrons from the surrounding rock. The detector halls include a muon detector system, consisting of an instrumented water shield and tracker, for tagging the residual cosmic muons. The signal and background rate in the underground halls are summarized in Table 0.2.

Careful construction, filling, calibration and monitoring of the detectors will reduce detector-related systematic uncertainties to a level comparable to or below the statistical uncertainty. Table 0.3 summarizes the systematic uncertainties for the experiment. The horizontal tunnels connecting the detector halls will facilitate cross-calibration and offer the possibility of swapping the detectors to further reduce systematic uncertainties.

Schedule

Civil construction is scheduled to begin in the spring of 2007. Deployment of the first pair of the detectors in the Daya Bay near hall will start in February 2009. Data taking using the baseline configuration of the two near halls and far hall will begin in June 2010. After three years of running the sensitivity of Daya Bay for $\sin^2 2\theta_{13}$ will be 0.008, relatively independent of the value of Δm^2_{31} within its allowed range.

	Daya Bay Near	Ling Ao Near	Far Hall
Baseline (m)	363	481 from Ling Ao 526 from Ling Ao II	1985 from Daya Bay 1615 from Ling Ao
Overburden (m)	98	112	350
Radioactivity (Hz)	<50	<50	<50
Muon rate (Hz)	36	22	1.2
Antineutrino Signal (events/day)	930	760	90
Accidental Background/Signal (%)	<0.2	<0.2	<0.1
Fast neutron Background/Signal (%)	0.1	0.1	0.1
^{8}He+^{9}Li Background/Signal (%)	0.3	0.2	0.2

Table 0.2. Summary of signal and background rates for each detector module at the different experimental sites.

Source	Uncertainty
Reactor Power	0.087% (4 cores) 0.13% (6 cores)
Detector (per module)	0.38% (baseline) 0.18% (goal)
Signal Statistics	0.2%

Table 0.3. Summary of uncertainties. The baseline value is realized through proven experimental methods, whereas the goal value should be attainable with additional research and development.

Contents

List of Figures

List of Tables

1 Physics

The goal of the Daya Bay reactor antineutrino experiment is to determine the unknown neutrino mixing angle θ_{13} with a sensitivity of 0.01 or better in $\sin^2 2\theta_{13}$, an order of magnitude better than the current limit. This section provides an overview of neutrino oscillation phenomenology and the scientific requirements of the experiment.

1.1 Neutrino Oscillation Phenomenology

Compelling evidence for transformation of one neutrino flavor to another (neutrino oscillations) has been observed in solar [1–4], atmospheric [5], reactor [6] and accelerator [7,8] experiments, using a wide variety of detector technologies. The only consistent explanation for these results is that neutrinos have mass and that the mass eigenstates are not the same as the flavor eigenstates (neutrino mixing).

1.1.1 Neutrino Mixing

For three neutrino flavors, the mixing matrix, usually called the Maki-Nakagawa-Sakata-Pontecorvo [9] mixing matrix, is defined to transform the mass eigenstates (ν_1, ν_2, ν_3) to the flavor eigenstates ($\nu_{\rm e}$, ν_μ, ν_τ) and can be parameterized as

$$\begin{aligned} U_{\rm MNSP} &= \begin{pmatrix} 1 & 0 & 0 \\ 0 & C_{23} & S_{23} \\ 0 & -S_{23} & C_{23} \end{pmatrix} \begin{pmatrix} C_{13} & 0 & \hat{S}_{13}^* \\ 0 & 1 & 0 \\ -\hat{S}_{13} & 0 & C_{13} \end{pmatrix} \begin{pmatrix} C_{12} & S_{12} & 0 \\ -S_{12} & C_{12} & 0 \\ 0 & 0 & 1 \end{pmatrix} \begin{pmatrix} e^{i\phi_1} & & \\ & e^{i\phi_2} & \\ & & 1 \end{pmatrix} \\ &= \begin{pmatrix} C_{12}C_{13} & C_{13}S_{12} & \hat{S}_{13}^* \\ -S_{12}C_{23} - C_{12}\hat{S}_{13}S_{23} & C_{12}C_{23} - S_{12}\hat{S}_{13}S_{23} & C_{13}S_{23} \\ S_{12}S_{23} - C_{12}\hat{S}_{13}C_{23} & -C_{12}S_{23} - S_{12}\hat{S}_{13}C_{23} & C_{13}C_{23} \end{pmatrix} \begin{pmatrix} e^{i\phi_1} & & \\ & e^{i\phi_2} & \\ & & 1 \end{pmatrix} \quad (1) \end{aligned}$$

where $C_{\rm jk} = \cos\theta_{\rm jk}$, $S_{\rm jk} = \sin\theta_{\rm jk}$, $\hat{S}_{13} = e^{i\delta_{CP}}\sin\theta_{13}$. The neutrino oscillation phenomenology is independent of the Majorana phases ϕ_1 and ϕ_2.

Neutrino oscillations of three flavors are completely described by six parameters: three mixing angles θ_{12}, θ_{13}, θ_{23}, two independent mass-squared differences, $\Delta m^2_{21} \equiv m_2^2 - m_1^2$, $\Delta m^2_{32} \equiv m_3^2 - m_2^2$, and one CP-violating phase δ_{CP} (note that $\Delta m^2_{31} \equiv m_3^2 - m_1^2 = \Delta m^2_{32} + \Delta m^2_{21}$).

1.1.2 Current Knowledge of Mixing Parameters

Results from solar, atmospheric, reactor, and accelerator neutrino experiments have been used to determine the mixing parameters separately and in global fits. The sixth parameter, the CP-violating phase δ_{CP}, is inaccessible to the present and near future oscillation experiments. We quote here the result of a recent global fit with 2σ (95% C.L.) ranges [10]:

$$\Delta m^2_{21} = 7.92(1.00 \pm 0.09) \times 10^{-5}\ {\rm eV}^2 \qquad \sin^2\theta_{12} = 0.314(1.00^{+0.18}_{-0.15}) \quad (2)$$

$$|\Delta m^2_{32}| = 2.4(1.00^{+0.21}_{-0.26}) \times 10^{-3}\ {\rm eV}^2 \qquad \sin^2\theta_{23} = 0.44(1.00^{+0.41}_{-0.22}) \quad (3)$$

$$\sin^2\theta_{13} = (0.9^{+2.3}_{-0.9}) \times 10^{-2} \quad (4)$$

Due to the absence of a signal, the global fits on θ_{13} result in upper bounds which vary significantly from one fit to another.

Another very recent global fit [11] with different inputs finds allowed ranges for the oscillation parameters that overlap significantly with the above results even at 1σ (68% C.L.). The latest MINOS neutrino oscillation results [8] significantly overlap those in the global fit [10]. All these signify the convergence to a set of accepted values of neutrino oscillation parameters Δm^2_{21}, $|\Delta m^2_{32}|$, $\sin^2\theta_{12}$, and $\sin^2\theta_{23}$.

The central value of θ_{13} extracted from Eq. 4 is about 5°. This corresponds to a value of 0.036 for $\sin^2 2\theta_{13}$, which should be compared to the best upper limit of 0.17 at 90% C.L. for $\Delta m^2_{31} = 2.5 \times 10^{-3}$

eV^2 obtained by Chooz (see Fig. 1.1). We can conclude that, unlike θ_{12} and θ_{23}, the mixing angle θ_{13} is relatively small. The three parameters that are not determined by present data are θ_{13}, the sign of Δm^2_{32}

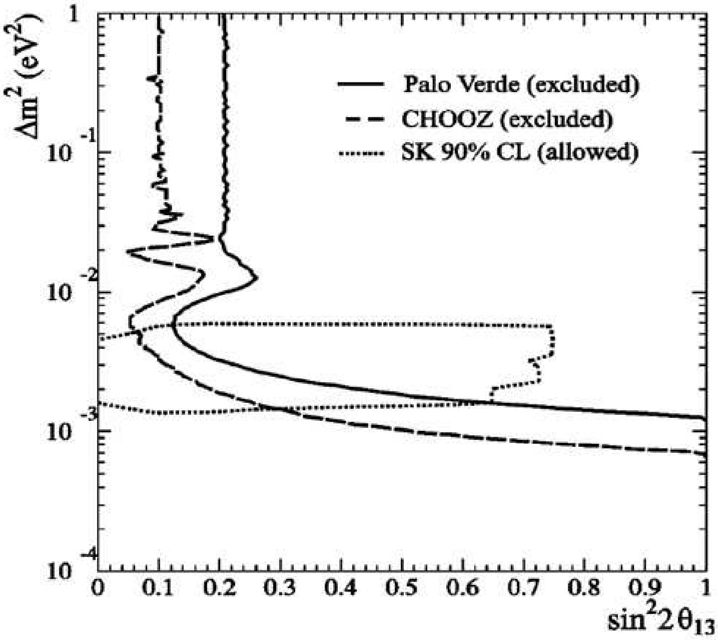

Fig. 1.1. Exclusion contours determined by Chooz, Palo Verde along with the allowed region obtained by Kamiokande. [12]

(which fixes the hierarchy of neutrino masses), and the Dirac CP-violating phase δ_{CP}.

1.1.3 Significance of the Mixing Angle θ_{13}

As one of the six neutrino mass parameters measurable in neutrino oscillations, θ_{13} is important in its own right and for further studies of neutrino oscillations. We need to know the value of θ_{13} to sufficient precision to design experiments to measure δ_{CP}. The matter effect, which can be used to determine the mass hierarchy, also depends on the size of θ_{13}. If $\theta_{13} > 0.01$, then the design of future experiments searching for CP violation is relatively straightforward [13]. However, for smaller θ_{13} new experimental techniques and accelerator technologies are likely required to carry out the measurements. In addition, θ_{13} is important in theoretical model building of the neutrino mass matrix, which can serve as a guide to the theoretical understanding of physics beyond the standard model. Based on these many considerations it is highly desirable to significantly improve our knowledge of θ_{13} in the near future. The February 28, 2006 report of the Neutrino Scientific Assessment Group (NuSAG) [14], which advises the DOE Offices of Nuclear Physics and High Energy Physics and the National Science Foundation, and the APS multi-divisional study's report on neutrino physics, *the Neutrino Matrix* [15], both recommend with high priority a reactor antineutrino experiment to measure $\sin^2 2\theta_{13}$ at the level of 0.01.

1.2 Determining θ_{13} with Nuclear Reactors

Reactor-based antineutrino experiments have the potential of uniquely determining θ_{13} at low cost and in a timely fashion. In this section we summarize the important features of nuclear reactors which are crucial to reactor-based antineutrino experiments.

1.2.1 Energy Spectrum and Flux of Reactor Antineutrinos

Many reactor antineutrino experiments to date have been carried out at pressurized water reactors (PWRs). Such a nuclear power plant derives its power from the fission of uranium and plutonium isotopes (mostly ^{235}U and ^{239}Pu) which are embedded in the fuel rods in the reactor core. The fission produces daughters, many of which beta decay because they are neutron-rich. Each fission on average releases approximately 200 MeV of energy and six antineutrinos. A typical reactor with 3 GW of thermal power (3 GW$_{\rm th}$) emits 6×10^{20} antineutrinos per second with antineutrino energies up to 8 MeV. The majority of the antineutrinos have very low energies; about 75% are below 1.8 MeV, the threshold of the inverse beta-decay reaction (IBD) that will be discussed in Section 1.2.2.

The antineutrino flux and energy spectrum of a PWR depend on several factors: the total thermal power of the reactor, the fraction of each fissile isotopes in the fuel, the fission rate of each fissile isotope, and the energy spectrum of antineutrinos of the individual fissile isotopes.

The antineutrino yield is directly proportional to the thermal power that is determined by measuring the temperature, pressure and the flow rate of the cooling water. The reactor thermal power is measured continuously by the power plant with a typical precision of about 1%.

Fissile materials in a reactor are continuously consumed while new fissile isotopes are produced from other fissionable isotopes in the fuel (mainly ^{238}U) by fast neutrons. Since the antineutrino energy spectra are slightly different for the four main isotopes, ^{235}U, ^{238}U, ^{239}Pu, and ^{241}Pu, the knowledge on the fission composition and its evolution over time are therefore critical to the determination of the antineutrino flux and energy spectrum. From the average thermal power and the effective energy released per fission [16], the average number of fissions per second of each isotope can be calculated as a function of time. Figure 1.2 shows the results of a computer simulation of the Palo Verde reactor cores [17].

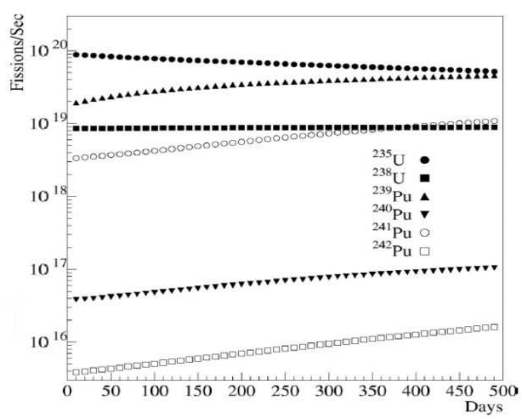

Fig. 1.2. Fission rate of reactor isotopes as a function of time from a Monte Carlo simulation [17].

It is common for a nuclear power plant to replace some of the fuel rods in the core periodically as the fuel is used up. Typically, a core will have 1/3 of its fuel changed every 18 months. At the beginning of each refueling cycle, 69% of the fissions are from ^{235}U, 21% from ^{239}Pu, 7% from ^{238}U, and 3% from ^{241}Pu. During operation the fissile isotopes ^{239}Pu and ^{241}Pu are produced continuously from ^{238}U. Toward the end of the fuel cycle, the fission rates from ^{235}U and ^{239}Pu are about equal. The average ("standard") fuel composition is 58% of ^{235}U, 30% of ^{239}Pu, 7% of ^{238}U, and 5% ^{241}Pu [18].

In general, the composite antineutrino energy spectrum is a function of the time-dependent contributions of the various fissile isotopes to the fission process. The Bugey 3 experiment compared three different models of the antineutrino spectrum with its measurement [19]. Good agreement was observed with the model that made use of the $\bar{\nu}_e$ spectra derived from the β spectra [20] measured at the Institute Laue-Langevin (ILL). However, there is no data for ^{238}U; only the theoretical prediction is used. The possible discrepancy between the predicted and the real spectra should not lead to significant errors since the contribution from ^{238}U is never higher than 8%. The overall normalization uncertainty of the ILL measured spectra is 1.9%. A global shape uncertainty is also introduced by the conversion procedure.

A widely used three-parameter parameterization of the antineutrino spectrum for the four main isotopes, as shown in Fig. 1.3, can be found in [21]. Per fission, ^{238}U produces the highest number of antineutrinos whereas ^{239}Pu generates the least. In addition, the spectra associated with ^{235}U and ^{241}Pu are almost identical.

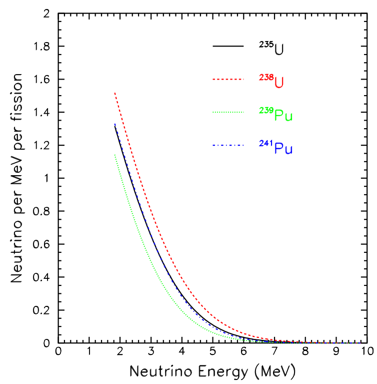

Fig. 1.3. Antineutrino energy spectrum for four isotopes following the parameterization of Vogel and Engel [21].

1.2.2 Inverse Beta-Decay Reaction

The reaction employed to detect the $\bar{\nu}_e$ from a reactor is the inverse beta-decay $\bar{\nu}_e + p \rightarrow e^+ + n$. The total cross section of this reaction, neglecting terms of order E_ν/M, where E_ν is the energy of the antineutrino and M is the nucleon mass, is

$$\sigma_{tot}^{(0)} = \sigma_0(f^2 + 3g^2)(E_e^{(0)} p_e^{(0)}/1\mathrm{MeV}^2) \tag{5}$$

where $E_e^{(0)} = E_\nu - (M_n - M_p)$ is the positron energy when neutron recoil energy is neglected, and $p_e^{(0)}$ is the positron momentum. The weak coupling constants are $f = 1$ and $g = 1.26$, and σ_0 is related to the Fermi coupling constant G_F, the Cabibbo angle θ_C, and an energy-independent inner radiative correction. The inverse beta-decay process has a threshold energy in the laboratory frame $E_\nu = [(m_\mathrm{n} + m_\mathrm{e})^2 - m_\mathrm{p}^2]/2m_\mathrm{p}$ = 1.806 MeV. The leading-order expression for the total cross section is

$$\sigma_{tot}^{(0)} = 0.0952 \times 10^{-42}\mathrm{cm}^2(E_e^{(0)} p_e^{(0)}/1\mathrm{MeV}^2) \tag{6}$$

Vogel and Beacom [22] have recently extended the calculation of the total cross section and angular distribution to order $1/M$ for the inverse beta-decay reaction. Figure 1.4 shows the comparison of the total cross sections obtained in the leading order and the next-to-leading order calculations. Noticeable differences are present for high antineutrino energies. We adopt the order $1/M$ formulae for describing the inverse beta-decay reaction. The calculated cross section can be related to the neutron lifetime, whose uncertainty is only 0.2%.

The expected recoil neutron energy spectrum, weighted by the antineutrino energy spectrum and the $\bar{\nu}_e + p \rightarrow e^+ + n$ cross section, is shown in Fig. 1.5. Due to the low antineutrino energy relative to the mass

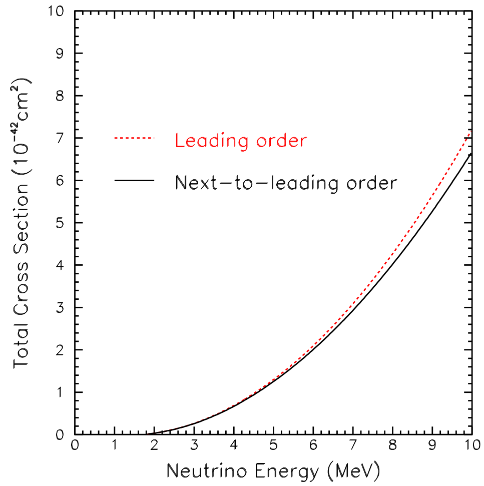

Fig. 1.4. Total cross section for inverse beta-decay calculated in leading order and next-to-leading order.

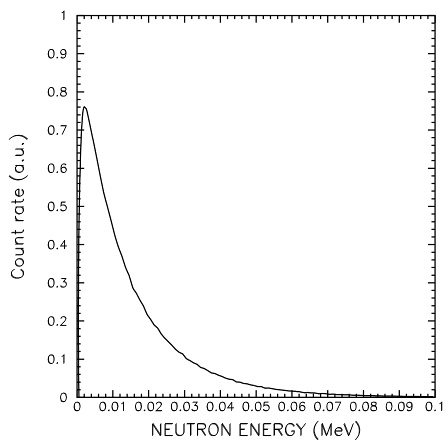

Fig. 1.5. Recoil neutron energy spectrum from inverse beta-decay weighted by the antineutrino energy spectrum.

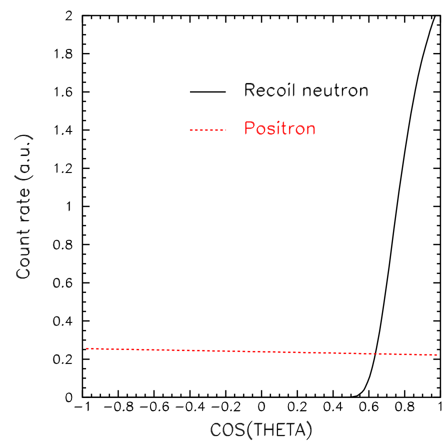

Fig. 1.6. Angular distributions of positrons and recoil neutrons from inverse beta-decay in the laboratory frame.

of the nucleon, the recoil neutron has low kinetic energy. While the positron angular distribution is slightly backward peaked in the laboratory frame, the angular distribution of the neutrons is strongly forward peaked, as shown in Fig. 1.6.

1.2.3 Observed Antineutrino Rate and Spectrum at Short Distance

The observed antineutrino spectrum in a liquid scintillator (LS) detector, which is rich in hydrogen, is a product of the reactor antineutrino spectrum and the cross section of inverse beta-decay. Figure 1.7 shows the differential antineutrino energy spectrum, the total cross section of the inverse beta-decay reaction, and the expected count rate as a function of the antineutrino energy. The differential energy distribution is the

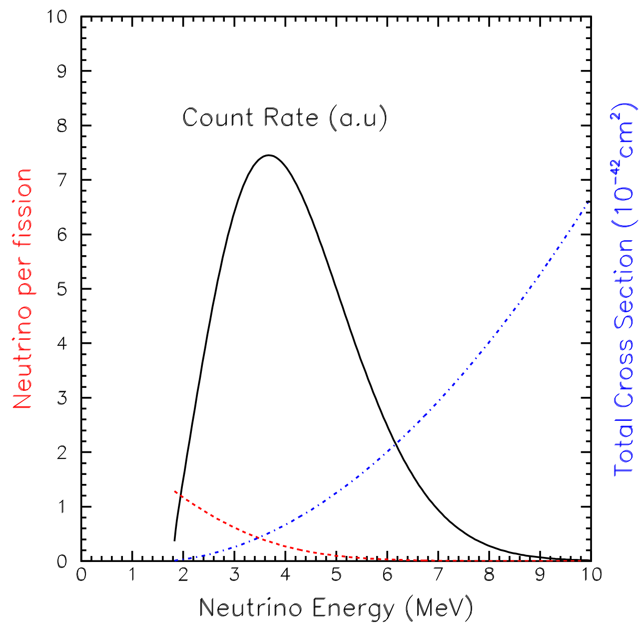

Fig. 1.7. Antineutrino energy spectrum (red dotted curve), total inverse beta-decay cross section (blue dotted-dash curve), and count rate (black solid curve) as a function of antineutrino energy.

sum of the antineutrino spectra of all the radio-isotopes in the fuel. It is thus sensitive to the variation of thermal power and composition of the nuclear fuel.

By integrating over the energy of the antineutrino, the number of events can be determined. With one-ton* of LS, a typical rate is about 100 antineutrinos per day per $\mathrm{GW_{th}}$ at 100 m from the reactor.

A small amount of Gd can be dissolved in the LS. After a moderation time of about ten μs, the neutron is captured by a Gd nucleus,† emitting several γ-ray photons with a total energy of about 8 MeV. This signal is called the delayed energy, E_d. The temporal correlation between the prompt energy (the positron signal) and the delayed energy constitutes a powerful tool for identifying the $\bar{\nu}_e$ and for suppressing backgrounds.

1.2.4 Reactor Antineutrino Disappearance Experiments

In a reactor-based antineutrino experiment the measured quantity is the survival probability for $\bar{\nu}_\mathrm{e} \to \bar{\nu}_\mathrm{e}$ at a baseline of the order of hundreds of meters to about a couple hundred kilometers with the $\bar{\nu}_\mathrm{e}$ energy from about 1.8 MeV to 8 MeV. The matter effect is totally negligible and so the vacuum formula for the survival probability is valid. In the notation of Eq. 1, this probability has a simple expression

$$P_\mathrm{sur} = 1 - C_{13}^4 \sin^2 2\theta_{12} \sin^2 \Delta_{21} - C_{12}^2 \sin^2 2\theta_{13} \sin^2 \Delta_{31} - S_{12}^2 \sin^2 2\theta_{13} \sin^2 \Delta_{32} \qquad (7)$$

where

$$\begin{aligned} \Delta_\mathrm{jk} &\equiv 1.267 \Delta m_\mathrm{jk}^2 (\mathrm{eV}^2) \times 10^3 \frac{L(\mathrm{km})}{E(\mathrm{MeV})} \\ \Delta m_\mathrm{jk}^2 &\equiv m_\mathrm{j}^2 - m_\mathrm{k}^2 \end{aligned} \qquad (8)$$

*Throughout this document we will use the term ton to refer to a metric ton of 1000 kg.

†The cross section of neutron capture by a proton is 0.3 b and 50,000 b on Gd.

L is the baseline in km, E the antineutrino energy in MeV, and $m_{\rm j}$ the j-th antineutrino mass in eV. The $\nu_{\rm e} \rightarrow \nu_{\rm e}$ survival probability is given by Eq. 7 which is independent of the CP phase angle δ_{CP} and the mixing angle θ_{23}.

To obtain the value of θ_{13}, the depletion of $\bar{\nu}_{\rm e}$ has to be extracted from the experimental $\bar{\nu}_{\rm e}$ disappearance probability,

$$\begin{aligned} P_{\rm dis} &\equiv 1 - P_{\rm sur} \\ &= C_{13}^4 \sin^2 2\theta_{12} \sin^2 \Delta_{21} + C_{12}^2 \sin^2 2\theta_{13} \sin^2 \Delta_{31} + S_{12}^2 \sin^2 2\theta_{13} \sin^2 \Delta_{32} \end{aligned} \tag{9}$$

Since θ_{13} is known to be less than 10°, we define the term that is insensitive to θ_{13} as

$$P_{12} = C_{13}^4 \sin^2 2\theta_{12} \sin^2 \Delta_{21} \approx \sin^2 2\theta_{12} \sin^2 \Delta_{21} \tag{10}$$

Then the part of the disappearance probability directly related to θ_{13} is given by

$$\begin{aligned} P_{13} &\equiv P_{\rm dis} - P_{12} \\ &= +C_{12}^2 \sin^2 2\theta_{13} \sin^2 \Delta_{31} + S_{12}^2 \sin^2 2\theta_{13} \sin^2 \Delta_{32} \end{aligned} \tag{11}$$

The above discussion shows that in order to obtain θ_{13} we have to subtract the θ_{13}-insensitive contribution P_{12} from the experimental measurement of $P_{\rm dis}$. To see their individual effect, we plot P_{13} in Fig. 1.8 together with $P_{\rm dis}$ and P_{12} as a function of the baseline from 100 m to 250 km. The antineutrino energy is

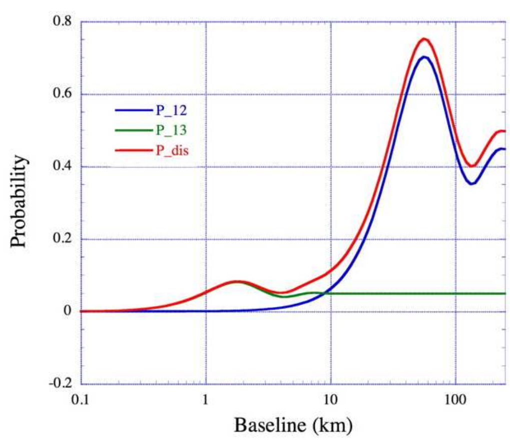

Fig. 1.8. Reactor antineutrino disappearance probability as a function of distance from the source. The values of the mixing parameters are given in Eq. 12. P_{12} is the slowly rising blue curve. P_{13} is the green curve that has a maximum near 2 km. The total disappearance probability $P_{\rm dis}$ is the red curve.

integrated from 1.8 MeV to 8 MeV. We also take $\sin^2 2\theta_{13} = 0.10$, which will be used for illustration in most of the discussions in this section. The other parameters are taken to be

$$\theta_{12} = 34^\circ, \quad \Delta m_{21}^2 = 7.9 \times 10^{-5} {\rm eV}^2, \quad \Delta m_{31}^2 = 2.5 \times 10^{-3} {\rm eV}^2 \tag{12}$$

The behavior of the curves in Fig. 1.8 are quite clear from their definitions, Eqs. (9), (10), and (11). Below a couple kilometers P_{12} is very small, and P_{13} and $P_{\rm dis}$ track each other well. This suggests that the measurement can be best performed at the first oscillation maximum of $P_{13}(\max) \simeq \sin^2 2\theta_{13}$. Beyond the first minimum P_{13} and $P_{\rm dis}$ deviate from each other more and more as L increases when P_{12} becomes dominant in $P_{\rm dis}$.

When we determine P_{13}(max) from the difference $P_{\rm dis} - P_{12}$, the uncertainties on θ_{12} and Δm^2_{21} will propagate to P_{13}. It is easy to check that, given the best fit values in Eq. 2, when $\sin^2 2\theta_{13}$ varies from 0.01 to 0.10 the relative size of P_{12} compared to P_{13} is about 25% to 2.6% at the first oscillation maximum. Yet the contribution of the uncertainty of P_{12} to the uncertainty in determining $\sin^2 2\theta_{13}$ is always less than 0.005.

In Fig. 1.9, $P_{\rm dis}$ integrated over E from 1.8 to 8 MeV is shown as a function of the baseline L for three values of Δm^2_{32} that cover the allowed range of Δm^2_{32} at 95% C.L. as given in Eq. 3. The curves show the

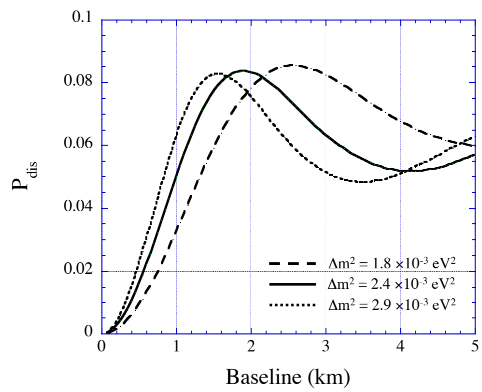

Fig. 1.9. Reactor antineutrino disappearance probability due to the mixing angle θ_{13} as a function of the baseline L over the allowed 2σ range in Δm^2_{32}.

location of the oscillation maximum is sensitive to Δm^2_{32}. For $\Delta m^2_{32} = (1.8,\ 2.4,\ 2.9) \times 10^{-3}$ eV^2, the oscillation maximum occurs at a baseline of 2.5 km, 1.9 km, and 1.5 km, respectively. From this simple study, placing the detector between 1.5 km and 2.5 km from the reactor looks to be a good choice.

We conclude from this phenomenological investigation that the choice of L be made so that it can cover as large a range of Δm^2_{31} as possible. A baseline near 2 km is particularly attractive since it is least sensitive to the value of Δm^2_{31}.

1.2.5 Precision Measurement of θ_{13}

The value of $\sin^2 2\theta_{13}$ can be determined by comparing the observed antineutrino rate and energy spectrum with predictions assuming no oscillations. The number of detected antineutrinos $N_{\rm det}$ is given by

$$N_{\rm det} = \frac{N_p}{4\pi L^2} \int \epsilon \sigma P_{\rm sur} S dE \tag{13}$$

where N_p is the number of free protons in the target, L is the distance of the detector from the reactor, ϵ is the efficiency of detecting an antineutrino, σ is the total cross section of the inverse beta-decay process, $P_{\rm sur}$ is the survival probability given in Eq. 7, and S is the differential energy distribution of the antineutrino at the reactor shown in Fig. 1.7.

With only one detector at a fixed baseline from a reactor, according to Eq. 13, we must determine the absolute antineutrino flux from the reactor, the absolute cross section of the inverse beta-decay reaction, and the efficiencies of the detector and event-selection requirements in order to measure $\sin^2 2\theta_{13}$. The prospect for determining $\sin^2 2\theta_{13}$ precisely with a single detector is not promising. It is a challenge to reduce the systematic uncertainties of such an absolute measurement to sub-percent level, especially for reactor-related uncertainties.

Mikaelyan and Sinev pointed out that the systematic uncertainties can be greatly suppressed or totally eliminated when two detectors positioned at two different baselines are utilized [23]. The near detector close to the reactor core is used to establish the flux and energy spectrum of the antineutrinos. This relaxes the requirement of knowing the details of the fission process and operational conditions of the reactor. In this approach, the value of $\sin^2 2\theta_{13}$ can be measured by comparing the antineutrino flux and energy distribution observed with the far detector to those of the near detector after scaling with distance squared. According to Eq. 13, the ratio of the number of antineutrino events with energy between E and $E + dE$ detected at distance L_f (far detector) to that at a baseline L_n (near detector) is given by

$$\frac{N_\mathrm{f}}{N_\mathrm{n}} = \left(\frac{N_\mathrm{p,f}}{N_\mathrm{p,n}}\right)\left(\frac{L_\mathrm{n}}{L_\mathrm{f}}\right)^2\left(\frac{\epsilon_\mathrm{f}}{\epsilon_\mathrm{n}}\right)\left[\frac{P_\mathrm{sur}(E,L_\mathrm{f})}{P_\mathrm{sur}(E,L_\mathrm{n})}\right] \tag{14}$$

By placing the near detector close to the core such that there is no significant oscillating effect and the contribution of θ_{12} is negligible, $\sin^2 2\theta_{13}$ is approximately given by

$$\sin^2 2\theta_{13} \approx \frac{1}{A(E,L_\mathrm{f})}\left[1 - \epsilon_r\left(\frac{N_\mathrm{f}}{N_\mathrm{n}}\right)\left(\frac{L_\mathrm{f}}{L_\mathrm{n}}\right)^2\right] \tag{15}$$

where $A(E, L_\mathrm{f}) = \sin^2 \Delta_{31}$ with Δ_{31} defined in Eq. 8 is the analyzing power and ϵ_r is the relative efficiency of the near and far detectors. The relative detector efficiency can be determined more precisely than the absolute efficiency. Indeed, from this simplified picture, it is clear that the two-detector scheme is an excellent approach for precisely determining the value of $\sin^2 2\theta_{13}$. In practice, we need to extend this idea to handle more complicated arrangements involving multiple reactors and multiple detectors as in the case of the Daya Bay experiment.

1.2.6 Requirements for a Precision Measurement of θ_{13} with Reactors

As discussed in Section 1.2.4, probing $\sin^2 2\theta_{13}$ with a sensitivity of 0.01 will be a significant advance in neutrino physics. In order to meet this goal, it is important to reduce the statistical and systematic uncertainties as well as to suppress backgrounds. A sensitivity of 0.01 (90% C.L.) implies the standard deviation of the measurement is about 0.0037 for a one-parameter fit (namely, $\sin^2 2\theta_{13}$).

- **High Statistics** The statistical uncertainty of this measurement is dominated by the total number of antineutrino events detected with the far detector that depends on the thermal power of the nuclear power plant, the target mass, and the amount of running time.

- **Optimization of baselines** In the generic design with two detectors, the near detector should be positioned as close to the reactor as possible so that the flux and the energy spectrum of the antineutrinos are not significantly affected by oscillations. The far detector should be placed near the first oscillation maximum, between 1.5 km and 2 km, so as to maximize the disappearance probability (this also minimizes the dependence on Δm^2_{31} as discussed in Section 1.2.4).

- **Reduction of systematic uncertainties** The two major sources of systematic uncertainties arise from variation of thermal power of the reactors and from slight variations in the performance and characteristics of the detectors. Since the uncertainty of this measurement is expected to be 0.0037, the total systematic uncertainty of the measurement must be controlled to better than this level. A significant fraction of the reactor-related systematic uncertainty can be removed by adopting a near-far arrangement of detectors as discussed in Section 1.2.5. In addition, since the value of $\sin^2 2\theta_{13}$ will be extracted by comparing the detected events in the near and far detectors, which is a *relative* measurement, the detector-related systematic uncertainty in this approach is greatly reduced. Furthermore, by ensuring the detectors are built to the same specifications, along with a comprehensive program of monitoring and calibration, it is expected that the total detector-related systematic uncertainty can be kept below the statistical uncertainty.

- **Background suppression** Since the signal rate is low, it is desirable to conduct the experiment underground to reduce cosmic-ray induced backgrounds from neutrons and the radioactive isotope ^{9}Li. Gamma rays originating from natural radioactivity in construction materials and the surrounding rock can contribute to accidentals as the random coincidence of a γ ray interaction in the detector and a neutron capture can mimic the signal. Since Chooz [12] had an overburden of $\sim$300 m.w.e. and achieved a background-to-signal ratio of approximately 0.09, the new generation of reactor-based θ_{13} experiments should have additional overburden and shielding enclosing the detectors to further suppress backgrounds.

1.2.7 Some Proposals for Precision Measurement of θ_{13} with Reactors

As of 2006, there are about 440 nuclear reactors producing electricity in the world. Approximately half of them are PWRs, the kind of reactor that all past reactor-based neutrino experiment have utilized. The majority of these PWRs being in France, Japan, and the United States. However, the majority of the most powerful PWR nuclear power plants reside in Japan [24], South Korea [25], and France [26] with local physicists interested in mounting reactor θ_{13} experiments with sensitivities between 0.02 and 0.03.

Palo Verde, in the United States, is the twelfth most powerful reactor in the world. The plant operator has shown no interest in supporting another experiment. Furthermore, this site is flat within a radius of several km, which would necessitate construction of large, deep vertical shafts for deploying detectors.

A proposal to use the Diablo Canyon plant in California to perform the measurement [13] is now defunct. This is an attractive site, with a mountain range several hundred meters away from twin reactors with a total thermal power of 6.7 $\mathrm{GW_{th}}$. The near site would be similar to Double Chooz requiring a slanted (or vertical) shaft to access the detector. However, environmental concerns and potential interference of the experiment's civil construction of the experiment with the plant's onsite waste storage terminated the project.

1.3 The Daya Bay Reactor Antineutrino Experiment

The objective of the Daya Bay experiment is to determine $\sin^2 2\theta_{13}$ with sensitivity of 0.01 or better. This experiment will be located at the Daya Bay nuclear power complex in southern China. Its location is shown in Fig. 1.10. The experimental site is about 55 km north-east from Victoria Harbor in Hong Kong. Figure 1.11 is a photograph of the complex. The complex consists of three nuclear power plants (NPPs): the Daya Bay NPP, the Ling Ao NPP, and the Ling Ao II NPP. The Ling Ao II NPP is under construction and will be operational by 2010–2011. Each plant has two identical reactor cores. Each core generates 2.9 $\mathrm{GW_{th}}$ during normal operation. The Ling Ao cores are about 1.1 km east of the Daya Bay cores, and about 400 m west of the Ling Ao II cores. There are mountain ranges to the north which provide sufficient overburden to suppress cosmogenic backgrounds in the underground experimental halls. Within 2 km of the site the elevation of the mountain varies generally from 185 m to 400 m.

The six cores can be roughly grouped into two clusters, the Daya Bay cluster of two cores and the Ling Ao cluster of four cores. We plan to deploy two identical sets of near detectors at distances between 300 m and 500 m from their respective cluster of cores to monitor the antineutrino fluxes. Another set of identical detectors, the far detectors, will be located approximately 1.5 km north of the two near detector sets. Since the overburden of the experimental site increases with distance from the cores, the cosmogenic background

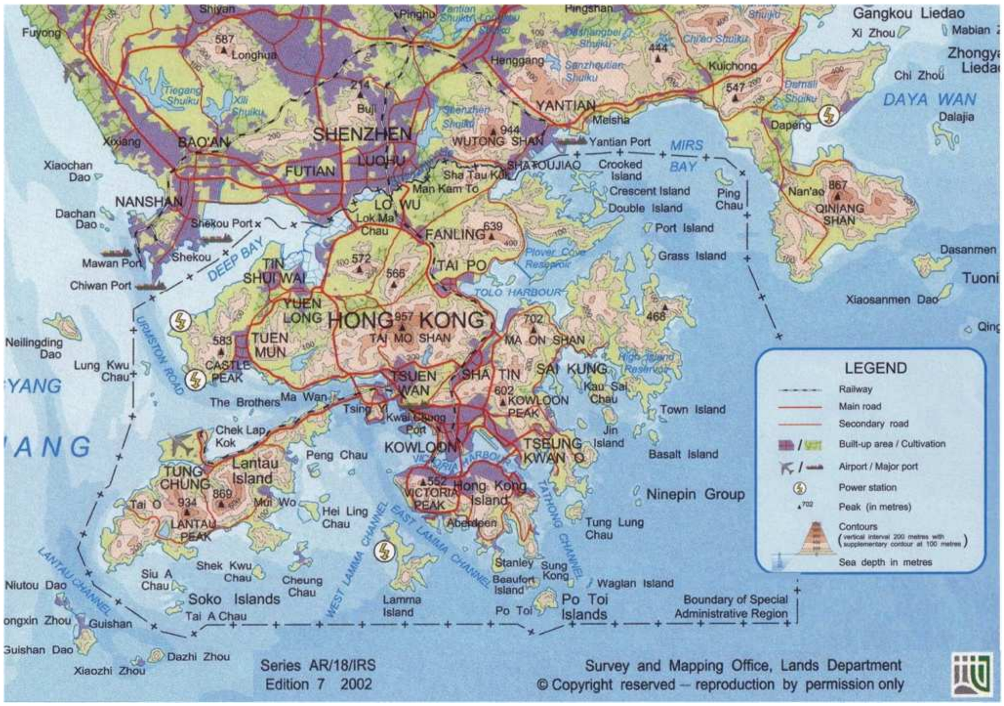

Fig. 1.10. Daya Bay and vicinity: The nuclear power complex is located 55 km from central Hong Kong on the bay “Daya Wan” at the upper right of the map.

Fig. 1.11. The Daya Bay nuclear power complex. The Daya Bay nuclear power plant is in the foreground. The Ling Ao nuclear power plant is in the background. The experimental halls will be underneath the hills to the left.

decreases as the signal decreases, hence keeping the background-to-signal ratio roughly constant. This is beneficial to controlling systematic uncertainties.

Detailed design of the experiment, including baseline optimization (accounting for statistical and systematic uncertainty, backgrounds and topographical information), will be discussed in the following chapters. We will determine $\sin^2 2\theta_{13}$ by comparing the antineutrino fluxes and energy spectra between the near and far detectors. From the baseline optimization, we also conclude we need to collect 170,000 events with the far detector to reach the designed sensitivity. Since the standard error will be 0.0061, Daya Bay would determine the central value of $\sin^2 2\theta_{13}$ derived from Eq. 4 with approximately a six-sigma significance.

Table 1.1 is a summary of the scientific requirements for determining $\sin^2 2\theta_{13}$ with a sensitivity of 0.01 at the 90% confidence level.

Table 1.1. Summary of scientific requirements

Item	Requirement
Sensitivity in $\sin^2 2\theta_{13}$ (90% C.L.)	$\leq$ 0.01
Standard error of $\sin^2 2\theta_{13}$	0.0061
Baseline of the far detector	$\leq$ 2 km
Number of events at the far site	170,000
Background/signal	$\leq$ 0.09

It is possible to instrument a mid detector site between the near and far sites. The mid detectors along with the near and far detectors can be used to carry out additional measurements for systematic studies and for internal consistency checks or to confirm an observed signal. In combination with the near detectors close to the Daya Bay NPP, they could also be utilized to provide a quick determination of $\sin^2 2\theta_{13}$, albeit with sensitivity only as good as Double Chooz, in the early stage of the experiment.

REFERENCES

1. B. T. Cleveland *et al.*, Astrophys. J. **496** (1998) 505.
2. Y. Fukuda *et al.* (SuperK Collaboration), Phys. Rev. Lett., **81** (1998) 1158 [arXiv:hep-ex/9805021]; **82** (1999) 2430 [arXiv:hep-ex/9812011]; S. Fukuda *et al.*, Phys. Rev. Lett. **86** (2001) 5651 [arXiv:hep-ex/010302]; M. B. Smy *et al.*, Phys. Rev. **D69** (2004) 011104 [arXiv:hep-ex/0309011].
3. J. N. Abdurashitov *et al.* (SAGE Collaboration), J. Exp. Theor. Phys. **95** (2002) 181 [arXiv:astro-ph/0204245]; W. Hampel *et al.* (GALLEX Collaboration), Phys. Lett. **B447** (1999) 127; M. Altman *et al.* (GNO Collaboration), Phys. Lett. **B490** (2000) 16 [arXiv:hep-ex/0006034].
4. Q.R. Ahmad et at. (SNO Collaboration), Phys. Rev. Lett **87** 071301 [arXiv:nucl-ex/0106015]; **89** (2002) 011301 [arXiv:nucl-ex/0204008]; **89** (2002) 011302 [arXiv:nucl-ex/0204009]; **92** (2004) 181301 [arXiv:nucl-ex/0309004]; Phys. Rev. **C72** (2005) 055502 [arXiv:nucl-ex/0502021].
5. Y. Fukuda et al. (SuperK Collaboration), Phys. Lett. **B433** (1998) 9 [arXiv:hep-ex/9803006]; **B436** (1998) 33 [arXiv:hep-ex/9805006]; Phys. Rev. Lett., **81** (1998) 1562 [arXiv:hep-ex/9807003]; S. Fukuda *et al.*, Phys. Rev. Lett. **85** (2000) 3999 [arXiv:hep-ex/0009001]; Y. Ashie *et al.*, Phys. Rev. Lett. **93** (2004) 101801 [arXiv:hep-ex/0404034].
6. K. Eguchi *et al*. (KamLAND Collaboration), Phys. Rev. Lett., **90** (2003) 021802 [arXiv:hep-ex/0212021]; **94** (2005) 081801 [arXiv:hep-ex/0406035].
7. E. Aliu *et al.* (K2K Collaboration), Phys. Rev. Lett. **94** (2005) 081802 [arXiv:hep-ex/0411038].
8. D.G. Michael *et at.* (MINOS Collaboration), Phys. Rev. Lett. **97** (2006) 191801 [arXiv:hep-ex/0607088].
9. Z. Maki, M. Nakagawa, and S. Sakata, Prog. Theor. Phys. **28** (1962) 870; B. Pontecorvo, Sov. Phys. JETP **26** (1968) 984; V.N. Gribov and B. Pontecorvo, Phys. Lett. **28B** (1969) 493.
10. G.L. Fogli, E. Lisi, A. Marrone, and A. Palazzo, and A.M. Rotunno, 40th Rencontres de Moriond on Electroweak Interactions and Unified Theories, La Thuile, Aosta Valley, Italy, 5-12 March 2005 [arXiv:hep-ph/0506307].
11. T. Schwetz, Talk given at 2nd Scandinavian Neutrino Workshop (SNOW 2006, Stockholm Sweden, 2-6 May 2006 [arXiv:hep-ph/0606060].
12. M. Apollonio *et al*. (Chooz Collaboration), Eur. Phys. J. C**27**, 331 (2003) [arXiv:hep-ex/0301017].
13. K. Anderson, *et al.*, *White paper report on using nuclear reactors to search for a value of* θ_{13}, arXiv:hep-ex/0402041.

14. ‘Recommendations to the Department of Energy and the National Science Foundation on a U.S. Program of Reactor- and Accelerator-based Neutrino Oscillations Experiments’, http://www.science.doe.gov/hep/NuSAG2ndRptFeb2006.pdf
15. The Neutrino Matrix, http://www.aps.org/neutrino/
16. M.F. James, J. Nucl. Energy **23** 517 (1969).
17. L. Miller, Ph.D Thesis, Stanford University, 2000, unpublished.
18. V.I. Kopeikin, Phys. Atom. Nucl. **66** (2003) 472 [arXiv:hep-ph/0110030].
19. B. Achkar *et al.*, Phys. Lett. **B374** 243 (1996).
20. K. Schreckenbach *et al.*, Phys. Lett. **B160**, 325 (1985); A. A. Hahn *et al.*, Phys. Lett. **B218**, 365 (1989).
21. P. Vogel and J. Engel, Phys. Rev. **D39**, 3378 (1989).
22. P. Vogel and J. F. Beacom, Phys. Rev. **D60**, 053003 (1999) [arXiv:hep-ph/9903554].
23. L.A. Mikaelyan and V.V. Sinev, Phys. Atomic Nucl. **63** 1002 (2000) [arXiv:hep-ex/9908047].
24. M. Kuze *et al.*, *The KASKA project - a Japanese medium-baseline reactor-neutrino oscillation experiment to measure the mixing angle* θ_{13}, arXiv:hep-ex/9908047.
25. K.K.Joo, *Progress Report on RENO*, talk presented at NOW 2006, Otranto, Italy, September 9-16, 2006.
26. F. Ardellier *et al.* (Double Chooz Collaboration), *Double Chooz: A Search for the Neutrino Mixing Angle* θ_{13}, arXiv:hep-ex/0606025.

2 Experimental Overview

To establish the presence of neutrino oscillation due to θ_{13}, and to determine $\sin^2 2\theta_{13}$ to a sensitivity of 0.01 or better at 90% confidence level, at least 170,000 detected events at the far site are needed, and systematic uncertainties in the ratios of near-to-far detector acceptance, antineutrino flux and background have to be controlled to a level almost an order of magnitude better than the previous experiments. Based on recent single-detector reactor experiments such as Chooz, Palo Verde and KamLAND, there are three main sources of systematic uncertainty: reactor-related uncertainty of (2–3)%, background-related uncertainty of (1–3)%, and detector-related uncertainty of (1–3)%. Each source of uncertainty can be further classified into correlated and uncorrelated uncertainties. Hence a carefully designed experiment, including the detector mass, efficiency and background control, is required. The primary considerations driving the improved performance are listed below:

- **identical near and far detectors** Use of identical antineutrino detectors at the near and far sites to cancel reactor-related systematic uncertainties, a technique first proposed by Mikaelyan et al. for the Kr2Det experiment in 1999 [1]. The event rate of the near detector will be used to predict the yield at the far detector. Even in the case of several reactors, reactor-related uncertainties can be controlled to negligible level by careful choice of the near and far site locations.

- **multiple modules** Employ multiple, identical modules at the near and far sites to cross check between modules at each location and reduce detector-related uncorrelated uncertainties. The use of multiple modules in each site enables internal consistency checks (to the limit of statistics). Multiple modules implies smaller detectors which are easier to move. In addition, small modules intercept fewer cosmic-ray muons, resulting in less dead time, less cosmogenic background and hence smaller systematic uncertainty. Taking calibration and monitoring of detectors, redundancy and cost into account, we have selected a design with two modules at each near site and four modules at the far site.

- **three-zone detector module** Each module is partitioned into three concentric zones. The innermost zone, filled with Gd-loaded liquid scintillator (Gd-LS), is the antineutrino target which is surrounded by a zone filled with unloaded LS called the γ-catcher. This middle zone is used to capture γ rays, from IBD events, that escape from the target. This arrangement can substantially reduce the systematic uncertainties related to the target volume and mass, positron energy threshold, and position cut. The outermost zone, filled with transparent mineral oil that does not scintillate, shields against external γ rays entering the active LS volume.

- **sufficient overburden and shielding** Locations of all underground detector halls are optimized to ensure sufficient overburden to reduce cosmogenic backgrounds to the level that can be measured with certainty. The antineutrino detector modules are enclosed with sufficient passive shielding to attenuate natural radiation and energetic spallation neutrons from the surrounding rocks and materials used in the experiment.

- **multiple muon detectors** By tagging incident muons, the associated cosmogenic background can be suppressed to a negligible level. This requires the muon detectors surrounding the antineutrino detectors to have a high efficiency that is known with high precision. Monte Carlo study shows that the efficiency of the muon detector should be $\geq$99.5% (with $\sigma_\epsilon \leq$0.25%). The muon system is designed to have at least two detector systems in each direction. One system utilizes the water shield as a Cherenkov detector, and another employs muon tracking detectors with decent position resolution. Each muon detector can easily be constructed with an efficiency of (90–95)% such that the overall efficiency of the muon system will be better than 99.5%. In addition, the two muon detectors can be used to measure the efficiency of each other to a uncertainty of better than 0.25%.

- **movable detectors** The detector modules are movable, such that swapping of modules between the near and far sites can be used to provide an even higher level of cancellation of detector-related uncertainties (to the extent that they remain unchanged before and after swapping). The residual uncertainties, being secondary, are caused by energy scale uncertainties not completely taken out by calibration, as well as other site-dependent uncertainties. The goal is to reduce the systematic uncertainties as much as possible by careful design and construction of detector modules such that swapping of detectors is not necessary. Further discussion of detector swapping will be given in Chapters 3 and 14.

With these improvements, the total detector-related systematic uncertainty is expected to be $\sim$0.2% in the near-to-far ratio per detector site.

2.1 Experimental layout

Taking the current value of $\Delta m^2_{31} = 2.5 \times 10^{-3}$ eV^2 (see equation 12), the first maximum of the oscillation associated with θ_{13} occurs at $\sim$1800 m. Considerations based on statistics alone will result in a somewhat shorter baseline, especially when the statistical uncertainty is larger than or comparable to the systematic uncertainty. For the Daya Bay experiment, the overburden influences the optimization since it varies along the baseline. In addition, a shorter tunnel will decrease the civil construction cost.

The Daya Bay experiment will use identical detectors at the near and far sites to cancel reactor-related systematic uncertainties, as well as part of the detector-related systematic uncertainties. The Daya Bay site currently has four cores in two groups: the Daya Bay NPP and the Ling Ao NPP. The two Ling Ao II cores will start to generate electricity in 2010–2011. Figure 2.1 shows the locations of all six cores. The

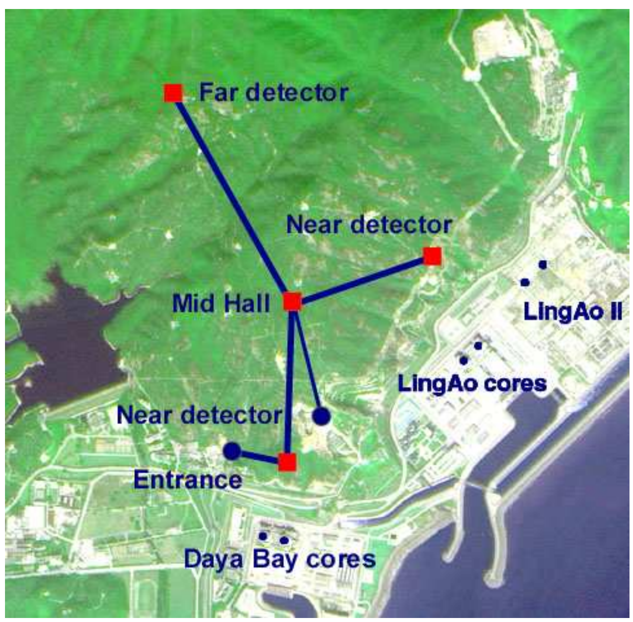

Fig. 2.1. Layout of the Daya Bay experiment.

distance between the two cores in each NPP is about 88 m. Daya Bay is 1100 m from Ling Ao, and the maximum distance between cores will be 1600 m when Ling Ao II starts operation. The experiment will locate detectors close to each reactor cluster to monitor the antineutrinos emitted from their cores as precisely as possible. At least two near sites are needed, one is primarily for monitoring the Daya Bay cores and the other primarily for monitoring the Ling Ao—Ling Ao II cores. The reactor-related systematic uncertainties can not be cancelled exactly, but can be reduced to a negligible revel, as low as 0.04% if the overburden is not taken into account. A global optimization taking all factors into account, especially balancing the overburden and reactor-related uncertainties, results in a residual reactor uncertainty of $<$0.1%

Three major factors are involved in optimizing the locations of the near sites. The first one is overburden. The slope of the hills near the site is around 30 degrees. Hence, the overburden falls rapidly as the detector site is moved closer to the cores. The second concern is oscillation loss. The oscillation probability is appreciable even at the near sites. For example, for the near detectors placed approximately 500 m from the center of gravity of the cores, the integrated oscillation probability is $0.19 \times \sin^2 2\theta_{13}$ (computed with $\Delta m^2_{31} = 2.5 \times 10^{-3}$ eV^2). The oscillation contribution of the other pair of cores, which is around 1100 m away, has been included. The third concern is the near-far cancellation of reactor uncertainties.

After careful study of many different experimental designs, the best configuration of the experiment is shown in Fig. 2.1 together with the tunnel layout. Based on this configuration, a global χ^2 fit (see Eq. 29) for the best sensitivity and baseline optimization was performed, taking into account backgrounds, mountain profile, detector systematics and residual reactor related uncertainties. The result is shown in Fig. 2.2.

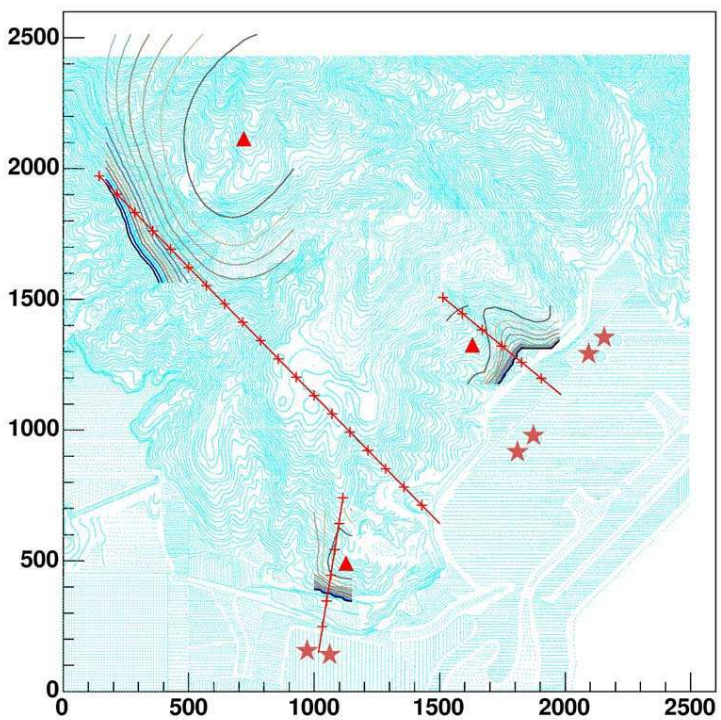

Fig. 2.2. Site optimization using the global χ^2 analysis. The optimal sites are labelled with red triangles. The stars show the reactors. The black contours show the sensitivity when one site's location is varied and the other two are fixed at optimal sites. The red lines with tick marks are the perpendicular bisectors of various combinations of reactors. The mountain contours are also shown on the plot (blue lines).

Ideally each near detector site should be positioned equidistant from the cores that it monitors so that the uncorrelated reactor uncertainties are cancelled. However, taking overburden and statistics into account while optimizing the experimental sensitivity, the Daya Bay near detector site is best located 363 m from the center of the Daya Bay cores. The overburden at this location is 98 m (255 m.w.e.).* The Ling Ao near

*The Daya Bay near detector site is about 40 m east of the perpendicular bisector of the Daya Bay two cores to gain more overburden.

detector hall is optimized to be 481 m from the center of the Ling Ao cores, and 526 m from the center of the Ling Ao II cores† where the overburden is 112 m (291 m.w.e).

The far detector site is about 1.5 km north of the two near sites. Ideally the far site should be equidistant between the Daya Bay and Ling Ao—Ling Ao II cores; however, the overburden at that location would be only 200 m (520 m.w.e). At the optimized locations, the distances from the far detector to the midpoint of the Daya Bay cores and to the mid point of the Ling Ao—Ling Ao II cores are 1985 m and 1615 m, respectively. The overburden is about 350 m (910 m.w.e). A summary of the distances to each detector is provided in Table 2.1.

	DYB	LA	Far
DYB cores	363	1347	1985
LA cores	857	481	1618
LA II cores	1307	526	1613

Table 2.1. Distances (in meters) from each detector site to the centroid of each pair of reactor cores.

It is possible to install a mid detector hall between the near and far sites that is 1156 m from the midpoint of the Daya Bay cores and 873 m from the midpoint of the Ling Ao and Ling Ao II cores. The overburden at the mid hall is 208 m (540 m.w.e.). This mid hall could be used for a quick measurement of $\sin^2 2\theta_{13}$, studies of systematics and internal consistency checks.

There are three branches for the main tunnel extending from a junction near the mid hall to the near and far underground detector halls. There are also access and construction tunnels. The length of the access tunnel, from the portal to the Daya Bay near site, is 292 m. It has a grade of 9.6% [2], which allows the underground facilities to be located deeper with more overburden.

2.2 Detector Design

As discussed above, the antineutrino detector employed at the near (far) site has two (four) modules while the muon detector consists of a cosmic-ray tracking device and active water shield. There are several possible configurations for the water shield and the muon tracking detector as discussed in Section 8. The baseline design is shown in Fig. 2.3.

The water shield in this case is a water pool, instrumented with photomultiplier tubes (PMTs) to serve as a Cherenkov detector. The outer region of the water pool is separated from the inner region by an optical barrier to provide two independent devices for detecting muons. Above the pool the muon tracking detector is made of light-weight resistive-plate chambers (RPCs). RPCs offer good performance and excellent position resolution for low cost.

The antineutrino detector modules are submerged in the water pool, shielding them from ambient radiation and spallation neutrons. Alternate water shielding configurations are discussed in Section 13.1.

2.2.1 Antineutrino detector

Antineutrinos are detected by an organic LS with high hydrogen content via the inverse beta-decay reaction:

$$\bar{\nu}_e + p \longrightarrow e^+ + n$$

The prompt positron signal and delayed neutron-capture signal are combined to define a neutrino event with timing and energy requirements on both signals. Neutrons are captured by hydrogen in the LS, emitting

†The Ling Ao near detector site is about 50 m west of the perpendicular bisector of the Ling Ao-Ling Ao II clusters to avoid installing it in a valley which is likely to be geologically weak, and to gain more overburden.

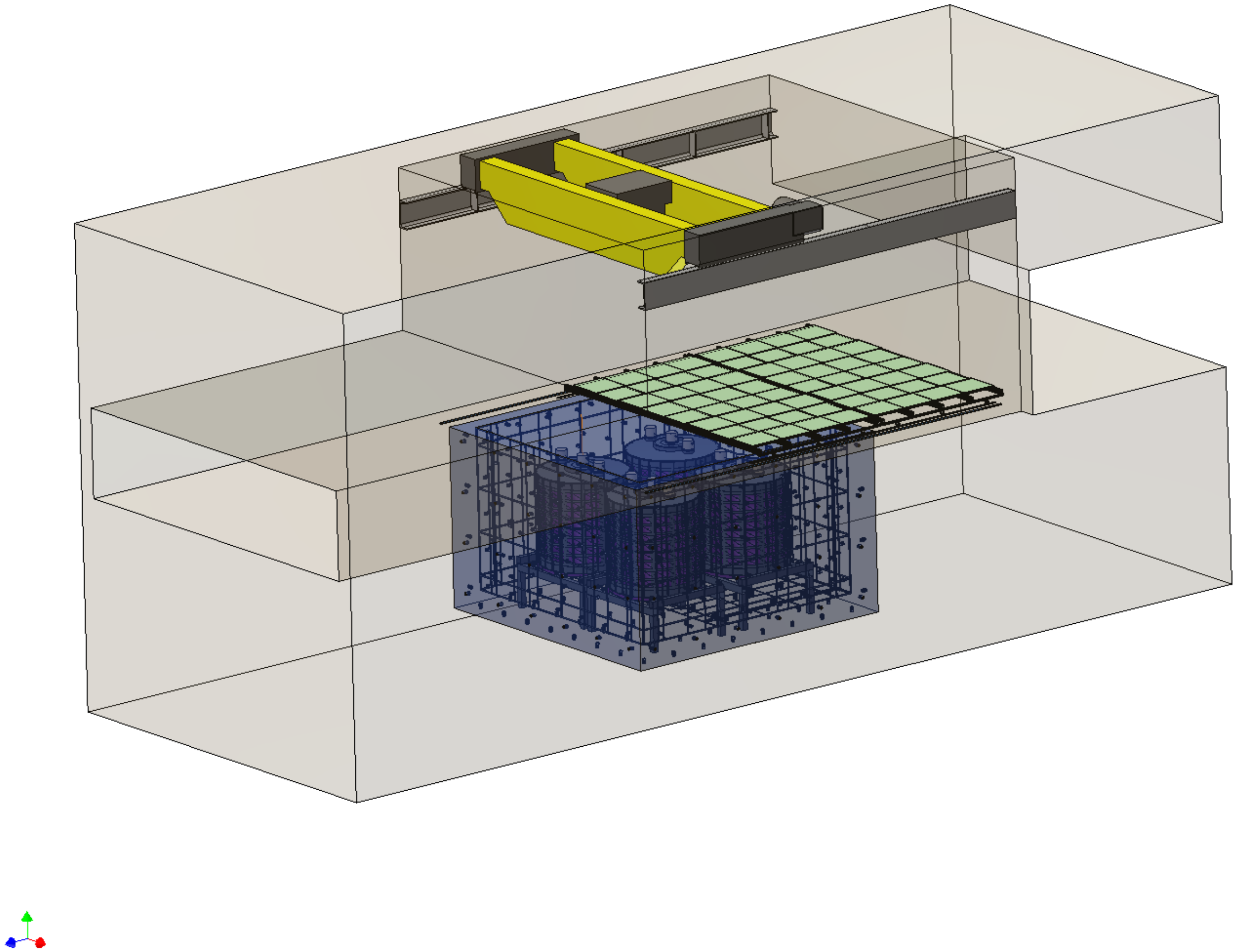

Fig. 2.3. Layout of the baseline design of the Daya Bay detector. Four antineutrino detector modules are shielded by a 1.5 m-thick active water Cherenkov shield. Surrounding this shield and optically isolated from it is another 1-meter of water Cherenkov shield. The muon system is completed with RPCs at the top.

2.2 MeV γ-rays with a capture time of 180 μs. On the other hand, when Gadolinium (Gd), with its large neutron-capture cross section and subsequent 8 MeV release of γ-ray energy, is loaded into LS the much higher γ energy cleanly separates the signal from natural radioactivity, which is mostly below 2.6 MeV, and the shorter capture time ($\sim$30 μs) reduces the background from accidental coincidences. Both Chooz [3] and Palo Verde [4] used 0.1% Gd-loaded LS that yielded a capture time of 28 μs, about a factor of seven shorter than in undoped LS. Backgrounds from random coincidences were thus reduced by a factor of seven as compared to unloaded LS.

The specifications for the design of the Daya Bay antineutrino detector modules are given as follows:

- Employ three-zone detector modules partitioned with acrylic tanks as shown in Fig. 2.4. The target

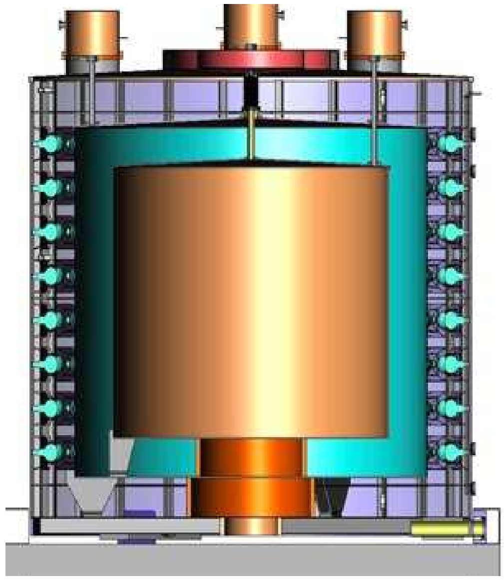

Fig. 2.4. Cross sectional slice of a 3-zone antineutrino detector module showing the acrylic vessels holding the Gd-LS at the center (20 ton), LS between the acrylic vessels (20 ton) and mineral oil (40 ton) in the outer region. The PMTs are mounted on the inside walls of the stainless steel tank.

  volume is defined by the physical dimensions of the central region of Gd-LS. This target volume is surrounded by an intermediate region filled with normal LS to catch γ rays escaping from the central region. The LS regions are embedded in a volume of mineral oil to separate the PMTs from the LS and suppress natural radioactivity from the PMT glass and other external sources.

  Four of these modules, each with 20 ton fiducial volume, will be deployed at the far site to obtain sufficient statistics and two modules will be deployed at each near site, enabling cross calibrations. Deploying an equal number of near and far detectors allows for flexibility in analyzing the data to minimize the systematic uncertainties, such as analyzing with matched near-far pairs.

  In this design, the homogeneous target volume is well determined without a position cut since neutrinos captured in the unloaded LS will not in general satisfy the neutron energy requirement. Each vessel will be carefully measured to determine its volume and each vessel will be filled with the same set of mass-flow and (volume) flow meters to minimize any variation in relative detector volume and mass. The effect of neutron spill-in and spill-out across the boundary between the two LS regions will be cancelled when pairs of identical detector modules are used at the near and far sites. With the shielding of mineral oil, the singles rate will be reduced substantially. The trigger threshold can thus be lowered to below 1.0 MeV, providing $\sim$100% detection efficiency for the prompt positron signal.

- The Gd-LS, which is the antineutrino target, should have the same composition and fraction of hydrogen for each pair of detectors (one at a near site and the other at the far site). The detectors will be filled in pairs (one near and one far detector) from a common storage vessel to assure that the composition is the same. Other detector components such as unloaded LS and PMTs will be characterized and distributed evenly to a pair of detector modules during assembly to equalize the properties of the modules.

- The energy resolution should be better than 15% at 1 MeV. Good energy resolution is desirable for reducing the energy-related systematic uncertainty on the neutron energy cut. Good energy resolution is also important for studying spectral distortion as a signature of neutrino oscillations. The primary driver for the energy resolution is to achieve sufficient energy calibration precision for neutron captures throughout the detector volume in a reasonable time.

- The time resolution should be better than 1 ns for determining the event time and for studying backgrounds.

Detector modules of different shapes, including cubical, cylindrical, and spherical, have been considered. From the point of view of ease of construction cubical and cylindrical shapes are particularly attractive. Monte Carlo simulation shows that modules of cylindrical shape can provide better energy and position resolutions for the same number of PMTs. Figure 2.4 shows the structure of a cylindrical module. The PMTs are arranged along the circumference of the outer cylinder. The surfaces at the top and the bottom of the outer-most cylinder are coated with diffuse reflective materials. Such an arrangement is feasible since 1) the event vertex is determined only with the center of gravity of the charge, not relying on the time-of-flight information,[‡] 2) the fiducial volume is well defined with a three-zone structure, thus no accurate vertex information is required. Details of the antineutrino detector will be discussed in Chapter 6.

2.2.2 Muon detector

Since most backgrounds originate from cosmic-ray muon interactions with nearby materials, it is desirable to have a very efficient muon detector with some tracking capability. This enables the study and rejection of cosmogenic backgrounds. The two detector technologies are water Cherenkov counters and RPCs. The combined water Cherenkov detector and RPC can achieve muon detection efficiencies close to 100%. Furthermore, these two independent detectors can cross check each other. Their inefficiencies and the associated uncertainties can be well determined by cross calibration during data taking. We expect the inefficiency will be lower than 0.5% and the uncertainty of the inefficiency will be better than 0.25%.

Besides being a shield against ambient radiation, the water shield can also be utilized as a water Cherenkov counter by installing PMTs in the water. The water Cherenkov detector is based on proven technology, and known to be very reliable. With sufficient PMT coverage and reflective surfaces, the efficiency of detecting muons should exceed 95%. The current baseline design of the water shield is a water pool, similar to a swimming pool with a dimensions of 16 m (length) $\times$ 16 m (width) $\times$ 10 m (height) for the far hall containing four detector modules, as shown in Fig. 2.5. The PMTs of the water Cherenkov counters are mounted facing the inside of each water volume. This is a simple and proven technology with very limited safety concerns. The water will effectively shield the antineutrino detectors from radioactivity in the surrounding rocks and from radon, with the attractive features of being simple, cost-effective and rapidly deployable.

RPCs are very economical for instrumenting large areas, and simple to fabricate. The Bakelite based RPC developed by IHEP for the BES-III detector has a typical efficiency of 95% and noise rate of 0.1 Hz/cm^2 per layer [5]. A possible configuration is to build four layers of RPC, and require three out of four layers hit within a time window of 20 ns to define a muon event. Such a scheme has an efficiency and low noise rate. Although RPCs are an ideal large area muon detector due to their light weight, good performance, excellent position resolution and low cost, it is hard to put them inside water to fully surround the water pool. The best choice seems to use them only at the top of the water pool.

[‡]Although time information may not be used in reconstructing the event vertex, it will be used in background studies. A time resolution of 0.5 ns can be easily realized in the readout electronics.

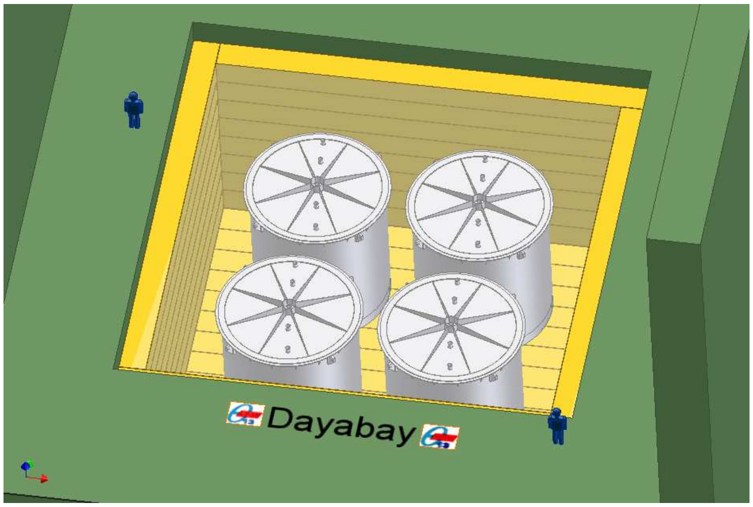

Fig. 2.5. The water pool with four antineutrino detector modules inside.

REFERENCES

1. L.A. Mikaelyan and V. V. Sinev, Phys. Atom. Nucl. **63**, 1002 (2000); L. Mikaelyan, Nucl. Phys. Proc. Suppl. **91**, 120 (2001); L.A. Mikaelyan, Phys. Atom. Nucl. **65**, 1173 (2002).
2. *Report of Preliminary Feasibility Study of Site Selection for the Daya Bay Neutrino Experiment*, prepared by Beijing Institute of Nuclear Energy, September, 2004.
3. M. Apollonio *et al*. (Chooz Collaboration), Phys. Lett. **B420**, 397 (1998); Phys. Lett. **B466**, 415 (1999); Eur. Phys. J. **C27**, 331 (2003).
4. F. Boehm *et al.* (Palo Verde Collaboration), Phys. Rev. Lett. **84**, 3764 (2000) [arXiv:hep-ex/9912050]; Phys. Rev. **D62**, 072002 (2000) [arXiv:hep-ex/0003022]; Phys. Rev. **D64**, 112001 (2001) [arXiv:hep-ex/0107009]; A. Piepke et al., Nucl. Instr. and Meth. **A432**, 392 (1999).
5. J.W. Zhang *et al.*, High Energy Phys. and Nucl. Phys., **27**, 615 (2003); JiaWen Zhang et al., Nucl. Inst. Meth. **A540**, 102 (2005).

3 Sensitivity & Systematic Uncertainties

The control of systematic uncertainties is critical to achieving the $\sin^2 2\theta_{13}$ sensitivity goal of this experiment. The most relevant previous experience is the Chooz experiment [1] which obtained $\sin^2 2\theta_{13} < 0.17$ for $\Delta m^2_{31} = 2.5 \times 10^{-3}\mathrm{eV}^2$ at 90% C.L., the best limit to date, with a systematic uncertainty of 2.7% and statistical uncertainty of 2.8% in the ratio of observed to expected events at the 'far' detector. In order to achieve a $\sin^2 2\theta_{13}$ sensitivity below 0.01, both the statistical and systematic uncertainties need to be an order of magnitude smaller than Chooz. The requirements on the statistical uncertainties, systematic uncertainties, and background measurements for the Daya Bay experiment to reach the design sensitivity are listed in Table 3.1. In this chapter we discuss our strategy for achieving the levels of uncertainty in

Requirement	**Near Site**	**Far Site**
Statistical uncertainty	0.05%	0.16%
Detector systematic uncertainty	0.38%/module	
Reactor power systematic	0.13%	
Background uncertainty	0.3%	0.2%

Table 3.1. Requirements on uncertainties necessary for achieving the sensitivity goal of $\sin^2 2\theta_{13} < 0.01$ at 90% C.L..

Table 3.1. Achieving these goals will require special care and substantial effort, and can only be realized by incorporating rigid constraints in the design of the experiment.

There are three main sources of systematic uncertainties: reactor, background, and detector. Each source of uncertainty can be further classified into correlated and uncorrelated uncertainties.

3.1 Reactor Related Uncertainties

For a reactor with only one core, all uncertainties from the reactor, correlated or uncorrelated, can be canceled precisely by using one far detector and one near detector (assuming the distances are precisely known) and forming the ratio of measured antineutrino fluxes [2]. In reality, the Daya Bay nuclear power complex has four cores in two groups, the Daya Bay NPP and the Ling Ao NPP. Another two cores will be installed adjacent to Ling Ao, called Ling Ao II, which will start to generate electricity in 2010–2011. Figure 2.1 shows the locations of the Daya Bay cores, Ling Ao cores, and the future Ling Ao II cores. Superimposed on the figure are the tunnels and detector sites. The distance between the two cores at each NPP is about 88 m. The midpoint of the Daya Bay cores is 1100 m from the midpoint of the Ling Ao cores, and will be 1600 m from the Ling Ao II cores. For this type of arrangement, with more reactor cores than near detectors, one must rely upon the measured reactor power levels in addition to forming ratios of measured antineutrino fluxes in the detectors. Thus there is a residual uncertainty in the extracted oscillation probability associated with the uncertainties in the knowledge of the reactor power levels. In addition to the reactor power uncertainties, there are uncertainties related to uncertainties in the effective locations of the cores relative to the detectors.

3.1.1 Power Fluctuations

Typically, the measured power level for each reactor core will have a correlated (common to all the reactors) uncertainty of the order of 2% and an uncorrelated uncertainty of similar size. Optimistically, we may be able to achieve uncorrelated uncertainties of 1%, but we conservatively assume that each reactor has 2% uncorrelated uncertainty in the following. (We note that both Chooz and Palo Verde achieved total reactor power uncertainties of 0.6–0.7%. The appropriate value for the Daya Bay reactors will need to be studied in detail with the power plant and could hopefully be reduced below 2% per core.) If the distances are precisely known, the correlated uncertainties will cancel in the near/far ratio.

For the geometry of the Daya Bay experiment, we have (effectively) two near detectors. One near site primarily samples the rate from the two Daya Bay cores and and the other primarily samples the rate from the (two or four) Ling Ao cores. The detectors at the far site do not sample the reactor cores equally, so one needs to consider the weighting of the data from the near sites relative to the far site. In order to provide optimal relative weights of the near sites one can utilize the following combination of ratios in the event rates of the far and near detectors:

$$\rho = \left[\alpha \sum_r \frac{\phi_r}{(L_r^{DB})^2} + \sum_r \frac{\phi_r}{(L_r^{LA})^2} \right] \Big/ \sum_r \frac{\phi_r}{(L_r^f)^2} \tag{16}$$

where ϕ_r is the antineutrino flux at unit distance from core r, L_r^f is the distance from reactor r to the far site, L_r^{DB} (L_r^{LA}) is the distance from reactor r to the near Daya Bay (Ling Ao) site, and α is a constant chosen to provide the proper weighting of the near site data and minimize the sensitivity of ρ to the uncertainties in the relative reactor power levels. (In Eq. 16 we have neglected neutrino oscillations. In the absence of oscillations and given a value of α, the quantity ρ is completely determined by the geometry. Thus a measurement of ρ that differs from this value could then be used to determine the oscillation probability that depends upon $\sin^2 2\theta_{13}$ with minimal systematic uncertainty due to the uncorrelated reactor power uncertainties.)

To illustrate the utility of the ratio ρ in Eq. 16, we can consider a slightly simplified geometry where there are only two cores and two near detectors. Each near detector is located at the same close distance from one reactor core. Assuming the cross-talk in a near detector from the other core can be neglected then the value of $\alpha = (L_{LA}^f / L_{DB}^f)^2$ will correct the ratio ρ for the fact that the two reactors are not sampled equally by the far detector. (Here L_{DB}^f and L_{LA}^f are the distances of the far detector from the two reactor cores.) Then the ratio ρ would be independent of the reactor power uncertainties.

For the more complex situation as in Fig. 2.1, the optimal choice of the weighting factor α is somewhat different, and can be computed from knowledge of the relative distances and powers of the reactor cores. One can also determine α by Monte Carlo simulations that minimize the systematic uncertainty in ρ due to uncorrelated reactor power uncertainties. The weighting of near sites using α does introduce a slight degradation (in our case $<$11% fractional increase) in the statistical uncertainty. The correlated uncertainties of the reactors are common to both the numerator and denominator of the ratio ρ, and therefore will cancel.

Using the detector configuration shown in Fig. 2.1, with two near sites at $\sim$500 m baselines to sample the reactor power and a far site at an average baseline of $\sim$1800 m, an uncorrelated uncertainty of 2% for each core and optimal choice of α leads to the estimated reactor power contribution to σ_ρ (i.e., the fractional uncertainty in the ratio ρ) shown in Table 3.2 for the case of four (six) reactor cores. In Section 3.4.1 below,

Number of cores	α	σ_ρ(power)	σ_ρ(location)	σ_ρ(total)
4	0.338	0.035%	0.08%	0.087%
6	0.392	0.097%	0.08%	0.126%

Table 3.2. Reactor-related systematic uncertainties for different reactor configurations. The uncorrelated uncertainty of the power of a single core is assumed to be 2%.

we study the sensitivity of the Daya Bay experiment to neutrino oscillations and $\sin^2 2\theta_{13}$ using a more general χ^2 analysis that includes all the significant sources of systematic uncertainty. The optimal weighting of near sites in that analysis is implemented by allowing all the reactor core powers to vary in the χ^2 minimization associated with the measured rates in the different detectors.

3.1.2 Location Uncertainties

The center of gravity of the antineutrino source in each core will be determined to a precision of about 30 cm. We assume that the location uncertainties are uncorrelated, and so their combined effect will be reduced by $\sim \sqrt{N_r}$ where N_r is the number of reactor cores. The resulting fractional uncertainty in the near/far event ratio is estimated to be 0.08% for the near baseline of $\sim$500 m.

3.1.3 Spent Fuel Uncertainties

In addition to fission, beta decay of some fission products can also produce antineutrinos with energy higher than the inverse beta decay threshold 1.8 MeV. Some of these have long lifetimes, such as [3]

$$\begin{aligned} {}^{106}\mathrm{Ru}(T_{1/2} = 372\,d) &\rightarrow {}^{106}\mathrm{Rh}(T_{1/2} = 20\,s, E_{\max} = 3.54\mathrm{MeV}) \\ {}^{144}\mathrm{Ce}(T_{1/2} = 285\,d) &\rightarrow {}^{144}\mathrm{Pr}(T_{1/2} = 17\,m, E_{\max} = 3.00\mathrm{MeV}) \\ {}^{90}\mathrm{Sr}(T_{1/2} = 28.6\,y) &\rightarrow {}^{90}\mathrm{Y}(T_{1/2} = 64\,h, E_{\max} = 2.28\mathrm{MeV}) \end{aligned} \tag{17}$$

These isotopes will accumulate in the core during operations. Normally a fuel rod will produce power in the core for 2–3 years. The inverse beta decay rate arising from these fission products will increase to 0.4–0.6% of the total event rate. In the 1.8–3.5 MeV range, the yield will increase to about 4%. Neutron capture by fission products will also increase the total rate by 0.2% [3].

The Daya Bay and Ling Ao NPPs store their spent fuel in water pools adjoining the cores. A manipulator moves the burnt-out fuel rods from the core to the water pool during refueling. The long lived isotopes mentioned in the previous paragraph will continue to contribute to the antineutrino flux. The spent fuel data, as well as the realtime running data, will be provided to the Daya Bay Collaboration by the power plant.

Taking the average of all fuel rods at different life cycles, and the decay in the spent fuel, these isotopes are estimated to contribute $<$0.5% to the event rate (prior to receiving the detailed reactor data). All of these events are in the low energy region. Since the spent fuel is stored adjoining to the core, the uncertainty in the flux will be canceled by the near-far relative measurement, in the same way as the cancellation of the reactor uncertainties. The uncertainty associated with the spent fuel is much smaller than the assumed 2% uncorrelated uncertainty of reactor fission, and thus we expect it will have negligible impact on the θ_{13} sensitivity.

3.2 Detector Performance

The measurement of $\sin^2 2\theta_{13}$ to a precision of 0.01 in the Daya Bay experiment will require special care in detector building, characterization of the detector properties, and frequent monitoring of the detector performance and condition. We begin this section by discussing our strategies and methods for addressing the fabrication and deployment issues that will result in well-understood detector modules. The properties of the detector affecting the performance goals must be then calibrated and monitored, and we will implement a comprehensive program for calibrating and monitoring the detector modules. Finally we then estimate the resulting expected detector-related systematic uncertainties.

3.2.1 Fabrication, Assembly, and Filling

The most stringent requirement for the detector construction is the control of detector geometry, the target mass, and the chemical composition of the scintillator liquid. Before transporting the detector modules underground, the geometry of the detector modules will be surveyed carefully with laser devices, which can achieve $<$25 μm precision in measuring detector dimensions. (Note that $<$0.1 mm precision is required to achieve a 0.01% precision in target volume measurement.) In-situ monitoring equipment inside the detector modules will then be used to track any changes during the transport or filling of the modules.

The filling of the detectors will be performed underground. Liquids from the same batch be used to fill a pair of detectors to ensure the same chemical composition. During the filling, the flow rate will be monitored constantly with high precision flowmeters to ensure the same target mass between the pair. In each detector module, we will have load sensors, liquid level sensors in each zone, as well as CCD cameras to monitor the detector conditions continuously.

3.2.2 Calibration/Monitoring Program

As discussed in Section 11.2.4, the filled detector modules will then be transported to the designated experimental halls where they will be located for data acquisition. At this point, critical differences between detector modules will be studied and understood at the level of normalization uncertainty of $\sim$0.1%. Subsequent changes in a particular detector module (over time or after relocation at another site) be monitored to insure that the normalization uncertainty remains below $\sim$0.1%. Achieving these goals will be accomplished through a comprehensive program of detector calibration and monitoring.

We have designed a program with three different classes of procedures:

1. "complete" characterization of a detector module,
2. "partial' characterization, and
3. routine monitoring.

We envision that the complete characterization (procedure #1) will generally be performed once during initial commissioning of a detector module before taking physics data. Procedure #2 would be employed after relocation of a detector module or after some other change that requires a careful investigation of the detector properties and will involve a subset of the activities in procedure #1. If substantial changes are detected during procedure #2, then we would likely opt for reverting to procedure #1. Finally, procedure #3 will involve both continuous monitoring of some detector parameters as well as frequent (i.e., daily or weekly) automated procedures to acquire data from LED light sources and radioactive sources deployed into the detector volume.

The requirements and proposed solutions for procedure #1 are listed in Table 3.3. These will be manually operated procedures using equipment and systems to be described below, and will likely entail several weeks activity.

Requirement	**Description**	**Proposed Solution(s)**
Optical Integrity	Spatial uniformity of response, light attenuation	LED, γ sources
PMT gains	Match gains of all PMTs	LED - single p.e. matching
PMT timing	$\sim$1 ns timing calibration for each PMT	Pulsed LED
Energy scale	Set scale of energy deposition	Gamma sources
H/Gd ratio	Measure relative Gd fraction	neutron source

Table 3.3. Requirements for the full manual calibration procedure #1.

Procedure #2 will be a subset (to be determined) of the activities in procedure #1. These will also be manually operated procedures using equipment and systems to be described below, and will likely entail several days activity.

The requirements and proposed solutions for procedure #3 are listed in Table 3.4. Procedure #3 will entail continuous in-situ monitoring (Section 7.3), monitoring of continuously produced spallation-induced activity (Section 3.2.2.3), and regularly scheduled automated deployment of sources (Section 3.2.2.2).

Requirement	Description	Proposed Solution(s)
Mechanical/thermal	Verify these properties are stable	Load sensors, thermometers, etc.
Optical stability	Track variations in light yield	Gamma sources, spallation products
Uniformity, light attenuation	Monitor spatial distribution of light	Gamma sources, spallation products
Detection efficiency	Monitor ϵ for neutrons and positrons	Gamma sources, neutron sources
PMT gains	Monitor 1 p.e. peaks	LED source

Table 3.4. Requirements for automated calibration procedure #3.

3.2.2.1 Commissioning

In the commissioning phase, a manual calibration system will be employed to characterize the entire (inner) detector response. During this procedure, the water pool must be full or mostly full in order to reduce the singles rate and maintain thermal stability of the detector. In each detector, we envision to deploy a few radioactive sources, and make point-to-point sampling of the inner detector volume every 40 cm, leading to about 200 measurements per source per detector. We also envision using common sources in different detectors to measure absolute rates and detection efficiency.

3.2.2.2 Automated Monitoring

Automated deployment systems will be used to monitor all detector modules on a routine (perhaps daily) basis. Each detector module will be instrumented with a few identical automated deployment systems, each will allow the full z access inside the detector. At present, we envision three such ports, one along the central z axis, one in the gamma catcher, and the other one along an off-center z axis. The configuration three axes are illustrated in Fig. 3.1.

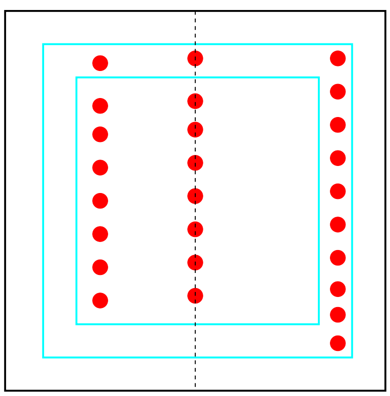

Fig. 3.1. Illustration of the source deployment axes.

Each deployment system will be capable of deploying four different sources into the detector. Currently, we plan to include ^{68}Ge (e^{+}), ^{60}Co (γ), and neutron (^{252}Cf, Am-Be, or ^{238}Pu-^{13}C) sources, plus a LED diffuser ball.

The automated deployment of sources will be scheduled simultaneously for all eight detector modules, and is expected to require about 2-3 hours. Data acquisition for antineutrino measurements will be suspended during this period, and these data runs will be designated as calibration runs. The automated calibration source system control computer will need to communicate and coordinate with the data acquisition system during these calibration runs so all the data are properly recorded and labeled.

Simulation studies have indicated that with the source data along these three axes, plus a few additional diagnostic measurements, one can monitor the detector conditions and achieve quantitative measurement of detector parameters to give a $\sim$0.2% detector-related systematic uncertainty. See more details in Section 3.2.2.5.

3.2.2.3 Cosmogenic Events

Cosmic muons passing through the detector modules will produce useful short-lived radioactive isotopes and spallation neutrons. These events will follow the muon signal (detected in the muon system as well as the detector) and will be uniformly distributed throughout the detector volume. Therefore, these provide very useful information on the full detector volume which is complementary to the information obtained by deploying point sources. Such events are used by KamLAND to study the energy and position reconstruction as well as to determine the fiducial volume. As with KamLAND, the Daya Bay experiment will use primarily spallation neutron capture and ^{12}B decay ($\tau = 29.1$ ms and $Q = 13.4$ MeV).

The rates of these events for Daya Bay are given in Table 3.5. These rates are sufficient to determine the energy stability relevant to the neutron capture efficiency to $\sigma_E/E$$\sim$0.5% for 100 pixels (200 kg each) in each detector on time scales of 1(10) days for the near(far) detector modules, respectively.

Event type	**Near Site Rate**	**Far Site Rate**
Neutrons	13500/day	1100/day
^{12}B	300/day	28/day

Table 3.5. Estimated production rates (per 20 ton detector module) for spallation neutron and ^{12}B events in the Daya Bay experiment.

As an example, the simulated detector response (total charge) for the 8 MeV n-Gd capture signals throughout the detector target volume is shown in Fig. 3.2. Regular monitoring of the full-volume response for these events, compared with the regular automated source deployments, will provide precise information on the stability (particularly of optical properties of the detector, but also general spatial uniformity of response) of the detector modules. With the addition of Monte Carlo simulations, this comparison can be used to accurately assess the relative efficiency of different detector modules as well as the stability of the efficiency of each module.

3.2.2.4 PMT Calibration and Monitoring

The timing, gain, and quantum efficiencies of the PMTs are crucial input to the energy measurement and position reconstruction. An LED system (470 nm) with a control trigger can be used to calibrate the PMT timing. Due to the cylindrical symmetry of the detector, we can deploy the LED diffuser ball along the central z axis and calibrate the PMT timing ring by ring so that we obtain 1 ns precision in the relative timing of all PMTs in a module. At the same time, the absolute gain of the PMTs can be calibrated by the ADC peaks of the single photoelectrons, after which individual discriminator thresholds can be set. Assuming azimuthal symmetry, the relative quantum efficiencies for different tubes in the same ring can be calibrated based on the measured rate during the LED z scan. A tight timing cut may be necessary to remove the background counts as well as photons reflected from the wall. In principle, only a global factor in QE will be left undetermined after this step for all the tubes in a detector module. Each PMT can be tracked on a weekly (or even daily, if necessary) basis using automated deployment of the LED ball.

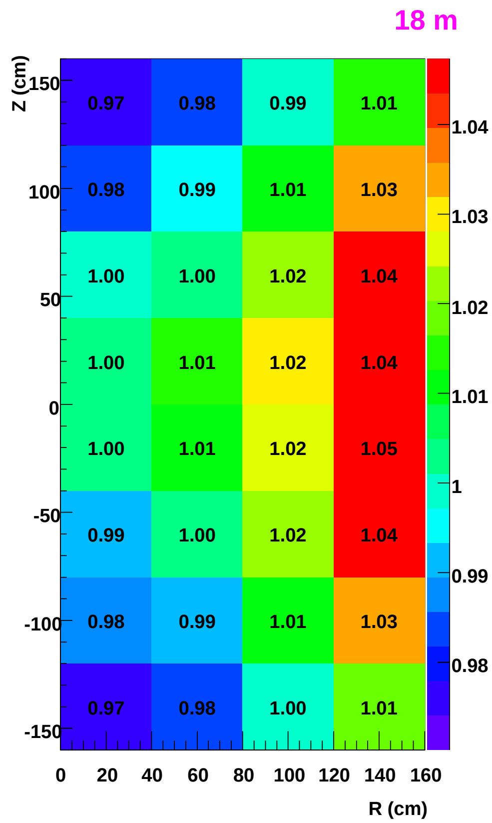

Fig. 3.2. The Gd capture p.e. yield for the spallation neutrons (normalized to the yield at the detector center) as a function of the neutron vertex (R, z).

3.2.2.5 Determination of Detector Optical Parameters

The generation, transmission, and reflection of optical photons in each detector must be well-understood. The associated detector optical parameters will be employed in the event reconstruction, so that reconstructed positron and neutron energies for all the detectors are "identical" to the required precision (generally $<$0.5%).

In general, the relevant optical properties of an AD can be characterized by the following set of parameters: the light yields in the target region ($Y_{\rm tgt}$) and the gamma catcher ($Y_{\rm gcat}$), the attenuation lengths of the target ($L_{\rm tgt}$), gamma catcher ($L_{\rm gcat}$), and mineral oil ($L_{\rm mo}$), the reflectivity of the top and bottom reflectors ($R_{\rm top}$ and $R_{\rm bottom}$). (The reflectivity of the side walls will be small so this should not be a significant factor in the optical properties.) Simulation studies have indicated that using the ^{68}Ge source, one can calibrate the positron efficiency readily to $\sim$0.05% precision. The 6 MeV visible energy cut for the neutrons, on the other hand, is in the middle of a rather long tail in the delayed energy spectrum, which is more difficult to calibrate. In the following Table 3.6, we summarize the required precision on individual parameters, determined from simulation, to achieve a $<$0.2% precision on the neutron efficiency. These specs should be interpreted as the precision to which one needs to calibrate a given parameter, rather than an absolute tolerance from a nominal value. That is, we need only know the measured values among all the detectors with this precision in order to meet the requirement on the detector systematic uncertainty and its effect on the measurement of $\sin^2 2\theta_{13}$. In what follows, we shall outline a comprehensive program, which can determine all of the parameters listed in Table 3.6.

Parameter	Tolerance
Y_{tgt}	$\pm$ 1.0%
Y_{gcat}	$\pm$ 1.6%
L_{tgt}	$\pm$ 5.4%
L_{gcat}	$\pm$ 11.2%
L_{mo}	$\pm$ 15.0%
R_{top}	$\pm$ 7.3%
R_{bottom}	$\pm$7.3%

Table 3.6. The nominal values of detector parameters considered in this study and their specs. See text for explanations.

Attenuation Lengths

Fixed LEDs can be deployed at three different positions in the oil buffer, as shown in Fig. 3.3. Two

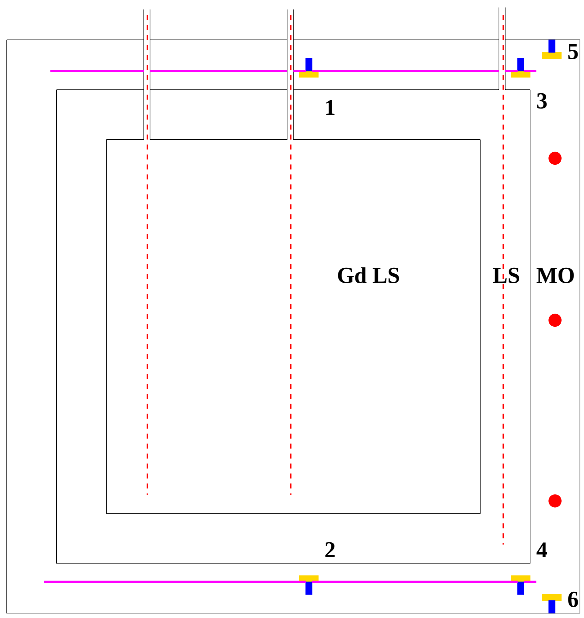

Fig. 3.3. A diagram for measuring the attenuation lengths in all three zones. The calibration PMTs are shown as blue blocks with yellow faces. The red balls indicate the LED diffuser ball positions for measurements of the buffer oil transparency. The magenta thick lines on the top and bottom represent the reflectors. The vertical dashed lines indicate regions of deployment for the LED ball for measurement of the transparencies of the central region and gamma catcher, as well as determination of the reflectivity of the top/bottom reflectors.

opposing phototubes (PMTs #5 and #6) are located at the top and bottom of the oil buffer as shown. The ratio of the rates measured for the three LED locations, corrected for the differing acceptance and reflections from the wall (see below), leads directly to the attenuation length of the mineral oil. With two such phototubes, the attenuation of the oil is determined with redundancy. Since the understanding of the acceptance is crucial for this application, it is desirable to use smaller phototubes.

A similar scheme can be used to determine the attenuation length of the gamma catcher. To have a longer lever arm, the LED ball should be placed at different vertical locations in the gamma catcher, as illustrated in Fig. 3.3. Light that is vertically transmitted through the gamma catcher region will be detected by phototubes located at the top and bottom of the tank (PMTs #3 and #4). By taking the ratio of rates for the diffuser ball at different z, the (constant) attenuation from the oil buffer will cancel. This leads to a clean determination of the attenuation in the gamma catcher. Preliminary simulation of this procedure is illustrated Fig. 3.4, where 2” phototubes are implemented in the Monte Carlo. With careful study of the

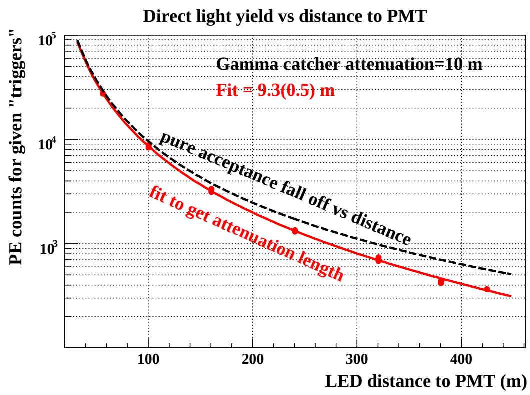

Fig. 3.4. Determination of the gamma catcher attenuation length by deploying the LED at different z locations.

phototube acceptance, we anticipate a very precise determination of the attenuation length.

Similarly, if one deploys the light source along the center or edge of the central target region, the attenuation length of the target region can be determined using PMTs deployed at the top and bottom of the detector (PMTs #1 and #2 in Fig. 3.3).

Top/Bottom Reflectivity

The top/bottom reflectivity can also be determined using the scheme in Fig. 3.3. Separation of the direct and reflected light is facilitated by using the time of arrival of the light. In Fig. 3.5, the hits timing of PMTs #1 (Fig. 3.3) is illustrated with an LED deployed at the center of the detector. The separation of direct and

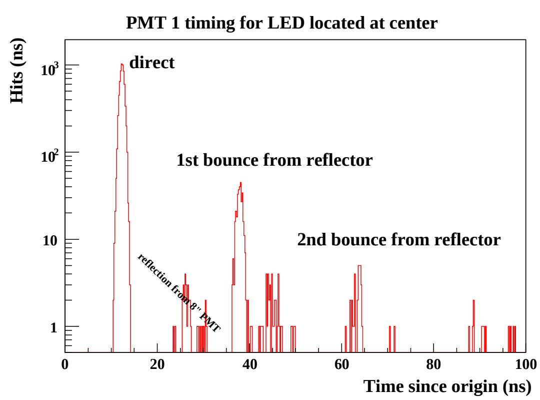

Fig. 3.5. The hits timing of PMT #1 for direct and reflected lights from a pulsing LED at the detector center.

reflected lights can be achieved easily with a multi-hit TDC with $\sim$ns precision. By comparing the measured reflected/direct light ratio with the Monte Carlo (with precisely measured attenuation lengths as inputs), the top/bottom reflectivity can then be determined accurately.

Global Fit Determination of Detector Optical Properties

Since we will not have absolute quantum efficiency values for all PMTs, it is not possible to determine the absolute light yield of the liquid scintillator. The total photoelectron (p.e.) yields of radioactive sources (like ^{60}Co) can be measured at the central region and this can be used to establish the energy calibration for each detector.

By studying the p.e. yields in different regions of the detector we can determine the ratio $Y_{\rm tgt}/Y_{\rm gcat}$. To first order, assuming that a calibration source deposits energy only locally, the ratio of light yields for the two regions can be determined after correction for the attenuation lengths. The attenuation length, on the other hand, causes the response of a given phototube to vary with vertex position. Therefore, by deploying a source at different locations in the detector module, and by analyzing the total light yield as well as the distribution of p.e. yields in the PMTs, one can make a simultaneous fit to determine $L_{\rm tgt}$ and the ratio $Y_{\rm tgt}/Y_{\rm gcat}$. In principle, all the detector optical properties can be determined using a global fit to a sufficiently complete set of data.

The feasibility of this approach was studied with simulation. We simulated the detector with various sets of $Y_{\rm tgt}/Y_{\rm gcat}$ and $L_{\rm tgt}$. In each case the detector was calibrated by a 1 MeV electron source * in different locations according to Fig. 3.1 along three z axes. The simulated data (p.e. for each PMT) were fitted by a likelihood function, which was constructed based on the Poisson probability of hits in individual phototubes. The expected rate in each tube is a function of the geometry (known), light yields, and the attenuation. To avoid complications due to the light reflection, timing cuts were applied to the tube hits. In Table 3.7, a comparison between the input and fitted values of $Y_{\rm tgt}/Y_{\rm gcat}$ and $L_{\rm tgt}$ for three example fits is made. One

Quantity	Input	Fit result
$Y_{\rm tgt}/Y_{\rm gcat}$	0.667	0.674
$L_{\rm tgt}$ (m)	9.0	9.32
$Y_{\rm tgt}/Y_{\rm gcat}$	0.75	0.743
$L_{\rm tgt}$ (m)	9.0	9.95
$Y_{\rm tgt}/Y_{\rm gcat}$	1.0	0.978
$L_{\rm tgt}$ (m)	4.5	4.6

Table 3.7. A comparison of the input and fitted values of various sets of parameters in the likelihood fitter.

sees that this fitting method is able to disentangle the change of light yield from a change of attenuation. We expect that the precision of the procedure can be improved to the desired level with additional simulation studies.

Precipitate at the Bottom of the Acrylic Vessel

Over time, some dust or other material from the liquid scintillator may precipitate onto the bottom of the acrylic tank, making the bottom acrylic more opaque than the top. A top/bottom asymmetry in detector response will be developed as a result. For illustration, in Fig. 3.6, the total p.e. yield of the detector as a function of the z position of a ^{60}Co source is plotted, for a rather opaque acrylic bottom with only 1 cm of attenuation length. Clearly the light originating from the bottom half of the detector get absorbed more than the top half. The precipitate also suppresses the yield in the bottom PMT ring, which is another symptom of

*For simplicity we used an electron source instead of a gamma source so that the ionization energy is deposited locally.

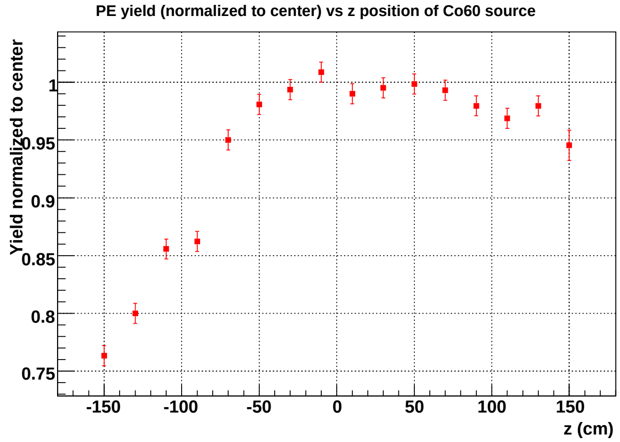

Fig. 3.6. The results of a scan of ^{60}Co source along the central z axis for a detector with bottom acrylic plate having a short 1 cm optical attenuation to simulate the effect of a precipitate.

such situation. One effective correction procedure is to brute force "fix" the p.e. measured by the bottom ring by a scaling factor according to the top ring. (This should yield similar results to a more correct procedure using a maximum likelihood method to determine the energy.) Simulations indicate that even under the extreme situation considered in Fig. 3.6 the positron efficiency is stable to 0.2%.

We are also exploring the possibility of using 2.2 MeV n-p capture signal in the bottom gamma catcher to detect and make effective corrections to this region of the gamma catcher which is not directly accessible to source deployments.

Additional Constraints from Spallation Neutrons

Besides the direct calibration devices we have discussed, the spallation neutron events serve as a unique and powerful calibration tool. The 2.2 MeV n-p and 8 MeV n-Gd capture signals are distributed uniformly throughout the detector. Combined with the vertex reconstruction, one can produce a full volume map of the detector response, as shown earlier in Fig. 3.2. Effectively, the topology of this map captures the combined effect of all detector parameters. Simulation has shown that even without detailed knowledge of individual parameters, we can use the spallation neutron capture peak to set the overall energy scale and achieve near/far "identical"neutron efficiency.

In terms of constraining the detector parameters, the anticipated utility of the spallation neutrons events is summarized below

- The spallation neutron capture events that reconstruct close to each of the three calibration axes should give the same energy response as the direct neutron source data from the corresponding axis. This provides essential validation of the calibration program by directly cross-checking the source data with the spallation data.

- The n-p capture signals in the gamma catcher can provide further information about the detector properties there. This is particularly useful at the bottom of the gamma catcher, where direct calibration device has no access.

- The reconstructed n-p capture peak should be at 2.2 MeV, and that of n-Gd capture should be at 8 MeV, *regardless of the vertex position*. If position non-uniformity is found, it either indicates that some parameters in the model are off, or that our detector modeling is imperfect. One should try best to diagnose and fix the problem, in effect, turning Fig. 3.2 into a flat energy map.

- ○ It is conceivable that after exhausting all techniques, some residual non-uniformity in the neutron energy map remains. Then one could consider taking the residual map to make the final position dependent energy correction.

The effectiveness of the 2nd bullet requires further Monte Carlo studies.

3.2.3 Detector Related Uncertainties

For the detector-related systematic uncertainties, we utilize two values for the Daya Bay experiment: baseline and goal. The baseline value is what we expect to be achievable through essentially proven methods with perhaps straightforward improvement in technique. The goal value is that which we consider achievable through improved methods and that will require additional R&D to demonstrate.

As emphasized in Section 1.2.5, we are essentially measuring a ratio of rates in near and far detector pairs. Therefore, we do not need to determine the *absolute* efficiency for each detector, but only the ratio for the two detectors in a pair. This ratio can be determined by measuring components of the efficiency for each detector using identical methods for the two detectors. If the measurement method has some common systematic uncertainty for the two detectors, this is not relevant for the ratio. We only need consider the uncorrelated uncertainties that will actually contribute to the uncertainty in the efficiency ratio. We will use the term “*relative* uncertainty” to refer to the contributions of such uncorrelated effects to the detector related uncertainties, as opposed to the term “*absolute* uncertainty” which refers to the uncertainty that contributes to the *absolute* efficiency. That is, the *relative* uncertainties are the only ones relevant to measurement of ratios of rates in the near and far detector pairs.

The estimated values of detector-related systematic uncertainties are summarized in Table 3.8 and discussed in the rest of this section.

Source of uncertainty		Chooz (*absolute*)	Daya Bay (*relative*) Baseline	Goal	Goal w/Swapping
# protons		0.8	0.3	0.1	0.006
Detector Efficiency	Energy cuts	0.8	0.2	0.1	0.1
	Position cuts	0.32	0.0	0.0	0.0
	Time cuts	0.4	0.1	0.03	0.03
	H/Gd ratio	1.0	0.1	0.1	0.0
	n multiplicity	0.5	0.05	0.05	0.05
	Trigger	0	0.01	0.01	0.01
	Live time	0	<0.01	<0.01	<0.01
Total detector-related uncertainty		1.7%	0.38%	0.18%	0.12%

Table 3.8. Comparison of detector-related systematic uncertainties (all in percent, per detector module) of the Chooz experiment (*absolute*) and projections for Daya Bay (*relative*). Baseline values for Daya Bay are achievable through essentially proven methods, whereas the goals should be attainable through additional R&D efforts described in the text. In addition, the potential improvement from detector swapping is indicated in the last column.

3.2.3.1 Number of Target Protons

The antineutrino targets are the free protons in the detector, so the event rate in the detector is proportional to the total number of free protons. As discussed in Chapter 6, the antineutrino detectors will be filled in pairs, each pair from a common batch of liquid scintillator carefully controlled so that there will be no difference in chemical composition between the two detectors. Then one of the two detectors will be deployed at a near site, and the other at the far site. Then the near and far members of a pair will have liquid scintillator with the same chemical composition and exactly the same number of protons per unit mass of liquid scintillator. The ratio of masses in the central volumes then provides the ratio of proton targets for the two detectors.

The mass of the antineutrino target is accurately determined in several ways. First the detector modules will be built to specified tolerance so that the volume is known to $\sim$0.6% (typically $<$5 mm dimension out of a radius of 1.6 meters). We will make a survey of the detector geometry and dimensions after construction to characterize the detector volumes to higher precision than 0.3%. Using optical measuring techniques and reflective survey targets built into the detector modules and attached to the surfaces of the acrylic vessels sub-mm precision is easily achievable with conventional surveying techniques.

Once the detectors are underground, we plan to fill each detector from a common tank using a variety of instrumentation to directly measure the mass and volume flow into the detector. A combination of Coriolis mass flow meters and volume flow meters, thermometers in the filling station and load sensors in both the storage tank and possibly the antineutrino detector, will allow us to determine the mass of the liquid scintillator reliably and with independent methods.

The various flow meters have an *absolute* calibrated precision of $0.1 - 0.2\%$, so we conservatively quote a baseline uncertainty of 0.3% for the detector mass. If the flow meters can be demonstrated to have better repeatable performance, we expect to improve the uncertainty on the detector mass to the goal value of 0.1%.

The absolute H/C ratio was determined by Chooz using scintillator combustion and analysis to 0.8% precision based on combining data from several analysis laboratories. By filling the near/far pairs from a common batch of scintillator, we expect to essentially eliminate this systematic uncertainty. Nevertheless, we will analyze samples from each detector to check that no difference is observed. These samples will be analyzed with a common apparatus, so common sources of systematic uncertainty will not contribute to the measurements. Thus the *relative* uncertainty for different samples can be known with an improved precision of 0.2% or better.

We are also presently engaged in a program of R&D with the goal of measuring the *relative* H/C ratio in different samples of liquid scintillator to $\sim$0.1% precision. We are exploring three different methods to achieve this goal: precision NMR, chemical analysis, and neutron capture. The neutron capture method would need to be utilized before the introduction of Gd into the scintillator, but could be used to precisely characterize the organic liquids used in the liquid scintillator cocktail. In principle, the other methods could be used on the final Gd-loaded scintillator.

We note that the γ-catcher will also be filled using scintillator from a common tank for both members of the detector pair. Thus there should also be no possibility of a systematic difference in the H/C ratio for the gamma catcher liquid. For the γ-catcher we need to control the H/C ratio to about 1% to constrain the amount of “spill-in” events. These “spill-in” events are where a neutron generated in the γ-catcher is captured in the Gd-loaded scintillator after thermal diffusion. We will also check samples of the γ-catcher to verify the H/C ratio is controlled to about 0.2%.

3.2.3.2 Position Cuts

Due to the design of the detector modules, the event rate is measured without resort to reconstruction of the event location. Therefore the uncertainty in the event rate is related to the physical parameters of the antineutrino volume. We do not anticipate employing cuts on reconstructed position to select events, and there should be no uncertainty related to this issue.

3.2.3.3 Positron Energy Cut

Due to the high background rates at low energy, Chooz employed a positron energy threshold of 1.3 MeV. This cut resulted in an estimated uncertainty of 0.8%. The improved shielding design of the Daya Bay detectors makes it possible to lower this threshold to below 1 MeV while keeping uncorrelated backgrounds as low as 0.1%. The threshold of visible energy of neutrino events is 1.022 MeV. Due to the finite energy resolution of $\sim$12% at 1 MeV, the reconstructed energy will have a tail below 1 MeV. The systematic uncertainty associated with this cut efficiency is studied by Monte Carlo simulation. The tail of the simulated energy spectrum is shown in Fig. 3.7 with the full spectrum shown in the inset. For this simulation, 200 PMTs are used to measure the energy deposited in a 20-ton module, yielding an energy resolution of $\sim$12% at 1 MeV. The inefficiencies are 0.32%, 0.37%, and 0.43% for cuts at 0.98 MeV, 1.0 MeV, and 1.02 MeV, respectively. Assuming the energy scale is established with the ^{78}Ge source with 2% uncertainty at 1 MeV, this inefficiency variation will produce a 0.05% uncertainty in the detected antineutrino rate. The upper energy requirement for the positron signal will be E<8 MeV and will also contribute a negligible uncertainty to the positron detection efficiency.

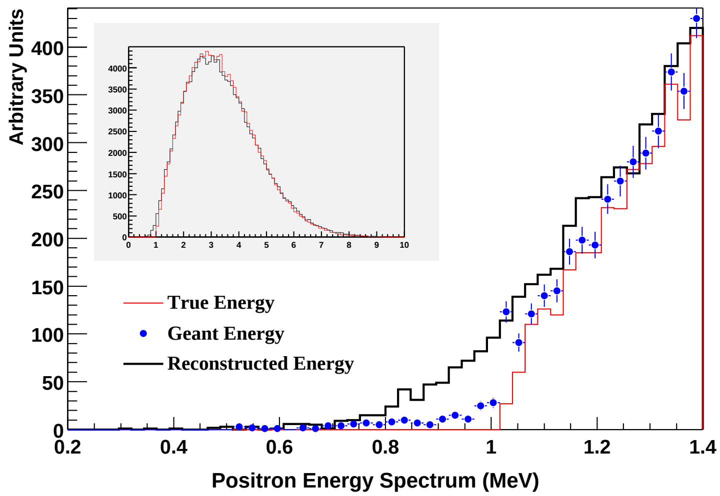

Fig. 3.7. Energy spectra associated with the positron's true energy, simulated energy (Geant Energy), and reconstructed energy at 1 MeV. The full spectrum is shown in the inset, where the red line corresponds to the true energy and the black one corresponds to the reconstructed energy.

3.2.3.4 Neutron Detection Efficiency

The delayed neutron from the inverse beta decay reaction is produced with $\sim$10 keV of kinetic energy. The neutron loses energy in the first few interactions with H and C in the scintillator, and reaches thermal energy in a few microseconds. The neutrons can capture on either H or Gd during or after the thermalization process. We will detect the neutrons that capture on Gd, yielding at least 6 MeV of visible energy from the resulting capture γ rays, during the time period 0.3<T<200 μs.

In order to measure the rates for two detectors (near and far) with a precision to reach $\sin^2 2\theta_{13} = 0.01$ the baseline requirement for the uncertainty on *relative* neutron detection efficiencies is 0.25%. The ϵ_n for neutrons at the center of a detector module can be determined directly by using a tagged neutron source (either ^{252}Cf, Am-Be or Pu(C) can be used) and counting the number of neutrons using the time and energy cuts after neutron producing event. (Corrections associated with uniformly distributed neutrons are studied with spallation neutrons, as discussed in Section 3.2.2.3.) This will require measurement of order 1 million neutron captures, and would likely require several hours of measurement. This will be established during the initial comprehensive calibration of each detector.

The efficiency for detecting the neutron can be written

$$\epsilon_n = P_{Gd}\epsilon_E\epsilon_T \tag{18}$$

in which P_{Gd} is the probability to capture on Gd (as opposed to H), ϵ_E is the efficiency of the E>6 MeV energy cut for Gd capture, and ϵ_T is the efficiency of the delayed time period cut. The individual components P_{Gd}, ϵ_E, and ϵ_T can be monitored separately as an additional check on the measurement of ϵ_n.

H/Gd ratio

Neutrons are thermalized during their first $10\ \mu$s of existence in the detector central volume. Thus for times longer than $10\ \mu$s the delayed neutron capture events will exhibit an exponential time constant, τ, related to the average concentration of Gd in the detector module. The rate of capture, $\Gamma \equiv 1/\tau$, is given by:

$$\Gamma = \Gamma_{Gd} + \Gamma_H = [n_{Gd}\sigma_{Gd} + n_H\sigma_H]v \tag{19}$$

where $n_{H(Gd)}$ is the number density of hydrogen (Gd) in the liquid scintillator and $\sigma_{H(Gd)}$ is the neutron capture cross section on hydrogen (Gd) and v is the thermal velocity. For liquid scintillator one generally obtains $1/\Gamma_H \sim 200\ \mu$sec, whereas for 0.1% Gd fraction in Gd-LS we expect $\tau \sim 30\ \mu$sec. The fraction of neutrons that capture on Gd rather than H is then

$$P_{Gd} = \frac{1}{1 + \Gamma_H/\Gamma_{Gd}} \tag{20}$$

and we would like to know this *relative* fraction between different detector modules to ∼0.1%. Thus we must measure the time constants τ for different detector modules to a *relative* precision of 0.2 μs, or about 0.5%. Such a measurement requires measuring about 30,000 neutron captures, which can be done in a few minutes with a neutron source. The Chooz experiment measured the (*absolute*) ∼30 μs capture time to ±0.5 μs precision.

Measurement of τ to 0.5% precision will provide a relative value of P_{Gd} to 0.1% uncertainty, which is the baseline and goal value in Table 3.8.

Energy cut efficiency

Another issue is the neutron detection efficiency associated with the signal from capture of neutrons on Gd in the antineutrino detector volume. An energy threshold of about 6 MeV will be employed to select these delayed events, and the efficiency (∼93%) of this criterion may vary between detector modules depending upon the detailed response of the module. However, this can be calibrated through the use of radioactive sources (see Section 7) and spallation neutron captures. The KamLAND detector gain is routinely (every two weeks) monitored with sources, and a relative long-term gain drift of ∼1% is readily monitored with a precision of 0.05%. Monte Carlo simulations of the Daya Bay detector response for the Gd capture γs indicate that 1% energy scale uncertainty will lead to 0.2% uncertainty in ϵ_E, and we use this value as the baseline systematic uncertainty.

We have also performed detailed Monte Carlo simulations of the detector response to neutron sources and spallation neutrons. The results of these studies indicate that we can indeed establish the relative value of ϵ_E to 0.1%, even for reasonable variations of detector properties (such as scintillator attenuation length). As an example, Fig. 3.8 shows how the source data can be used with uniform spallation neutrons to bootstrap a non-linear energy scale that corrects the spectrum, independent of attenuation length over the extreme range of 4.5–18 m. Therefore, we estimate a value of 0.1% for the goal systematic uncertainty in ϵ_E.

Finally, we note that deployment of ^{238}Pu-^{13}C neutron sources in the detector will enable establishing a very precise energy threshold using the 6.13 MeV gamma ray line in ^{16}O. This source is under development

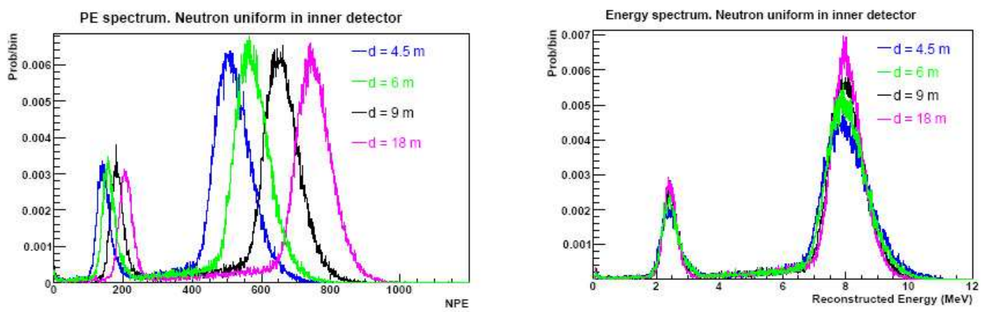

Fig. 3.8. Spallation neutron response for detector modules with scintillator optical attenuation lengths of $4.5 \leq d \leq 18$ m. The left panel shows the raw photoelectron spectra, whereas the right panel shows the spectra rescaled according to a non-linear rescaling procedure we have developed. The rescaled 6 MeV effective energy threshold produces a constant value of $\epsilon_E = 93\%$ to within 0.4% over this extreme range of attenuation length.

at the China Institute for Atomic Energy and we expect to test one in the prototype detector at IHEP in the near future.

Time cuts

The time correlation of the prompt (positron) event and the delayed (neutron) event is a critical aspect of the event signature. Matching the time delays of the start and end times of this time window between detector modules is crucial to reducing systematic uncertainties associated with this aspect of the antineutrino signal. If the starting time ($\sim$0.3 μs) and ending time ($\sim$200 μs) of the delayed event window is determined to $\sim$10 ns precision, the resulting uncertainty associated with missed events is $\sim$0.03%. We will insure that this timing is equivalent for different detector modules by slaving all detector electronics to one master clock. We estimate that with due care, the relative neutron efficiency for different modules due to timing is known to $\sim$0.03%, and we use this value as the estimated goal systematic uncertainty. We use a more conservative 0.1% value for the baseline value.

3.2.3.5 Neutron Multiplicity

Chooz required a cut on the neutron multiplicity to eliminate events where it appeared that there were two neutron captures following the positron signal, resulting in a 2.6% inefficiency and associated 0.5% systematic uncertainty. These multiple neutron events are due to muon-induced spallation neutrons, and will be reduced to a much lower level by the increased overburden available at the Daya Bay site. For the near site at 500 m baseline, the muon rate relative to the signal rate will be more than a factor nine lower than for the Chooz site. Therefore, events with multiple neutron signals will be reduced by this factor relative to Chooz, and should present a much smaller problem for the Daya Bay site. We therefore estimate a 0.05% value for this systematic uncertainty and use this for both the baseline and goal values.

3.2.3.6 Trigger

The trigger efficiency can be measured to high precision (0.01%) using studies with pulsed light sources in the detector. (We note that KamLAND has used this method to determine 99.8% absolute trigger efficiency [4].) In addition, we will employ redundant triggers so that they can be used to cross-check each other to high precision. We estimate a systematic uncertainty of 0.01% can be achieved, and use this for both the baseline and goal values.

3.2.3.7 Live Time

The detector live time can be measured accurately by counting a 100 MHz clock using the detector electronics, and normalizing to the number of clock ticks in a second (as defined by a GPS receiver signal). The uncertainty associated with this procedure should be extremely small, and certainly negligible relative to the other systematic uncertainties. For example, SNO measured the relative live times for their day/night analysis with a fractional uncertainty of 5×10^{-7}.

3.2.4 Detector Swapping

The connection of the two near detector halls and the far hall by horizontal tunnels provides the Daya Bay experiment with the unique and important option of swapping the detectors between the locations. This could enable the further reduction of detector-related systematic uncertainties in the measurement of the ratio of neutrino fluxes at the near and far locations. Although the estimated baseline and goal systematic uncertainties in Table 3.8 are sufficient to achieve a sensitivity of 0.01 in $\sin^2 2\theta_{13}$, implementation of detector swapping could provide an important method to further reduce systematic uncertainties and increase confidence in the experimental results.

The swapping concept is easy to demonstrate for a simple scenario with a single neutrino source and only two detectors deployed at two locations, near and far. The desired measurement is the ratio of event rates at the near and far locations: N/F. With detector #1 (efficiency ϵ_1) at the near location and detector #2 (efficiency ϵ_2)at the far location we would measure

$$\frac{N_1}{F_2} = \left(\frac{\epsilon_1}{\epsilon_2}\right)\frac{N}{F} \tag{21}$$

By swapping the two detectors and making another measurement, we can measure

$$\frac{N_2}{F_1} = \left(\frac{\epsilon_2}{\epsilon_1}\right)\frac{N}{F} \tag{22}$$

where we have assumed that the detector properties (e.g., efficiencies) do not change when the detector is relocated. We can now combine these two measurements to obtain a value of N/F that is, to first order, independent of the detector efficiencies:

$$\frac{1}{2}\left(\frac{N_1}{F_2} + \frac{N_2}{F_1}\right) = \frac{N}{F}\left(1 + \frac{\delta^2}{2}\right) \tag{23}$$

where we have defined

$$\delta \equiv \frac{\epsilon_2}{\epsilon_1} - 1 \tag{24}$$

Note that even if the detector efficiencies are different by as much as 1%, we can determine N/F to a fractional precision better than 10^{-4}.

The layout of the Daya Bay experiment involves two near sites with two detectors each, and a far site with four detectors. The simplest plan is to designate the eight detectors as four pairs: (1,2), (3,4), (5,6), (7,8). Using four running periods (designated I, II, III, IV, separated by three detector swaps) we can arrange for each detector to be located at the far site half the time and a near site half the time by swapping two pairs between running periods, as shown in Table 3.9. Ratios of event rates can be combined in a fashion analogous to the above discussion to provide cancellation of detector-related systematic uncertainties and also reactor power systematic uncertainties. Careful calibration of the detectors following each swap will be necessary to insure that each detector's performance does not change significantly due to relocation. In particular, all the parameters in Table 3.8 need to be checked and, if necessary, corrections applied to restore the detection efficiency to the required precision through, e.g., changes in calibration constants.

Run Period	Near(DB)	Near(LA)	Far
I	1,3	5,7	2,4,6,8
II	2,3	6,7	1,4,5,8
III	2,4	6,8	1,3,5,7
IV	1,4	5,8	2,3,6,7

Table 3.9. Swapping scheme with four running periods. The detectors (labelled 1–8) are deployed at the Near(DB), Near(LA), and Far sites during each period as indicated in this table.

Successful implementation of this swapping concept could lead to substantial reduction in many of the detector-related systematic uncertainties. Any residual systematic differences associated with the H/C and H/Gd ratios should be completely eliminated. By measuring the fluid levels before and after swapping, we can insure that the detector volume will be the same with negligible uncertainty. However, due to the residual uncertainty in the monitored temperature of the detector module (0.1° C), there will be a residual uncertainty in the detector mass of 0.006%, and this is the value quoted in Table 3.8.

At present, we envision running the experiment for a period of time (probably 3 years) before considering implementation of the swapping option.

3.2.5 Detector Cross-calibration

Another important feature of the design of the Daya Bay experiment is the presence of two detector modules at each near site. During a single running period (I, II, III, or IV) each near detector module will measure the neutrino rate with 0.23% statistical precision. If the systematic uncertainties are smaller than this, the two detectors at the near site should measure the same rate, giving a detector asymmetry of 0 ± 0.34% (statistical uncertainty only). Combining all the detector pairs in all 4 running periods should yield an asymmetry of 0 ± 0.04% (statistical uncertainty only). These asymmetries are an important check to ensure that the detector-related systematic uncertainties are under control. In addition, this analysis can provide information on the the degree to which the detector-related systematic uncertainties are correlated or uncorrelated so that we know how to handle them in the full analysis including the far site.

Finally, the near detector data can provide important information on the reactor power measurements. We will measure the ratio

$$R_{\rm near} = \frac{S_{DB}}{S_{LA}} \tag{25}$$

where S_{DB} (S_{LA}) is the detector signal (background subtracted, normalized to the reactor power) for the Daya Bay (Ling Ao) near site. If the reactor powers are correct (and the detector systematic uncertainties are under control) then we expect $R_{\rm near} = 1.0 \pm 0.24\% \pm 0.51\%$, where the first uncertainty is statistical (only 1 of the 4 running periods) and the second uncertainty is the detector (baseline) systematic uncertainty. Note that these uncertainties are small relative to the expected 2% uncorrelated reactor power uncertainty, so measurement of $R_{\rm near}$ will provide an important check (and even perhaps additional information) on the reactor powers. Furthermore, studies of the measured neutrino spectra in the different near detectors during different parts of the reactor fuel cycle can help provide constraints on the fuel cycle effects on the spectrum.

3.3 Backgrounds

In the Daya Bay experiment, the signal events (inverse beta decay reactions) have a distinct signature: a prompt positron followed by a neutron-capture. Background events are logically divisible into two categories, correlated and uncorrelated. A correlated background is one in which two reactions triggered by a single source, such as a cosmic muon, mimic the time-ordered pattern of a signal. An uncorrelated background is one in which the two-component pattern is accidentally formed by two distinct sources.

There are three important sources of backgrounds in the Daya Bay experiment: fast neutrons, ^{8}He/^{9}Li, and natural radioactivity. A fast neutron produced by cosmic muons in the surrounding rock or the detector can produce a signal mimicking the inverse beta decay reaction in the detector: the recoil proton generates the prompt signal and the capture of the thermalized neutron provides the delayed signal. The ^{8}He/^{9}Li isotopes produced by cosmic muons have substantial beta-neutron decay branching fractions, 16% for ^{8}He and 49.5% for ^{9}Li. The beta energy of the beta-neutron cascade overlaps the positron signal of neutrino events, simulating the prompt signal, and the neutron emission forms the delayed signal. Fast neutrons and ^{8}He/^{9}Li isotopes create correlated backgrounds since both the prompt and delayed signals are from the same single parent muon. Some neutrons produced by cosmic muons are captured in the detector without proton recoil energy. A single neutron capture signal has some probability to fall accidentally within the time window of a preceding signal due to natural radioactivity in the detector, producing an accidental background. In this case, the prompt and delayed signals are from different sources, forming an uncorrelated background.

All three major backgrounds are related to cosmic muons. Locating the detectors at sites with adequate overburden is the only way to reduce the muon flux and the associated background to a tolerable level. The overburden requirements for the near and far sites are quite different because the signal rates differ by more than a factor of 10. Supplemented with a good muon identifier outside the detector, we can tag the muons going through or near the detector modules and reject backgrounds efficiently.

In this section, we describe our background studies and our strategies for background management. We conclude that the background-to-signal ratio will be around 0.3% at the near sites and around 0.2% at the far site, and that the major sources of background can be quantitatively studied *in-situ*.

3.3.1 Cosmic Muons in the Underground Laboratories

The most effective and reliable approach to minimize the backgrounds in the Daya Bay experiment is to have sufficient amount of overburden over the detectors. The Daya Bay site is particularly attractive because it is located next to a 700-m high mountain. The overburden is a major factor in determining the optimal detector sites. The location of detector sites has been optimized by using a global χ^2 analysis described in Section 3.4.1.

Detailed simulation of the cosmogenic background requires accurate information of the mountain profile and rock composition. Figure 3.9 shows the mountain profile converted from a digitized 1:5000 topographic map. The horizontal tunnel and detector sites are designed to be about -20 m PRD.† Several rock samples at different locations of the Daya Bay site were analyzed by two independent groups. The measured rock density ranges from 2.58 to 2.68 g/cm^3. We assume an uniform rock density of 2.60 g/cm^3 in the present background simulation. A detailed description of the topography and geology of the Daya Bay area is given in Chapter 5.

The standard Gaisser formula [5] is known to poorly describe the muon flux at large zenith angle and at low energies. This is relevant for the Daya Bay experiment since the overburden at the near sites is only $\sim$100 m. We modified the Gaisser formula as

$$\frac{dI}{dE_\mu d\cos\theta} = 0.14\left(\frac{E_\mu}{\mathrm{GeV}}\left(1+\frac{3.64\,\mathrm{GeV}}{E_\mu(\cos\theta^*)^{1.29}}\right)\right)^{-2.7}\left[\frac{1}{1+\frac{1.1E_\mu\cos\theta^*}{115\,\mathrm{GeV}}}+\frac{0.054}{1+\frac{1.1E_\mu\cos\theta^*}{850\,\mathrm{GeV}}}\right] \tag{26}$$

which is the same as the standard formula, except that the polar angle θ is substituted with θ^*,

$$\cos\theta^* = \sqrt{\frac{(\cos\theta)^2+P_1^2+P_2(\cos\theta)^{P_3}+P_4(\cos\theta)^{P_5}}{1+P_1^2+P_2+P_4}} \tag{27}$$

†PRD is the height measured relative to the mouth of the Zhu Jiang River (Pearl River), the major river in South China.

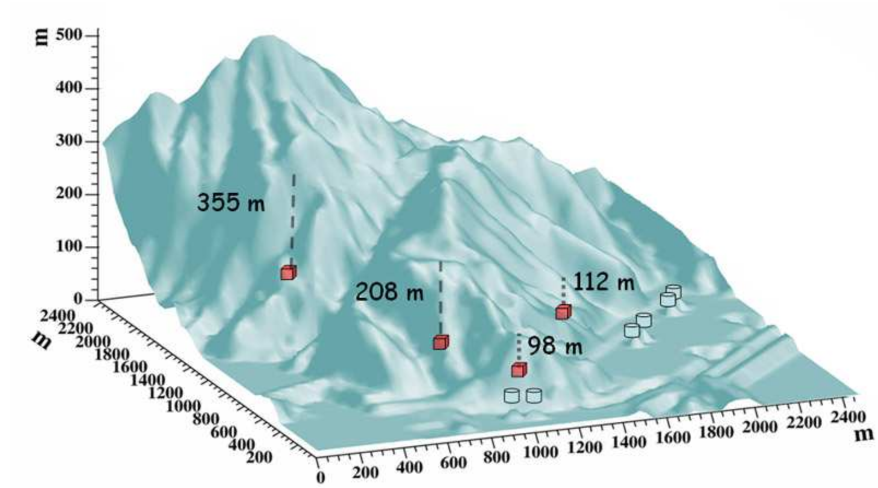

Fig. 3.9. Three dimensional profile of Pai Ya Mountain, where the Daya Bay experimental halls will be located, generated from a 1:5000 topographic map of the Daya Bay area.

as defined in [6]. The parameters are determined to be $P_1 = 0.102573$, $P_2 = -0.068287$, $P_3 = 0.958633$, $P_4 = 0.0407253$, and $P_5 = 0.817285$, by using CORSIKA to simulate the muon production in the atmosphere. The comparison of the modified formula with data is shown in Fig. 3.10, where the calculations with the standard Gaisser formula are also shown. At muon energies of several tens of GeV, the

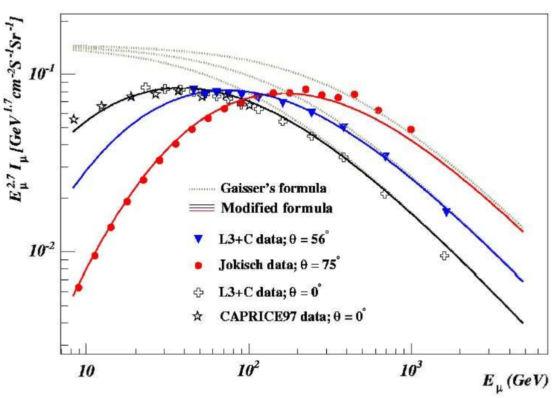

Fig. 3.10. Comparison of the modified formula (solid lines) with data. Calculations with the standard Gaisser's formula are shown in dashed lines. The data are taken from Ref. [7,8].

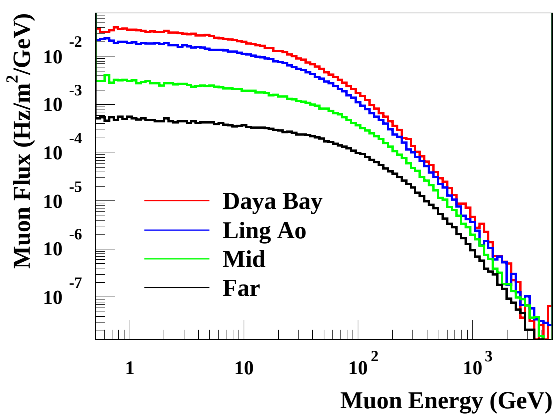

Fig. 3.11. Muon flux as a function of the energy of the surviving muons. The four curves from upper to lower correspond to the Daya Bay near site, the Ling Ao near site, the mid site and the far site, respectively.

standard Gaisser formula has large discrepancies with data while the modified formula agrees with data in the whole energy range.

Using the mountain profile data, the cosmic muons are transported from the atmosphere to the underground detector sites using the MUSIC package [9]. Simulation results are shown in Table 3.10 for the optimal detector sites. The muon energy spectra at the detector sites are shown in Fig. 3.11. The four curves

	DYB site	LA site	Mid site	Far site
Vertical overburden (m)	98	112	208	355
Muon Flux (Hz/m^2)	1.16	0.73	0.17	0.041
Muon Mean Energy (GeV)	55	60	97	138

Table 3.10. Vertical overburden of the detector sites and the corresponding muon flux and mean energy.

from upper to lower corresponds to the Daya Bay near site, the Ling Ao near site, the mid site and the far site, respectively.

3.3.2 Simulation of Neutron Backgrounds

The neutron production rates will depend upon the cosmic muon flux and average energy at the detector. However, the neutron backgrounds in the detector also depend on the local detector shielding. The neutrino detectors will be shielded by at least 2.5 meters of water. This water buffer will be used as a Cherenkov detector to detect muons. Thus neutrons produced by muons in the detector module or the water buffer will be identified by the muon signal in the water Cherenkov detector. In addition, neutrons created by muons in the surrounding rock will be effectively attenuated by the 2.5 m water buffer. Together with another muon tracker outside the water buffer, the combined muon tag efficiency is designed to be 99.5%, with an uncertainty smaller than 0.25%.

From the detailed muon flux and mean energy at each detector site, the neutron yield, energy spectrum, and angular distribution can be estimated with an empirical formula [10] which has been tested against experimental data whenever available. A full Monte Carlo simulation has been carried out to propagate the primary neutrons produced by muons in the surrounding rocks, the water buffer, and the oil buffer layer of the neutrino detector, to the detector. The primary neutrons are associated with their parent muons in the simulation so that we know if they can be tagged by the muon detector. Neutrons produced by a muons that pass through the liquid scintillator neutrino detector will be tagged with 100% efficiency. Assuming a muon detection efficiency of 99.5%, neutrons produced in the water buffer will be tagged with at least an efficiency of 99.5%, since their parent muons must pass through the muon system as well(this point will be further elaborated below). Neutrons produced in the rocks, however, have to traverse at least 2.5 meters of water to reach a detector module. About 70% of the neutrons that enter the detector modules from the surrounding rock arise from parent muons that leave a signal in the muon system (i.e., “tagged”). About 30% of the neutrons that enter the detector modules from the surrounding rocks arise from muons that miss the muon system ($\equiv$ “untagged”). The neutron background after muon rejection is the sum of the untagged events and 0.5% (due to veto inefficiency) of the tagged events.

Some energetic neutrons will produce tertiary particles, including neutrons. For those events that have energy deposited in the liquid scintillator, many have a complex time structure due to multiple neutron scattering and captures. These events are split into sub-events in 50 ns time bins. We are interested in two kinds of events. The first kind has two sub-events. The first sub-event has deposited energy in the range of 1 to 8 MeV, followed by a sub-event with deposited energy in the range of 6 to 12 MeV in a time window of 1 to 200 μs. These events, called fast neutron events, can mimic the antineutrino signal as correlated backgrounds. The energy spectrum of the prompt signal of the fast neutron events, e.g. at the far site, is shown in Fig. 3.12 up to 50 MeV. The other kind of events has only one sub-event with deposited energy in range of 6 to 12 MeV. These events, when combined with the natural radioactivity events, can provide the delayed signal to form the uncorrelated backgrounds. We call them single neutron events. Most of the single

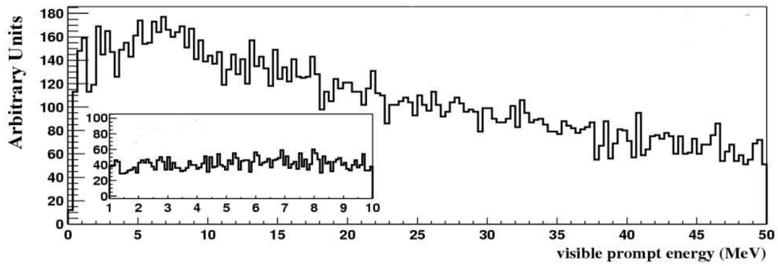

Fig. 3.12. The prompt energy spectrum of fast neutron background at the Daya Bay far detector. The inset is an expanded view of the spectrum from 1 to 10 MeV.

neutron events are real thermalized neutrons while others are recoil protons that fall into the 6–12 MeV energy range accidentally. A few thermalized neutrons will survive the 200 μs cut, even though the parent muon is tagged. These neutrons contribute to the untagged single neutron rate, along with those where the veto misses the muon due to inefficiency. The neutron simulation results are listed in Table 3.11.

		DYB site	LA site	far site
fast neutron (/day/module)	tagged	19.6	13.1	2.0
	untagged	0.5	0.35	0.03
single neutron (/day/module)	tagged	476	320	45
	untagged	8.5	5.7	0.63

Table 3.11. Neutron production rates in a 20-ton module at the Daya Bay sites. The rows labeled ”tagged” refer to the case where the parent muon track traversed and was detected by the muon detectors, and thus it could be tagged. Rows labeled “untagged” refer to the case where the muon track was not identified by the muon detectors.

As mentioned in the caption, the “untagged” neutron background in Table 3.11 can be broken up into two pieces: (a) neutrons whose parent muons traverse the muon detector (in principle “taggable”), but are untagged due to the detector inefficiency, and (b) neutrons whose parent muons are “untaggable”, e.g. those “rock” muons that never enter the water. By comparing “tagged” (99.5% of the “taggable”) background, and “untagged” neutron rates in Table 3.11, we note that (b) is the dominating background.

The rate and energy spectrum of background (a) can be studied with the tagged sample. Furthermore, simulation has shown that the actual efficiency for tagging “taggable” neutrons is higher than the muon detection efficiency (i.e. 99.5% is too conservative). This can be understood from the fact that muons corresponding to background (a) generally have short track length in the water shield (which do not give enough Čerenkov lights). Therefore they are less probable to produce spallation neutrons, leading to a fortunate suppression in the tagging inefficiency of this type of background. Thus, background (a) is relatively well-controlled.

From the systematics point of view, it is then desirable to obtain additional handle on background (b). Simulation studies have been made on a muon system with a “roof” detector above the water Čerenkov detector (e.g. RPC), extending some distance into the surrounding rock. With 1 m rock “overhang”, the “roof” detector can tag $\sim$1/3 of background (b), which would have otherwise been totally missed by the water Čerenkov detector. These additional tagged events will allow us to validate/tune the Monte Carlo in order to calculate the residual untagged neutron background.

3.3.3 Cosmogenic Isotopes

Cosmic muons, even if they are tagged by the muon identifier, can produce radioactive isotopes in the detector scintillator which decay by emitting both a beta and a neutron (β-neutron emission isotopes). Some of these so-called cosmogenic radioactive isotopes live long enough such that their decay cannot be reliably associated with the last tagged muon. Among them, ^{8}He and ^{9}Li with half-lives of 0.12 s and 0.18 s, respectively, constitute the most serious correlated background sources. The production cross section of these two isotopes has been measured with muons at an energy of 190 GeV at CERN [11]. Their combined cross section is $\sigma(^8\mathrm{He} +^9 \mathrm{Li}) = (2.12 \pm 0.35)\ \mu\mathrm{barn}$. Since their lifetimes are so close, it is hard to extract individual cross sections. About 16% of ^{8}He and 49.5% of ^{9}Li will decay by β-neutron emission. Using the muon flux and mean energy at each detector site (from Section 3.3.1) and an energy dependent cross section, $\sigma_{\mathrm{tot}}(E_\mu) \propto E_\mu^\alpha$, with $\alpha = 0.73$, the estimated ^{8}He+^{9}Li backgrounds are listed in Table 3.12.

	DYB site	LA site	Far site
(^{8}He+^{9}Li)/day/module	3.7	2.5	0.26

Table 3.12. ^{8}He+^{9}Li rates in a 20-ton module at the Daya Bay sites.

The recent Double Chooz paper [14] includes new reactor-off data from Chooz [1] that allow a better separation of ^{9}Li from fast neutron background. This basically comes from including previously unreleased high energy data in the fit. The extracted ^{9}Li background level was 0.7$\pm$0.2 events/day. The mean muon energy in Chooz was $\sim$60 GeV, almost the same as the Daya Bay near site (55 GeV) and the Ling Ao near site (60 GeV). The fitting is based on the assumption that the fast neutron background is flat in energy spectrum. Scaling from the Chooz result, the Daya Bay experiment will have 8.0, 5.4, and 0.57 ^{9}Li events per module per day at the Daya Bay near site, the Ling Ao near site, and the far site, respectively. These estimates are twice as large as the estimates from the CERN cross section.

The KamLAND experiment [15] measures this ^{8}He/^{9}Li background very well by fitting the time interval since last muon. The muon rate is 0.3 Hz in the active volume of KamLAND detector. The mean time interval of successive muons is $\sim$ 3 seconds, much longer than the lifetimes of ^{8}He/^{9}Li. For the Daya Bay experiment, the target volume of a 20 ton detector module has a cross section around 10 m^2, thus the muon rate is around 10 Hz at the near sites, resulting in a mean time interval of successive muons shorter than the lifetimes of ^{8}He/^{9}Li. With a modified fitting algorithm, we find that it is still feasible to measure the isotope background *in-situ*.

From the decay time and β-energy spectra fit, the contribution of ^{8}He relative to that of ^{9}Li was determined by KamLAND to be less than 15% at 90% confidence level [16]. Furthermore, the ^{8}He contribution can be identified by tagging the double cascade $^8\mathrm{He} \rightarrow {}^8\mathrm{Li} \rightarrow {}^8\mathrm{Be}$. So we assume that all isotope backgrounds are ^{9}Li. They can be determined with a maximum likelihood fitting even at 10 Hz muon rate, by taking all contributions from the preceding muons into account. The resolution of the background-to-signal ratio can be determined to be [17]

$$\sigma_b = \frac{1}{\sqrt{N}} \cdot \sqrt{(1+\tau R_\mu)^2 - 1} \tag{28}$$

where N is the total number of neutrino candidates, τ is the lifetime of ^{9}Li, and R_μ is the muon rate in the target volume of detector. The resolution is insensitive to the ^{9}Li level since the statistical fluctuation of neutrino events dominates the uncertainty. The ^{9}Li background can be measured to a $\sim$0.3% fraction of the antineutrino signal with two 20-ton modules at the near sites of the Daya Bay experiment and $\sim$0.1% at the far site with four 20-ton modules, with the data sample of three years of running. The fitting uses time information only. Inclusion of energy and vertex information could further improve the precision.

A Monte Carlo has been carried out to check the fitting algorithm. The background-to-signal ratio is fixed at 1%. The total number of neutrino candidates is 2.5×10^5, corresponding to the far site statistical uncertainty, 0.2%. Figure 3.13 shows the fitting results as a function of muon rate. The data sample genera-

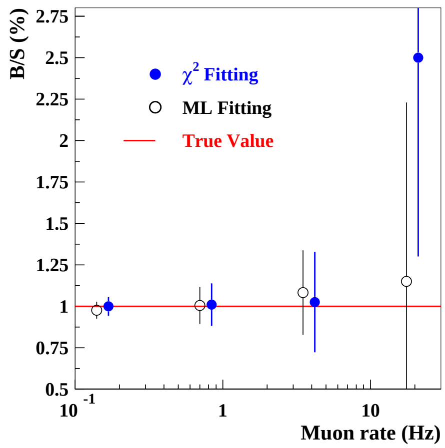

Fig. 3.13. Fitting results as a function of the muon rate. The uncertainty bars show the precision of the fitting. The χ^2 fitting uses the same muon rate as the maximum likelihood fitting and is shown to the right of it.

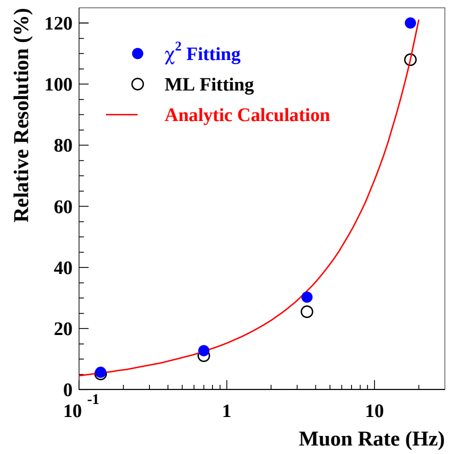

Fig. 3.14. The fitting precision as a function of the muon rate, comparing with the analytic estimation of Eq. 28. The y-axis shows the relative resolution of the background-to-signal ratio.

tion and fitting were performed 400 times for each point to get the fitting precision. In Fig. 3.14 the fitting precision is compared to the analytic formula Eq. 28 with the same Monte Carlo samples. The Monte Carlo results for minimizing χ^2, the maximum likelihood fit, and the simple analytical estimation are in excellent agreement.

KamLAND also found that most ^{8}He/^{9}Li background are produced by showering muons [15,16]. A 2-second veto of the whole detector is applied at KamLAND to reject these backgrounds. Roughly 3% of cosmic muons shower in the detector. It is not feasible for Daya Bay to apply a 2-second veto since the dead time of the near detector would be more than 50%. However, if the Daya Bay detector is vetoed for 0.5 s after a showering muon, about 85% of the ^{8}He/^{9}Li backgrounds caused by shower muons can be rejected. Approximately 30% of the ^{8}He/^{9}Li background will remain: $\sim$15% from non-showering muons and $\sim$15% from showering muons. Although additional uncertainties may be introduced due to the uncertainties in the relative contributions from showering and non-showering muons and the uncertainties arising from the additional cuts (e.g., increased dead time), this rejection method can cross check the fitting method and firmly determine the background-to-signal ratio to 0.3% at the near sites and to 0.1% at the far site.

Some other long-lived cosmogenic isotopes, such as ^{12}B/^{12}N, beta decay without an accompanying neutron. They can not form backgrounds themselves but can fake the delayed 'neutron' signal of an accidental background if they have beta decay energy in the 6–10 MeV range. The expected rates from these decays in the antineutrino detector are listed in Table 3.13. The ^{12}B/^{12}N cross section is taken from KamLAND [16] and the others are taken from measurement at CERN [11]. They are extrapolated to Daya Bay mean muon energies using the power law $\sigma_{\rm tot}(E_\mu) \propto E_\mu^{0.73}$. The total rates of all these isotopes of visible energy in detector in the 6–10 MeV range, where they can be misidentified as a neutron capture signal on Gadolinium, are 210, 141, and 14.6 events per module per day at the Daya Bay near site, the Ling Ao near site, and the far site, respectively. The dominant contribution is from ^{12}B/^{12}N. KamLAND found that ^{12}N yield is smaller than 1% of ^{12}B. Since the half-life of ^{12}B is short comparing to the mean muon interval, the rate can be well determined *in situ* by fitting the time since last muon. Using Eq. 28, the yield can be determined to a precision of 0.34, 0.25, and 0.015 events per module per day at the Daya Bay near site, the Ling Ao near site, and the far site, respectively, using three years' data sample. Therefore, we expect those isotopes will introduce very little uncertainties in the background subtraction. On the other side, these isotopes, uniformly produced inside the detector, can be used to monitor detector response.

isotopes	$E_{\max}$ (MeV)	$T_{1/2}$(s) (s)	DYB site (/day/module)	LA site (/day/module)	far site (/day/module)
^{12}B/^{12}N	13.4 (β^-)	0.02/0.01	396	267	27.5
^{9}C	16.0 (β^+)	0.13	16.6	11.2	1.15
^{8}B	13.7 (β^+)	0.77	24.5	16.5	1.71
^{8}Li	16.0 (β^-)	0.84	13.9	9.3	0.96
^{11}Be	11.5 (β^-)	13.8	$<$8.0	$<$5.4	$<$0.56
Total in 6-10 MeV			210	141	14.6

Table 3.13. Cosmogenic radioactive isotopes without neutron emission but with beta decay energy greater than 6 MeV. Cross sections are taken from KamLAND [16] (^{12}B/^{12}N) and Hagner [11] (others).

3.3.4 Radioactivity

Natural radioactivity and the single neutron events induced by cosmic muons may occur within a given time window accidentally to form an uncorrelated background. The coincidence rate is given by $R_\gamma R_n \tau$, where R_γ is the rate of natural radioactivity events, R_n is the rate of spallation neutron, and τ is the length of the time window. With the single neutron event rate given in the previous section, the radioactivity should be controlled to 50 Hz to limit the accidental backgrounds $<$0.1%. The accidental backgrounds can be well determined *in-situ* by measurement of the individual single rates from radioactivity and the single neutrons. The energy spectrum can be also well determined.

Past experiments suppressed uncorrelated backgrounds with a combination of carefully selected construction materials, self-shielding, and absorbers with large neutron capture cross section. However, additional care is necessary to lower the detector energy threshold much below 1 MeV. A higher threshold will introduce a systematic uncertainty in the efficiency of detecting the positron. In the following, the singles rate is from radioactivity depositing $>$1 MeV of visible energy in detector.

Radioactive background can come from a variety of sources. For simplicity, U, Th, K, Co, Rn, Kr in the following text always mean their radioactive isotopes ^{238}U, ^{232}Th, ^{40}K, ^{60}Co, ^{222}Rn, ^{85}Kr. The radioactive sources include

- U/Th/K in the rocks around the detector hall.
- U/Th/K in the water buffer.
- Co in the detector vessel and other supporting structures.
- U/Th/K in weld rods.
- U/Th/K in the PMT glass.
- U/Th/K in the scintillator.

- U/Th/K in materials used in the detector.
- Dust and other impurities
- Rn and Kr in air.
- Cosmogenic isotopes.

The radioactivity of rock samples from the Daya Bay site has been measured by several independent groups, including the Institute for Geology and Geophysics (IGG). The concentrations are: $\sim$10 ppm for U, $\sim$30 ppm for Th, and $\sim$5 ppm for K. The effect of the rock radioactivity on the antineutrino detectors has been studied with Monte Carlo. With the shielding of 2.5-meter water buffer and 45 cm oil buffer, there are 0.65 Hz, 2.6 Hz, and 0.26 Hz singles rates with visible energy greater than 1 MeV in each antineutrino detector module for U/Th/K, respectively. The total rate is $\sim$3.5 Hz.

The geological environment and rock composition are very similar in Hong Kong and Daya Bay. The spectrum of natural radioactivity that we have measured of the rock in the Aberdeen Tunnel in Hong Kong is shown in Fig. 3.15.

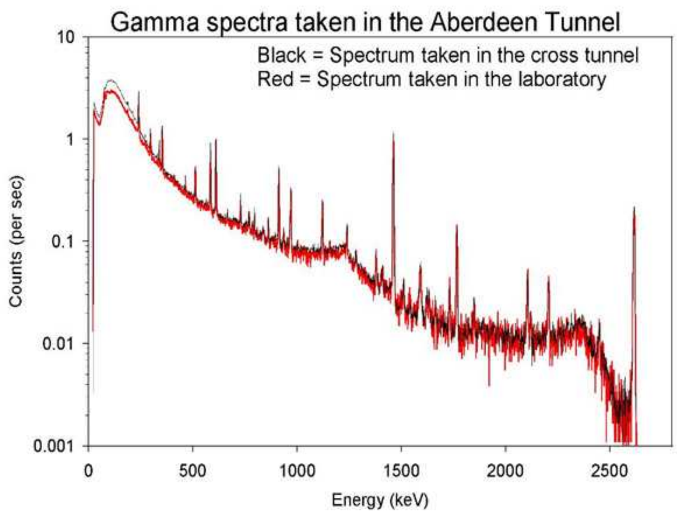

Fig. 3.15. Spectrum of natural radioactivity measured with a Ge crystal in the Hong Kong Aberdeen Tunnel. Prominent peaks for ^{40}K (1.461 MeV) and ^{208}Tl (2.615 MeV) are clearly evident along with many other lines associated with the U/Th series.

The water buffer will be circulated and purified to achieve a long attenuation length for Cherenkov light as well as low radioactivity. Normally tap water has 1 ppb U, 1 ppb Th, and also 1 ppb K. If filling with tap water, the water buffer will contribute 1.8 Hz, 0.4 Hz, and 6.3 Hz single rates from U/Th/K, respectively. Purified water in the water pool will have much lower radioactivity. Thus the radioactivity from water buffer can be ignored.

The Co in stainless steel varies from batch to batch and should be measured before use as detector material, such as the outer vessel. U/Th/K concentration in normal weld rods are very high. There are non-radioactivity weld rods commercially available. Weld rods TIG308 used in KamLAND were measured to have $<$1 ppb Th, 0.2 ± 0.08 ppb U, 0.1 ± 0.03 ppb K, and 2.5 ± 0.04 mBq/kg Co, five orders of magnitude lower than normal weld rods. The welded stainless steel in KamLAND has an average radioactivity of 3 ppb Th, 2 ppb U, 0.2 ppb K, and 15 mBq/kg Co. Assuming the same radioactivity for the vessel of the Daya

Bay neutrino detector module, the corresponding rate from a 20-ton welded stainless steel vessel are 7 Hz, 4.6 Hz, 1.5 Hz, 4.5 Hz for U/Th/K/Co, respectively for a total of 17.6 Hz.

A potential PMT candidate is the Hamamatsu R5912[‡] with low radioactivity glass. The concentrations of U and Th are both less than 40 ppb in the glass, and that of K is 25 ppb. The Monte Carlo study shows that the single rate is 2.2 Hz, 1 Hz, 4.5 Hz for U/Th/K, respectively, with a 20 cm oil buffer from the PMT surface to the liquid scintillator. The total rate from the PMT glass is 7.7 Hz.

Following the design experience of Borexino and Chooz, backgrounds from impurities in the liquid scintillator can be reduced to the required levels. A major source is the U/Th contamination in the Gadolinium, which can be purified before doped into liquid scintillator. The U/Th/K concentration of $10^{-12} g/g$ in liquid scintillator will contribute only 0.8 Hz of uncorrelated background in a 20-ton detector module.

The radioactivity inside the liquid scintillator can also make *correlated* background. The alpha particles from the U/Th impurity can make $(\alpha$,n$)^{16}$O reaction with ^{13}C in the liquid scintillator, which leads to a correlated background if (a) the neutron is fast enough, or (b) there is an accompanying photon from the excited state of ^{16}O. Assuming a 10^{-12}g/g U/Th concentration, this contributes to a correlated background rate of $\sim$4/year/module. Compared to Table 3.11, this is about 40% of the muon-induced fast neutron rate at the far site. The cross section of ^{13}C$(\alpha$,n$)^{16}$O is known to $\sim$20% for an alpha energy $<$10 MeV (highest energy α from U/Th is about 9 MeV). Thus for a given U/Th concentration, this background can be evaluated relatively precisely. Therefore, we shall omit it in the systematic uncertainty calculation in Section 3.3.5.

The alpha particles from U/Th chains in the rock or PMT glasses can also make $(\alpha$,n) reaction with ^{18}O, ^{29}Si, and ^{30}Si (0.20%, 4.68%, and 3.09% naturally abundant, respectively) in these materials. Similar to ^{13}C above, gamma rays can be released from these reactions due to excited final states. Upper limit of the gamma rate is estimated to be $\sim$1/day/module, based on the total $(\alpha$,n) reaction cross section on the three nuclei [13]. A small fraction of these gamma can have rather high energy, and generate “neutron-like” signal ($>$6 MeV) in the scintillator. Nevertheless, compared to the “neutron-like” rate due to cosmogenic beta emitters in Table 3.13, this contribution is negligible. The average emitting neutron energies from these reactions are about 2.5 MeV. Even for those neutrons from the PMT glass, they will be attenuated by $\sim 10^{-5}$ due to the shielding of the mineral oil and gamma catcher before entering the target. Therefore, the *correlated* (γ and neutron) background here is also negligible compared to, for example, the fast neutron background in Table 3.11.

Radon is one of the radioactive daughters of ^{238}U, which can increase the background rate of the experiment. The Radon concentration in the experimental halls can be kept to an acceptable level by ventilation with fresh air from outside. Since the neutrino detector modules are immersed in a 2.5-meter thick water buffer, it is expected that the radon contribution, as well as the krypton, can be safely ignored for the water pool design.

The β decay of long lived radioactive isotopes produced by cosmic muons in the scintillator will contribute a couple of Hz at the near detector, and less than 0.1 Hz at the far detector. The rate of muon decay or muon capture are 2–6% of the muon rate. So they can be ignored when viewed as a source of singles.

3.3.5 Background Subtraction Uncertainty

There are other sources of backgrounds, such as cosmogenic nuclei, stopped-muon decay, and muon capture. While they are important for a shallow site, our study shows that they can be safely ignored at Daya Bay.

The major backgrounds are summarized in Table 3.14. The rates assume a muon tagging efficiency of 99.5% and a neutron efficiency of 78% (product of 0.85 Gd fraction and 0.93 energy cut). In our sensitivity study, the uncertainties were taken to be 100% for the accidental and fast neutron backgrounds. The ^{8}He/^{9}Li background can be measured to an uncertainty of 0.3% and 0.1% at the near and far sites, respectively.

[‡]The R5912 is a newer version of the R1408 used by SNO [12].

	DYB site	LA site	far site
Antineutrino rate (/day/module)	930	760	90
Natural radiation (Hz)	<50	<50	<50
Single neutron (/day/module)	18	12	1.5
β-emission isotopes	210	141	14.6
Accidental/Signal	<0.2%	<0.2%	<0.1%
Fast neutron/Signal	0.1%	0.1%	0.1%
^{8}He^{9}Li/Signal	0.3%	0.2%	0.2%

Table 3.14. Summary of signal and background rates in the antineutrino detectors at Daya Bay. A neutron detection efficiency of 78% has been applied to the antineutrino and single-neutron rates.

The rates and energy spectra of all three major backgrounds can be measured *in-situ*. Thus the backgrounds at the Daya Bay experiment are well controlled. The simulated energy spectra of backgrounds are shown in Fig. 3.16. The background-to-signal ratios are taken at the far site.

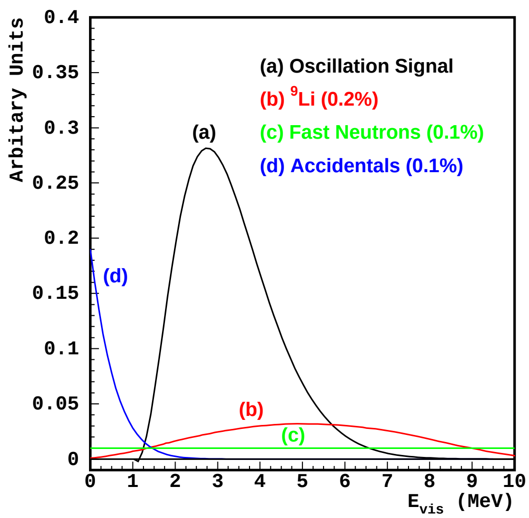

Fig. 3.16. Spectra of three major backgrounds for the Daya Bay experiment and their size relative to the oscillation signal, which is the difference of the expected neutrino signal without oscillation and the 'observed' signal with oscillation for $\sin^2 2\theta_{13} = 0.01$.

3.4 Sensitivity

If θ_{13} is non-zero, a rate deficit will be present at the far detector (primarily) due to oscillation. At the same time, the energy spectra of neutrino events at the near and far detectors will be different because neutrinos of different energies oscillate at different frequencies. Both rate deficit and spectral distortion of neutrino signal will be exploited in the final analysis to obtain maximum sensitivity. When the neutrino event statistics are low (<400 ton$\cdot$GW$_{\rm th}\cdot$y), the sensitivity is dominated by the rate deficit. For luminosity higher than 8000 ton$\cdot$GW$_{\rm th}\cdot$y, the sensitivity is dominated by the spectral distortion [18]. The Daya Bay experiment will have $\sim$4000 ton$\cdot$GW$_{\rm th}\cdot$y exposure in three years, so both rate deficit and shape distortion effects will be important to the analysis.

The antineutrino rates in the detector modules determine the statistical uncertainty contribution to the experimental sensitivity. The efficiency factors that have been assumed to compute the expected rates (no oscillation) are given in Table 3.15.

Source	Efficiency	
	Near	Far
Neutron detection	0.78	0.78
Positron detection	0.98	0.98
Muon Veto deadtime	0.95	0.95
Calibration runs	0.99	0.99
Reactor/experiment downtime	0.82	0.82

Table 3.15. Sources of inefficiency leading to loss of statistical precision.

3.4.1 Global χ^2 Analysis

Many systematic uncertainties will contribute to the final sensitivity of the Daya Bay experiment, and many of them are correlated. The correlation of the uncertainties must be taken into account correctly. A rigorous analysis of systematic uncertainties can be done by constructing a χ^2 function with pull terms, where the uncertainty correlations can be introduced naturally [18–21]:

$$\begin{aligned}\chi^2 &= \min_{\gamma} \sum_{A=1}^{8} \sum_{i=1}^{N_{bins}} \frac{\left[M_i^A - T_i^A\left(1+\alpha_c+\sum_r \omega_r^A \alpha_r + \beta_i + \varepsilon_D + \varepsilon_d^A\right) - \eta_f^A F_i^A - \eta_n^A N_i^A - \eta_s^A S_i^A\right]^2}{T_i^A + (\sigma_{b2b} T_i^A)^2} \\ &+ \frac{\alpha_c^2}{\sigma_c^2} + \sum_r \frac{\alpha_r^2}{\sigma_r^2} + \sum_{i=1}^{N_{bins}} \frac{\beta_i^2}{\sigma_{\rm shp}^2} + \frac{\varepsilon_D^2}{\sigma_D^2} + \sum_{A=1}^{8}\left[\left(\frac{\varepsilon_d^A}{\sigma_d}\right)^2 + \left(\frac{\eta_f^A}{\sigma_f^A}\right)^2 + \left(\frac{\eta_n^A}{\sigma_n^A}\right)^2 + \left(\frac{\eta_s^A}{\sigma_s^A}\right)^2\right] \end{aligned} \tag{29}$$

where A sums over detector modules, i sums over energy bins, and γ denotes the set of minimization parameters, $\gamma = \{\alpha_c, \alpha_r, \beta_i, \varepsilon_D, \varepsilon_d^A, \eta_f^A, \eta_n^A, \eta_s^A\}$. The γ's are used to introduce different sources of systematic uncertainties. The standard deviations of the corresponding parameters are $\{\sigma_c, \sigma_r, \sigma_{\rm shp}, \sigma_D, \sigma_d, \sigma_f^A, \sigma_n^A, \sigma_s^A\}$. They will be described in the following text. T_i^A is the expected events in the i-th energy bin in detector A, and M_i^A is the corresponding measured events. F_i^A, N_i^A, S_i^A are number of fast neutron, accidental, and ^{8}He/^{9}Li backgrounds, respectively. For each energy bin, there is a variance T_i^A and a bin-to-bin systematic uncertainty σ_{b2b}. For each point in the oscillation space, the χ^2 function is minimized with respect to the parameters γ.

Assuming each uncertainty can be approximated by a Gaussian, this form of χ^2 can be proven to be strictly equivalent to the more familiar covariance matrix form $\chi^2 = (M-T)^T V^{-1}(M-T)$, where V is the covariance matrix of $(M-T)$ with systematic uncertainties included properly [19].

To explore the sensitivity to θ_{13}, we use the single parameter raster scan method. We make an assumption of no oscillations so that T_i^A are the event numbers without oscillation. For each given Δm_{31}^2, the "measured" event numbers M_i^A are calculated with different $\sin^2 2\theta_{13}$. The $\sin^2 2\theta_{13}$ value corresponding to $\chi^2 = 2.71$ is the limit of the experiment to exclude the "no oscillation" assumption at 90% confidence level.

The systematic uncertainties are described in detail:

- The reactor-related correlated uncertainty is $\sigma_c \approx 2\%$. This fully correlated uncertainty will be cancelled by the near-far relative measurement and has little impact on the sensitivity.

- The reactor-related uncorrelated uncertainty for core r is $\sigma_r \approx 2\%$. These enter the normalization of the predicted event rate for each detector A according to the weight fractions ω_r^A. After minimization, the σ_r contribute a total of ∼0.1% to the relative normalization of neutrino rate. This is essentially equivalent to the analysis described in Section 3.1, and takes into account the correlations of this uncertainty with the others (like the detector efficiencies ε_d^A).

- The spectrum shape uncertainty is $\sigma_{\mathrm{shp}} \approx 2\%$: The shape uncertainty is the uncertainty in the neutrino energy spectra calculated from the reactor information. This uncertainty is uncorrelated between different energy bins but correlated between different detectors. Since we have enough statistics at near detector to measure the neutrino energy spectrum to much better than 2%, it has little effect on the Daya Bay sensitivity.

- The detector-related correlated uncertainty is $\sigma_D \approx 2\%$. Some detection uncertainties are common to all detectors, such as H/Gd ratio, H/C ratio, neutron capture time on Gd, and spill in/out effects, assuming we use the same batch of liquid scintillator and identical detectors. Based on the Chooz experience, σ_D is (1–2)%. Like other fully correlated uncertainties, it has little impact on sensitivity.

- The detector-related uncorrelated uncertainty is $\sigma_d = 0.38\%$. We take the baseline systematic uncertainty as described in Section 3.2.3. The goal systematic uncertainty with swapping is estimated to be 0.12%.

- The background rate uncertainties σ_f^A, σ_n^A, and σ_s^A, corresponding to the rate uncertainty of fast neutron, accidental backgrounds, and ^{8}He/^{9}Li isotopes. They are listed in Section 3.3.5.

- Bin-to-bin uncertainty σ_{b2b}: The bin-to-bin uncertainty is the systematic uncertainty that is uncorrelated between energy bins and uncorrelated between different detector modules. The bin-to-bin uncertainties normally arise from the different energy scale at different energies and uncertainties of background energy spectra during background subtraction. The only previous reactor neutrino experiment that performed spectral analysis with large statistics is Bugey, which used a bin-to-bin uncertainty of order of 0.5% [22,23]. With better designed detectors and much less background, we should have much smaller bin-to-bin uncertainties than Bugey. The bin-to-bin uncertainty can be studied by comparing the spectra of two detector modules at the same site. We will use 0.3%, the same level as the background-to-signal ratio, in the sensitivity analysis. The sensitivity is not sensitive to σ_{b2b} at this level. For example, varying σ_{b2b} from 0 to 0.5% will change the $\sin^2 2\theta_{13}$ sensitivity from 0.0082 to 0.0087 at the best fit Δm^2_{31}.

There are other uncertainties not included in the χ^2 function. 1) Due to the energy resolution, the spectra are distorted. However, the energy bins used for sensitivity analysis (∼30 bins) are 2∼6 times larger than the energy resolution, and the distortion happens at all detectors in the same way. It has little impact on the final sensitivity. 2) Detector energy scale uncertainty has significant impact on detection uncertainties (neutron efficiency and positron efficiency) which has been taken into account in σ_d. An energy scale uncertainty will shift the whole spectrum, thus directly impacting the analysis, especially on the best fit values. However, this shift has very little impact on our sensitivity computations. 3) Current knowledge on θ_{12} and Δm_{21} has around 10% uncertainties. Although the primary oscillation effect at the Daya Bay baseline is related to θ_{13} only, the subtraction of θ_{12} oscillation effects introduce very small uncertainties (see Section 1.2.4). We have studied the above three sources of uncertainty and found that none of them have a significant impact on the sensitivity of the Daya Bay experiment. For simplicity, they are ignored in our χ^2 analysis of sensitivity.

3.4.2 θ_{13} Sensitivity

Figure 3.17 shows the sensitivity contour in the $\sin^2 2\theta_{13}$ versus Δm^2_{31} plane for three years (we assume 1 year $\equiv$ 300 live days) of data, using the global χ^2 analysis and the baseline values for detector-related systematic uncertainties. The green shaded area shows the 90% confidence region of Δm^2_{31} determined by

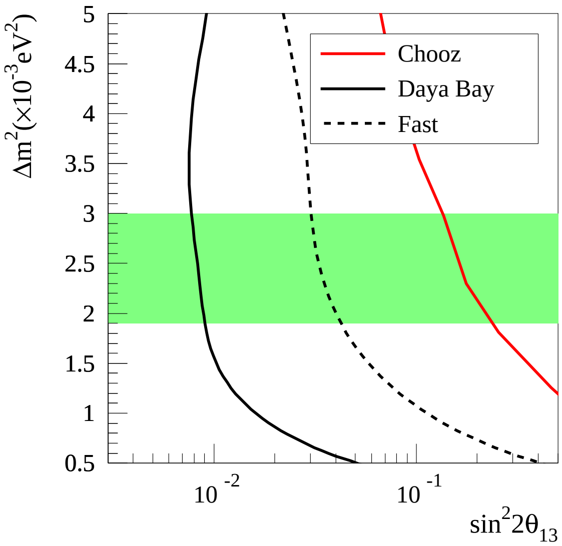

Fig. 3.17. Expected $\sin^2 2\theta_{13}$ sensitivity at 90% C.L. with 3 years of data, as shown in solid black line. The dashed line shows the sensitivity of a fast measurement with the DYB near site and mid site only which would be made if additional funds are obtained. The red line shows the current upper limit measured by Chooz.

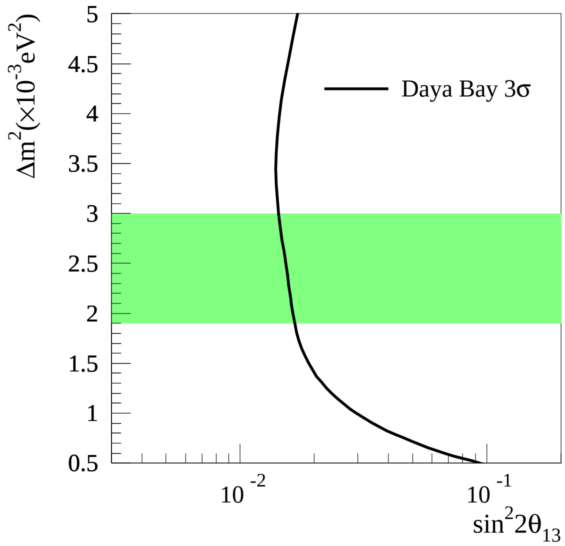

Fig. 3.18. Expected 3σ discovery limit for $\sin^2 2\theta_{13}$ at Daya Bay with 3 years of data.

atmospheric neutrino experiments. Assuming four 20-ton modules at the far site and two 20-ton modules at each near site, the statistical uncertainty is around 0.2%. The sensitivity of the Daya Bay experiment with this design can achieve the challenging goal of 0.01 with 90% confidence level over the entire allowed (90% C.L.) range of Δm^2_{31}. At the best fit $\Delta m^2_{31} = 2.5 \times 10^{-3}$ eV^2, the sensitivity is around 0.008 with 3 years of data. The corresponding values for other assumptions of systematic uncertainties are shown in Table 3.16.

Systematic Uncertainty Assumptions:	Baseline	Goal	Goal with swapping
90% C.L. Limit:	0.008	0.007	0.006

Table 3.16. 90% C.L. sensitivity limit for $\sin^2 2\theta_{13}$ at $\Delta m^2_{31} = 2.5 \times 10^{-3}$ eV^2 for different assumptions of detector related systematic uncertainties as considered in Section 3.2.3. We assume 3 years running for each scenario.

Figure 3.18 shows the 3σ discovery limit for $\sin^2 2\theta_{13}$ at Daya Bay with 3 years of data. At $\Delta m^2_{31} = 2.5 \times 10^{-3}$ eV^2, the corresponding $\sin^2 2\theta_{13}$ discovery limit is 0.015. Figure 3.19 shows the sensitivity

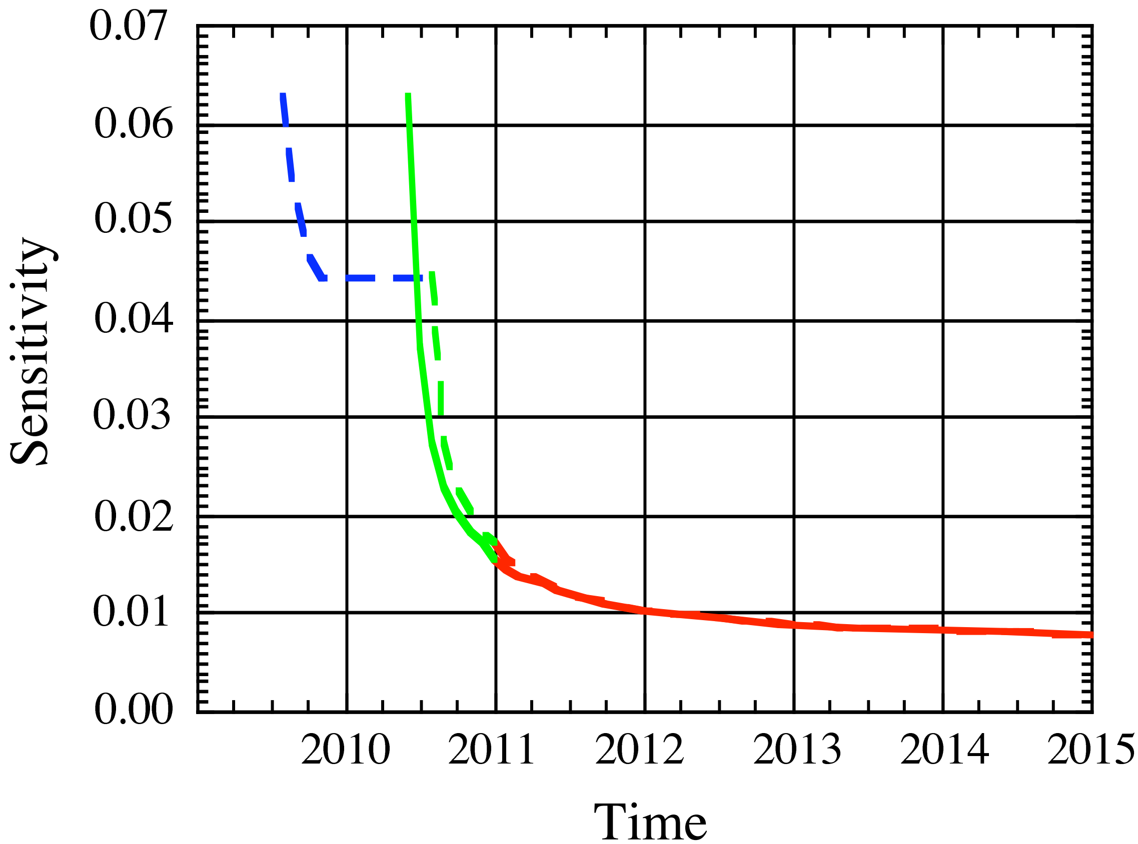

Fig. 3.19. Expected $\sin^2 2\theta_{13}$ sensitivity at 90% C.L. versus time. The solid curve is with two near sites and one far site. The dashed curve includes running first with one near and one mid site. The value of Δm^2_{31} is taken to be 2.5×10^{-3} eV^2.

The tunnel of the Daya Bay experiment will have a total length around 3 km. The tunnelling will take $\sim$2 years. To accelerate the experiment, the first completed experimental hall, the Daya Bay near hall, can be used for detector commissioning. Furthermore, it is possible to conduct a fast experiment with only two detector sites, the Daya Bay near site and the mid site. For this fast experiment, the 'far detector', which is located at the mid hall, is not at the optimal baseline. At the same time, the reactor-related uncertainty would be 0.7%, very large compared with that of the full experiment. However, the sensitivity is still much better than the current best limit of $\sin^2 2\theta_{13}$. It is noteworthy that the improvement comes from better background shielding and improved experiment design including the addition of near detectors. The sensitivity of the fast option for one year of data taking is shown in the dashed line in Fig. 3.17. With one year of data, the sensitivity is $\sim$0.035 for $\Delta m^2 = 2.5 \times 10^{-3}$ eV^2, compared with the current limit of 0.17 from the Chooz experiment. This fast option will allow us to gain valuable experience and a preliminary physics result while construction is being completed. The higher precision of the completed experiment will be necessary to fully complement the future long baseline accelerator experiments as discussed in Section 1.1.3.

REFERENCES

1. M. Apollonio *et al.*, Phys. Lett. **B420**, 397 (1998); Phys. Lett. **B466**, 415 (1999); Euro. Phys. J. C **27**, 331 (2003).
2. L. A. Mikaelyan and V. V. Sinev, Phys. Atom. Nucl. **63**, 1002 (2000); L. Mikaelyan, Nucl. Phys. Proc. Suppl. **91**, 120 (2001); L. A. Mikaelyan, Phys. Atom. Nucl. **65**, 1173 (2002).
3. V. Kopeikin, L. Mikaelyan, V. Sinev, Phys. Atom. Nucl. **64**, 849 (2001); V. Kopeikin, L. Mikaelyan, V. Sinev, hep-ph/0412044.
4. K. Eguchi *et al.*, Phys. Rev. Lett. **90**, 021802 (2003).
5. T. Gaisser, *Cosmic Rays and Particle Physics*, Cambridge University Press, 1991.
6. D. Chirkin, hep-ph/0407078.
7. J. Kremer *et al.*, Phys. Rev. Lett. **83**, 4241 (1999)
8. H. Jokisch *et al.*, Phys. Rev. **D19**, 1368 (1979).
9. P. Antonioli *et al.*, Astro. Phys. **7**, 357 (1997).
10. Y. F. Wang *et al.*, Phys. Rev. **D64**, 013012 (2001).
11. T. Hagner *et al.*, Astro. Phys. **14**, 33 (2000).
12. J. Boger *et al.*, Nucl. Instr. and Meth. **A449**, 172 (2000).
13. JENDL (α,n) Reaction Data File 2005, http://wwwndc.tokai-sc.jaea.go.jp/ftpnd/jendl/jendl-an-2005.html
14. M.G.T. Lasserre, hep-ex/0606025.
15. KamLAND collaboration, private communication.
16. T. Araki *et al.*, (KamLAND Collaboration) Phys. Rev. Lett. **94**, 081801 (2005).
17. Liangjian Wen *et al.*, Nucl. Instr. and Meth. **A564**, 471 (2006).
18. P. Huber, M Lindner, T. Schwetz, and W. Winter, Nucl. Phys. **B665**, 487 (2003); Nucl. Phys. **B645**, 3 (2002).
19. D. Stump *et al.*, Phys. Rev. **D65**, 014012 (2001).
20. Y. Fukuda *et al.*, Phys. Rev. Lett. **81**, 1562 (1998); Y. Ashie *et al.*, hep-ex/0501064.
21. H. Minakata, H. Sugiyama, O. Yasuda, K. Inoue, and F. Suekane, Phys. Rev. **D68**, 033017 (2003); H. Minakata and H. Sugiyama, Phys. Lett. **B580**, 216 (2004).
22. Y. Declais *et al.*, Phys. Lett.**B338**, 383 (1994). B. Ackar *et al.*, Nucl. Phys. **B434**, 503 (1995); B. Ackar *et al.*, Phys. Lett. **B374**, 243 (1996).
23. H. Sugiyama and O. Yasuda, hep-ph/0508090.

4 Work Breakdown Structure

The Daya Bay work breakdown structure (WBS) has nine major categories as shown in Table 4.1. China will take the lead role on 1.1, 1.4 and 1.6; the U.S. will take the lead role on 1.2 and 1.3. The remaining tasks: 1.5, 1.7, 1.8 and 1.9 will be jointly led.

WBS element	Task Name
1.1	Antineutrino Detector
1.2	Muon System
1.3	Calibration and Monitoring Systems
1.4	Electronics, Trigger, DAQ and Online
1.5	Offline
1.6	Conventional Construction and Equipment
1.7	Installation and Test
1.8	Integration
1.9	Project Management

Table 4.1. Daya Bay Work Breakdown Structure (WBS) shown at L2.

4.1 WBS Dictionary

The WBS dictionary descriptions at L2 and the complete WBS down to L3 are described below. The WBS includes the entire project scope; for details on the U.S. scope see Section 19.2.1.

WBS 1.1: Antineutrino Detector

This element covers labor, materials and equipment associated with the design, further prototyping, construction, delivery, assembly and testing of the antineutrino detector, its tanks, support structures and rigging equipment. This element also includes the liquid scintillator, Gd-loaded LS, mineral oil buffer and liquid handling/purification systems. The element includes the PMTs and associated cables. The interface between this element and element 1.4 is the connector on the front panel of the FEE board. It also includes safety systems needed specifically for these elements. This element includes any special fixtures required to fabricate, assemble and install the antineutrino detectors at the Daya Bay Site. Note that this element will provide system experts and cognizant engineering oversight along with relevant procedures and installation documentation for final assembly in the Surface Assembly Building and installation of the antineutrino detectors in the experimental halls, plus subsequent in-situ system testing; while 1.7 provides the technician, trade and supervisor resources and scheduling of this effort at the Daya Bay facilities. All required management activities associated specifically with the antineutrino detector are included here. The complete WBS for the antineutrino detector to L3 is shown in Table 4.2.

WBS 1.2: Muon System

This element covers labor, materials and equipment associated with the design, further prototyping, construction, delivery, assembly and testing of the muon system, its tracking chambers, water Cherenkov system, support structures, gas systems, front-end/readout electronics and associated power supplies and cables. This element also includes the water handling, filtering, temperature control system including plumbing, but not the source, storage or disposal which is the scope of 1.6. It also includes safety systems needed specifically for these elements. This element includes any special fixtures required to fabricate, assemble, test and install the muon systems in their experimental halls. Note that this element will provide system experts and cognizant engineering oversight along with relevant procedures and installation documentation for testing of the muon system element in the Surface Assembly Building, installation of the muon system elements in the experimental halls, plus subsequent in-situ system testing; while 1.7 provides the technician,

WBS	Description
1.1	**Antineutrino Detector**
1.1.1	Detector Tank
1.1.2	Acrylic Vessels
1.1.3	Liquid Scintillator and Mineral Oil
1.1.4	Photomultiplier Tubes (PMTs)
1.1.5	Properties Measurement and Monitoring
1.1.6	Lifting and Transport
1.1.7	Materials Testing
1.1.8	Safety & Specialized Detector Systems
1.1.9	Subsystem Management

Table 4.2. Daya Bay WBS for the Antineutrino Detector shown to L3.

trade and supervisor resources and scheduling of this effort at the Daya Bay facilities. All required management activities associated specifically with the muon system are included here. The complete WBS for the Muon System to L3 is shown in Table 4.3.

WBS	Description
1.2	**Muon System**
1.2.1	Mechanical Elements
1.2.2	Water Cherenkov System Elements
1.2.3	RPC
1.2.4	Scintillator Option
1.2.5	HV Decoupler
1.2.6	Safety Systems
1.2.7	Subsystem Management

Table 4.3. Daya Bay WBS for the Muon Detector, shown to L3.

WBS 1.3: Calibration

This element covers labor, materials and equipment associated with the design, prototyping, construction, delivery, assembly and testing of the Calibration system, its mechanisms, plumbing, light/radiation sources, shutters, valves and devices. It also includes the control system, readout electronics and associated power supplies and cables. This element includes safety and administrative custodial requirements for source security, handling and shipping. It includes any special fixtures required to fabricate, assemble and install the Calibration system elements in the Surface Assembly Building or experimental halls. Note that this element will provide system experts and cognizant engineering oversight along with relevant procedures and installation documentation for installation of the Calibration system elements while in the Surface Assembly Building, in the experimental hall, and subsequent in-situ system testing; while 1.7 provides the technician, trade and supervisor resources and scheduling of this effort at the Daya Bay facilities. All required management activities associated specifically with the Calibration System are included here. The complete WBS for the Calibration and Monitoring System to L3 is shown in Table 4.4.

WBS 1.4: Electronics and Online systems

This element covers labor, materials and equipment associated with the design, prototyping, construction, delivery, assembly and testing of detector readout electronics, trigger and clock systems, data acquisition, and online hardware and software. It also covers all non-physicist labor associated with the spec-

WBS	Description
1.3	**Calibration and Monitoring Systems**
1.3.1	Automated Deployment System
1.3.2	Manual Calibration Systems
1.3.3	LED System
1.3.4	Radioactive Calibration Sources
1.3.5	Detector Component Monitoring Systems
1.3.6	Low-Background Counting System
1.3.7	Safety Systems
1.3.8	Prototypes
1.3.9	Assembly
1.3.10	Subsystem Test
1.3.11	Subsystem Management

Table 4.4. Daya Bay WBS for Calibration and Monitoring, shown to L3.

ification, design, prototyping, coding, integration and testing of these systems. The hardware includes all racks, crates, power supplies, internal cables, AC power distribution and circuit breakers, remote network power switches, uninterruptible power supplies, custom and off-the-shelf boards, as well as computers and communication equipment. (Interface documents will be developed with strict interface definitions between readout electronics and each of the detector elements.) This also includes any air or water cooling systems, plumbing, leak detection, ducting, fans and heat exchangers that may be required. (The strict definition of the interface with conventional utilities (see WBS 1.6.5) will be documented elsewhere.) It also includes safety systems needed specifically for these elements (in rack smoke detection and fire suppression for example). This element includes any special fixtures required to assemble and install these hardware elements in the Surface Assembly Building or experimental halls. This element does not include sensor and control technologies specific to the detector and calibration systems (AD sensors are covered under WBS 1.1, muon sensors under WBS 1.2, etc), but does include the electronic and computer resources necessary to collect and record this information into a database.

This element will provide system experts and cognizant engineering oversight along with relevant procedures and installation documentation for installation of the electronic and online hardware elements while in the Surface Assembly Building, the experimental hall, and subsequent in-situ system testing; while 1.7 provides the technician, trade and supervisor resources and scheduling of this effort at the Daya Bay facilities. All required management activities associated specifically with electronic and online hardware and software are included here. The complete WBS for the electronics and online systems to L3 is shown in Table 4.5.

WBS 1.5: Offline Hardware and Software

This element covers all non-physicist labor associated with the specification, design, prototyping, coding, integration and testing of the offline hardware and software. It also includes hardware and code written for controls and monitoring functions. The simulation efforts for each of the subsystems and the overall experiment are also included in this element. All required management activities associated specifically with offline hardware and software are included here. The complete WBS for the Offline Hardware and Software to L3 is shown in Table 4.6.

WBS 1.6: Civil Construction

This element covers all labor, materials and equipment associated with the design and construction of the underground tunnels and caverns. It covers the design and construction of the entrance, the ancillary rooms for the LS and water purification systems as well as all underground utilities for the tunnels, halls

WBS	Description
1.4	**Electronics and Online**
1.4.1	PMT readout electronics
1.4.2	RPC readout electronics
1.4.3	Trigger and clock systems
1.4.4	Data acquisition
1.4.5	Monitoring and controls
1.4.6	Online
1.4.7	Infrastructure
1.4.8	Subsystem Test
1.4.9	Subsystem Management

Table 4.5. Daya Bay WBS for Electronics and Online systems, shown to L3.

WBS	Description
1.5	**Offline**
1.5.1	Hardware, Networking and data transfer
1.5.2	Core Software
1.5.3	Physics Simulation and Analysis
1.5.4	Subsystem Test
1.5.5	Subsystem Management

Table 4.6. Daya Bay WBS for Offline, shown to L3.

and experiment. This element also covers the design and construction of the surface buildings at the site. All ‘universal’ or non detector specific life and equipment safety systems — ventilation, smoke detection, fire suppression, emergency lighting and power, ODH, etc. are included here. Detector specific safety interlock systems will be included under their WBS scope. All required management activities associated specifically with the Civil Construction and Infrastructure are included here. The complete WBS for the Conventional Construction to L3 is shown in Table 4.7.

WBS	Description
1.6	**Conventional Construction and Equipment**
1.6.1	Tunnels
1.6.2	Tunnel Entrance and Surroundings
1.6.3	Experimental Halls
1.6.4	Other Underground Rooms
1.6.5	Conventional Utilities
1.6.6	Communication Systems
1.6.7	Surface Buildings
1.6.8	Safety Systems
1.6.9	Subsystem Management

Table 4.7. Daya Bay WBS for Conventional Construction, shown to L3.

WBS 1.7: Installation Planning & Support

This element supports the overall planning, staging, control and execution of the final assembly and installation of the experimental hardware on site at Daya Bay. It includes labor, materials and universal (not associated with a single detector subsystem above) equipment required to perform these functions. For example, lift trucks, scaffolding, hand-tools and general rigging equipment. It does include the cost of a custom transport vehicle to deliver antineutrino detectors and LS tanks from the surface to experimental halls; however, it does not include the custom installation and test hardware required for individual detector elements — these are included in the WBS elements above. It also includes the overall system testing and commissioning of the experiment once installed. The element includes activities in the surface assembly buildings as well as in the underground caverns and rooms. It includes all technician, trades, supervisory and engineering labor required to install the detector elements, but not the physicist and engineering efforts from the subsystems supporting the installation and test activities. All required management activities associated specifically with Installation and Test are included here. The complete WBS for Installation and Test to L3 is shown in Table 4.8.

WBS	Description
1.7	**Installation Planning & Support**
1.7.1	Installation
1.7.2	Detector Test and Commissioning
1.7.3	Subsystem Management

Table 4.8. Daya Bay WBS for Installation and Test, shown to L3.

WBS 1.8: Integration

The scope of effort for this element includes the cost of labor and materials to assist experimental subsystems and their managers in developing, defining, and controlling the mechanical systems, electrical systems, experimental assembly, safety systems, and civil construction interface between each subsystem. To this end this element will act as liaisons between each subsystem to coordinate and document efforts in resolving all physical interface issues. Engineering and design effort is being devoted to ensure that subsystem hardware can fit together, be assembled and serviced, and have minimal negative impact on other subsystem performance. This element will communicate integration issues and their resolution based on change control policy to L2 managers, project management and the collaboration in general on interface issues. This element must approve and process all Engineering Change Request and Engineering Change Notice (ECR/ECN) dealing with subsystem interface, experimental assembly and physical envelope related issues. To accomplish this effort the subsystem has been subdivided into five WBS L3 subcategories. The complete WBS for the System Integration to L3 is shown in Table 4.9.

WBS	Description
1.8	**Integration**
1.8.1	Mechanical Systems Integration
1.8.2	Electrical Systems Integration
1.8.3	Experimental Assembly
1.8.4	Safety Systems Integration
1.8.5	Subsystem Management

Table 4.9. Daya Bay WBS for System Integration, shown to L3.

WBS 1.9: Project Management

This WBS element includes the cost of labor and materials necessary to plan, track, manage, maintain effective communications, distribute drawings and documents, conduct reviews and perform necessary

EH&S and QA tasks during all phases of the project. However, subsystem related management and support activities for planning, estimating, tracking and reporting as well as their specific EH&S and QA tasks are included in each of the subsystems. The complete WBS for the Project Management to L3 is shown in Table 4.10.

WBS	Description
1.9	**Project Management**
1.9.1	Planning
1.9.2	Management
1.9.3	Tracking and Reporting
1.9.4	Meetings and Reviews
1.9.5	Project Contingency Funds

Table 4.10. Daya Bay WBS for Project Management, shown to L3.

5 Experimental Site and Laboratories

The Daya Bay site is an ideal place to search for oscillations of antineutrinos from reactors. The nearby mountain range provides excellent overburden to suppress cosmogenic background at the underground experimental halls. Since the Daya Bay nuclear power complex consists of multiple reactor cores, there will be two near detector sites to monitor the yield of antineutrinos from these cores and one far detector site to look for disappearance of antineutrinos. It is possible to instrument another detector site about half way between the near and far detectors to provide independent consistency checks.

The proposed experimental site is located at the east side of the Dapeng peninsula, on the west coast of Daya Bay, where the coastline goes from southwest to northeast (see Fig. 1.10). It is in the Dapeng township of the Longgang Administrative District, Shenzhen Municipality, Guangdong Province. Two mega cities, Hong Kong and Shenzhen are nearby. Shenzhen City* is 45 km to the west and Hong Kong is 55 km to the southwest (all measured in a straight line). The geographic location is east longitude 114°33’00” and north latitude 22°36’00”. Daya Bay is semi-tropical and the climate is dominated by the south Asia tropical monsoon. It is warm and rainy with frequent rainstorms during the typhoon season in one half of the year, while relatively dry in the other half. Frost is rare.

The Daya Bay Nuclear Power Plant (NPP) is situated to the southwest and the Ling Ao NPP to the northeast along the coastline. Each NPP has two cores that are separated by 88 m. The distance between the centers of the two NPPs is about 1100 m. The thermal power of each core is 2.9 $\mathrm{GW_{th}}$. Hence the total thermal power available is 11.6 $\mathrm{GW_{th}}$. A third NPP, Ling Ao II, is under construction and scheduled to come online by 2010–2011. This new NPP is built roughly along the line extended from Daya Bay to Ling Ao, about 400 m northeast of Ling Ao. The core type is the same as that of the Ling Ao NPP. When the Daya Bay—Ling Ao—Ling Ao II NPP are all in operation, the complex can provide a total thermal power of 17.4 $\mathrm{GW_{th}}$.

The site is surrounded to the north by a group of hills which slope upward from southwest to northeast. The slopes of the hills vary from 10° to 45°. The ridges roll up and down with smooth round hill tops. Within 2 km of the site the elevation of the hills are generally vary from 185 m to 400 m. The summit, called Pai Ya Shan, is 707 m PRD†. Due to the construction of the Daya Bay and Ling Ao NPPs, the foothills along the coast from the southwest to the northeast have been levelled to a height of 6.6 m to 20 m PRD. Daya Bay experiment laboratories are located inside the mountain north of the Daya Bay and Ling Ao NPPs.

There is no railway within a radius of 15 km of the site. The highway from Daya Bay NPP to Dapeng Township (Wang Mu) is of second-class grade and 12 m wide. Dapeng Town is connected to Shenzhen, Hong Kong, and the provincial capital Guangzhou by highways which are either of first-class grade or expressways.

There are two maritime shipping lines near the site in Daya Bay, one on the east side and the other on the west side. Oil tankers to and from Nanhai Petrochemical use the east side. Huizhou Harbor, which is located in Daya Bay is 13 km to the north. Two general-purpose 10,000-ton docks were constructed in 1989. Their functions include transporting passengers, dry goods, construction materials, and petroleum products. The ships using these two docks take the west line. The minimum distance from the west line to the power plant site is about 6 km. Two restricted docks of 3000-ton and 5000-ton capacity, respectively, have been constructed on the power plant site during the construction of the Daya Bay NPP [1].

5.1 General Laboratory Facilities

The laboratory facilities include access tunnels connected to the entrance portal, a construction tunnel for waste rock transfer, a main tunnel connecting all the four underground detector halls, a filling hall,

*Shenzhen is the first Special Economic Zone in China. With a total population of about 7 million, many international corporations have their Asian headquarters there. It is both a key commercial and tourist site in South China.

†PRD is the height measured relative to the mouth of the Zhu Jiang River (Pearl River), the major river in South China.

counting rooms, water and electricity supplies, air ventilation, and communication. There is an assembly hall and a control room near the entrance portal on surface. The approximate location of the experiment halls and the layout of the tunnels are shown in Fig. 5.1. All experimental halls are located at similar elevations, approximately −20 m PRD.

Fig. 5.1. Layout of the Daya Bay and Ling Ao cores, the future Ling Ao II cores and possible experiment halls. The entrance portal is shown at the bottom-left. Five experimental halls marked as #1 (Daya Bay near hall), #2 (Ling Ao near hall), #3 (far hall), #4 (mid hall), #5 (LS filling hall) are shown. The green line represents the access tunnel, the blue lines represent the main tunnels and the pink line represents the construction tunnel. The total tunnel length is about 2700 m. It should be noted that the default design does not contain a mid hall. The mid hall is an option and we keep it in the discussion for completeness.

5.1.1 Tunnels

A sketch of the layout of the tunnels is shown in Fig. 5.2. There are three major branches of the main tunnels, which are represented by line{3-7-4-5}, line{4-8-Ling Ao near} and line{5-far site}. They are horizontal tunnels extending from a junction near the mid hall to the near and far underground detector halls. We should note that the reference to the mid hall is for convenience. The default design does not contain a mid hall. However, mid hall is an interesting option. So we will include it in the current discussion of the civil construction. The lines marked as A, B, C, D and E are for the geophysical survey. Line E, which is a dashed line on the top of figure across the far site, is the line of the geophysical survey made to investigate if the far site needs to be pushed further from the reactor cores for future optimizations. Line{1-

2-3} is the access tunnel with a length of 292 m. The lines B and C mark surveys made for the alternative designs of the construction tunnel (which may have different options for cost optimization).

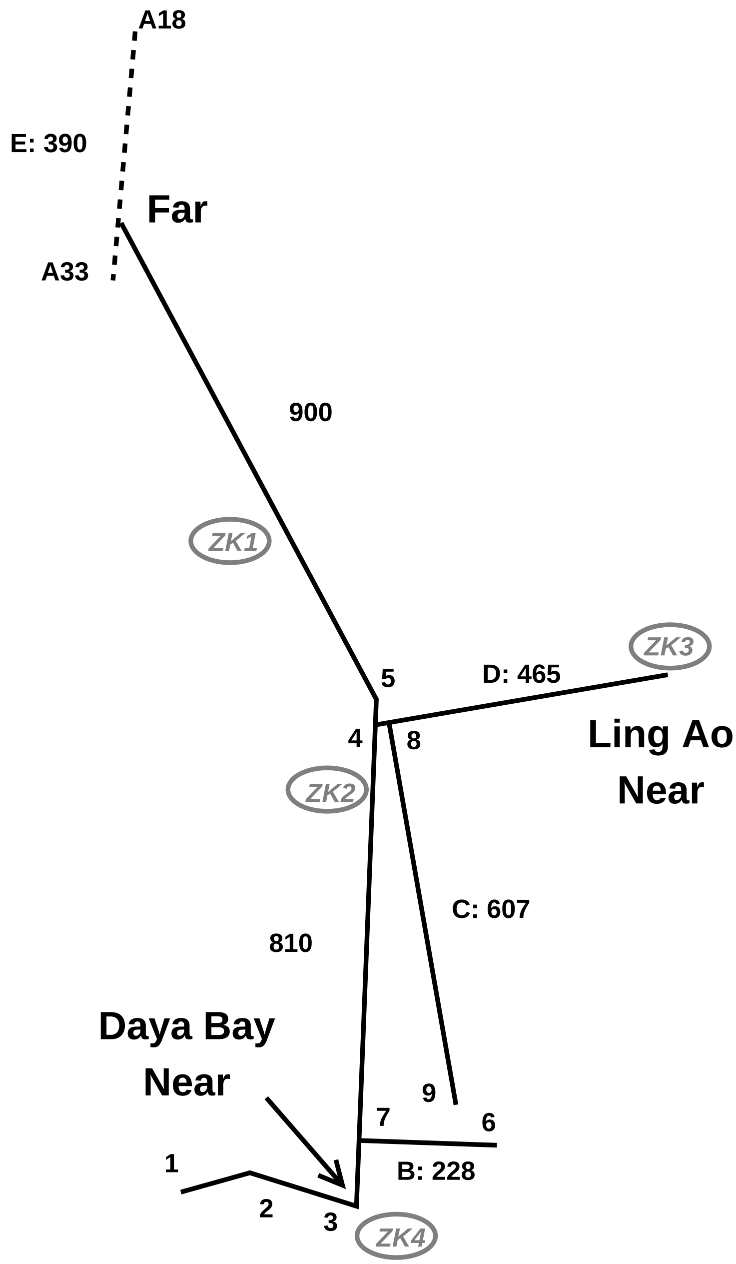

Fig. 5.2. Plan view of the experimental halls and tunnels from the site survey (not a detailed tunnel design). All distances are in meters. Line A{1-2-3-7-4-5-far site} has a total length of 2002 m; Line B{7-6} has a total length of 228 m; Line C{8-9} has a total length of 607 m; Line D{4-8-Ling Ao near} has a total length of 465 m. Line E is the dashed line on the top across far site. The four bore hole sites are marked as ZK1, ZK2, ZK3, ZK4 from north to south.

As shown in Fig. 5.1 the entrance portal to the underground site is located behind the on-site hospital and lies to the west of the Daya Bay near site. The access tunnel from the portal to the Daya Bay near hall is sloped downward with a 9.6% grade. The downward sloping access tunnel allows the underground facilities to be located deeper with more overburden.

The access and main tunnels will be able to accommodate vehicles transporting equipment of different size and weight. The grade of the main tunnel will be 0.3% upward from the Daya Bay near hall to the mid hall, and from the mid hall to both the Ling Ao hall and the far hall. The slightly sloped tunnel has two important functions: to ensure a nearly level surface for the movement of the heavy detectors filled with liquid scintillator inside the main tunnel and to channel any water seeping into the tunnel to a collection pit which is located at the lowest point near the Daya Bay near site. The collected water will be pumped to the surface.

The entrance portal of the construction tunnel (Line{7-6}) is near the lower level of the Daya Bay Quarry. The length of this tunnel is 228 m from the entrance to the junction point with the main tunnel if the shortest construction tunnel option is chosen (see Fig. 5.1). During most of the tunnel construction, all the waste rock and dirt is transferred through this tunnel to the outside in order to minimize the interference with the operation of the hospital and speed up the tunnel construction. We expect the access tunnel and the Daya Bay near hall to be finished earlier than the far and Ling Ao halls since much less tunnelling is required. After the work on this section of tunnel is finished, the Daya Bay near hall will be available for detector installation. Since the construction tunnel is far from the access tunnel and the Daya Bay near hall, interference with the rest of the excavation activities can be minimized and the assembly of detectors in the Daya Bay near site can proceed in parallel. We expect that the Daya Bay near site can be beneficially occupied about 14 months after the start of civil construction. The rock is removed by tram up a slope of about 40% in this case.

There is an alternative design of the construction tunnel as shown in Fig. 2.1, Line {8-9}. It is, from the lower level of Daya Bay quarry to a junction near the mid hall. In this case, the construction tunnel is 380 m longer than the previous options. The slope of this construction tunnel is about one quarter of that of the previous one and therefore normal heavy trucks can be used for debris removal which is easier and faster than tram. The present estimate shows that these two different construction tunnels are not significantly different in cost or schedule for the whole tunnelling of experiment. A choice will be made later in the final design to optimize the tunnel construction.

The cross section of the construction tunnel can be smaller than the other tunnels; it is only required to be large enough for rock and dirt transportation. The grade and the length of this construction tunnel will be determined later to optimize the construction cost and schedule.

Excavation will begin from the construction portal. When it reaches the main tunnel, the excavation will proceed in parallel in the directions of the Daya Bay near hall and the mid hall. Once the tunnelling reaches the the mid hall, it will proceed in parallel in the direction of the far hall and the Ling Ao hall.

The total length of the tunnel is about 2700 m. The amount of waste to be removed will be about 200,000 m^3. About half of the waste will be dumped in the Daya Bay Quarry to provide additional overburden to the Daya near site which is not far away from the Quarry. This requires additional protection slopes and retaining walls. The rest of the waste can be disposed of along with the waste from the construction of the Ling Ao II NPP. Our tunnel waste is about one tenth of the Ling Ao II NPP waste.

5.2 Site Survey

The geological integrity of the Daya Bay site was studied in order to determine its suitability for the construction of the underground experimental halls and the tunnels connecting them. The survey consisted of a set of detailed geological surveys and studies: (1) topographic survey, (2) engineering geological mapping, (3) geophysical exploration, (4) engineering drilling, (5) On-site tests at boreholes and (6) laboratory tests. The site survey has been conducted by the Institute of Geology and Geophysics (IGG) of Chinese Academy of Sciences (CAS). The work started in May 2005 and was completed in June 2006.

5.2.1 Topographic Survey

The topographic survey is essential for determining the position of the tunnels and experimental halls. From the topographic survey the location of the cores relative to the experimental halls is determined, as is the overburden above each of the experimental halls. This measurement of the overburden was input to the optimization of the experimental sensitivity. It is also needed for the portal design and construction. Appropriate maps are constructed out of this measurement. The area surveyed lies to the north of the Daya Bay complex The area of the survey extends 2.5 km in the north-south direction and varies from 450 m to 1.3 km in the east-west direction as determined by the location of the experimental halls and tunnels. The total area measured is 1.839 km^2. The results of the survey are plotted in a scale of 1:2000.

The instrument used for the topographic measurement is a LEICA TCA2003 Total Station, with a precision of $\pm$0.5" in angle and $\pm$1 mm in distance. Based on four very high standard control points that exist in the area, twenty-six high grade control points and forty-five map baseline points are selected. In total, 7000 points are used to obtain the topographic map. As an example, Fig. 5.3 shows the topographic map around the far site. The altitude difference between adjacent contour lines is one meter. The area around the

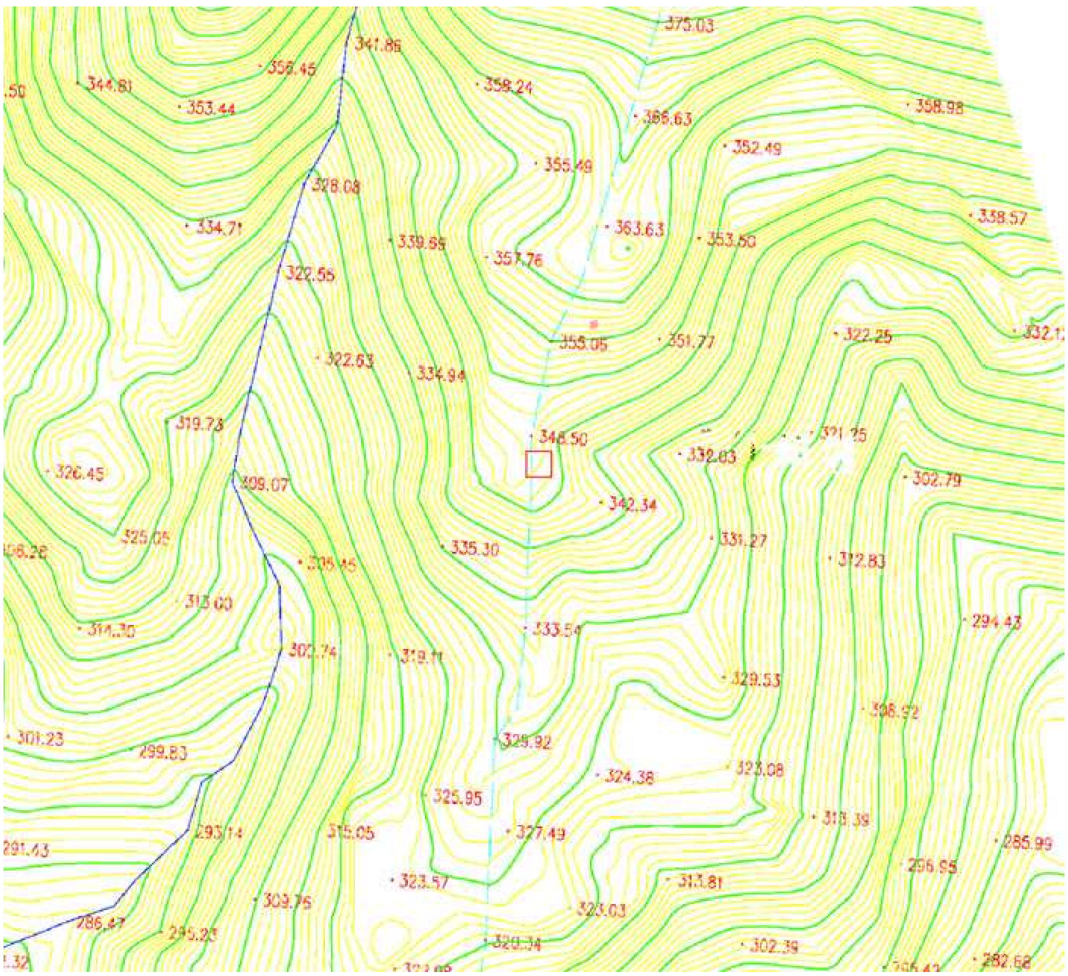

Fig. 5.3. Topographical map in the vicinity of the far site. The location of the far detector hall is marked by a red square in the middle of the map.

entrance portal, which is behind the local hospital, and the two possible construction portals are measured at the higher resolution of 1:500. The cross sections along the tunnel line for the access and construction portals are measured at an even higher resolution of 1:200. The positions of the experimental halls, the entrance portal, and the construction portal are marked on the topographic map.

5.2.2 Engineering Geological Mapping

Geological mapping has been conducted in an area extending about 2.5 km in the north-south direction and about 3 km in the east-west direction. From an on-the-spot survey to fill in the geological map of the area, a list of the geological faults, underground water distribution and contact interface between different types of rocks and weathering zones can be deduced. The statistical information on the orientation of joints is used to deduce the general property of the underground rocks, and the determination of the optimal tunnel axes. The survey includes all the areas through which the tunnels will pass and those occupied by the experimental halls. Reconnaissance has been performed along 28 geological routes, of 18.5 km total length. Statistics of 2000 joints and rock mine skeletons are made at 78 spots. Rock mine appraisals are done with 36 sliced samples.

Surface exploration and trenching exposure show that the landforms and terrain are in good condition. There are no karsts, landslides, collapses, mud slides, empty pockets, ground sinking asymmetry, or hot springs that would affect the stability of the site. There are only a few pieces of weathered granite scattered around the region.

The mountain slopes in the experimental area, which vary from $10°$ to $30°$, are stable and the surface consists mostly of lightly effloresced granite. The rock body is comparatively integrated. Although there is copious rainfall which can cause erosion in this coastal area, there is no evidence of large-scale landslide or collapse in the area under survey. However, there are small-scale isolated collapses due to efflorescence of the granite, rolling and displacement of effloresced spheroid rocks.

The engineering geological survey found mainly four types of rocks in this area: (1) hard nubby and eroded but hard nubby mid-fine grained biotite granite, (2) gray white thick bedding conglomerate and gravel-bearing sandstone, (3) siltstone, (4) sandy conglomerate sandstone. Most of the areas are of hard nubby granite, extended close to the far detector site in the north and reaching to the south, east, and west boundaries of the investigated area. There exists a sub-area, measured about 150 m (north-south) by 100 m (east-west), which contains eroded but still hard nubby granite north of a conspicuous valley existing in this region.[‡] Mildly weathered and weathered granite lies on top of the granite layer. Devonian sandstones are located in the north close to the far detector site. There are also scattered sandstones distributed on the top of the granite. The granite is generally very stable, with only three small landslides found around the middle of the above mentioned valley. The total area of the slide is about 20 m^2 and the thickness is about 1 m. Four faults and two weathering bags have been identified. The weathering bags are shallow with no or at most a slight effect for the rocks at the tunnel depth. The faults are all of widths of tens centimeter and can be crossed quickly during tunnelling. A detailed geological map is shown in Fig. 5.4 and explained in the caption.

The accumulation and distribution of underground water depends generally on the local climate, hydrology, landform, lithology of stratum, and detailed geological structure. In the investigated area of the Daya Bay site, the amount of underground water flux depends, in a complicated way, on the atmospheric precipitation and the underground water seeping that occurs. The sandstone area is rich in underground water seeping in, mainly through joints caused by weathering of crannies that formed in the structure. No circulation is found between the underground water and outside boundary water in this area. Underground water mainly comes from the atmospheric precipitation, and emerges in the low land and is fed into the ocean.

[‡]The valley extends in the north-east direction from the north-east edge of the reservoir. The valley can be seen in Fig. 5.1, as a dark strip crossing midway along the planned tunnel connecting the mid hall and the far hall.

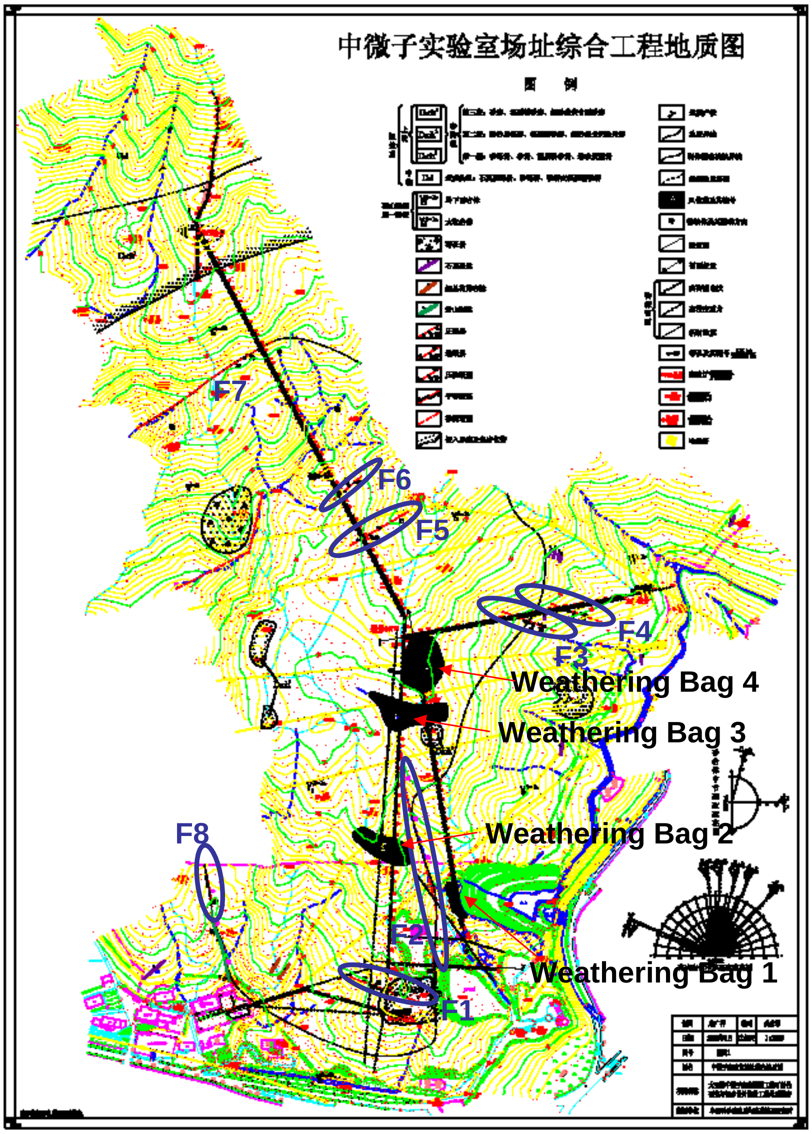

Fig. 5.4. Geological map of the experimental site. The faults are shown as red line segments and marked by blue ellipses. Faults F2, F6, F7, and F8 are revealed by the Geological Mapping (see Section 5.2.2) and Faults F1, F3, F4, and F5 by Geological Exploration (see Section 5.2.3). Four weathering bags marked as black areas and as indicated explicitly are also revealed, two each, by the Mapping and Exploration.

Table 5.1 gives the values of various aspects of the meteorology of the Daya Bay area. A direct comparison shows that the weather elements in Daya Bay are similar to those in the Hong Kong—Shenzhen area. Plots of the average monthly rainfall and temperature at the Da Ken station for 1985 are shown in Fig. 5.5.

According to the historical record back to December 31, 1994, there have been 63 earthquakes above magnitude 4.7 on the Richter scale (RS), including aftershocks, within a radius of 320 km of the site.§ Among the stronger ones, there was one 7.3 RS, one 7.0 RS, and ten 6.0–6.75 RS. There were 51 medium quakes between 4.7 and 5.9 RS. The strongest, 7.3 RS, took place in Nan Ao, 270 km northeast of Daya Bay,

§The seismic activity quoted here is taken from a Ling Ao NPP report [2].

Meteorological Data	Units	Magnitude
Average air speed	m/s	3.29
Yearly dominant wind direction		E
Average temperature	°C	22.3
Highest temperature	°C	36.9
Lowest temperature	°C	3.7
Average relative humidity	%	79
Average pressure	hPa	1012.0
Average rainfall	mm	1990.8

Table 5.1. Average values of meteorological data from the Da Ken station in 1985.

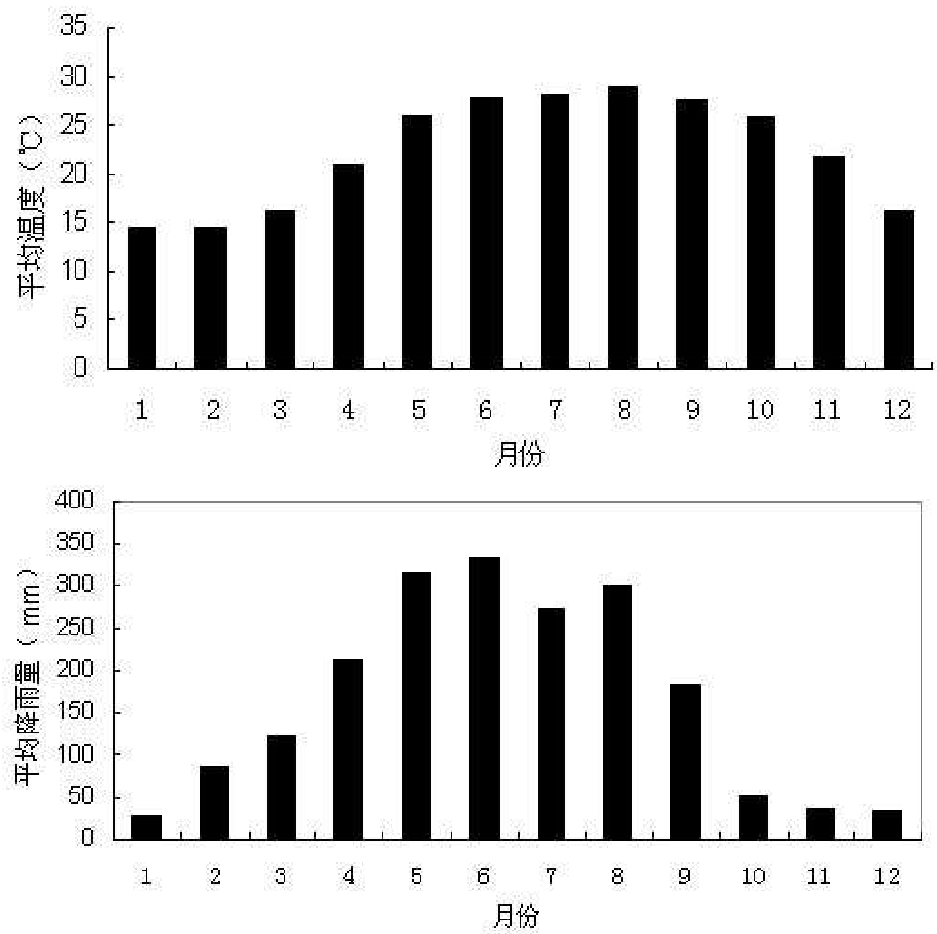

Fig. 5.5. Monthly average temperature and rainfall from data provided by the Da Ken weather station. The horizontal axis gives the months from January to December and the vertical axis is the average temperature in centigrade (rainfall in mm).

in 1918. The most recent one in 1969 in Yang Jiang at 6.4 RS. In addition, there have been earthquakes in the southeast of China and one 7.3 RS quake occurred in the Taiwan Strait on Sept. 16, 1994. The epicenters of the quakes were at a depth of roughly 5 to 25 km. These statistics show that the seismic activities in this region originate from shallow sources which lie in the earth crust. The strength of the quakes generally decreases from the ocean shelf to inland.

Within a radius of 25 km of the experimental site, there is no record of earth quakes of $\mathrm{M_s} \geq 3.0$ $(\mathrm{M_L} \geq 3.5)$[¶], and there is no record of even weak quakes within 5 km of the site. The distribution of the weak quakes is isolated in time and separated in space from one another, and without any obvious pattern of regularity.

According to the Ling Ao NPP site selection report [3], activity in the seismic belt of the southeast sea has shown a decreasing trend. In the next one hundred years, this region will be in a residual energy-releasing period to be followed by a calm period. It is expected that no earthquake greater than 7 RS will likely occur within a radius of 300 km around the site; the strongest seismic activity will be no more than 6 RS. In conclusion, the experimental site is in a good region above the lithosphere, as was ascertained when the NPP site was selected.

5.2.3 Geophysical Exploration

Three methods are commonly used in geophysical prospecting: high density electrical resistivity method, high resolution gravity method, and seismic refraction image method using mechanical hammer. The first two methods together with the third as supplement have been used for the Daya Bay geophysical study[‖]. The combination of these three methods reveal the underground structure, including: faults, type of granite, rock mine contact interface, weathering zone interface, and underground water distribution.

Geophysical exploration revealed another four faults and two weathering bags along the tunnel lines. Figure 5.6 shows the regions of the geophysical survey, including the experimental halls and tunnel sections from the Daya Bay near hall to the mid hall and the far hall. The experimental halls (located near 0 mark for the near hall, 800 mark for the mid hall, and 1800 mark for the far hall), the tunnel sections (white horizontal line at the lower part of the top and lower figures with the three small white squares to indicate the experimental halls), faults and weathering bags are marked by blue and green in the figure. The electrical resistivity measurements are shown in the middle part of the figures, represented by the almost overlapping solid and dashed lines. The high resolution density measurements is given in the bottom figure, and two sections of seismic refraction measurement is in the top figure. Because of the complexity and variety of underground structures, the electrical resistivity was measured in boreholes ZK1 and ZK2. The resistivity and density of the rock samples from the boreholes were used for calibration of the resistivity map. Depending on the characteristics of the granite and its geological structure, the electrical resistivity of this area can vary from tens of ohm-m to more than 10k ohm-m. The non-weathered granite has the highest electrical resistivity, whereas the sandstone has medium resistivity due to trapped moisture. The weathered zone, consisting of weathered bursa and faults, has relatively low resistivity.

5.2.4 Engineering Drilling

Based on the information about faults, zones with relative high density of joints, weathering bags, low resistivity areas revealed from previous geological survey, four borehole positions were determined. The purpose of the boreholes was essentially to prove or exclude the inferences from the previous survey approaches above ground. These four boreholes are labelled as ZK1, ZK2, ZK3, ZK4 from north to south in Fig. 5.2. The depth of the four boreholes are 213.1 m, 210.6 m, 130.3 m, 133.0 m respectively (all to at least the tunnel depth). Figure 5.7 shows sections of rock samples obtained from borehole ZK1. Similar samples

[¶] M_s is the magnitude of the seismic surface wave and M_L the seismic local magnitude. M_s provides the information of the normal characteristics of an earthquake. There is a complicated location-dependent relationship between M_s and M_L. In Daya Bay $\mathrm{M_s} \geq 3.0$ is equivalent to $\mathrm{M_L} \geq 3.5$.

[‖] In order not to affect the construction work of Ling Ao II, a heavy blaster cannot be used as a source of the seismic refraction measurement, as required for deep underground measurement. Therefore seismic refraction cannot be used as a major tool for the Daya Bay prospecting.

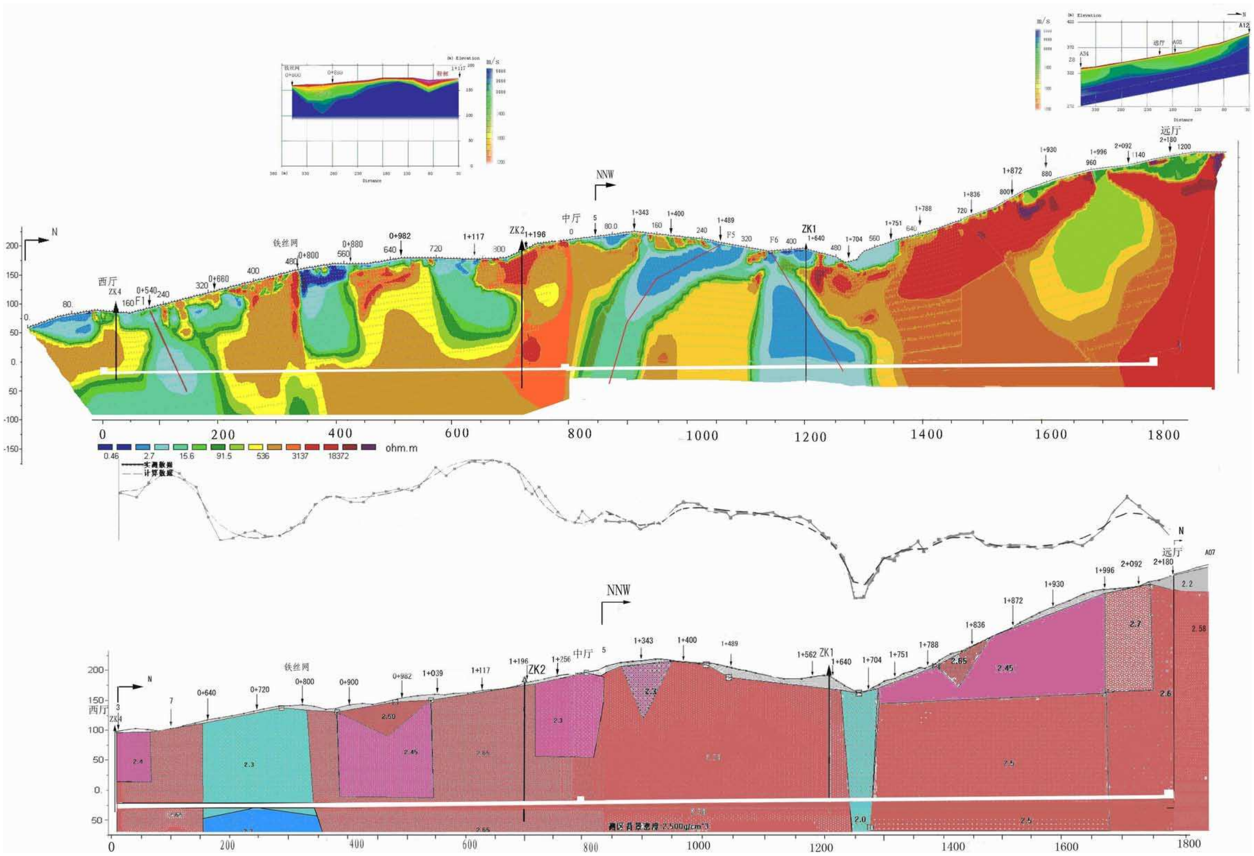

Fig. 5.6. Seismic refraction, electrical resistivity and high resolution density maps along the tunnel cross section from the Daya Bay experimental hall (left end) to the far hall (right end).

are obtained in the other three boreholes. The samples are used for various laboratory tests.

5.2.5 On-site Test at Boreholes

A number of on-site tests have been performed at the boreholes:

1. High density electrical resistivity measurement in boreholes ZK1 and ZK2.

2. Permeability tests at different time and depth are made in the boreholes during borehole drilling and at completion. The test shows that all measured values of the permeability parameter K are less than $0.0009\ \mathrm{m/d}$. The K values in ZK2, Zk3 are smaller than that in ZK1 and ZK4. Figure 5.8 shows the water level variation vs time from pouring tests in the four boreholes during the five months period, from December 22, 2005 to June 1, 2006. The horizontal axis is the date and the vertical axis is the water level measured in meters from 0 to 100 m.

3. Acoustic logging, which is tested at different segments separated by 0.5 m. There are 66, 26, 34, 23 segments tested in ZK1, ZK2, ZK3, ZK4 respectively. The combined results give the velocity of longitudinal wavelength $V_{\mathrm{p}} = 5500\ \mathrm{m/s}$ in the fresh granite.

4. Geo-stress test.

Fig. 5.7. Rock samples from borehole ZK1.

5. Digital video.

6. The radon emanation rate inside the borehole ZK4 was measured up to a depth of 27 m with an electronic radon dosimeter inserted into the borehole. An average rate of 0.58×10^{-3} Bq m^{-2} s^{-1} was determined at depths of 14–27 m after correction for back diffusion. These values generally agree with the rates (0.13–2.56) $\times 10^{-3}$ Bq m^{-2} s^{-1} measured directly from the rock samples extracted from the borehole.

7. Measurements of the rock chemical composition. The chemical elements of the rock were measured, among these elements, the amount of radioactive U was measured to be 10.7, 16.6, 14.5 and 14.2 ppm from the samples in each of the four boreholes, respectively. The Th concentrations were measured to be 25.2, 49.6, 29.4 and 41.9 ppm in each of the borehole respectively.

8. Water chemical analysis. Water samples from the four boreholes and a surface stream have a pH slightly smaller than 7.5, considered to be neutral. The water hardness is smaller than 42 mg/l which

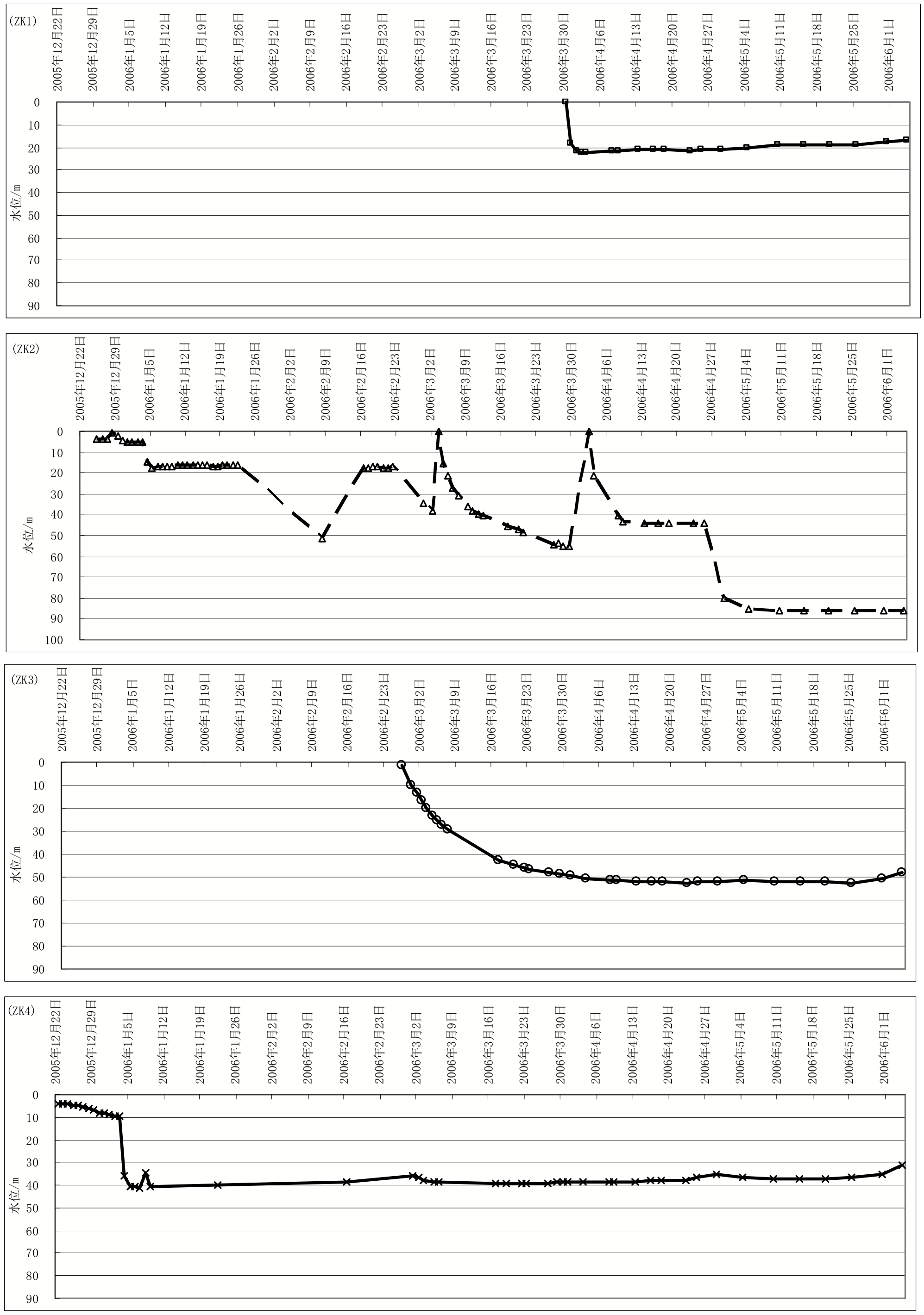

Fig. 5.8. Water level variation vs time in the four boreholes. There is no measurement during holidays in January 2006 in ZK2. The cause of the sudden drop of the water level in April 2006 is unknown. The unit of the x coordinate is 7 days, the date reads as year/month/day. The unit of the y coordinate is the water level in meters down the borehole.

is considered to be very soft. The underground water is thus very weakly corrosive to the structure of steel, but is not corrosive to reinforced concrete.

5.2.6 Laboratory Tests

Laboratory tests performed includes: rock chemical properties, mineral elements, physical and mechanical property tests. The following data are some of the physical properties of slightly weathered or fresh rock which are the most comment type of rocks in the tunnel construction:

- Density of milled rock: $2.609 \sim 2.620\ g/cm^3$
- Density of bulk rock: $2.59 \sim 2.60\ g/cm^3$
- Percentage of interstice: $0.765\% \sim 1.495\%$
- Speed of longitudinal wave (V_p) : $4800 \sim 5500\ m/s$
- Pressure resistance strength of a saturated single stalk: $85.92 \sim 131.48\ MPa$
- Pressure resistance strength of a dry single stalk: $87.88 \sim 125.79\ MPa$
- Softening coefficient: $0.924 \sim 1.000$
- Elastic modulus: $32.78 \sim 48.97\ GPa$
- Poisson ratio: $0.163 \sim 0.233$

5.2.7 Survey Summary

Based on the combined analyses of the survey and tests described above, IGG concludes that the geological structure of the proposed experimental site is rather simple, consisting mainly of massive, slightly weathered or fresh blocky granite. There are only a few small faults with widths varying from 0.5 m to 2 m, and the affected zone width varies from 10 m to 80 m. There are a total of four weathering bags along the tunnel from the Daya Bay near site to the mid site and on the longer construction tunnel option from the Daya Bay quarry to the mid site. The weathering depth and width are 50–100 m. Just below the surface, the granite is mild to mid weathered. These weathered zones are well above the tunnel, more than three times tunnel diameter away, so the tunnel is not expected to be affected by these weathering bags. Nevertheless, there are joints around this region and some sections of the tunnel will need extra support.

The far hall, at a depth of 350 m is thought to consist of lightly effloresced or fresh granites; the far hall is most likely surrounded by hard granite. The distance to the interface with Devonian sandstone is about 100 m (to the North) as indicated by the present analysis.

The rock along the tunnel is lightly effloresced or fresh granite, and the mechanical tests found that it is actually hard rock. No circulation is found between the underground water and the outside boundary water in this area, underground water mainly comes from the atmospheric precipitation. Water borehole permeability tests show that underground water circulation is poor and no uniform underground water level at the tunnel depth. At the tunnel depth the stress is 10 MPa, which lies in the normal stress regime. The quality of most of the rock mass varies from grade II to grade III (RQD around 70% which indicates good and excellent rock quality). From the ZK1 and ZK2 stress measurements and structure analysis, the orientation of the main compressive stress is NWW. For the east-west oriented excavation tunnel, this is a favorable condition for tunnel stability. For the 810 m segment of the main tunnel from the Daya Bay near hall (#1) to the mid hall (#4) the tunnel orientation will run sub-perpendicular to the orientation of the maximum principal stress and it will thus be subject to higher stress levels at the excavation perimeter. These higher stress levels are not expected to cause significant stability problems due to the strength of the granite rock mass. There are some tunnel sections, including the access tunnel, where the rock mass quality belongs to grade IV, and some belongs to grade V. Figure 5.9 shows the details of the engineering geological section along Line A. Detailed results from the site survey by IGG can be found in references [4,7–12].

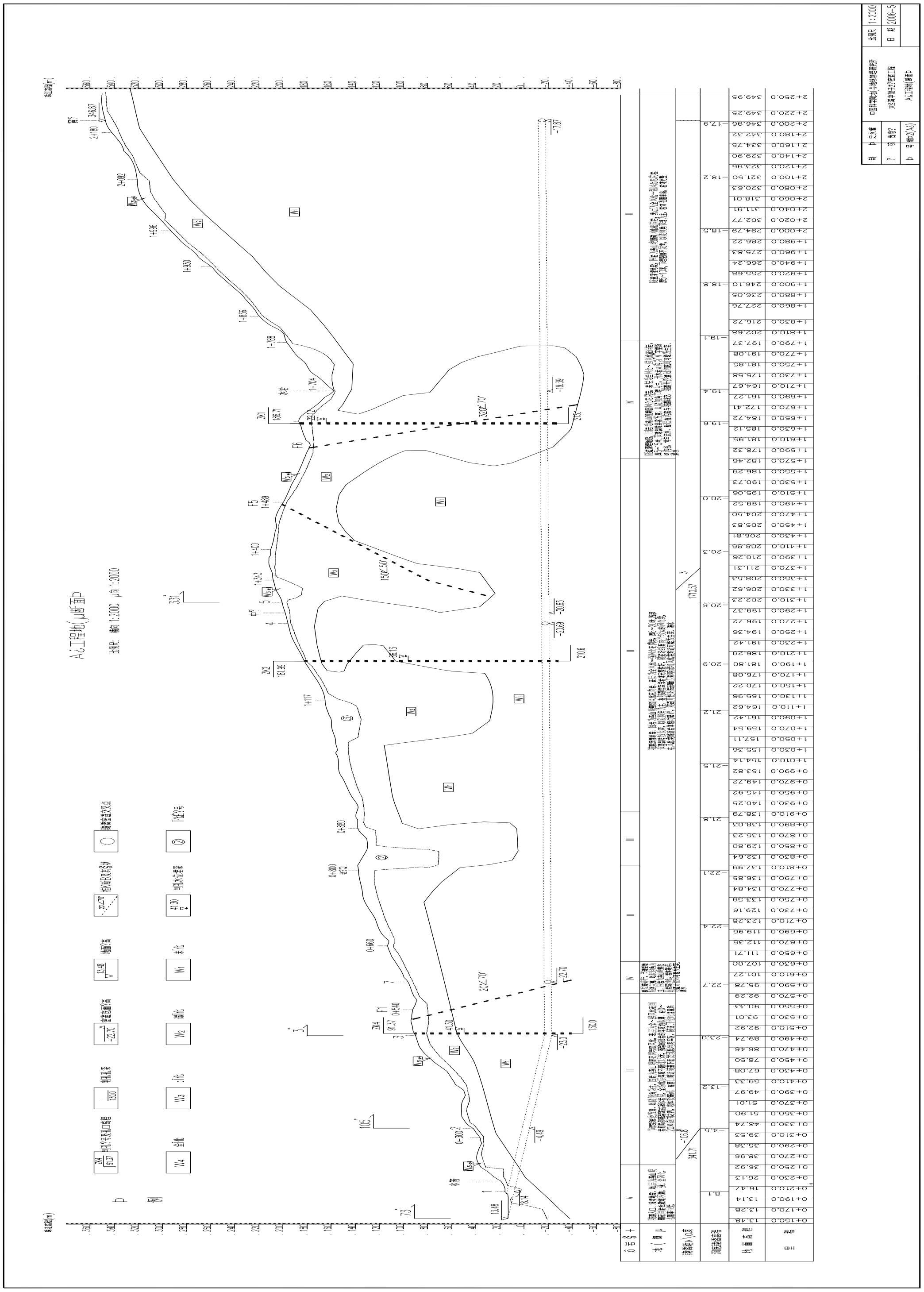

Fig. 5.9. Engineering geological section in line A: the faults, weathering bags and tunnel are shown on the figure. The first curve down from the surface shows the boundary of the weathered granite and the second curve down shows the boundary of the slightly weathered granite. The tunnel passes through one region of slightly weathered granite.

5.3 Conceptual Design

In June 2006 a bid package for the conceptual design of the civil construction was released. The purpose of this effort was to further refine our understanding of the cost of various options and to make sure that we do not leave any important points out of the final design specifications. The major items of the conceptual design included: (1) the underground experimental halls, the connecting, access, and construction tunnels; (2) the infrastructure buildings above ground; (3) the electric power, communication, monitor, ventilation system, water supply and drainage, safety, blast control, and environmental protection. Two design firms were selected: the Fourth Survey and Design Institute of China Railways (TSY) and the Yellow River Engineering Consulting Co. Ltd. (YREC). TSY has expertise in the design of railway tunnels, and YREC has a great deal of experience in underground hydroelectric engineering projects. These design efforts were completed in early August 2006. These two reports were helpful in writing the specifications for the bid of the detailed tunnel design.

5.3.1 Transportation Vehicle for the Antineutrino Detectors

The biggest items to transport in the tunnel are the antineutrino detector (AD) modules. Each module is a cylinder of 100 ton with an outer diameter 5 m and a height of 5 m, with ports extending above. The transportation of the antineutrino detector determines the cross section of the tunnel and directly affects the total tunnelling construction plan.

The space in the tunnel is limited, so the AD transporter should be easy to operate, maneuverable, yet smooth and stable when operating in a straight line. The tunnels interconnecting the Surface Assembly Building and the underground halls will have parallel side walls 6.2 m in width with a domed ceiling less than 8 m in height at the apex. Heavy truck tractors with lowboy trailers that must always be in a towing configuration have limited maneuverability in tight quarters. They also require that the load be lifted on and off with overhead crane. For these reasons we have investigated a custom transport vehicle of the design supplied by such commercial manufacturers as Goldhofer and Doerfer Companies, Wheelift Systems Group (http://www.wheelift.com/), as shown in Fig. 5.10. These types of transport vehicles have low flatbed load platforms supported by multiple independently computer controlled dual wheel sets with hydraulic lift capability. With an AD designed to perch atop vertical support legs at the base, a 3 m wide vehicle can maneuver under the AD and between support legs to gently lift the load for transport. The transporter flatbed top surface will be no greater in height than 0.5 m off the tunnel floor and will automatically maintain a load level orientation during transport of an AD. Such a vehicle is dynamically capable of either moving forward, reverse or in any transverse direction, with complete rotation about the load center (the turn radius is limited only by the length of the vehicle and load). The vehicle can be manually controlled by an operator or capable of pre-programmable unmanned operation. The vehicle can be powered by propane engine during long tunnel transports or connected to AC power when maneuvering at destination sites.

The Doerfer Companies has shown interest in this application and supplied the following operational parameters on an applicable transport vehicle for tunnel civil construction requirements.

- Rated capacity of a dual (12 inch diameter $\times$ 6 inch wide) wheel module is 12,700 kg; with 10 dual wheel modules the total capacity is 127,000 kg.
- Spacing between dual wheel modules is 1.04 m longitudinal $\times$ 2.1 m lateral.
- Floor contact area of each wheel under load is 92.5 cm^2.
- Outer dimension of vehicle is 3.0 m $\times$ 7.1 m, and load platform is 3.0 m $\times$ 5.6 m.
- Load platform vertical lift range of motion is 0.46 m to 0.57 m.
- Maximum vehicle speed without load is 2.74 kph, and with load 1.46 kph.
- Smallest turn radius is on center rotation with programmable fixed turn radii.
- Minimum tunnel floor crown or valley is 25 m.

Fig. 5.10. Photo of a Doerfer 140-ton capacity transporter from underside showing multiple dual wheel modules under vehicle load bed.

- Maximum floor height imperfection without load 19.0 mm and with load 3.0 mm, with a minimum flatness within 20.0 mm over a 30.0 cm span.
- Climb slope 3-5% preferred; 10% with optional driving train.
- Floor surface can be concrete, asphalt, tiles, or compressed rock with relatively uniform surface texture.
- Maximum slope correction by tilt of transporter surface is 3%.

5.3.2 Lifting System for the Antineutrino Detectors

Lifting systems, mainly for handling the antineutrino detectors, have been investigated. The lifting system should be low in order to minimize the height of the experimental hall to gain overburden. Both gantry cranes (suggested by TSY) and bridge style cranes (suggested by YREC) satisfy our requirement. The heights of the experimental halls required to install and lift the antineutrino detector with these two types of cranes are similar: about 14–15 m. Figure 5.11 show a picture of a bridge style crane. Sensitivity in handling the AD is extremely important and therefore requires crane controls with variable frequency motor drives for smooth acceleration and speed control of bridge, trolley, and hoist motion. A digital load cell integrated into hoist motion will enhance operator feedback in handling and transfer of loads. The final choice of a crane system needs further study.

5.3.3 Experimental Hall Layout

A layout of the experimental hall is shown in Fig. 5.12 (designed by YREC). The auxiliary facility rooms are located adjacent to the pool on one side of the hall to minimize electronic cable length runs between detectors and counting room. Although only one is shown, additional rooms for gas systems, water purification, will be adjoining rooms in a more flexible arrangement, as is shown in the three dimensional view of the Daya Bay Hall in Fig. 5.13. A secondary personnel egress tunnel links these auxiliary rooms to the main access tunnel.

Fig. 5.11. A photo of a bridge style crane, the crane rail is fixed to the wall of the experimental hall.

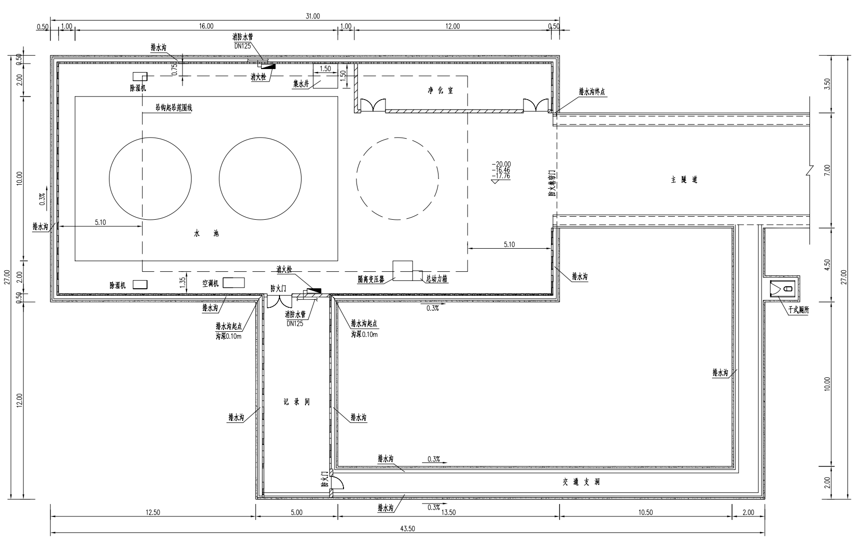

Fig. 5.12. Layout of the experimental hall where the counting room, etc., are along one side of the hall (as proposed by YREC).

The experimental halls have been globally oriented in the same longitudinal direction. This allows the access tunnel the same alignment to Daya Bay (#1), mid (#4) and far (#3) experimental halls. While the Ling Ao near hall (#2) has the access tunnel entering at right angles in this orientation scheme.

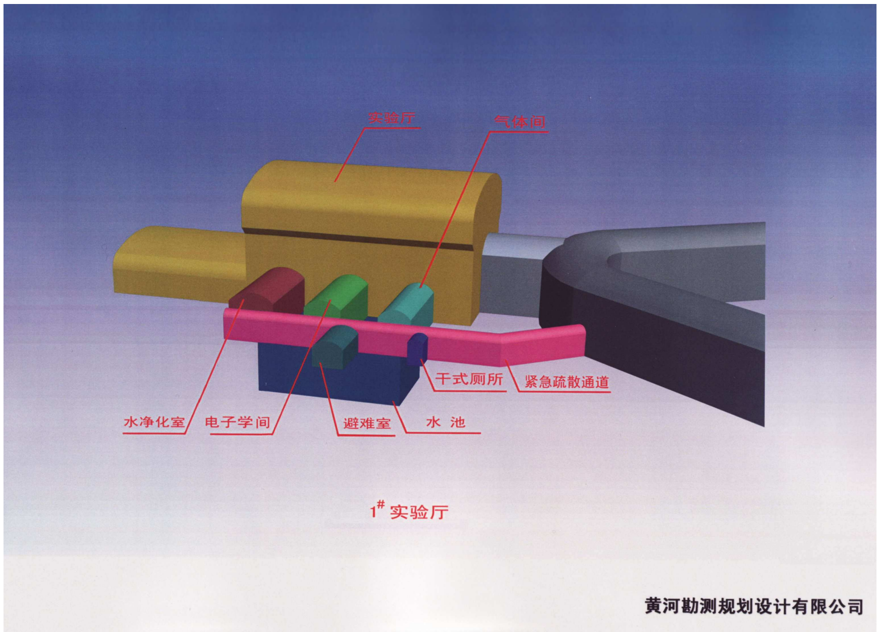

Fig. 5.13. View of the Daya Bay hall cavern and tunnel.

The LS filling hall will be 12 m × 28 m and located near the Daya Bay hall (#1) to minimize the transport distance of liquid materials from the surface. As with the experimental halls, relatively good rock conditions are required to minimize structural support costs of this hall.

5.3.4 Design of Tunnel

To minimize the excavation cost yet accommodate the antineutrino detectors, the cross section of the main tunnel are defined as:

- Total width of the tunnel: 6.2 m.
- Purity water supply pipe, fire suppression pipes, cable trays are mounted on one side of the tunnel wall from ground level up vertically, extending out of the wall in less than 20 cm.
- Safety clearance to each side of tunnel wall: 0.5 m.
- About 100 m each section in the tunnel, there will be a by-pass to allow two vehicles to pass with full load transporter stop.
- Width of drainage channel: 0.5 m on each side of the tunnel
- Total height of the tunnel: 0.5 m (height of transporting vehicle) + 5.0 m (height of antineutrino detector) + 0.5 m (safety distance to the duct) + height of duct.

Figure 5.14 shows the cross section of the main tunnel. The cable trays and water supply pipes will be installed along the side wall of the tunnel. At locations where the tunnel branches, the height of the tunnel will increase to allow for cable and ventilation duct crossover.

The lining of the tunnel depends on the rock quality. At the Daya Bay site the rock quality varies from grades I to V: grade I being excellent and grade V poor. According to the site survey, more than 90% of the rock is grade I, II or III (stable rocks). Some very short sections of the tunnel have grade IV rock with some grade V rock only in the first tens of meters at the main portal. The lining for different quality of rocks are designed according to the requirements for these rock types.

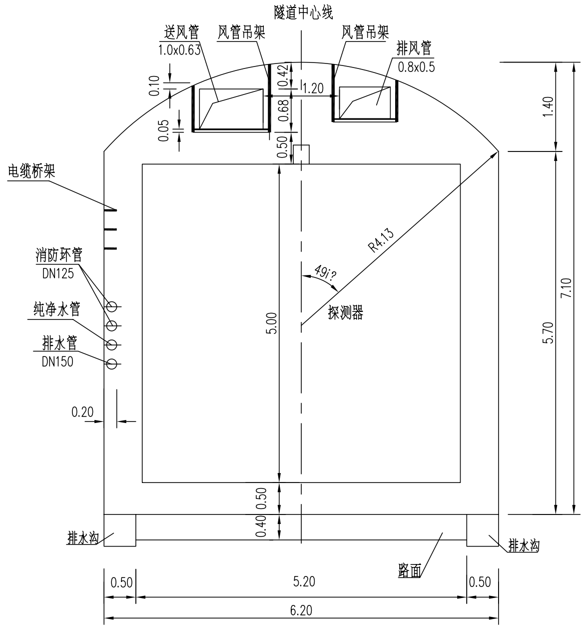

Fig. 5.14. An engineering schematic diagram of the tunnel layout Proposed by YREC. The dimensions are in meters.

There are two possible design strategies for the tunnel construction. One option is to transport the excavated rock by heavy truck (the tunnel layout shown in Fig. 2.1 Line {7-6}), a second option is to transport the rock by tram (the tunnel layout shown in Fig. 5.1 Line {8-9}). In the truck option, the maximum allowed slope is 13% (TSY), the width of this tunnel is 5.0 m and height 5.8 m. There will be a passing section every 80 m along the tunnel for two trucks to cross in opposite directions. The total length of such a tunnel is 607 m. If a tram is used for rock removal, the tunnel can have a much steeper slope, up to 42% ($<23°$). The tunnel length can be as short as 228 m and the cross section is 4.6 m wide by 4.08 m high. Construction with a tram will allow a shorter tunnel, saving both time and money. However, rock removal by tram is more complicated than by heavy truck, and requires more time and money to remove the same amount of rock. The present estimation shows that these two options are not significantly different inn overall cost or schedule. For the case of a tram, since special tools are needed, the number of qualified construction companies bidding on the tunnel construction may be more limited.

A possible layout of the main portal behind the local hospital is shown in Fig. 5.15 (YREC's design). The surface assembly building (SAB) is under design and will be put in a separate bid for construction once the design is finished. An artist's conception of the portal area with the SAB is shown in Fig. 5.16.

5.3.5 Electricity

The 6.3 kV power line will be pulled from a local transformer, which is near the main portal, via two independent loops. An uninterrupted supply of power is expected except for normal power maintenance and inspection for which we will be informed in advance.

There will be 6.3/0.4 kV, 630 kVA transformers at the power control room located at the main portal. Considering the different distances between experimental halls, there are local transformers in the far hall (#3) and the mid hall (#4). There will be an isolation transformer for the power supply of the electronic equipment in each experimental hall.

Each experimental hall has two independent grounds, the resistance of each ground is smaller than

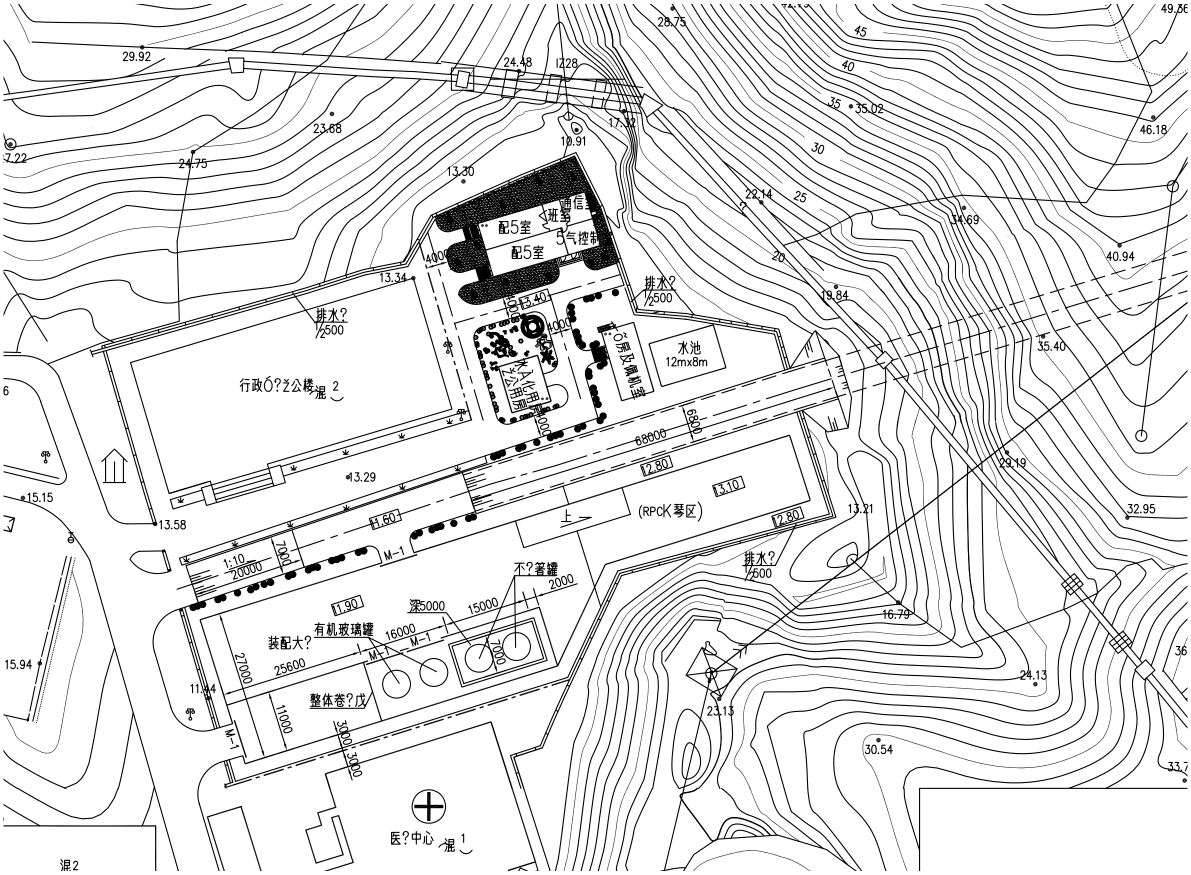

Fig. 5.15. A schematic diagram of the the main portal and the layout of auxiliary buildings.

0.5 ohm.

The lighting in the tunnel and experiment halls will meet Chinese regulations. The total power consumption includes those of the crane, heating, cooling, ventilation, water purification system, water supply, drainage, and experiment hall.

5.3.6 Ventilation System

The ventilation system is composed of inlet and outflow ducts. The ventilation rate is designed to replace the entire air volume of each experimental hall at least six times a day. The ventilation capacity is designed to allow a maximum of 30 workers simultaneously in each experimental hall. The ventilation system should be quiet in operation while providing ambient air dehumidification, heating/cooling and filtration. Additional dehumidification units will be devoted to each experimental hall with large water pools. To reduce power consumption, the average temperature will be controlled close to the original (natural) temperature of the cavern to within $\pm 2°$C.

5.3.7 Water Supply and Drainage

The experiment will use city water. The initial water usage will be large for filling the muon water pools (5,000 m^3 or 1.32×10^6 US-gal), but the filling of the three pools is not simultaneous. Daily operational water needs are minimal for purified experimental make-up water, personnel consumption and fire suppression. There will be a 300 m^3 water storage tank located at the main portal as a supply buffer. Mainly the drainage

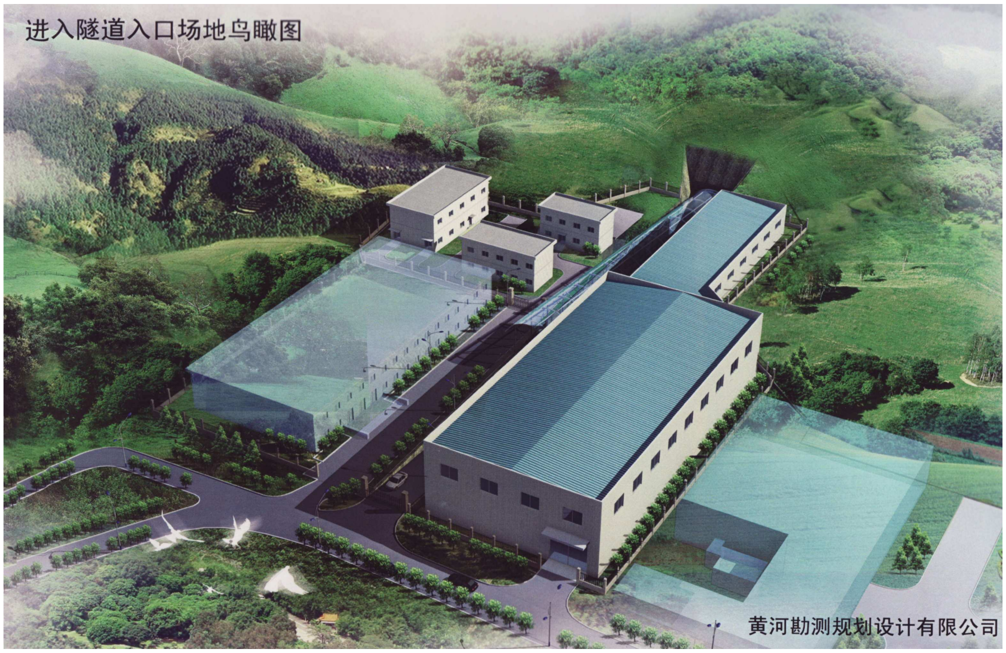

Fig. 5.16. An artist's conception of the Surface Assembly Building, situated adjacent to the access tunnel portal.

of seeped water from rock, and other water monitored will be pumped out. The size of pump pit will be about 9 m long, 6 m wide and 4.5 m deep.

5.3.8 Communication

ShenZhen local telephone, wire interphone system will be installed in the tunnel and experiment halls. Internet connection will be available in the experimental areas.

5.3.9 Safety Systems

Environmental, Safety, Security and Health issues for the project will fall within those policies established by the host country, China, and must meet minimum standards, as negotiated, for all collaborative members working at the experimental complex. These polices will include life safety concerns for radiological controls, chemical inventory controls (MSDS), emergency egress and access controls, fire protection and suppression systems, laser operation, cryogens, oxygen deficiency hazards, fall protection, personnel protective equipment, electrical and mechanical hazards, and liquid spill confinement and cleanup controls.

Equipment protection systems will also be incorporated into the experimental operational safety envelope. A system will be developed using a programmable logic controller (PLC) as the heart of a safety interlocks system to alarm subsystem fault conditions and automatically bring experimental hardware to a preprogrammed safe state. These fault interlock conditions will automatically valve off liquid and gas sources and turn off electrical power to designated hardware based on cooling water leak detection and flammable gas detection. It will also alarm and interlock AC power based on smoke detection near electronics, and alarm and ventilate based on ODH and flammable gas conditions.

5.3.10 Blast Control

The maximum allowable force caused by blasts in the tunnel construction at the Daya Bay Complex is 0.01 g. Test blasts will be performed at the beginning of construction and the vibration caused by all blasts will be monitored during the construction period.

5.3.11 Environmental Effect Evaluations

The environmental impact evaluations include: (1) construction dust and noise; (2) rock disposal and treatment measurements; (3) temporary disruption and restoration after the construction work is completed.

All the details are included in the conceptual design reports submitted by TSY [13] and YREC [14].

5.4 Civil Construction Overview

Based on the conceptual designs and further work of the collaboration, we have drafted the final civil construction design specs. The Yellow River Engineering Consulting Co. Ltd. was selected by a bidding process as the final winner of civil construction on January 22, 2007. The final design will take about 2 months. When the civil design is finished in April 2007, the bidding for civil construction will start. An oversight agency is needed for the construction. We expect the civil construction to start around July of 2007. The civil construction will last 20–24 months as estimated in the conceptual design.

The main civil construction work items are listed in Table 5.2. A construction management firm will be hired to monitor the construction work. IHEP will have an onsite representative to oversee the work. IHEP will also provide an onsite person to interface with the power plant. The power and water needed during the construction will be provided by the power plant and this cost is included in the civil construction package.

Construction item	Volume (m^3)
Excavation debris from surface	17,068
Excavation debris from tunnel	202,745
Concrete	8,740
Eject concrete	7,774

Table 5.2. Table of the main civil construction work items.

The estimated civil construction costs are listed in Table 5.3.

Civil construction item	Unit (10K RMB)
Hall #1, #2	628
Hall #3	425
Hall #5	60
Construction tunnel	610
Main tunnel	2346
Entrance	198
Surface lab.	500
Design and management	630
Tax, fee and others	745
Contingency	486
Total cost	6628

Table 5.3. Cost estimation of the civil construction.

The estimated utility and safety system costs are listed in Table 5.4.

Utility and safety system item	Unit (10K RMB)
Electric system	822
Ventilation system	480
Fire suppression system	50
Water supply and drainage system	90
Communication and networks	75
Monitoring and control system	113
Clean room	100
Crane in surface assemble building	120
Crane in experiment halls	540
Transportation vehicle	500
Total cost	2890

Table 5.4. Cost estimation of utilities and safety systems.

REFERENCES

1. *Report of Preliminary Feasibility Study of Site Selection for the Daya Bay Neutrino Experiment*, prepared by Beijing Institute of Nuclear Energy, September, 2004.
2. *Catalog of Chinese Earthquakes*, Quoted in the *Preliminary Safety Report on Ling Ao Nuclear Power Plant*.
3. *Report of Ling Ao Nuclear Power Plant*.
4. *Report on Geo-technical Survey(Feasibility Study and Conceptual Design)*, Institute of Geology and Geophysics, CAS, May, 2006.
5. *Final Report on Topographic Survey of the Neutrino Experimental Site*, Institute of Geology and Geophysics, CAS, June, 2006;
6. *Map obtained from Topographic Survey of the Neutrino Experimental Site*, Institute of Geology and Geophysics, CAS, December, 2005;
7. *Report on Engineering Geology of the Neutrino Experimental Site*, Institute of Geology and Geophysics, CAS, May 6, 2006;
8. *Report on Geophysical Survey of the Neutrino Experimental Site*, Institute of Geology and Geophysics, CAS, May 6, 2006;
9. *Report on Bore Drilling and In-situ Sonic Investigation of the Neutrino Experimental Site*, Institute of Geology and Geophysics, CAS, May, 2006;
10. *Report on Stress-loading in Bore Holes at the neutrino Experimental Site*, Institute of Geology and Geophysics, CAS, April 18, 2006;
11. *Report on Ultra-sonic Imaging in Bore holes at the Neutrino Experimental Site*, Institute of Geology and Geophysics, CAS, May, 2006;
12. *Report on Laboratory Study of the Neutrino Experimental Site*, Institute of Geology and Geophysics, CAS, May 6, 2006.
13. *Feasibility study about Daya Bay neutrino experiment engineering work*, The Fourth Survey and Design Inst. of China Railway, July 2006
14. *Feasibility study about Daya Bay neutrino experiment engineering work*, Yellow River Engineering Consulting Co. Ltd., August 2006

6 Antineutrino Detectors

The measurement of $\sin^2 2\theta_{13}$ to <0.01 is an experimental challenge. A value of 0.01 for $\sin^2 2\theta_{13}$ yields a tiny oscillation effect. This corresponds to a small difference in the number of antineutrino events observed at the far site from the expectation based on the number of events detected at the near site after correcting for the distance under the assumption of no oscillation. To observe such a small change, the detector must be carefully designed following the guidelines discussed in Chapter 2, and possible systematic uncertainties discussed in Chapter 3. To make this measurement the antineutrino detector must meet the physics performance requirements summarized in Table 6.1. The technical requirements of the individual

Item	Requirement &Justification
target mass per detector	$\geq$20 tons
precision on target mass	$\leq$0.2% - also, precise knowledge of the proton to carbon ratio
energy resolution	$15\%/\sqrt{E}$ - good energy resolution helps reduce systematics (see Chapter 3)
efficiency uncertainty	$< 0.2\%$
energy threshold	$\leq$1 MeV to be fully efficient for positrons of all energies
radioactivity singles rate	$\leq$100 Hz
event time	$\leq$25 ns

Table 6.1. Physics performance requirements of the antineutrino detector.

subsystems for the antineutrino detector are summarized in similar format at the beginning of each of the following sections.

In addition, the following considerations enter the design of the antineutrino detector:

1. The detector modules should be homogeneous to minimize edge effects.

2. It is important to precisely know the target mass and composition. The number of protons in the target liquid scintillator should be well known, implying that the scintillator mass and the proton to carbon ratio should be precisely determined. The target scintillator should come from the same batch for each pair of near-far detector modules or for all detectors, and the mixing procedure should be well controlled to ensure that the composition of each antineutrino target is the same.

3. The detector module should not be too large; otherwise, it would be difficult to move from one detector site to another for cross check to reduce systematic effects. In addition, beyond a certain size, the rate of cosmic-ray muons passing through the detector module is too high to be able to measure the ^{9}Li background.

6.1 Detector Geometry and Dimensions

Several previous neutrino experiments have designed spherical or ellipsoidal detectors to insure uniform energy response in the entire volume. This type of detector vessel is expensive and requires many PMTs for 4π coverage. Two types of alternative detector geometries have been investigated: cubic and cylindrical. Both are attractive from the viewpoint of construction. Monte Carlo simulation shows that a cylindrical shape, as shown in Fig. 2.3, can deliver better energy and position resolution while maintaining good uniformity of light response over the volume, similar to that of a sphere or ellipsoid. This design is verified by prototype tests as discussed in Section 6.7. An optical reflector can be put at the top and bottom of the cylinder, so that PMTs are only positioned on the circumference of the cylinder, to reduce the number of PMTs by almost half.

This design, which allows a tremendous reduction of the detector cost including savings on the PMT readout, steel and acrylic vessel construction, is practical due to the following considerations:

1. The event vertex is determined by the charge pattern in the AD phototubes without reliance on time-of-flight, so that the light reflected from the top and bottom of the cylinder will not worsen the performance of the detector module. The hit times are measured to a resolution of 0.5 ns for background studies.

2. The fiducial volume is well defined with a three-zone-structure as discussed below wherein no accurate vertex information is needed.

6.1.1 Target Mass

The total target mass at the far site is determined by the sensitivity goal as is shown in Fig. 6.1 as a function of the far site detector mass. To measure $\sin^2 2\theta_{13}$ to better than 0.01, a total target mass of 80–

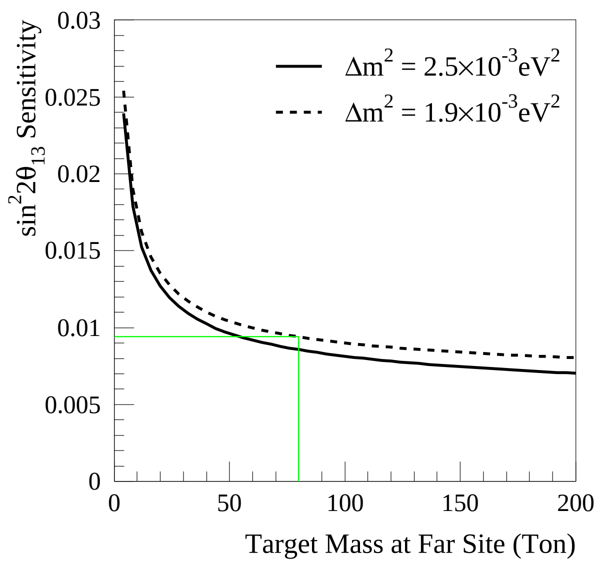

Fig. 6.1. Sensitivity of $\sin^2 2\theta_{13}$ at the 90% C.L. as a function of the target mass at the far site. The solid line corresponds to the current best-fit central value of Δm^2_{31} and the dashed line corresponds to the 90% C.L. lower limit on Δm^2_{31}.

100 ton is needed, which corresponds to a statistical uncertainty of $\sim$0.2% after three years data taking. A larger target mass is not attractive since the sensitivity improves rather slowly when the target mass goes beyond 100 ton. By adopting a multiple-module-scheme as discussed in Chapter 2, two modules are chosen for each near site to allow a cross check of the systematic uncertainties (within the limit of statistical uncertainties at the near site). For the far detector site, at least four modules are needed for sufficient statistics to reach the designed sensitivity while maintaining the number of modules at a manageable level. A detector scheme of eight identical modules, each with a target mass of 20 ton, is chosen. About 930 events per day per module will be detected at the Daya Bay near site (300–500 m) with about 90 events per day per module at the far site ($>$1800 m).

6.1.2 Antineutrino Detector with Three Zones

A Chooz-type detector [1] with suitable upgrades can in principle fulfill the requirements although completely new concepts are not excluded. The energy threshold of a Chooz-type scintillator detector can be reduced by a three-zone structure as shown in Figure 6.2.

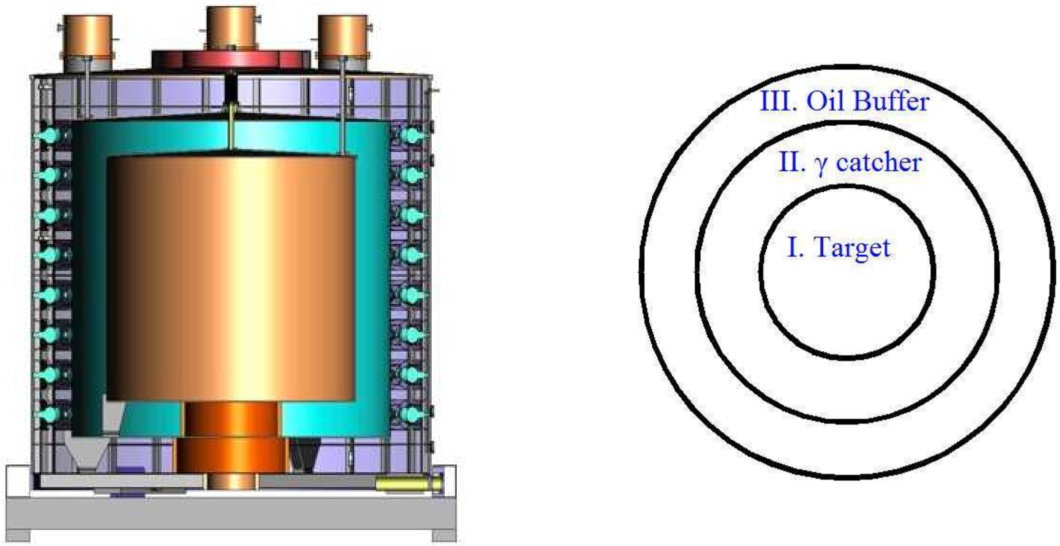

Fig. 6.2. *Left:* Transparent cross-section of the antineutrino detector on the transporter. This figure shows a complete design of one of the options of the antineutrino detector with the automated calibration boxes and overflow tanks at the top. *Right:* Schematic top view of the different zones of the antineutrino detector.

The inner-most zone (region I) is the Gd-loaded liquid scintillator antineutrino target. The second zone (region II) is filled with normal liquid scintillator and serves as a γ-catcher to contain the energy of γ rays from neutron capture or positron annihilation. This zone does not serve as an antineutrino target as neutron-capture on hydrogen does not release sufficient energy to satisfy the 6 MeV neutron detection threshold. The outer-most zone (region III) contains mineral oil that shields external radiation from entering the fiducial volume. This buffer substantially reduces the singles rates and allows the threshold to be lowered below 1.0 MeV and improves the uniformity of light collection at the PMTs. The three regions are partitioned with transparent acrylic tanks so that the target mass contained in region I can be well determined without the need for event vertex reconstruction and a position cut.

The cost of the tunnel construction is proportional to the cross section of the tunnel. With optimization described in the following subsections, the minimum outer dimension of the detector that satisfy our physics requirement is found to be a cylinder with diameter of 5 m and height of 5 m. Figure 6.3 shows the fit of such a detector on a transporter in tunnel. The neutrino target is a cylinder of 3.1 m height and 1.55 m radius. The γ-catcher is 0.425 m thick and the oil buffer is 0.488 m thick. The diameter of the stainless steel vessel is 5.0 m, with a height of 5.0 m and a total mass of 100 ton.

Fig. 6.4 shows the visual output of the geometry of the antineutrino detector in Geant4 simulation code of Daya Bay, G4dyb. The simulation code is used to optimize the detector design as well as verifying the detector performance.

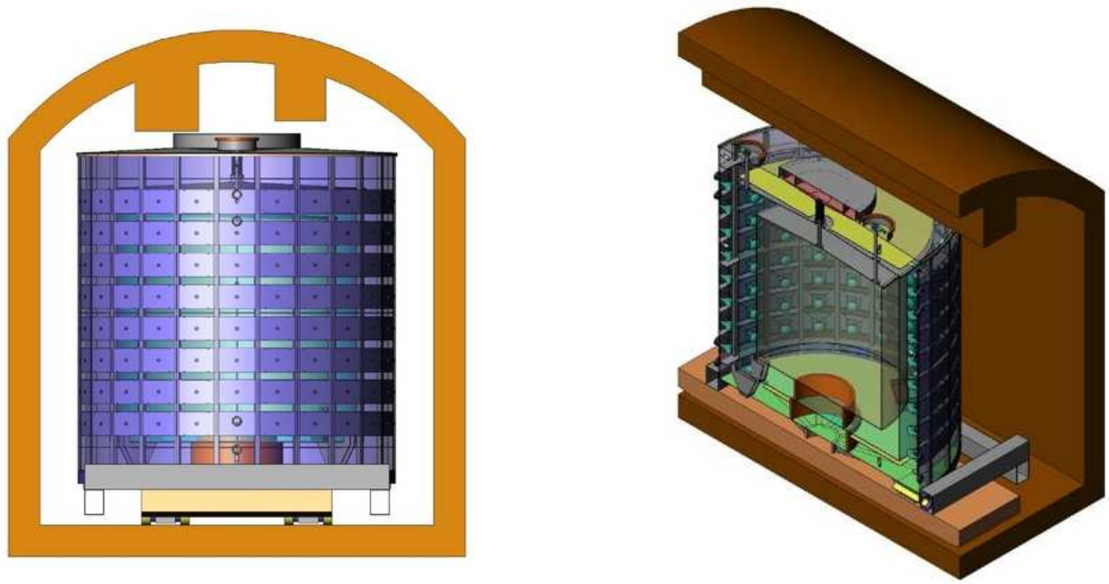

Fig. 6.3. Cross-section of the tunnel and antineutrino detector in the horizontal tunnel connecting the experimental halls. The outline of the tunnel cross-section including the air ducts and other infrastructure are shown in yellow. Detailed studies of the interference of the detector with the infrastructure in the tunnel are underway.

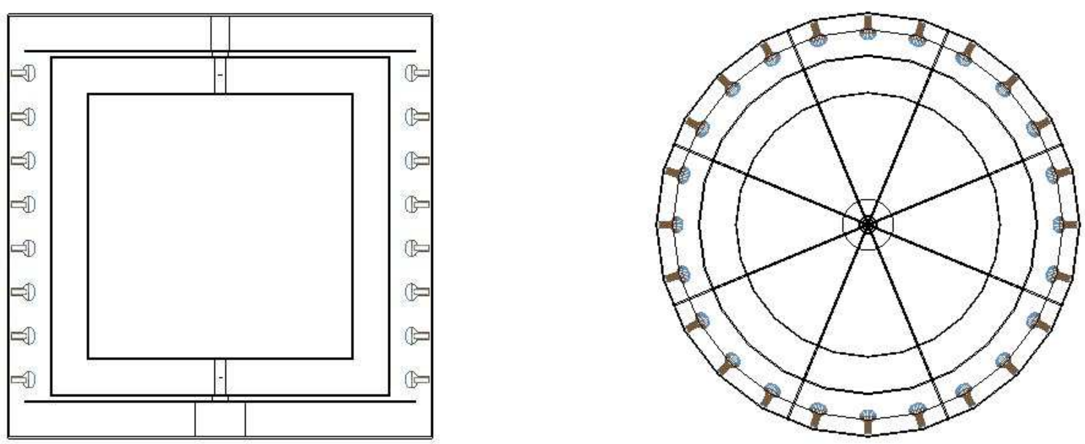

Fig. 6.4. Detector geometry in G4dyb. Left: side view. Three region from the center to the wall are target, γ-catcher, and buffer oil, respectively. Reflective panels are in buffer oil at the top and bottom. Right: top view. Eight radial reinforcing ribs can be seen. The reinforcing ribs of the stainless steel tank and two acrylic vessels are overlapped.

6.1.3 Inner Antineutrino Target

The target vessel will contain 20-ton Gd-LS as the antineutrino target. It is designed to be a cylinder of an inner diameter of 3.1 m and inner height of 3.1 m. The density of the Gd-LS, consisting of 99% linear alkylbenzene, is 0.855–0.870 g/ml. The target mass is 20.0–20.3 ton.

6.1.4 Gamma Catcher

The γ rays produced in the target region by positron annihilation or neutron capture will undergo many collisions with the LS molecules to transfer most of their energy to the liquid scintillator before converting to visible scintillation light. However, the γ rays can also escape from this target region and deposit energy outside of this region. To capture the escaping γ rays a layer of undoped liquid scintillator surrounding the target zone is added, significantly reducing this energy loss mechanism. The energy spectrum of the delayed neutron capture signal is shown in Fig. 6.5. The tail to low energies is from events with at least one escaping

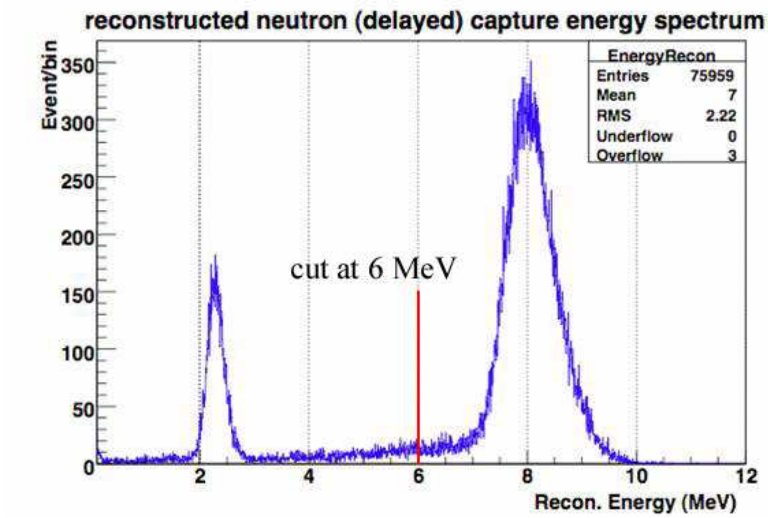

Fig. 6.5. The neutron capture energy spectrum as obtained from the Geant4 simulation (reconstructed by scaling the total charge). The peak at $\sim$8 MeV corresponds to the n-capture on gadolinium. The tail to lower energies is from events with at least one escaping gamma.

γ. The Gd capture peak at 8 MeV is dominated by the two most abundant isotopes of gadolinium, ^{155}Gd and ^{157}Gd, with total γ energies of 7.93 and 8.53 MeV, respectively.

A threshold of 6 MeV cleanly separates the 8 MeV neutron capture signal from the background due to natural radioactivity. However, this threshold will cause a loss of some neutron capture events and a corresponding loss of detection efficiency. A simulation of the detector giving the correlation between the thickness of the γ-catcher region and the neutron detection efficiency is shown in Fig. 6.6. The figure shows that with a γ-catcher thickness of 42.5 cm the neutron detection efficiency is 91%. Chooz had a smaller detector and a γ-catcher thickness of 70 cm, and neutron source test showed a (94.6$\pm$0.4)% detection efficiency [1]. The uncertainty includes a vertex selection uncertainty that Daya Bay will not have. Chooz, Palo Verde and KamLAND all claimed an uncertainty on the energy scale at 6 MeV of better than 1%. Our detector simulation shows that a 1% uncertainty in energy calibration will cause a 0.2% uncertainty in the relative neutron detection efficiencies of different detector modules for a 6 MeV threshold. After subtracting the vertex selection uncertainty, the resulting efficiency values are consistent with simulation. After a comprehensive study of detector size, detection efficiency, and experimental uncertainties, we choose 42.5 cm as the thickness of the γ-catcher.

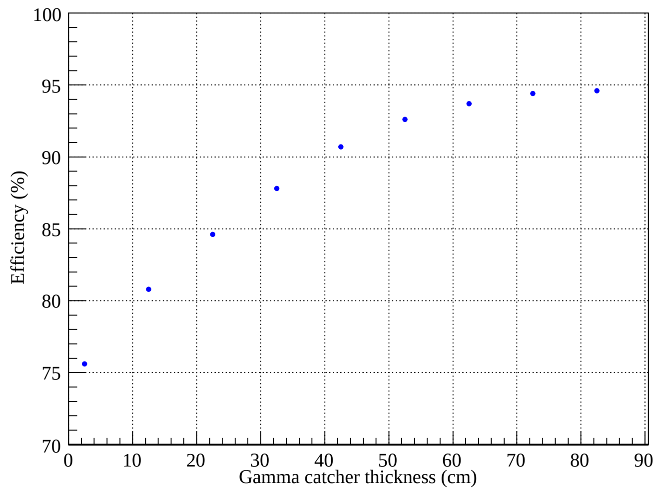

Fig. 6.6. The neutron detection efficiency as a function of the thickness of the γ-catcher. The neutron energy cut is set at 6 MeV. The thickness of the γ catcher of the Daya Bay experiment will be 42.5 cm.

6.1.5 Oil Buffer

The outermost zone of the detector module is composed of mineral oil. The PMTs will be mounted in the mineral oil next to the stainless steel vessel wall, facing radially inward. This mineral oil layer is optically transparent and emits very little scintillation light. There are two primary purposes for this layer: 1) to attenuate radiation from the PMT glass, steel tank and other sources outside of the module; and 2) to assure that PMTs are sufficiently far from the liquid scintillator so that the light yield is quite uniform. Simulations indicate that the location of light emission should be at least 15 cm away from the PMT surface, as indicated in Fig. 6.7. The oil buffer is also used to attenuate radiation from the PMT glass into the fiducial volume. Simulation shows that with 20 cm of oil buffer between the PMT glass and the liquid scintillator, the radiation from the PMT glass detected in the liquid scintillator is 7.7 Hz, as summarized in Table 6.2.

Isotope	Concentration	Distance of PMT Front Face to Gamma Catcher 20 cm (Hz)	25 cm (Hz)	30 cm (Hz)	40 cm (Hz)
^{238}U	40 ppb	2.2	1.6	1.1	0.6
^{232}Th	40 ppb	1.0	0.7	0.6	0.3
^{40}K	25 ppb	4.5	3.2	2.2	1.3
Total		7.7	5.5	3.9	2.2

Table 6.2. Radiation from the PMT glass detected in the Gd-scintillator (in Hz) as a function of the oil-buffer thickness (in cm). An oil buffer of more than 45 cm thickness will provide 20 cm of shielding against radiation from the PMT glass.

The welded stainless steel in KamLAND has an average radioactivity of 3 ppb Th, 2 ppb U, 0.2 ppb K, and 15 mBq/kg Co. Assuming the same radioactivity levels for the vessel of the Daya Bay antineutrino detector module, the corresponding rate from a 20 ton welded stainless steel vessel shielded by at least 45 cm

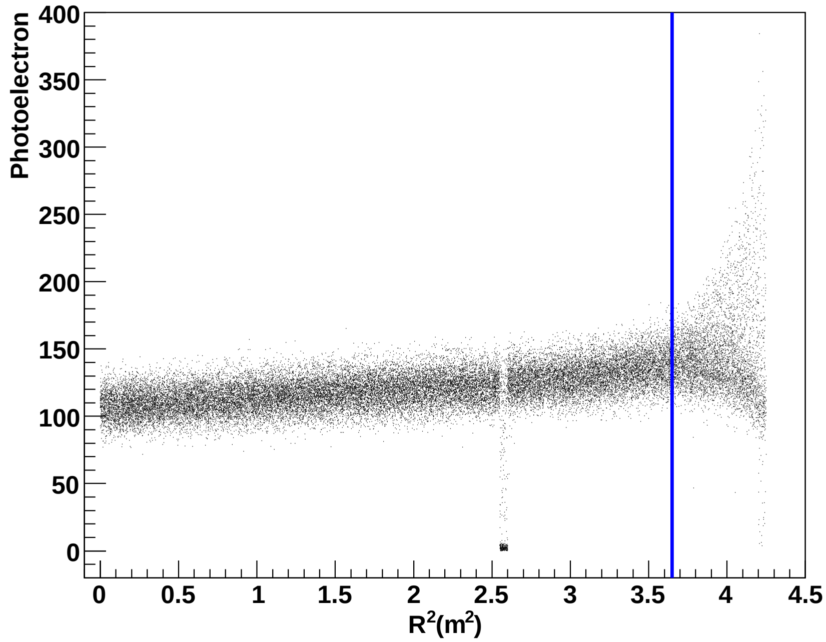

Fig. 6.7. Antineutrino detector response (in number of photoelectrons) as a function of radial location of a 1 MeV electron energy deposit. The mineral oil volume has been removed and the PMTs are positioned directly outside the γ-catcher volume. The vertical red line is 15 cm from the PMT surface and indicates the need for 15 cm of buffer between the PMT surface and the region of active energy deposit in order to maintain uniform detector response.

of oil buffer are 7 Hz, 4.5 Hz, 1.5 Hz and 4.5 Hz for U/Th/K/Co, respectively at a threshold of 1 MeV. The total is 17.6 Hz. The natural radioactivity of rock, buffer water, mineral oil, dust, radon and krypton in air play a minor role, as described in Section 3.3.4. The total γ rate is $<$50 Hz. The oil buffer will be sufficient to suppress the γ rate and the subsequent uncorrelated backgrounds to an acceptable level. The dimensions of the antineutrino detector modules are shown in Table 6.3.

Region	IR(m)	OR(m)	inner height(m)	outer height(m)	thickness(mm)	material
target	0.000	1.550	0.000	3.100	10.0	Gd-LS
γ-catcher	1.560	1.985	3.120	3.970	15.0	LS
buffer	2.000	2.488	4.000	4.976	12.0	Mineral oil

Table 6.3. Dimensions of the mechanical structure and materials of the antineutrino detector modules.

6.1.6 Comparison of 2-Zone and 3-Zone Detectors

The possibility of adopting a detector module design with a 2-zone structure, by removing the γ-catcher from the current 3-zone design, has been carefully studied. A 2-zone detector module with the same outer dimension as the 3-zone structure has a target mass of 40 ton (keeping the same oil buffer and γ-catcher thicknesses). The efficiency of the neutron energy cut at 6 MeV will be $\sim$70%, compared to $\sim$90% with the γ-catcher and the 2-zone 40 ton detector module will have only $\sim$60% more detected events than the 3-zone 20 ton detector module. The reduction of efficiency in the neutron energy cut will introduce a larger uncertainty due to the energy scale uncertainty. This uncertainty is not removable by the near/far relative measurement, in the different detector modules due to differences in the energy scales.

The energy scale is possibly site-dependent due to variation of calibration conditions in the different sites. According to the experience gained from KamLAND, a 1% energy scale stability at 8 MeV and 2% at 1 MeV can be readily achieved. The uncertainties in neutron detection efficiency for a 1% relative energy scale uncertainty have been studied by Monte Carlo for the 2-zone 40 ton detector module and the 3-zone 20 ton detector module. The uncertainty in the relative neutron detection efficiency for the 2-zone detector module is 0.4% at 6 MeV as compared with 0.22% for the 3-zone detector module. Similar uncertainties at 4 MeV have also been studied, see Table 6.4. This uncertainty will be the dominant residual detector

Configuration	6 MeV	4 MeV
2-zone	0.40%	0.26%
3-zone	0.22%	0.07%

Table 6.4. Uncertainty of the neutron energy threshold efficiency caused by uncertainty in the energy scale for 2-zone and 3-zone detector modules. The energy scale uncertainty is taken to be 1% and 1.2% at 6 MeV and 4 MeV, respectively.

uncertainty (see Table 3.8), while other uncertainties are cancelled by detector module swapping this one is not (e.g., a doubling of this uncertainty will significantly degrade the $\sin^2 2\theta_{13}$ sensitivity that can be achieved).

As shown in Table 6.4, lowering the energy cut to 4 MeV can reduce the neutron energy threshold efficiency uncertainty. However, the intrinsic radioactivity from the Gd-doped liquid scintillator and the acrylic vessel will cause a significant increase of the accidental background rate. For external sources (such as radioactivity from the PMTs and the rock) only γ rays, with an upper limit of $\sim$3.5 MeV, can enter the detector module. For internal sources, however, γ rays, but also β and α particles contribute — these can produce significant rates of signals above 3.5 MeV (e.g. ^{208}Tl has an endpoint of 5 MeV) as observed by KamLAND. Chooz has also observed a significant number of events of delayed energy of 4–6 MeV (see Fig. 6.8). In addition, gadolinium has contamination from ^{232}Th which increases the rate of ^{208}Tl decay in the scintillator. All of these factors make a reduction of the neutron threshold from 6 MeV to 4 MeV undesirable. The accidental background rate would be a couple of orders of magnitude larger with the lower threshold at 4 MeV.

6.1.7 Optical Reflective Panels

Optical reflective panels will be put at the top and bottom of the cylinder. PMT numbers can be reduced to nearly one half comparing to the 4π PMT installation, while keeping the same photocathode coverage. The reflective panels can be put close to the top and bottom of the γ-catcher vessel to enlarge the photocathode coverage. As shown in Fig. 6.7, the photoelectron yield get larger when the light source approaching to the wall of the detector. However, the detector response will be uniform along the cylinder direction if reflector with $\sim$100% specular reflectivity is used. While specular and diffuse reflection has no difference in the total photoelectron yield, specular reflection is preferred because the vertex fitting algorithm will be easier.

Using reflector can also greatly simplify the mechanics design and assembly of the detector. To have the target as large as possible within limited detector outer dimension, the necessary reinforcing ribs are designed inside the stainless steel tank. Installing PMTs among ribs is not easy. On the contrary, the detector

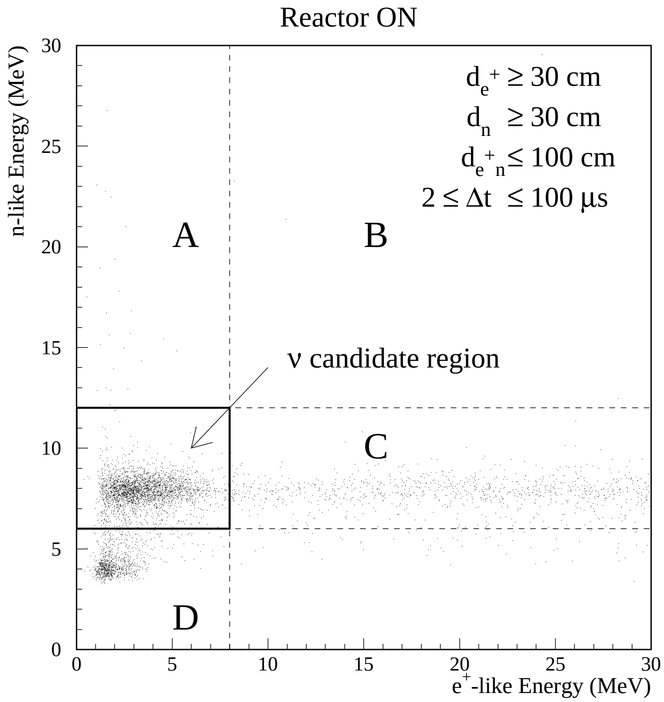

Fig. 6.8. The energy distribution observed by Chooz, horizontal axis is the prompt signal energy; the vertical axis is the delayed signal energy. In the region labelled D there are many background events with delayed signal falling into the 3–5 MeV energy range.

volume beyond the reflector is not sensitive. Support structure or other detector parts can be used without worry about the impacts on the detector response.

The most attractive candidate of the reflective film is the Enhanced Specular Reflector (ESR) [16], a thin, mirror-like, non-metallic film that offers greater than 98% specular reflectivity across the entire visible spectrum. The measured reflectivity is shown in Fig. 6.9. For wavelength $>$400 nm, the total reflectivity (specular + diffuse) is greater than 99%. The rising edge is at 380–390 nm. Comparing to the light emission spectrum of Gd-LS (see Fig. 6.24), the ESR has perfect reflectivity over almost the whole range of the scintillation light. Another candidate is aluminum film. The reflectivity is not as good as the ESR but it extends to shorter wavelength covering the whole scintillation spectrum. Tyvek film for diffuse reflection has also been considered. Tyvek film will become semi-transparent when soaked in mineral oil. So it has to be sealed to be used in the detector.

The reflective film will be sandwiched between two acrylic panels. The sandwich structure can 1) protect the reflective film from scratch during assembly and installation; 2) avoid the possible contamination to mineral oil from the glue to stick the film in long term; 3) avoid the possible degradation of reflectivity when the film is merged in mineral oil for years. R&D has been started to study the optical property of the sandwich reflective panel.

6.1.8 Expected Performance of the 3-Zone Detector

With reflectors at the top and bottom the effective photocathode coverage is 12% with 192 PMTs, the light yield is $\sim$105 p.e./MeV and the energy resolution is around 5.4% for 8 MeV electrons when

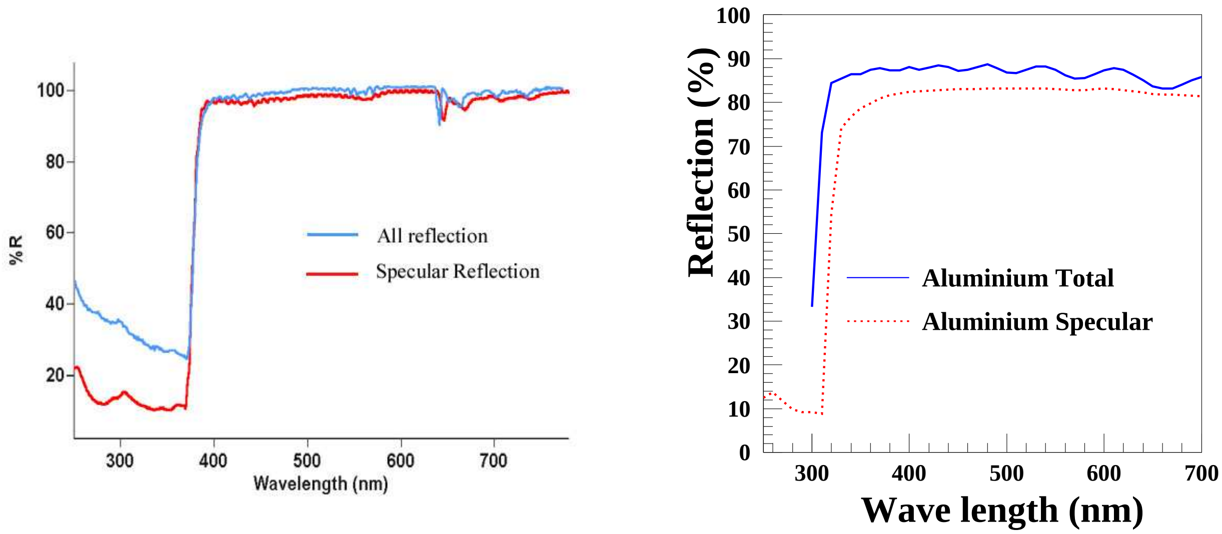

Fig. 6.9. Left: Measured reflectivity of ESR film. The red line is that for specular reflectivity and the blue line corresponds to total reflectivity including diffuse light. Right: Measured reflectivity of Aluminum film.

the total-charge method is used, or 4.5% with a maximum likelihood fit approach. The vertex can also be reconstructed with a resolution similar to a design with 12% PMT coverage on all surfaces. The vertex reconstruction resolution is $\sim$12.5 cm for a 8 MeV electron event using the maximum likelihood fit, as shown in Fig. 6.10. The energy resolution of the 8-MeV γ''s from n-capture on Gd is 6.9% (total charge) and 5.7% (reconstructed) respectively. The horizontal axis is the distance of the reconstructed vertex to the true vertex and the vertical axis is the number of events. Such a vertex resolution is acceptable since the neutron capture vertex has $\sim$20 cm intrinsic smearing, as found by Chooz [1] and by our Monte Carlo simulation as well. The intrinsic smearing of the neutron capture vertex is caused by the difference in the position of the neutron capture vertex and the true center-of-gravity of the energy deposition of the γ's emitted from the capture.

6.2 Mechanical Design and Structure of the Antineutrino Detector

6.2.1 Detector Tank

The stainless steel vessel is the outer tank of the antineutrino detector module, and surrounds the buffer oil region. It will be built with low radioactivity 304L stainless steel and will satisfy the requirements listed in Table 6.5:

The stainless steel vessel is a cylinder of 5000 mm height and 5000 mm diameter (external dimensions) with a 12 mm wall thickness. There are radial internal reinforcing ribs at the bottom as well as the tank cover. The mechanical strength of the tank has been carefully analyzed using Finite Element Analysis (FEA), as depicted in Fig. 6.11. Stress and distortion has be calculated for all possible detector conditions, such lifting empty without cover, lifting with full load, transporting with 1.2 g acceleration, merged in water, etc. The stainless steel vessel weighs about 20 ton (including the support structures) and has a volume of $\sim$95 m^3 (without the chimney).

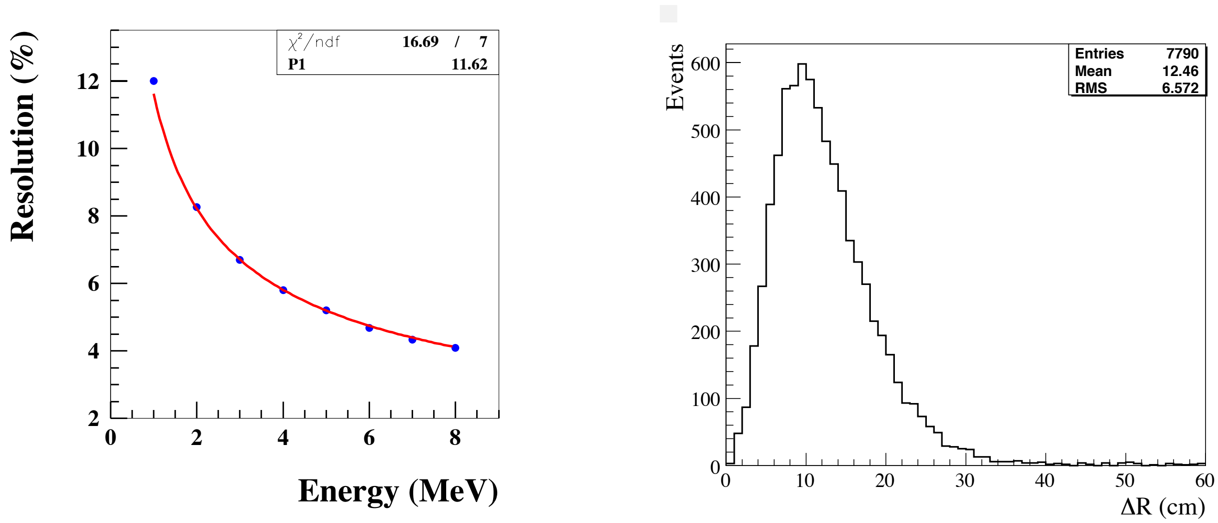

Fig. 6.10. *Left:* The reconstructed energy resolution for electron events uniformly generated in the target region is $11.6\%/\sqrt{E(MeV)}$ using the total PMT digitized charge. The reconstructed energy resolution is $10.5\%/\sqrt{E(MeV)}$ using the undigitized total charge. *Right:* The vertex reconstruction resolution for 8 MeV electron events uniformly generated in the target region using a maximum likelihood fit to the energy and position. The x-axis is the distance of the reconstructed vertex to the true vertex and the y-axis is the number of events.

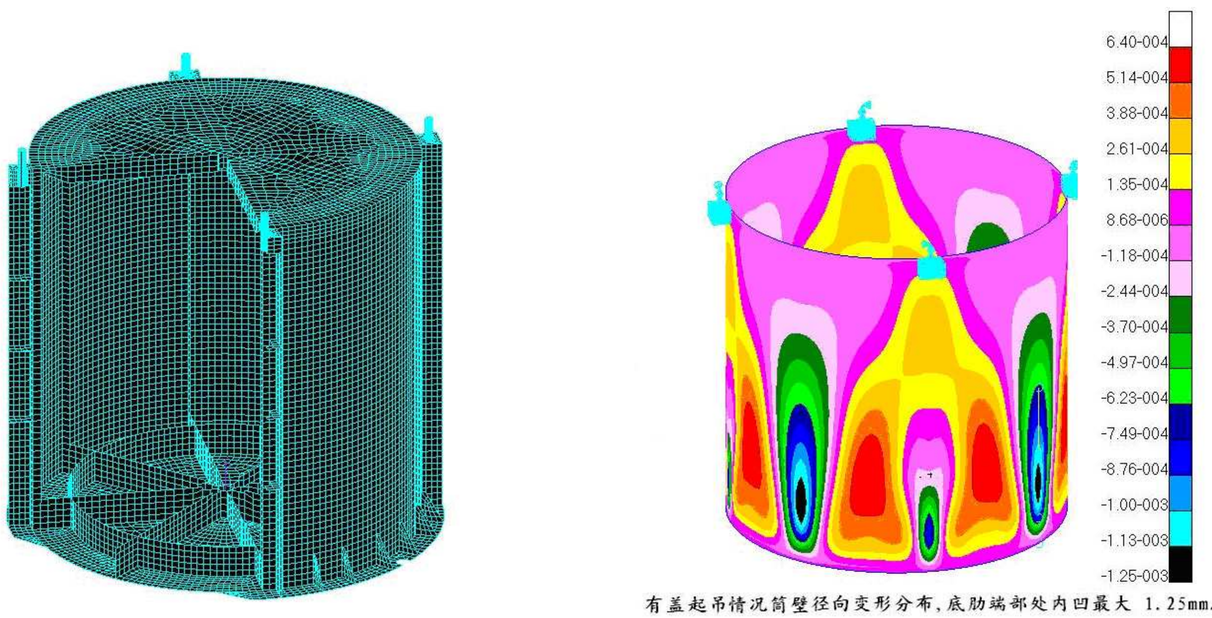

Fig. 6.11. Left: model of the stainless steel tank in FEA. Right: An example of the FEA results, the distortion of tank wall during lifting. The maximum distortion is 1.25 mm at the bottom.

6.2.2 Surface Coating of Detector Tank and Optical Barriers

We plan to coat the inside of the antineutrino detectors with a black "paint" such that the PMTs only detect light directly from the antineutrino interaction in the liquid scintillator. This improves the position

Item	Requirement & Justification
height	$\leq$5 m to clear tunnel ducts
diameter	$\leq$5 m - diameter is constrained by tunnel width - detector structure can exceed dimensions along tunnel
height of external tanks and ports	$\leq$0.3 m
accuracy of outer radius	$\leq$5 mm
accuracy of height	$\leq$5 mm
wall thickness	- minimal material so as to reduce backgrounds from radioactivity in the steel and welds
leak tightness	- leak proof to oil for $>$5 years - leak proof when submerged in water
tilt	- allowable tilt when empty $<$9.6%
lift	- allowable lift by crane when full
ports tank material	- can be drained or pumped out for emergency - non-magnetic - compatible with mineral oil
strength	- tank can be lifted when full - can support PMT structure - can handle stresses induced by lifting and transport

Table 6.5. Requirements on the steel tank of the antineutrino detector.

resolution of the positron interaction and of the neutron capture, at some expense in energy resolution. A high quality black coating is for example, Avian Black-S [20]. The Avian Black-S coating is perhaps the blackest black available in the form of a paint. Its reflectivity is less than 3.5% over the entire near-UV and visible spectrum. Avian Black-S coating is a spray on, two part water based urethane coating that exhibits low reflectance over a wide wavelength range. The water-borne coating exhibits very low gloss and is quite durable compared to most low reflectance coatings. It is easily mixed and applied with standard spraying equipment. Cleanup is easily done with water and detergent.

Alternatively, we are considering the use of a black barrier offset from the steel vessel. It would occlude all of the PMT support structure and the PMT except for the photocathode. In this case, light produced behind the PMTs will be less troublesome just as light above and below the reflectors is less troublesome.

We also consider an ultrawhite coating, Avian-D [21], from the same manufacturer, that would be suitable for coating the exterior of the antineutrino detectors to improve the performance of the muon system. The present baseline design is for no coating on the exterior of the stainless steel antineutrino detectors. The reflectivity of (stainless) steel is about 60%, if its surface is not special prepared for good optical performance. We can estimate that the 40% absorption of light on the exterior surface of the antineutrino detectors corresponds to an effective loss of about 10% of the light that could reflect off the surfaces of the water muon system. This lost light could be recovered by painting the exterior of the antineutrino detectors with a water- compatible white paint with high reflectivity in the near UV. A candidate paint is the Avian D paint, whose reflectivity is shown in Fig. 6.12. Painting the exterior of the antineutrino detector would allow us to improve the system performance at the relatively minor expense of coating the exterior of the detector tanks.

Avian-D coating is a two-part water based urethane coating that can be applied to a wide variety of substrates. The applied coating is water proof and quite durable. The coating is a two part coating with

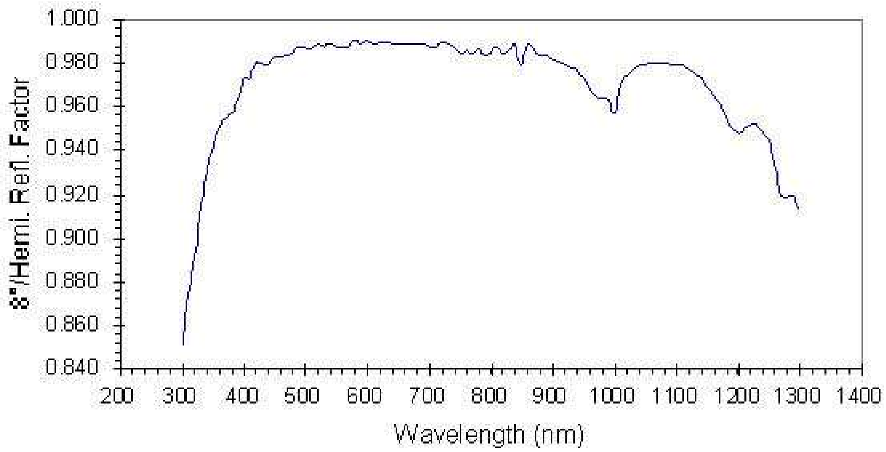

Fig. 6.12. Typical hemispherical reflectance data for Avian-D white reflectance coating [21].

a water phase with pigment and an activator. The reflectance of Avian-D coating matches that of barium sulfate based coating in the visible region of the spectrum. The coating is effective down into the near-UV and up to the very near-IR. Avian-D coating is ideal for field applications where the coating will experience variations in temperature and humidity. The coating is also ideal for large integrating spheres used in lamp measurement photometry where large amounts of UV are not present.

6.2.3 Detector Target and Acrylic Vessels

The acrylic vessels for Daya Bay consist of the following basic components:

- a pair of nested acrylic vessels
- a support structure (ribs, rings, or feet) for the acrylic vessels that support the assembly when empty
- three calibration pipes at the top to calibrate the detector along z at different radii
- a fill-drain mechanism to allow for the filling and emptying of all detector volumes
- closed overflow tanks that capture all liquids during expansion due to temperature variations of the antineutrino detector

and should meet the requirements outlines in Table 6.6.

Different design options are currently being studied by IHEP and the University of Wisconsin. One of the main challenges is to find a design that allows easy and reliable assembly of the nested acrylic vessels, either at the manufacturer or on-site at Daya Bay.

The target vessel is a cylinder of 3100 mm height and 3100 mm diameter (external dimensions) with 10 mm wall thickness (acrylic). It weighs $\sim$580 kg, and contains a volume of $\sim$25 m^3 (without chimneys). The γ-catcher vessel surrounding the target is a cylinder of 4100 mm height and 4100 mm diameter (external dimensions) with a 15 mm wall thickness (acrylic). It weighs 1420 kg, and contains a volume of 28 m^3 ($53\ m^3 - 25\ m^3$) (without the chimneys). At the top of the inner target vessel, there are two chimneys for the insertion of radioactive calibration sources at the center as well as off-axis. There will be one chimney for the γ-catcher as well. The inner diameter of the calibration pipes will be $\sim$50 mm.

The target and γ-catcher vessels will be built of acrylic which is transparent to photons with wavelength above $\sim$300 nm (50% at 300 nm [2]). Both vessels are designed to contain aromatic liquids with a long term

Item	Requirement & Justification
general volume uniformity	- all 16 vessels constructed to volume uniformity of 1%
volume uniformity of inner tank pairs	- matched to 0.3%
materials compatibility	- chemically compatible with scintillator for $>$5 years
dimension stability	- dimensionally stable for years to $<$1 mm
optical properties	- high-degree of transparency to near UV light - high optical quality bonds
leak tightness	- leak tight between acrylic volumes - no leakage into mineral oil volume - leak tight penetrations for filling and calibration
surface crazing	- absence of surface crazing after fabrication, assembly, and transport

Table 6.6. Requirements on the acrylic vessels for the antineutrino detector.

leak-tightness (free from leakage for ten years) and stability. The critical constraint is the chemical compatibility between the vessel and the scintillating liquids, for at least five years. There must be no degradation of the liquid properties (scintillation efficiency, absorption length) nor any significant degradation of the acrylic material (yellowing or crazing of more than a few percent of the acrylic surface area). The γ-catcher vessel will also be chemically compatible with the mineral oil in the buffer region.

Acrylic is normally PMMA plus additional ingredients to prevent aging and UV light absorption. Different manufacturing companies have different formulas and trade secrets for the additional ingredients, resulting in different appearance, chemical compatibility, and aging effects. For the material choice, we have surveyed many kinds of organic plastic and identified a number of suppliers and manufacturers. See below.

In the polymerization gluing method, they add the same raw materials as the acrylic (PMMA + ingredients) into the gap between the plates. Thus the joints consist of exactly the same acrylic material as the joined plates, and there is no difference in their mechanical, chemical and optical properties. During polymerization, UV light is used instead of heating, in order to prevent the bent sheets from rebounding. The speed of polymerization is controlled to minimize the remaining stress. Once the tank is fabricated in shape, it will be put in a thermally insulated enclosure for up to a month ($\sim$1 week in our case) to be heated for releasing the stresses. The temperature will be controlled within $\pm 1^\circ$ C. Different acrylic types, shapes, thicknesses, etc., need different temperature curves for bending and curing. Hence experience is very important. According to Gold Aqua System Technical Company, one of the potential manufacturers, the geometric precision of the cylindric vessels can be controlled to $\pm$1 mm for a 2 m-diameter tank. The tank can have reinforcement structures at both the top and bottom to provide the necessary mechanical strength. However, a thin sheet tends to have more residual stress which may be problematic for chemical compatibility. The minimum thickness of our tank will be chosen after engineering calculations have been performed and compatibility tests of acrylic sheets with liquid scintillator and mineral oil are completed. Figure 6.13 shows a example of an acrylic plastic vessel produced by Gold Aqua System Technical Company in Taiwan.

The Daya Bay detectors will consist of a pair of concentric, nested acrylic vessels inside a stainless steel tank. The nested design of the target vessels is a unique technical challenge, both in engineering and fabrication. Two design options are currently being pursued: One is based on a modular structure with removable top lids to allow the shipping of individual vessels and the mechanical assembly of the nested

Fig. 6.13. *Left:* Mandrel used for shaping acrylic sheets into a cylinder. *Right:* An acrylic vessel (right) produced by bending acrylic sheets around a mandrel (left) at the Gold Aqua Technical Company. in Taiwan. The diameter and height are both 2 m.

pair on-site at Daya Bay. The other option is a fully-bonded option in which the entire assembly of the nested pair is done at the manufacturer. We can also imagine a hybrid solution between these two options. This is currently under investigation.

Modular Design of the Acrylic Vessels

In the modular design the acrylic vessel assembly consists of a pair of nested vessels with removable tops and calibration ports. This allows the on-site assembly of the nested arrangement inside the steel tank. The bottom of the vessels would be bonded to minimize the number of O-ring seals and flanges and to maximize the optical transparency of the vessels. In the modular assembly the calibration pipes are attached to the vessels by means of acrylic flanges, fasteners, and O-rings seals. See for example Fig. 6.14 for a prototype of an acrylic flange. Penetrations through the γ-catcher vessel can be designed with double O-ring seals or flexible teflon tubing that allows small lateral movements of the acrylic vessels with respect to each others.

Fully-Bonded Design of the Vessels

A simple design of the acrylic vessels is to bond the inner and outer acrylic vessel together at the top and bottom where the reinforcing ribs attach, as shown in Fig. 6.15. The alignment of two vessels with locators will be done by the manufacturer. This design has smaller dead area and it avoids problems associated with large O-rings in liquid scintillator but has less flexibility.

Manufacturers and Fabrication

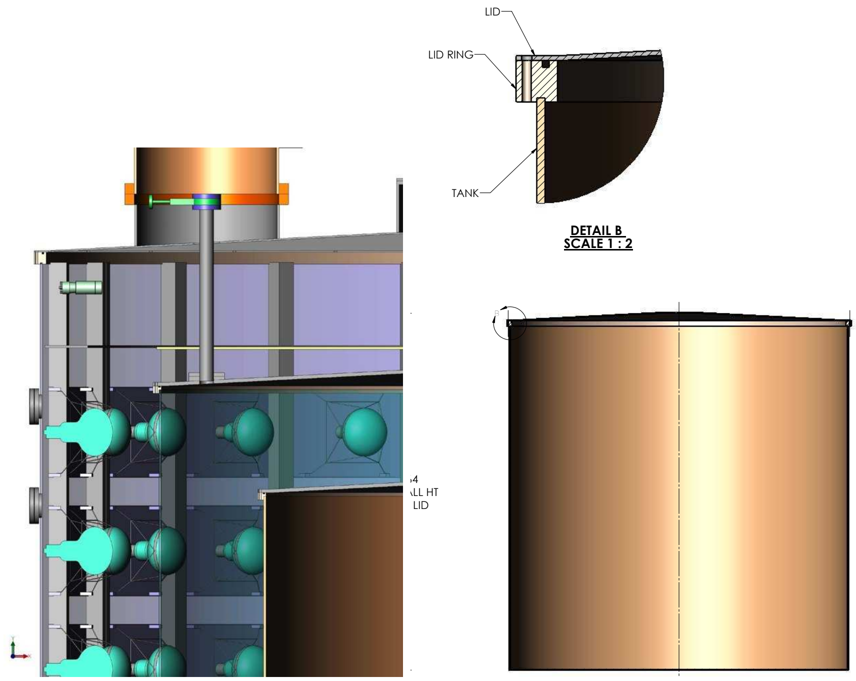

Fig. 6.14. Conceptual study of an acrylic vessel with removable lid and conical top. The shaped top is used to avoid the trapping of bubbles during filling. Further R&D is necessary to determine the slope of the top and to see if bubbles can be trapped below the bottom of the vessels. The conical shape can be machined out of a sheet of flat cast acrylic. *Left:* Cross-section of the top corner of the detector. The three nested cylindrical tanks are shown as well as the PMTs, one of the calibration boxes, and a calibration pipe from the calibration box to the γ-catcher volume. *Right:* Outer view of one of the acrylic vessels with shaped, conical top and a flange for the connection of the top lid. The support feet of the vessel tanks as well as reinforcing ribs in the top or bottom are not shown.

As part of the ongoing R&D effort we are investigating a number vendors worldwide as suppliers for the acrylic raw material and manufacturers for the acrylic vessel. Two possible manufacturers of acrylic vessel have been identified in Taiwan and the US:

Gold Aqua System Technical Co. [17] in Kaoshiung, Taiwan, is a subsidiary of Nakano Ltd. [18] They are experienced in the design and construction of acrylic-based structures for aquariums, museums, and residential homes. They are interested in the development of acrylic vessels for the Daya Bay experiment. The approach of Gold Acqua is to use bent plate sheets to be glued together by the polymerization method. It appears at this time that this method will be preferable as it should provide a higher quality vessel. The vessel for the Hong Kong neutron detector (which is being built by a subset of the Daya Bay collaboration) has been ordered from Gold Aqua in Taiwan. On March 1, 2007, Daya Bay collaborators including the US L2 manager for the antineutrino detector met at Gold Aqua in Taiwan to view their facilities and discuss the design of the Daya Bay vessels. The current cost estimate for the acrylic vessels in the Daya Bay experiment is based on the production cost at Gold Acqua in Taiwan.

We are also discussing the design of the Daya Bay vessels with Reynolds Polymer Technology [19] in Co, USA. With their international reputation and impressive portfolio including experience in research projects such as the Sudbury Neutrino Observatory they are ideally suited to help develop the design of the

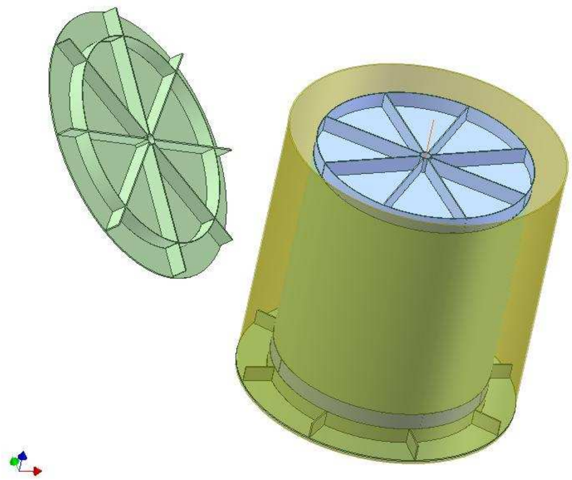

Fig. 6.15. Conceptiual design of a fully-bonded design of acrylic vessels. The nested vessels are show along with the reinforcement ribs at the top and bottom. The calibration pipes are not shown in the picture.

Daya Bay vessels, provide consulting, and technical feedback. Although Reynolds Polymer has recently opened a production facility in Thailand we expect the production costs for the Daya Bay vessels to be somewhat higher than at Gold Aqua in Taiwan. As part of the ongoing R&D effort we will continue to work with both manufacturers — and also explore new vendors, of course — to design, cost, and prototype the acrylic vessels for the Daya Bay experiment.

An important consideration in the choice of vendor is the transportation of the vessels to Daya Bay and the assembly of the nested vessels. Simulations have shown that the transportation phase is hazardous for a double acrylic vessel which has been completely assembled. In general, upright transportation of the acrylic vessels is preferred as this is the strongest position for the vessels with the least risk of cracking, sagging, or damage during transport. A special cargo company needs to be enlisted to provide the transport of this over 5-m high acrylic structure. Transportation equipment will be chosen to isolate shock and vibration loads. At this point it is unclear if its feasible at all to transport the vessel as one assembled, nested pair. This problem can be solved by transporting the target and γ-catcher vessels separately to Daya Bay and assemble them on-site inside a cleanroom of the Surface Assembly Building. See Chapter 11 for more details. These options will be evaluated in the ongoing R&D phase and together with the manufacturers. In this context, production facilities in the vicinity of Daya Bay and possibly with port access such as Gold Acqua in Kaohsiung, Taiwan, have a certain logistical advantage.

6.2.4 Overflow Tanks, Calibration Ports, and Vessel Penetrations

The detectors consist of three nested vessels: An inner target vessel filled with Gd-loaded liquid scintillator, the γ-catcher filled with liquid scintillator, and the outer steel tank containing the target vessels and a mineral oil buffer. The design of the acrylic vessels allows for the insertion of the calibration sources into the inner target volumes as well as the thermal expansion of the liquids during transport or data taking. The three volumes of the detectors are designed vacuum-tight to prevent mixing of the three fluids or their vapors.

Overflow tanks are positioned directly below the calibration hardware and they are connected to the calibration pipes and target vessels. The small gate valve separates the overflow tank from the calibration hardware during data collection. The overflow tanks provide a capacity of 100-150 l to accommodate the liquid expansion in temperature changes of up to 6-8 degrees C.

In addition to the central chimney port, the buffer vessel lid will have two more ports, each 50 mm diameter, to facilitate the deployment of radioactive calibration sources and light sources. These ports will have gate valves to isolate the calibration devices when they are not in use and facilitate their removal. Around the side wall of the stainless steel vessel there will be several ports for high voltage, signal, and instrumentation cables.

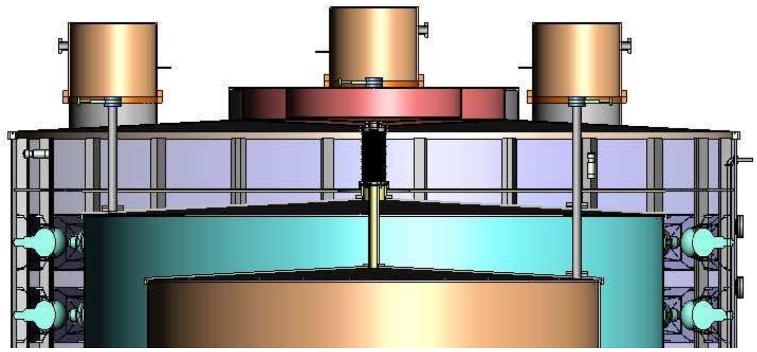

Fig. 6.16. Cross-section of the current conceptual design of the top of the antineutrino detectors. Three penetrations connect the calibration boxes (yellow) and overflow tanks (red) to the two different target vessel volumes. The ports can be sealed with gate valves when the calibration boxes are removed during transport or filling of the detectors.

At first glance one is tempted to solve the penetration problem by long nested acrylic tubes bonded to the tops of the acrylic tanks. However, one pays for the simplicity of the penetrations in the following ways. The acrylic lids will require tubes of 1 and 0.5 meter length. This is a fragile protrusion, especially during transport and shipping. The outer lid must be lowered precisely during the assembly or damage will occur. With bonded calibration tubes any lateral motion of the vessels with respect to each other or with respect to the outer steel tank can damage the calibration pipes and penetrations.

The present design addresses these problems by using flexible Teflon joints along the acrylic tubes. These absorb translation and rotation motion in all possible directions [3]. Instead of long bonded acrylic tubes with bonded plates or stub tubes flanges with O-ring seals are used. The associated acrylic hardware can be manufactured in machine shop separate from the acrylic tank company and attached in the surface assembly building. Support spools are required to mount the calibration boxes on the lid of the detector. In one of the design options under consideration the support spools for the calibration boxes are used as overflow tanks.

A critical element in the current design are acrylic O-ring flanges. A prototype flange for connecting the calibration tube to a vessel flange has been constructed and is shown in Figure 6.17. Further R&D is necessary to test the reliability and leak tightness of such a flange.

After the detectors have been filled in Hall 5 the will be transported to the experimental halls. During data taking they will operate under water in the pools of the experimental halls. During the course of their livetime the detectors may experience temperature fluctuations of several degrees C. We expect that the range of temperatures the detectors are exposed to will be between 12-20 degree C. Hall 5 and the tunnels will be airconditioned to 18-20 degrees C. The rock temperature at underground locations such as KamLAND is usually 10-12 degrees C. To allow for the expansion of the detector liquids, overflow tanks are part of the

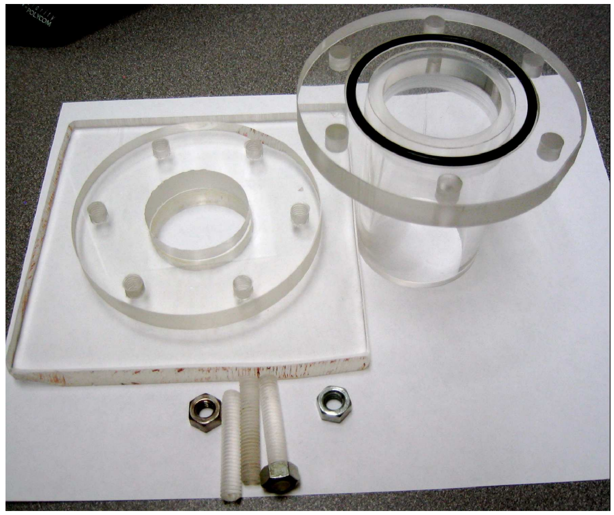

Fig. 6.17. Prototype of a plate to plate and a tube to plate bond for attaching penetration tubing to acrylic tank tops. If required all clamping hardware could be acrylic by use of threaded studs and acrylic nuts.

detector design. Based on the typical expansion of liquid scintillator and mineral oil of $\sim 7\times10^{-4}$per degree C we expect the volume of the liquids to change by 15-20 liters/degree C. The overflow tanks are designed to accommodate 100-150 l of fluids for each one of the volumes. The volume in the overflow tank needs to be constantly monitored to a precision of about 1–2 l so that we can correct for the loss of events that the overflow fluid would have contributed. The entire overflow system is constrained to be inside a 300 mm high zone above the stainless tank top surface. The requirements for the overflow tanks are listed in Table 6.7.

Item	Requirement&Justification
assembly height	$<$300 mm
size	- buffers largest anticipated fluid expansion/contraction
geometry and dimensions	- simple geometry to allow volumetric measurement
non-capturing overflow	- passive emptying back into main volume
materials compatibility	- chemically comparable with scintillator for $>$5 years

Table 6.7. Requirements on the overflow tanks of the antineutrino detector.

Two different designs are currently being considered for the overflow tanks. They are illustrated below. One design uses single overflow tanks for every calibration port. Acrylic tubes connect the target volume to the overflow tanks. The tubes are coupled to the vessels by an acrylic flange. Corrugated Teflon tubing couples the acrylic tubing to the connections of the overflow tanks. The bottoms of the overflow tanks are sloped to permit passive draining of their contents. A small gate valve isolated the detector from the calibration hardware.

A variation in which concentric, nested overflow tanks are located in the center of the top of the antineutrino detector is shown in Figure 6.18. In this design all overflow volumes can be combined in one nested tank underneath the center calibration box. This option reduces the number of individual overflow tanks on top of the antineutrino detector but requires a set of concentric pipes at the center of the detector.

Both schemes permit domed top faces to the acrylic vessels which will provide additional structural strength and allow the escape of gas bubbles into the overflow volumes.

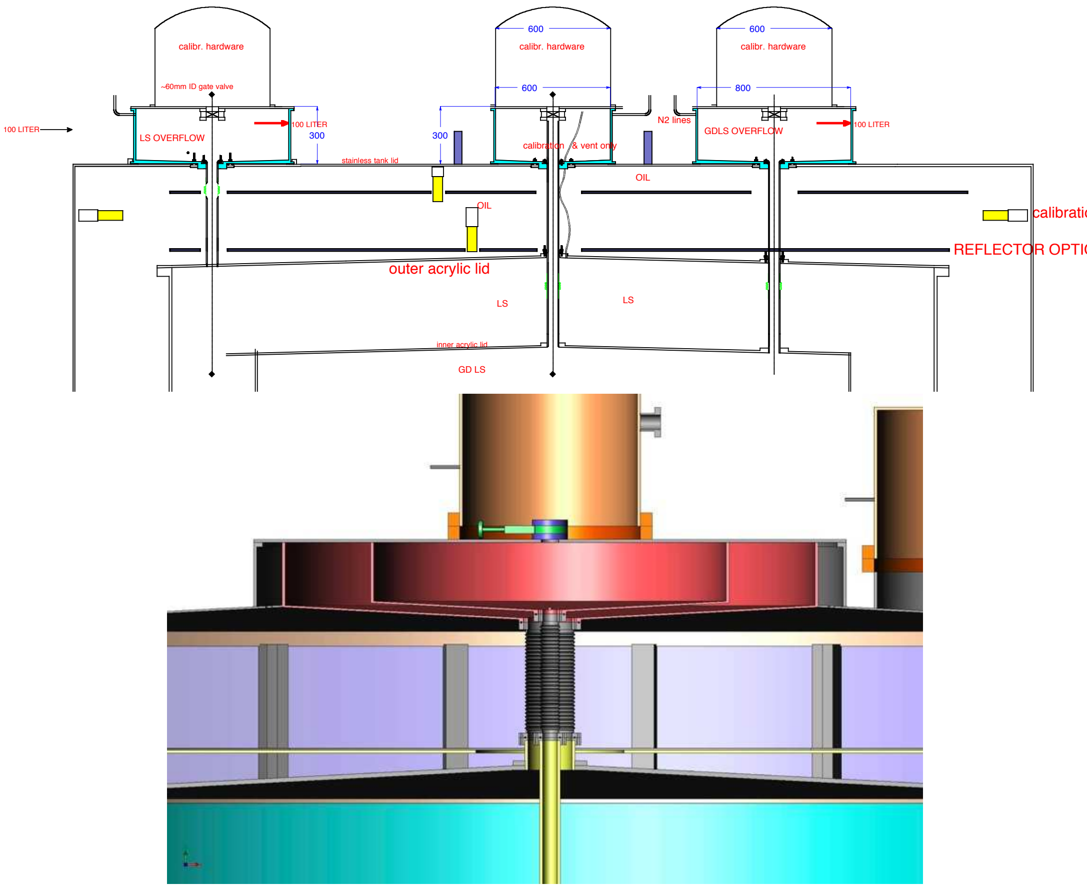

Fig. 6.18. *Top:* Single overflow tank for every calbration port. Conceptual design of simple penetrations between the acrylic vessels, the overflow volumes, and the automated calibration boxes. *Bottom:* Concentric, nested overflow tanks. Alternative design of the overflow tank utilizing a concentric penetration in the center of the detector.

6.2.5 Fill and Drain Mechanism

Filling the Daya Bay detector modules is a critical step of the assembly process. It involves the simultaneous filling of the Gd-loaded liquids scintillator, the undoped liquid scintillator, and the mineral oil into the detector volumes. The main purpose of this system is to provide a mechanism for filling the detector with the liquid scintillators and oil after assembly and for draining the detector for repair and decommissioning at the end of the experiment. The internal structure of the detector pose stringent mechanical constraints on the filling and draining process. All three regions in the antineutrino detector have to be filled simultaneously to minimize stresses on the acrylic target vessels. During the filling the mass of the Gd-loaded liquid scintillator has to be measured precisely to be able to determine the detector's target mass to $< 0.1\%$. The filling process and measurement of the target mass are described below. Several options are currently under consideration for the design of the fill-drain mechanism of the antineutrino detectors. The baseline design of the fill and drain mechanism is described below with a preliminary discussion of the characteristics and technical challenges. Design studies, prototyping, and R&D are underway to evaluate the conceptual design and develop a detailed technical solution. The basic requirements for the fill- and drain mechanism of the detector are summarized in Table 6.8.

Before and during filling the interior of the antineutrino detector is kept in a dry nitrogen atmosphere. The detector will first be purged after the assembly and cleaning in the surface assembly building, and then again before filling in Hall 5. The purge gas will be dry, boil-of nitrogen supplied from a movable liquid nitrogen tank or nitrogen buggy. We may consider flowing the boil-off nitrogen through an activated charcoal trap for further reduction of radon but this may not be necessary. After filling it is necessary to maintain the flow of purge gas at all times to avoid degradation of the Gd-loaded liquid scintillator from oxygen and contaminants in the air. Liquid nitrogen will be delivered to Hall 5 and the experimental halls on a regular basis during the commissioning and operation of the experiment.

It is preferable that the liquid flow into the tank volumes be laminar with little or no splashing. This minimizes the creation of bubbles in the scintillator that can stick to the surface of the acrylic vessels during filling. It is possible to meet these requirements with a system using concentric filling tubes from the bottom of the nested tanks. But this requires additional and complicated penetrations. Fixed filling lines from the side are also possible but that system requires that tubes be left in place during data taking. The default solution is a removable fill/drain probe that can meet the above requirements. It is described below.

Item	Requirement & Justification
ports and fill access to all three zones	- need to fill all volumes simultaneously
vacuum tight ports and fill lines	- detector needs to be filled under nitrogen - avoid degradation of liquid scintillator
capability of emptying detector	- to repair or service detector if necessary - to empty detector during decommissioning
capacity of fill lines	- large enough to allow filling in 1-2 days
capacity of drain mechanism	- large enough to allow draining in 1-2 days
residual liquid volume after emptying	- $<$tens of liters
no need to retain liquids after draining	- plan to produce more scintillator than we need - simplifies technical challenges of fill/drain mechanism - detector can be opened to air during emptying
bubbles in scintillator	- minimize bubbles during filling with suitable fill mechanism

Table 6.8. Technical requirements for the fill/drain mechanism of the antineutrino detector.

To minimize the number of penetrations into the detector we intend to use the calibration ports as fill ports. In this case the liquids are introduced from the top of the detector, as shown in Fig. 6.16.

To avoid splashing of the liquids under gravity into the empty vessels it we plan to insert small fill tubes down the calibration ports to the bottom of the target volume and the γ-catcher. These tubes can be used to fill the detectors from the bottom and to pump out the volumes when the detectors are emptied. When the detector are pumped with tubes from the top a small residual mount of scintillator is likely to remain in the vessels. This is unavoidable for all mechanisms that require pumping out the liquids to the top. The features of this mechanism are listed below:

- Small fill- and drain lines will run through the calibration ports to the bottom of the detector volumes.
- This design requires no additional penetrations to the acrylic vessels thus simplifying the construction and minimizing optical obstruction and interference in the detector.

◦ The interference of the insertion of calibration devices with the fill- and drain lines has to be studied.

s

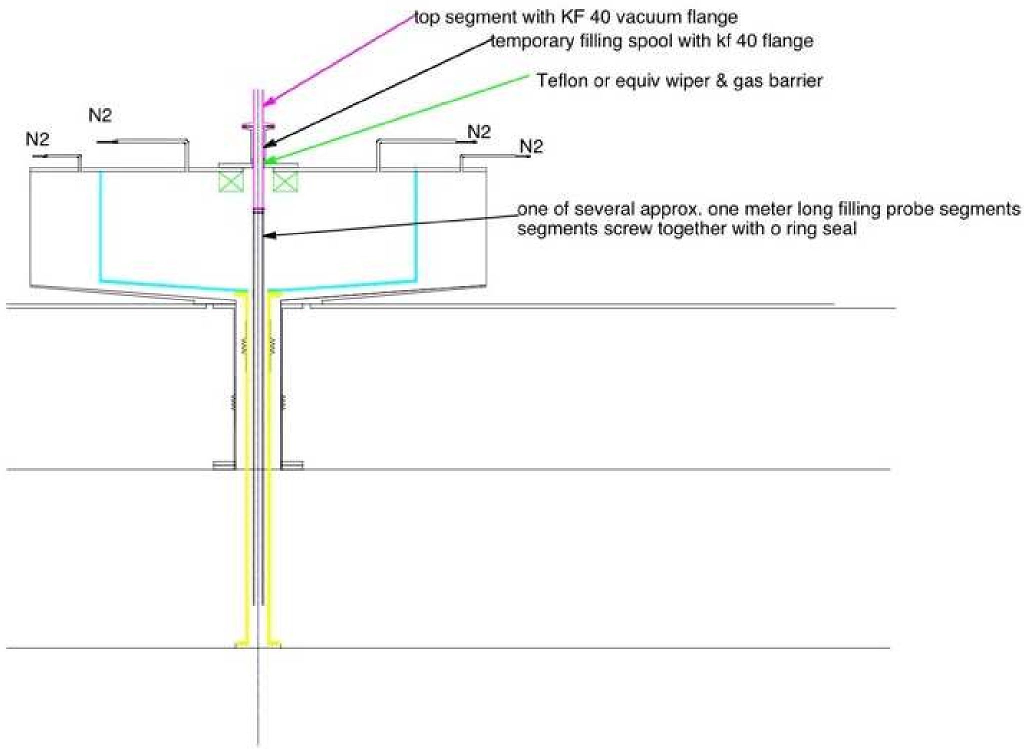

Fig. 6.19. Schematic drawing of a filling system for the Gd-loaded liquids scintillator. A probe is inserted through the calibration port and the overflow tank into the inner target vessel. All connections are made leak tight under a back-pressure of nitrogen to avoid air and radon to enter the detector. Filling of the undoped liquid scintillator into the γ-catcher would occur using a duplicate system located over the appropriate calibration penetration. This figure shows the option of nested, concentric overflow tanks located in the center of the top lid of the antineutrino detector.

The detectors will be filled in a dedicated filling station in Hall 5. On the floor of Hall 5 the top flange connections on top of the detector will be at a height of about 5.7 meters in an 8 meter tall ceiling height. Thus it is necessary to either insert flexible tubing or rigid tubing by sections. The latter is chosen for the fill-drain mechanism. During the filling or pumpout of the detector a temporary spool is clamped and sealed to the top plate of the overflow tank. This is the same plate that will later hold and locate the calibration domes. The temporary spool has a center passage allowing a sliding fit of the filling probe segments. Segments are inserted into the spool sequentially and attached to each other just above the spool. Elastomer seals at the joints contain the fluid flow to the inside of the probe sections. The probe diameter is in the range of 25 mm. During insertion, temporary safety clamps prevent accidental loss of probe sections. Welded to the last section is a commercial vacuum grade clamp flange (type KF-40). The KF flange provides a positive final stop for the probe assembly and permits leak tight attachment of the supply line to the probe.

Gas flow into the tanks is constrained to leave the system predominately through the normal overflow tank vent port because the sliding fit between the probe and the temporary spool has a low gas conductance.

In addition there is a Teflon wiper on the inner spool surface to reduce fluid residue on the probes as they are withdrawn. Lowering and raising will either be by hand or by mechanical hand winch.

Once the fill-drain probe has been inserted the detector is filled until the liquid level raises into the overflow tanks. Level sensors in the overflow tanks will provide continusous monitoring of the liquid levels (and hence target mass) in the detectors.

6.3 Liquid Scintillator and Detector Liquids

The requirements for the LS are described in Table 6.9.

Item	Requirement & Justification
long-term chemical stability of Gd-LS	$>$3–5 years
high optical transparency for oil, LS and Gd-LS	$>$10 m
high photon production for Gd-LS	
ultra-low impurity content	$<10^{-12}$ g/g
C/H ratio determination	$<$0.1%
homogeneous distribution of Gd in LS	- thoroughly dissolving and mixing Gd in LS
chemical identity of oil, LS and Gd-LS between each detector module	- single-batch liquid storage for each phase before filling

Table 6.9. Requirements on the liquid scintillator of the antineutrino detector.

The gadolinium-loaded organic liquid scintillator, Gd-LS, is a crucial component of the antineutrino detector. The H atoms in the LS serve as the target for the inverse beta-decay (IBD) reaction, and the Gd atoms produce the delayed coincidence, so important for background reduction, between the prompt positron and the delayed neutron from the IBD. The LS contains ∼10% hydrogen. Gd has a very large neutron-capture cross section; the σ of natural abundance Gd is 49,000 barns so that isotopic enrichment of the Gd is not required. Two stable isotopes of Gd contribute most of this cross section: $\sigma(^{155}\mathrm{Gd}) = 61,400$ barns and $\sigma(^{157}\mathrm{Gd}) = 255,000$ barns. Furthermore, neutron-capture on Gd leads to emission of γ rays with a total energy of ∼8 MeV, that is much higher than the energies of the γ rays from natural radioactivity which are normally below 3.5 MeV. Hence, organic LS doped with a small amount of Gd is an ideal antineutrino target and detector. Both Chooz and Palo Verde [4] used 0.1% Gd-doping (1 g Gd per kg LS) that yielded a capture time of τ ∼28 μs, about a factor of seven shorter than that on protons in undoped liquid scintillator, (τ ∼180 μs). This shorter capture time reduces the backgrounds from random coincidences by a factor ∼7.

To detect reactor antineutrinos with high precision, the Gd-LS must have the following key properties: a) high optical transparency (long optical attenuation length, on the order of several meters,) (b) high photon production (high light yield) by the scintillator, (c) ultra-low impurity content, mainly of the natural radioactive contaminants, such as U, Th, Ra, K, and Rn, and (d) long-term chemical stability, over a period of several years. It is necessary to avoid any chemical decomposition, hydrolysis, formation of colloids, or polymerization, which can lead over time in the LS to development of color, cloudy suspensions, or formation of gels or precipitates, all of which can degrade the optical properties of the LS. To achieve these criteria, R&D is required on a variety of topics, such as: (1) selection of the proper organic LS, (2) development of chemical procedures to synthesize an organo-Gd complex that is soluble and chemically stable in the LS, (3) purification of the components of the Gd-LS, and (4) development of analytical methods to measure these key properties of the Gd-LS over time. These topics will be discussed in the subsections below.

Major R&D efforts on LS and Gd-LS are being carried out at BNL in the U.S., IHEP in the Peoples Republic of China and JINR in Russia:

A. The Solar-Neutrino/Nuclear-Chemistry Group in the BNL Chemistry Department has been involved since 2000 in R&D of chemical techniques for synthesizing and characterizing organic liquid scintillators loaded with metallic elements (M-LS) using solvent extraction techniques. They helped to develop a proposed new low-energy solar-neutrino detector, LENS/Sol [5]. Concentrations of M in the LS ∼5-10% by weight were achieved to serve as targets for solar neutrino capture, with M being ytterbium (Yb^{3+}) and indium (In^{3+}). It was obvious that these chemical results could readily be extended to the new reactor antineutrino experiments, to prepare Gd-LS (with Gd^{3+}) at the much lower concentrations required for neutron detection, ∼0.1%. BNL began R&D in 2004 on solvent extraction methods to synthesize Gd-LS.

B. Nuclear chemists at IHEP also began their R&D on Gd-LS in 2004. They have focused on preparing solid organo-Gd complexes, the idea being that the solid should be readily dissolvable in the solvent LS, to allow preparation of the desired Gd-LS at the Daya Bay reactor site.

C. The JINR chemists, who have long experience in the development of plastic scintillators, are currently studying the characteristics of different LS solvents, especially Linear Alkyl Benzene. They have also began some collaborative work on Gd-LS with chemists at the Institute of Physical Chemistry of the Russian Academy of Sciences, who also did R&D on In-LS for LENS/Sol starting in about 2001.

It should be noted that the general approach of these different groups is pretty much the same, to prepare organo-Gd complexes that are soluble and stable in the LS organic solvent. However, the chemical details of their R&D programs do differ in significant respects at present, such as in the purification procedures, the control of pH, and reliance on either solvent-extraction methods or formation of Gd-precipitates to isolate the Gd organo-complex. We discuss the current status of the major similarities and differences of these approaches. We note that the differences cited do not seriously affect the general goals of the experiment and are acceptable at this CD-1 stage of the experiment. In recent months closer cooperative R&D ties between these groups have increased and plans for the comparison of Gd-LS samples at the University of Hong Kong have been developed.

6.3.1 Selection of Solvents

Several aromatic (organic compounds based on benzene) scintillation liquids were studied at BNL to test their applicability as solvents for Gd-LS. (1) Pseudocumene (PC), which is the 1,2,4-isomer of trimethylbenzene (and mesitylene, the 1,3,5-isomer), has been the most commonly used solvent for Gd-LS in previous neutrino experiments. But it has a low flash point (48° C) and aggressively attacks acrylic plastic. (2) Phenylcyclohexane (PCH) has a lower reactivity than PC, but only half of the light yield. (3) Both diisopropylnaphthalene (DIN) and 1-phenyl-1-xylyl ethane (PXE) have optical absorption bands in the UV region below 450-nm that cannot be removed by our purification procedures (although we note that Double Chooz has chosen PXE as a satisfactory solution for their requirements). (4) Recently, we have been working with a new LS solvent, Linear Alkyl Benzene (LAB) [6], which is an excellent solvent for Gd-LS. LAB is composed of a linear alkyl chain of 10–13 carbon atoms attached to a benzene ring, and has a light yield comparable to PC. LAB also has a high flash point ($>$130°), which significantly reduces safety concerns. It is claimed by the manufacturers to be biodegradable, and is relatively inexpensive, since it is an article of commerce, with worldwide annual production in hundreds of thousands of tons, mainly for the manufacture of detergents. (5) Mineral oil (MO) and dodecane (DD) both have very good light transmission in the UV-visible region so that no further purification is required. They produce little or no scintillating light. It has been reported that mixtures of PC + mineral oil will not attack acrylic.

PC and LAB, as well as mixtures of PC with DD and of LAB with PC, have been selected as the candidate scintillation liquids for loading Gd in the Daya Bay neutrino detector. In China, an unpurified LAB sample obtained from Fushun Petroleum Chemical, Inc. has an attenuation length longer than 30 m; if its quality is uniform from production batch to batch, it can be used directly as the required solvent without further purification. In the U.S., pure LAB has been obtained from the Petresa Company in Canada. Even though this LAB is quite pure, BNL routinely uses purification procedures to ensure that all of its LAB samples have uniform properties. The chemical properties and physical performance of these scintillation solvents, plus mineral oil and dodecane, are summarized in Table 6.10.

LS	Gd Loading in LS	Density (g/cm^3)	abs_{430}	Purification Method	Relative Light Yield	Flash Point
PC	Yes	0.889	0.002	Distillation	1	48°C
PCH	Yes	0.95	0.001	Column	0.46	99°C
DIN	Yes	0.96	0.023	Column	0.87	≥140°C
PXE	Yes, but is not stable	0.985	0.022	Column	0.87	167°C
LAB	Yes	0.86	0.000	Column	0.98	130°C
MO	No	0.85	0.001	Not needed	NA	215°C
DD	No	0.75	0.000	Not needed	NA	71°C

Table 6.10. Properties of Selected Liquid Scintillators, as compiled at BNL

6.3.2 Preparation of Gadolinium Complexes

One of the major research challenges is how to dissolve the Gd into the liquid scintillator. Since the LS detector is made of an aromatic organic solvent, it is difficult to add inorganic salts of Gd into the organic LS. The only solution to this problem is to form organometallic complexes of Gd with organic ligands that are soluble in the organic LS.

The recent Chooz and Palo Verde antineutrino experiments used different methods to produce their Gd-doped liquid scintillator. In the Chooz experiment, $Gd(NO_3)_3$ was directly dissolved in the LS, resulting in a scintillator whose attenuation length decreased at a relatively rapid rate, 0.4% per day. As a result, Chooz had to be shut down prematurely. On the other hand, the Palo Verde experiment used the organic complex, Gd-ethylhexanoate, yielding a scintillator which aged at a much slower rate, 0.03% per day.

In the Periodic Table, Gd belongs to the lanthanide (Ln) or rare-earth series of elements. Lanthanides such as Gd can form stable organometallic complexes with ligands that contain oxygen, nitrogen, and phosphorus, such as carboxylic acids, organophosphorus compounds, and beta-diketones. Several recipes for Ln-LS have been developed based on these organic ligands. For example, Gd-ethylhexanoate (Palo Verde, Univ. Sheffield, Bicron), In-, Yb- and Gd-carboxylates (BNL for LENS and Daya Bay), Gd-triethylphosphate (Univ. Sheffield), Yb-dibutyl-butylphosphonate (LENS), and Gd-acetylacetonate (Double-Chooz).

Complexants that have been studied at BNL are (i) carboxylic acids (R-COOH) that can be neutralized with inorganic bases such as NH_4OH to form carboxylate anions that can then complex the Ln^{3+} ion, and (ii) organic phosphorus-oxygen compounds, ”R-P-O”, such as tributyl phosphate (TBP), or trioctyl phosphine oxide (TOPO), that can form complexes with neutral inorganic species such as $LnCl_3$ [7]. Initially, work was done with the R-P-O compounds. The extraction of Ln is effective, but the attenuation length is only a few meters and the final Ln-LS was not stable for more than a few months. On the other hand, the carboxylic acids, ”RCOOH”, form organic-metal carboxylate complexes that can be loaded into the LS with more than 95% efficiency using solvent-solvent extraction. Moreover the carboxylic acids are preferable because they are less expensive and easier to dispose of as chemical waste, compared to the phosphorus-containing compounds. In principle, the chemical reactions are (a) neutralization, $RCOOH + NH_4OH \rightarrow RCOO^- + NH_4^+ + H_2O$ in the aqueous phase, followed by (b) Ln-complex formation, $Ln^{3+} + 3RCOO^- \rightarrow Ln(RCOO)_3$, which is soluble in the organic LS. These reactions are very sensitive to pH: the neutralization step to form the $RCOO^-$ depends on the acidity of the aqueous solution, and hydrolysis of the Ln^{3+} can compete with formation of the Ln(RCOO)$_3$ complex.

A range of liquid carboxylic acids with alkyl chains containing from 2 to 9 carbons was studied. It was found that acetic acid (C2) and propionic acid (C3) have very low efficiencies for extraction of Ln into the organic phase. Isobutyl acid (C4) and isovaleric acid (C5) both have strong unpleasant odors and require R-P-O ligands to achieve high extraction efficiencies for Ln. Carboxylic acids containing more than 7 carbons are difficult to handle because of their high viscosity; also as the number of carbon atoms increases in the carboxylate complex, the relative concentration by weight of Ln decreases. The best complexant found to date is the C6 compound, 2-methylvaleric acid, C_5H_{11}COOH or "HMVA", the C8 compound, 2-ethylhexanoic acid, C_7H_{15}COOH or "HEHA" and the C9 compound, 3,5,5-trimethylhexanoic acid, C_8H_{17}COOH or "TMHA".

Several instrumental and chemical analytical techniques have been used at BNL as guides for optimization of the synthesis procedures for Gd-LS. Besides the measurements of light yield and optical attenuation length to be described below, are measurements in the LS of the concentrations of: (1) Gd^{3+} by spectrophotometry, (2) the total carboxylic acid, R-COOH, by acid-base titrations, (3) the uncomplexed R-COOH by IR spectroscopy, (4) the different organo-Gd complexes in the organic liquid by IR spectroscopy, (5) the H_2O by Karl-Fischer titration, and (6) the NH_4^+ and Cl^- by electrochemistry with specific ion-sensitive electrodes. These measurements produced very interesting results that indicated that the chemistry of the Gd-LS is more varied and complicated than what is expected from the simple chemical reactions (a) and (b) listed above. The Gd molecular complex in the LS is not simply Gd(RCOO)$_3$, but contains some OH as well, and the form of this complex changes with changing pH. So, even though the long-term studies consistently show that the Gd-LS is chemically stable for periods $\geq$1 year, there is the lingering concern that hydrolysis reactions might occur over long times in the LS. Careful attention to chemical details, especially pH control, is crucial here, as is long-term monitoring of the Gd-LS.

To date at BNL, many hundreds of Ln-LS samples have been synthesized, including scores of Gd-LS. [8] There are two approaches for preparing batches of the Gd-LS: (i) synthesizing each batch at the desired final Gd concentration, 0.1–0.2%, or (ii) synthesizing more concentrated batches, $\geq$1–2% Gd, and then diluting with the organic LS by a factor $\geq$10 to the desired concentration. The two approaches are not identical, with regard to possible long-term effects such as hydrolysis and polymerization. Approach (ii) is currently favored because it simplifies the logistics of preparing and transporting very large volumes of Gd-LS. At IHEP, thirteen organic ligands including four organophosphorus compounds, five carboxylic acids, and four β-diketones have been tested. The carboxylic acids seem most suitable; three of them have been used for further study. The Gd carboxylate can be synthesized by the following methods: [a.] Carboxylic acids are neutralized by ammonium hydroxide and reacted with $GdCl_3$ to form a precipitate. The solid is collected by filtration, washed with distilled water, and dried at room temperature. [b.] Carboxylic acids are dissolved in an organic solvent that is also the LS and mixed with a $GdCl_3$ water solution. Then the pH of the solution is adjusted with ammonium hydroxide. The Gd-carboxylate is simultaneously formed and extracted into the LS solvent. Method [a], the preparation of the solid Gd complex, is currently being emphasized at IHEP.

After the Gd-complex is synthesized and dissolved in the LS, a primary fluorescent additive and a secondary spectrum shifter (both called "fluors") are added. At IHEP, the final concentration of the solutes includes 1 g/L Gd, 5 g/L PPO (primary), and 10 mg/L bis-MSB (secondary). The resulting liquid is then pumped through a 0.22-μm filter and bubbled with nitrogen for the removal of air. At BNL, the fluors, butyl-PBD (3 g/L) and bis-MSB (15 mg/L), are used. No filtration is applied.

6.3.3 Purification of Individual Components for Gd-LS

Most purification steps developed at BNL are applied before and during the synthesis of the Gd-LS [9]. Chemical separation schemes that would be used after the Gd-LS has been synthesized are usually unsuitable because they would likely remove some of the Gd as well as other inorganic impurities.

The removal of non-radioactive chemical impurities can increase the transmission of the light in the LS and enhance the long-term stability of the Gd-LS, since some impurities can induce slow chemical reactions that gradually reduce the transparency of the Gd-LS. Chemical purification steps have been developed for use prior to or during the chemical synthesis: (1) The purification of chemical ingredients in the aqueous phase, such as ammonium hydroxide and ammonium carboxylate, is done by solvent extraction with toluene mixed with tributyl phosphine oxide (TBPO). (2) LAB, which has low volatility, is purified by absorption on a column of activated Al_2O_3. (3) High-volatility liquids, such as the carboxylic acids and PC, are purified by temperature-dependent vacuum distillation at $\leq$0.04 bar. Vacuum distillation should remove any radioisotopic impurities, including radon. Figure 6.20 compares the optical spectra for LAB before and after

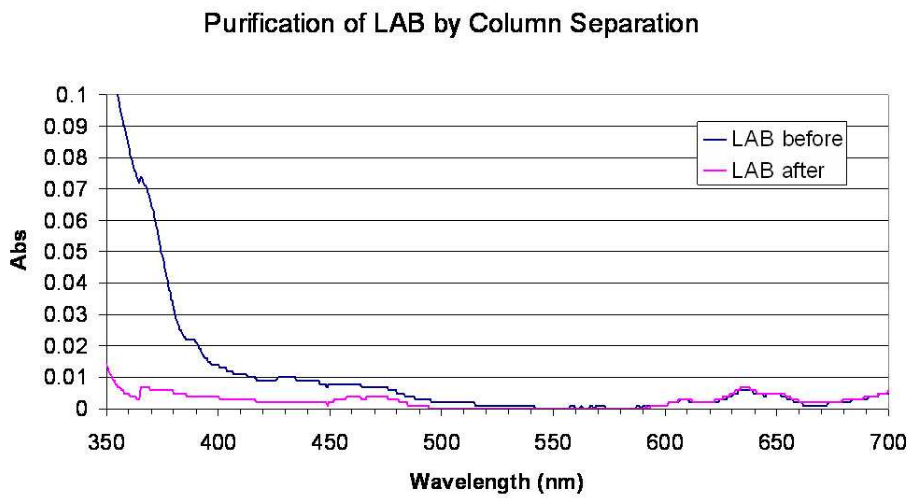

Fig. 6.20. UV-visible spectra of LAB before and after purification

purification with the activated Al_2O_3 column.

Two methods, cation exchange and solvent extraction, are being considered at BNL for the purification of radioactive impurities associated with Gd, mainly the U and Th decay chains. The contents of the radioactive impurities in the commercially obtained 99% and 99.999% $GdCl_3.6H_2O$ solids that are used as starting materials were measured by low-level counting at BNL and at the New York State Department of Health and found to be less than the detectable limits (10^{-8} g/g). More sophisticated radioactivity measurement steps will have to be developed to quantify these radioactive species at concentrations of 10^{-9} g/g in the Gd (implying impurity levels of 10^{-12} g/g in the final 0.1% Gd-LS) to fulfill our criterion of a random singles rate below 50 Hz (with 0.8 Hz from radioactive contamination of ^{238}U, ^{232}Th, and ^{40}K in the Gd-LS). Although this goal is achievable routinely for unloaded LS (i.e., without added Gd), [10], special care is required for Gd-loaded LS since the Gd (and other lanthanides) obtained in China usually contain ^{232}Th at a level of $\sim$0.1 ppm. For Gd loading of 0.1% by weight in the antineutrino detector, the Gd starting material has to be purified to a level $\leq 10^{-10}$g/g. In order to eliminate the Th, Gd_2O_3 powder at IHEP is dissolved in hydrochloric acid and passed through a cation-exchange resin column. Preliminary assays at IHEP showed that this Gd purification procedure reduced the Th content at the ppb level by a factor of four.

6.3.4 Characterization of Gd-LS

The long-term stability of the Gd-LS preparations is periodically monitored in a ”QC”, quality control, program, by measuring their light absorbance and light yield. Samples from the same synthesis batch are sealed respectively in 10-cm optical glass cells for UV absorption measurements, and in scintillation vials for light yield measurements. Monitoring the UV absorption spectrum as a function of time gives a more direct indication of chemical stability than does the light yield. In Fig. 6.21, the UV absorption values

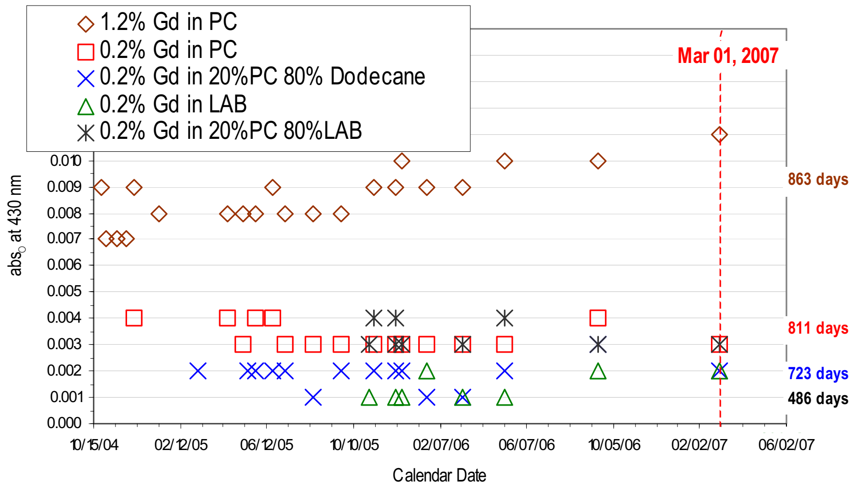

Fig. 6.21. The UV absorption values of BNL Gd-LS samples at 430 nm as a function of time

for a wavelength of 430 nm (in the UV spectrometer) are plotted for BNL Gd-LS samples as a function of calendar date, until March 2007, for different concentrations of Gd from 0.2% to 1.2% by weight in a variety of solvent systems — pure PC, pure LAB, and mixtures of PC+dodecane and of PC+LAB. The figure shows that, since synthesis, samples of: (a) the 1.2% and 0.2% of Gd in pure PC have so far been stable for more than 2.5 and 2 years, respectively; (b) the 0.2% of Gd in the mixture of 20% PC and 80% dodecane has so far been stable for more than 2 years; and (c) the recently developed 0.2% of Gd in pure LAB and in 20% PC + 80% LAB have been stable so far for approximately 1.5 years.

The value of the optical attenuation length, L, is extrapolated from the UV absorption data. It is defined as the distance at which the light transmitted through the sample has its intensity reduced to $1/e$ of the initial value: L = 0.434 d/a, where a is the absorbance of light (at a reference wavelength, usually 430 nm) measured in an optical cell of length d. Note that for d = 10 cm, a value of a = 0.004 translates into an attenuation length L∼11 m. However, it is difficult to extract accurate optical attenuation lengths from these short pathlength measurements because the a values are close to zero. Measurements over much longer pathlengths are needed. BNL has constructed a system with a 1-meter-pathlength, horizontally aligned quartz tube. The light source is a He-Cd, blue laser with λ = 442 nm. The light beam is split into two beams with 80% of the light passing through the 1-m tube containing the Gd-LS before arriving at a photodiode detector. The remaining 20% of the light passes through an air-filled 10-cm cell and reaches another photodiode detector to measure the fluctuations of the laser intensity, without any interactions in the liquid. Use of this dual-beam laser system with 1-m pathlength confirmed the values of the attenuation length extrapolated from the measurements with the 10-cm cell in the UV Spectrometer. For 0.2% Gd in a 20% PC + 80% dodecane mixture without fluors, the 1-m measurement gave 95.23% transmission, corresponding to attenuation length ∼22 m. This agreed with the value ∼21.7 m that was extrapolated from the measured a= 0.002 in the 10-cm cell.

The long-term stability of the Gd-LS developed at IHEP has also been investigated with a UV-Vis spectrophotometer using a 10-cm optical cell. Figure 6.22 shows the long term stability over time of four IHEP Gd-LS samples as measured by optical absorption at 430 nm. In all of these IHEP samples, fluors

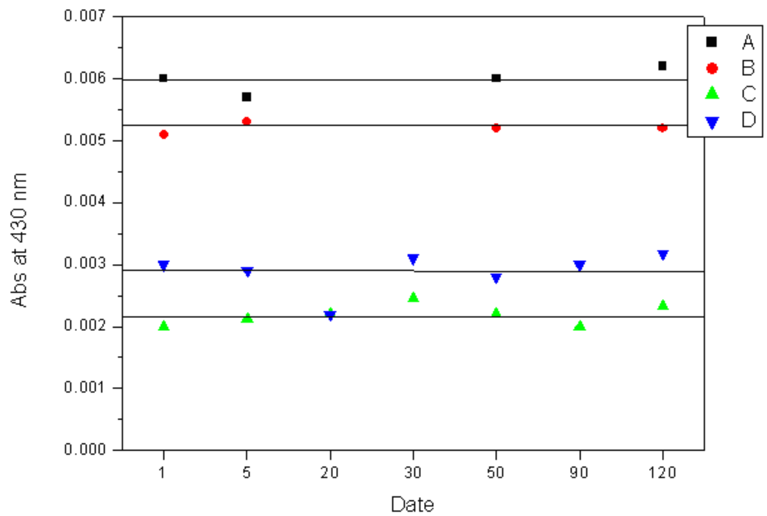

Fig. 6.22. Long-term Stability Test: IHEP Gd-LS with 0.2% Gd as a function of Time.

were added, 5 g/L PPO and 10 mg/L bis-MSB. The concentrations of Gd, complexing ligand, and solvent in the four samples are: [A.] 2 g/L Gd, isonanoate as ligand, 4: 6 Mesitylene/dodecane; [B.] 2 g/L Gd, ethylhexanoate as ligand, 2: 8 Mesitylene/dodecane; [C.] 2 g/L Gd, isonanoate as ligand, LAB; [D.] 2 g/L Gd, 2:8 ethylhexanoate as ligand, 2: 8 Mesitylene/LAB; The IHEP results show that the variations of the absorption values are very small during the four-month period for all four samples. The attenuation lengths of samples C and D are longer than 10 m. The IHEP QC program of long-term stability testing will continue for >1 year.

IHEP has developed an optical system with variable vertical pathlengths up to ~ 1 m to measure the attenuation length more accurately. To measure liquid of ~ 20 m attenuation length to a precision of ± 1 m, the transmission should be determined to 0.25%. It is a challenge to any absolute measurement. By varying the liquid level and fit the measured transmitted light to an exponential curve, the systematic uncertainty of the system will cancel out. An example of the measurement is shown in Fig. 6.23. The attenuation length of the measured liquid is determined to be 23.1 ± 0.87 m. In phase I of IHEP prototype experiment (See Section 6.7), 700 L pseudocumene based normal LS has been used. In phase II, 700 L LAB based Gd-LS has been synthesized and filled into detector. The sample of these LS as well as the buffer oil has been drawn out from the detector after filling completed, and measured using the 1-m tube system, as shown in Fig. 6.23. The Gd-LS has been measured twice. The cycle points shows the first measurement immediately after the Gd-LS filled. The black dots shows the second measurement 2 weeks later. The attenuation length of the Gd-LS is around 15 m at 430 nm.

The emission spectrum of the Gd-LS is studied at IHEP. No remarkable difference is found for the Gd-LS with different solvents (LAB or PC+Oil) or different complexants (TMHA, EHA, or TOPO), but with the same fluors. The emission spectrum of Gd-LS with 5 g/L PPO and 10 mg/L bis-MSB is shown in Fig. 6.24. The peak of the emitted light is well fit to the most sensitive range of the 8” PMT candidates.

The light yield of the Gd-LS is also measured at BNL, IHEP, and JINR. At BNL, a scintillation vial containing ten mL of Gd-LS plus the wavelength-shifting fluors, butyl-PBD (3 g/L) and bis-MSB (15 mg/L), is used for measurement of the photon production. The value of the Gd-LS light yield, which is determined from the Compton-scattering spectrum produced by an external ^{137}Cs γ-ray source that irradiates the sample, is quoted in terms of S%, relative to a value of 100% for pure PC with no Gd loading. Measured S% values

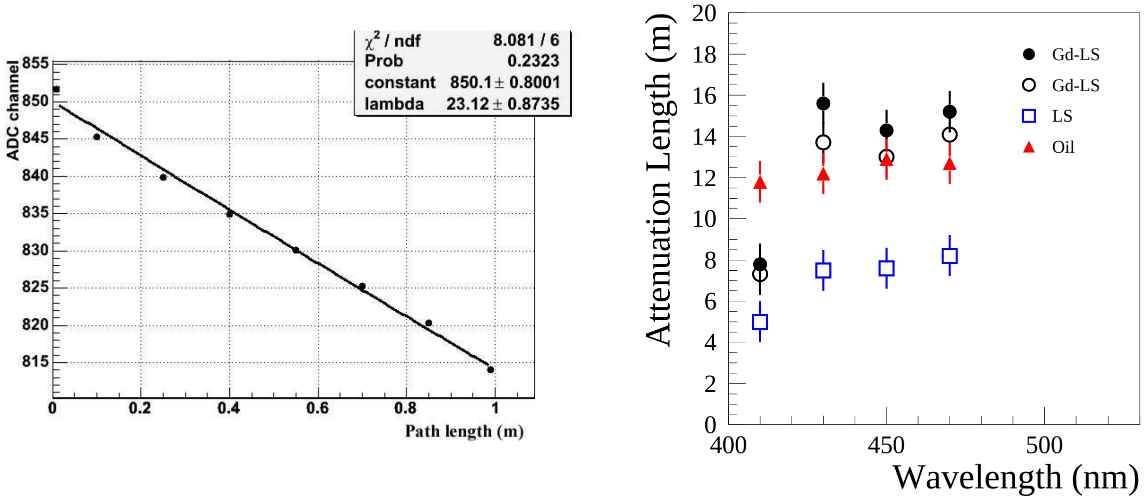

Fig. 6.23. Left: an example of the attenuation length measurement using the 1-m tube system. The transmission of different pathlengths are fitted to an exponential curve. Right: Black dots and cycles are attenuation lengths of the 700 L LAB based Gd-LS used in the IHEP prototype experiment. Blue squares are that for PC based normal LS. Red triangles are that for mineral oil.

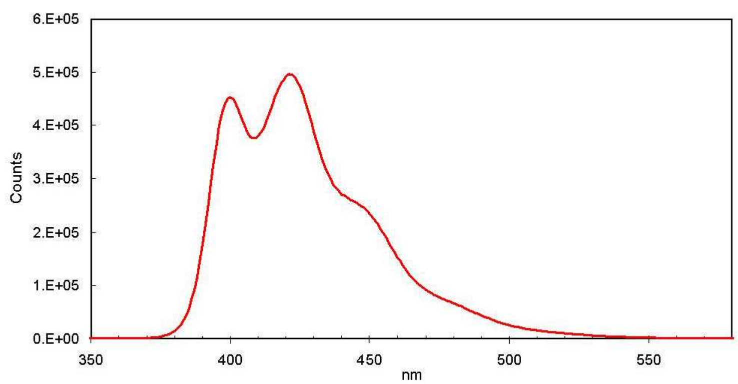

Fig. 6.24. The emission spectrum of Gd-LS with 5 g/L PPO and 10 mg/L bis-MSB. The Gd concentration is 0.2% and the complexant is TMHA.

are respectively 95% for 95% LAB + 5% PC, and 55% for 0.1% Gd in 20% PC + 80% dodecane.

Table 6.11 lists the light yield for several IHEP Gd-LS samples, relative to a value of 100% for an anthracene crystal. It is seen that the concentration of Gd loading has very little effect on the light yield.

6.3.5 Comparisons with Commercial Gd-LS

At BNL, a sample of commercially available Gd-LS, purchased from Bicron, BC-521, containing 1% Gd in pure PC, has been compared with a BNL Gd-LS sample containing 1.2% Gd in PC. BC-521 is the concentrated Gd-doped scintillator with organic complexing agent in PC that was used in the Palo Verde reactor experiment after it was diluted to 40% PC + 60% mineral oil. The light yields of the respective BNL and Bicron samples were found to be comparable, 82% vs. 85%, when measured at BNL relative to

Gd(g/L)	Scintillator	Complex	Solvent	Light Yield
—	PPO bis-MSB	—	PC:dodecane	0.459
—	PPO bis-MSB	—	LAB	0.542
1.5	PPO bis-MSB	Gd-ethylhexanoate	2:8 PC:LAB	0.538
2.0	PPO bis-MSB	Gd-ethylhexanoate	2:8 PC:LAB	0.528
1.5	PPO bis-MSB	Gd-isononanoic acid	LAB	0.492
2.0	PPO bis-MSB	Gd-isononanoic acid	LAB	0.478

Table 6.11. Light yield for several Gd-LS samples prepared at IHEP, measured relative to an anthracene crystal.

100% PC, and, as quoted by Bicron, 57% relative to anthracene. However, the attenuation length for the BNL-prepared Gd-LS was $\sim$2.5 times longer than the value for the Bicron BC-521 sample, 6.2 m vs. 2.6 m as measured at BNL; Bicron quoted a value $>$4.0 m for its sample. This significant difference in attenuation may reflect the care put into the BNL pre-synthesis purification steps.

The chemical stability of these BNL and Bicron BC-521 samples are being followed in our QC program. No perceptible worsening of the optical properties of these samples has been observed over periods of 2.5 and $\sim$2 years, respectively. Note that Bicron simply characterizes the stability of its BC-521 as being ”long term”.

6.3.6 Large Scale Production of Gd-LS

Tasks that have begun or will be undertaken in the next several months are as follows: (1) to continue the QC program of long-term stability of different Gd-LS preparations; (2) to determine the quality, quantity, and types of fluors required to add to the Gd-LS to optimize photon production and light attenuation, in order to decide upon a final recipe for the Gd-LS synthesis; (3) to build a closed synthesis system that eliminates exposure of the Gd-LS to air; (4) to scale the chemical procedures for Gd-LS synthesis up from the current lab-bench scale to volumes of several hundred liters, for prototype detector module studies, and as a prelude to industrial-scale production on the level of 180 ton; (5) to automate many of these chemical procedures, which are currently done by hand; (6) to use standardized ASTM-type tests to study the chemical compatibility of the LS with the materials that will be used to construct the detector vessel, e.g., acrylic; (7) to find methods to measure accurately, with high precision, the concentration ratios, C/H and Gd/H, and the H and C concentrations.

We have made significant progress in several of the area noted above. Relevant to point (2), the decision has been made to use PPO and bis-MSB as the fluors in all future Gd-LS samples. The baseline is to adopt 3 g/L PPO and 15 mg/L bis-MSB. Concerning items (3), (4), and (5) large-scale chemical systems have been designed and built at IHEP and at BNL. The products of these systems, on the order of $\sim$1 ton of Gd-LS, will be used in prototypes of the Daya Bay central detector, that will be tested with IHEP Gd-LS at IHEP, and with BNL Gd-LS at the University of Hong Kong. With regard to (6), BNL has built and used a copy of the system that had been used to test the compatibility of SNO acrylic with various chemicals. The results to date show that PC aggressively attacks acrylic, while PC + dodecane and LAB do not. And concerning item (7), initial results have been provided by a commercial chemistry-testing laboratory on the C and H content of pure LAB and Gd-LAB, obtained by combustion of the organic compounds and determination of the resulting CO_2 and H_2O. These results are encouraging in that the company claims that its precision on these measurements is 0.3%. However, more work needs to be done to quantify the degree of reproducibility of these methods.

6.3.7 General Points Regarding LS at Daya Bay

The current design of the Daya Bay antineutrino detector requires $\sim$200 ton of 0.1% gadolinium-loaded LS (Gd-LS, including $\sim$20 ton of 1% Gd-LAB + $\sim$180 ton of LAB + $\sim$0.7 ton of fluors) for the inner antineutrino target, $\sim$200 ton of unloaded LS (LAB + fluors) for the γ-catcher and $\sim$400 ton of mineral oil for the buffer region, in a total of eight 'identical' detector modules. To ensure the identity of the chemical components for all detector modules, the total amounts of organic liquids needed for each phase have to be accumulated on-site and stored individually before filling the detectors. Several chemical requirements and conditions must be considered for the mixing, storage and filling steps: (1) Compatibility of the organic liquids with the materials that they will be in contact with, for example, the storage tanks, detector vessels, calibration units etc. (2) Homogeneous mixing. (3) Secondary containment in case of leakage or spills of the liquids during the filling process. (4) Storage of these liquids on the surface or underground will pose different temperature-control requirements. (5) Transportation over long distances (from BNL, IHEP or vendors to Daya Bay) or short distances (from surface to underground or neighborhood areas in Shenzhen or Hong Kong to Daya Bay) will pose different handling logistics. (6) The stability of solvents as a function of temperature for storage and transportation. (7) Local monthly temperature variations for best detector-filling timing. (8) Nitrogen purging or blanket to prevent radon or air from entering the solvents. (9) All the organic liquids from the vendors will have to pass the quality-assurance criteria imposed by Daya Bay scientists.

6.3.8 Storage of 0.1% Gd-LS, LS and Mineral Oil

One 200 ton storage mixer (storage tank with mixing apparatus) for the Gd-LS for the inner antineutrino target and another 200 ton storage tank for normal LS for the γ-catcher can be located either on surface or underground.

The locations for each storage tank have not been finalized yet. First option is to have the 200 ton storage mixer and 200 ton storage tank located underground in the Filling Hall. The advantages are (1) no transportation between surface to underground; (2) easier environmental and temperature controls; and (3) the solvents can be transferred to each detector module through transporting pipes (materials not decided yet). However these will require more excavated space in the Filling Hall. Second option is to have the storage tanks on surface. This saves the engineering cost for the extra underground excavation, but requires extra operational cost, such as for tighter temperature controls or the construction of surface buildings to hold these tanks. Considering that the solvents have to be preserved over periods from several months to year, the long-term solvent stability at elevated temperature ($\sim$38° C in summer for Daya Bay) could be a challenge. Yet the storage of mineral oil has not been considered.

6.3.9 Mixing Schemes for LS and 0.1% Gd-LS

All the mixing processes will be conducted in the 200 ton storage mixer. The preparation of unloaded LS should be done first. The procedures are described as follows:

1. Preparation of LS for the γ-catcher
   (a) load $\sim$200 ton of pure LAB in the 200 ton storage mixer;
   (b) dissolve 750 kg of fluors (PPO at 3 g/L and bis-MSB at 15 mg/L) in the LAB and mix the LS thoroughly;
   (c) empty the storage mixer, transfer the LS to the 200 ton storage tank, and eventually transport the LS to the Filling Hall (if the storage tank is located on surface).
2. Preparation of 0.1% Gd-LS for the inner antineutrino target
   (a) load $\sim$180 ton of pure LAB in the 200 ton storage mixer;

(b) dissolve 750 kg of fluors (PPO at 3 g/L and bis-MSB at 15 mg/L) in the LAB and mix the LS thoroughly;

(c) add the ∼20 ton of ∼1% Gd-LS at adequate speed to avoid localization of Gd, which could lead to irreversible oligomerization process, and mix the 0.1% Gd-LS thoroughly;

(d) keep in the same storage mixer and eventually transport the Gd-LS to the Filling Hall. (if the storage tank is located on surface).

3. Mineral oil will be stored and loaded as is for filling the buffer region without any blending or mixing process.

6.3.10 Underground Filling Station

The filling process for antineutrino detector will be handled in the underground Filling Hall. The 0.1% Gd-LS and LS storage tanks, along with a transportation tank for mineral oil (from surface storage) will be outfitted with exit ports that will connect to a centralized, instrumented system with plumbing designed to allow the filling of the three zones of each detector module simultaneously: the inner zone with 0.1% Gd-LS, the intermediate zone with undoped LS, the outer zone with mineral oil. The details of filling procedure and monitoring tools are described in Chapter 11.

6.3.11 Transportation Schemes

The main scintillator components, 1% Gd-LAB, unloaded LAB and mineral oil, will arrive at the Daya Bay site via two possible transportation routes, either long-distance from BNL, IHEP or from vendors to Daya Bay, or short- distance from Shenzhen or Hong Kong to Daya Bay or from surface to underground. Both routes require careful liquid handling and solvent preserving controls. The chemically resistant ISO (International Standards Organization) tanks, which have been widely used in transportation for chemical and petrochemical enterprises and for other neutrino experiments (NOνA or Double-CHOOZ), are proposed to be utilized for Daya Bay. A 26,000 L or 6800 gallon ISO tank can be leased with a minimum 1-year contract for ∼$8,000 per year. The leasing company (EXSIF, same tank supplier for NOνA) has no limitation of how and where the tanks are used, and the leaser takes the full responsibility for their use. Critical temperature-control systems for heating or cooling can be installed on the ISO tanks upon request. If needed, the ISO tanks can also be stacked up to five high with fully loaded liquid inside and serve as a temporary buffer storage region. The numbers and sizes of the ISO tanks will depend on the production capability of each responsible institute or vendors.

6.4 Photomultiplier Tubes, Mounts, and Signal Cables

Optical photons produced by charged particles or γ rays in the antineutrino detector are detected with 192 PMTs submerged in the buffer oil inside the steel vessel. The PMTs are arranged in eight horizontal rings, each with 24 evenly distributed PMTs around the circumference. The rings are positioned in such a way that the PMTs on two adjacent rings are aligned vertically. The requirements for the PMTs are listed in Table 6.12 and 6.13.

Simulation studies indicate the adopted number of PMTs and configuration can provide good energy resolution, about 15% at 1 MeV. From the experience of other experiments, the failure of PMTs in the detector is expected to be about 1% over the lifetime of the experiment. We thus have sufficient number of PMTs in each detector module to ensure reliable performance.

We require the PMT to have a spectral response that matches the emission spectrum of the liquid scintillator and good quantum efficiency for detecting single optical photon at a nominal gain of about 10^7. It is desirable to have good charge response, i.e. the peak-to-valley ratio, for identifying the single photo-electron spectrum from the noise distribution. Since the energy of an event is directly related to the number of optical photons collected, the PMTs operating at the nominal gain must have excellent linearity over a

Item	Requirement & Justification
Spectral Sensitivity	PMT Quantum Efficiency peak to be grater than: 20% at 400 nm, 12% at 300 nm 13% at 500 nm
Gain	$\geq 10^7$ for all PMTs with appropriate tapered resistive base - PMTs must achieve a gain of 3×10^7 at V0 $\leq$2 kV
Pre- and after- Pulsing	- probability for the PMT anode signal pre-pulsing and afterpulsing not to exceed 1.5%. - PMT anode signal not to exhibit after-pulsing with probability of more than 1.5% for photoelectron within 100 ns interval of the defined after-pulse interval (0.1–40 μs)
Rise and Fall Times	- rise time not to exceed 6.5-ns and a fall time not to exceed 10 ns for a single photoelectron pulse
Transit Time Spread (TTS) (FWHM)	- not to exceed $\sim$2.5 ns at a gain of 10^7
Photocathode Uniformity	- maximum quantum efficiency non-uniformity not to exceed 15%
Pulse Linearity	- PMT anode pulse linearity must be better than 5% over the dynamic range of 0–1 nC at a gain of 10^7
Timing Resolution	- effective timing resolution shall be less than 1.7 ns
Relative Anode Efficiency	- minimum relative anode efficiency EA be greater than 1

Table 6.12. Requirements on the PMTs, PMT support, and PMT cables of the antineutrino detector.

reasonable broad dynamic range. In addition, the dark current, pre-pulse and after pulse should be low to minimize the noise contribution to the energy measurement. Furthermore, the natural radioactivity of the materials of the PMT must be kept low so that the γ-ray background in the detector module is as small as possible. These specifications will be quantified with simulations and by detailed studies of a small number of PMTs purchased from the manufacturers prior to the production order.

Taking into consideration the requirements for the photo-cathode coverage of the detector module, the allowed cost, and the dimensional constraints of the antineutrino detector we plan to use 20-cm-diameter PMTs for the antineutrino detector modules.

6.4.1 PMT Selection

There are currently two candidates of photomultiplier tubes that would meet our requirements, the Hamamatsu R5912 [11] and the Electron Tubes 9354KB [12]. Both are 2π PMTs with a 190 mm-wide photocathode and a spectral response peaked near 400 nm. They are similar in design and construction. However, the R5912 has 10 dynodes while the 9354KB has 12. The Hamamatsu R5912 is an improved version over the R1408, which was used by SNO [13]. The R5912 is used by MILAGRO and AMANDA. Both PMTs will be extensively tested.

Item	Requirement & Justification
Radioactivity	- borosilicate glass - total mass of following elements in the PMT including the glass bulb shall not exceed: Th: 5×10^5 E_A/A_{min} μg, U: 5×10^5 E_A/A_{min} μg, K: 1.6×10^3 E_A/A_{min} μg
Single Photoelectron Response (Charge Resolution)	- peak to valley ratio $\geq$2.0 at a gain of 10^7
Dark Pulse Rate	$\leq$25 Hz/cm^2 at 20° C - fractional increase in dark count rate in going from a gain of 1.0×10^7 to a gain of 3.0×10^7 shall not be more than 30% greater than the increase in dark pulse rate in going from a gain of 0.3×10^7 to a gain of 1.0×10^7
Mechanical strength	- to withstand a vibration level corresponding to a 1.5 mm displacement at 15 Hz (equivalent to an acceleration of 2g) for three cycles (i.e., 200 ms) along each of three perpendicular directions with less than 1% change in gain or timing responses. - all PMTs must survive a pressure of 2 atmosphere +30% - optical changes of the PMT's bulb (i.e., transmission and discoloration) must be less than 3% per year for all PMTs

Table 6.13. Requirements on the PMTs, PMT support, and PMT cables of the antineutrino detector.

UCLA will develop the PMT bases both for the antineutrino detector and the muon veto systems. The PMT bases will use positive high voltage and will be of tapered resistive divider type with a zener stage to set a constant potential difference between the photocathode and the first dynode. The zener stage will allow the collection efficiency of the photoelectrons onto the first dynode stage to remain constant (i.e., constant electric field due to constant k-d1 potential) while one changes the high voltage to increase the gain. The tapering of the PMT resistive divider is optimized to maintain the linearity of the PMT response to better than 5% at peak currents of 80–100 mA (500 photoelectrons).

The mechanical design of the potted bases will be based on the Hamamatsu's design used in KamLAND. The signal and high voltage cables will be RG303 coaxial cables; each is approximately 40-meter-long. These PTFE sleeved cables will be etched at the PMT end and will be potted into the mechanical housing made of acrylic or low-radioactivity PVC rod stock which is approximately 10–12.5 cm in external diameter.

To minimize the number of cables in the antineutrino detector we have the option of using a single RG303 to supply HV and extract the signal from the base, with the HV and signal AC-decoupled. The decouplers are part of the PMT system baseline design.

The PMT bases will be manufactured using low radioactivity components. To insure high reliability of the potted bases, all components will be through-hole type. In particular the filtering high-voltage capacitors will be polypropylene film capacitors designed for high pulse current.

The final decision on the selection of PMTs will depend on the radiopurity of the PMT glass, and the results of our test and characterization R&D program to identify which best meets our specifications. We have approximately 600 PMTs originally used in the MACRO experiment. These will be deployed in the muon Cherenkov system. However, new potted bases have to be developed for them.

6.4.2 PMT Support Structure

The PMTs are held in individual mounts and secured in the antineutrino detector using a PMT support structure. In this section we describe the design considerations for the PMT mounts and the support structure. A number of conceptual models are presented. To simplify the design process and make the production of the PMT mounts more economical we are considering to use the same (or similar) PMT mounts both in the antineutrino detector and the muon system. The muon and antineutrino detector groups will pursue a joint R&D and design effort to find an optimized, common design for the PMT support system.

Past experiments such as KamLAND and MiniBooNE have mounted PMTs in individual frames that are directly attached to the wall of the detector tank. This approach is economical and uses the least amount of materials but requires labor-intensive mounting of the PMTs on the walls of the detector tank. This can be complicated especially in a small tank of the size we are considering for the Daya Bay detectors. Also, to simplify the assembly of the antineutrino detectors at Daya Bay we are considering to pre-mount all PMTs on a support structure which can then be installed as a module in the detector tank, as shown in Fig. 6.25. The PMT cabling will be integrated into the support structure and brought out of the antineutrino detector

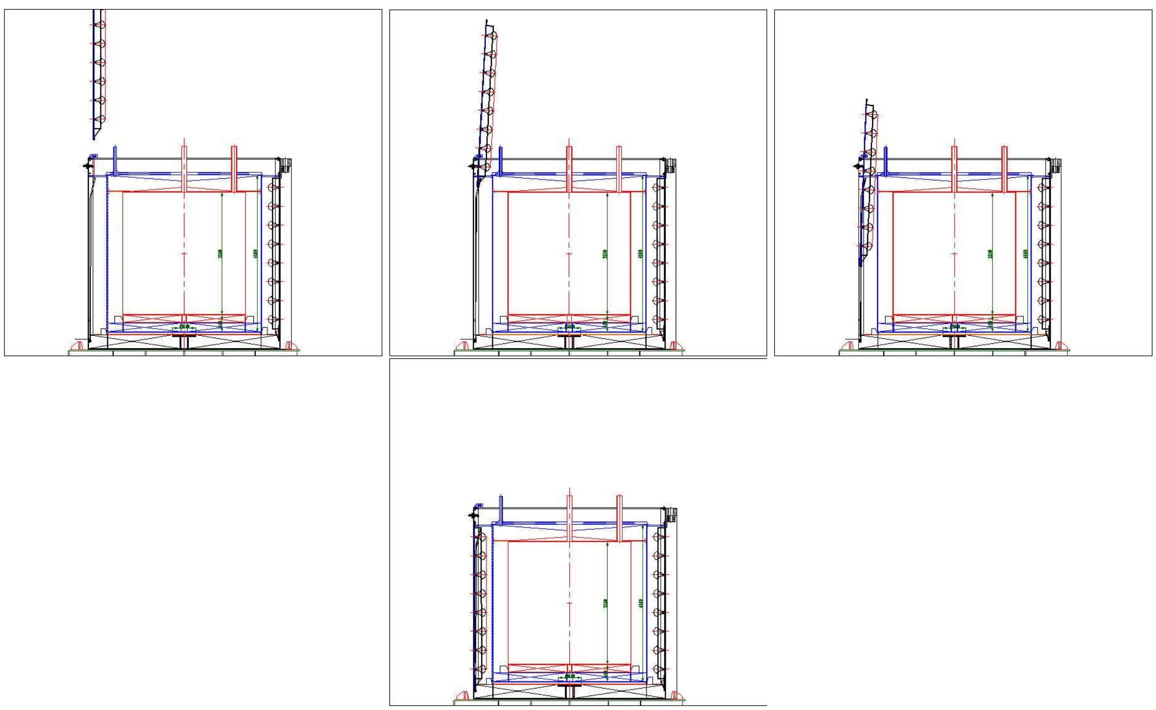

Fig. 6.25. Installation sequence of the PMT support structure. All the PMTs are pre-mounted on the support structure.

through penetrations in the wall of the outer steel cylinder of the detector. After passing a quality-assurance procedure eight sections with 24 pre-mounted PMTs are lowered into the stainless steel vessel through vertical guides attached to the vessel. In addition to simplifying the installation process, a modular support structure allows the easy replacement of any bad PMTs before the detector is sealed. This structure is made of suitable strong, radioactively pure, and non-magnetic material. Figure 6.26 illustrates this concept.

The PMTs are mounted on the curved frame of the ladder-like structure before it is installed inside the

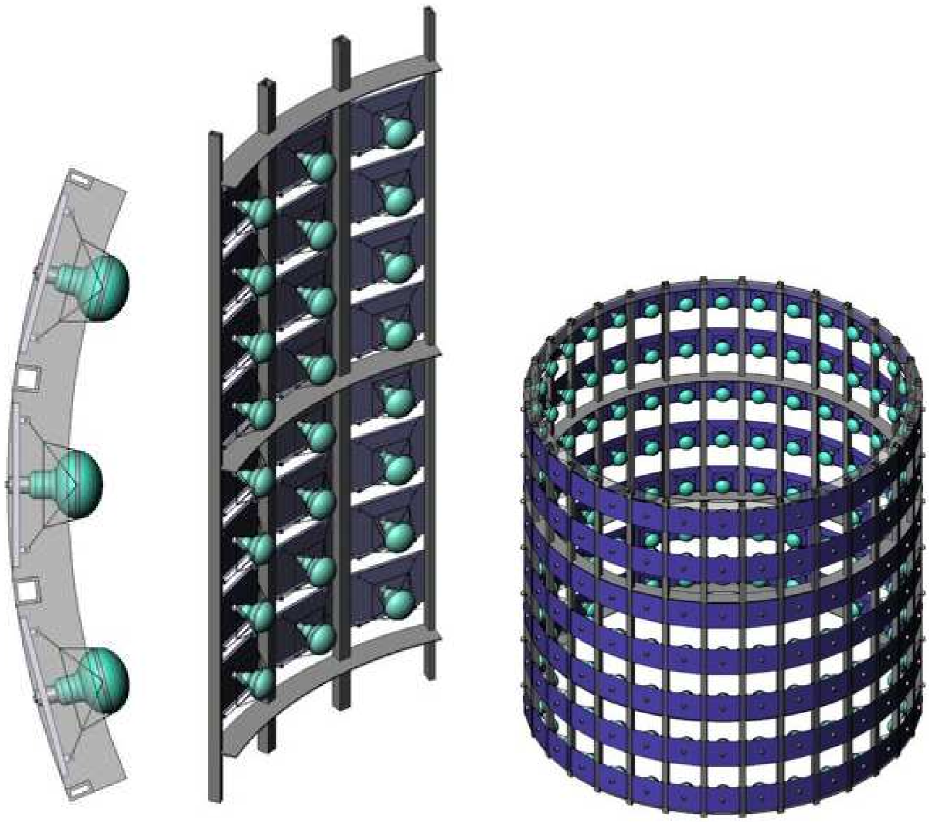

Fig. 6.26. From left to right: Top-view of an angular section of the ring-like, removable PMT support structure. The support structure is made of eight sections. Together they form a complete ring. Each section carries 24 PMTs. The sections can be vertically lowered into the antineutrino detector and secured.

stainless steel tank. There are eight such support structures for each antineutrino detector (see Fig. 6.26). Each structure holds a total of 24 PMTs. Together they form the circular PMT arrangement. The PMTs are mounted radially on the inner rim of the circular support structure. The PMT support structure holds 24 PMTs in 8 rows equally spaced around the circumference of the structure, or a total of 192 PMTs. A detailed model of the PMT arrangement on the support structure and of the PMTs mounts is shown in Fig. 6.27.

Each PMT is held in a mount that connects the PMT to the support structure. Several designs are currently under consideration. They are shown in Figure 6.28. The common features of these mounts are:

- the PMT is held in place with an adjustable collar wrapped around the equator of the glass bulb;
- the mount is attached to the sheet metal of the support structure.
- the PMT is facing radially inward, perpendicular to the wall of the detector tank

To allow the PMTs to be used in both the antineutrino detector and muon system the mounting points of the PMT mounts need to be able to connect to to both the detector support frame as well as the structure of the muon system. We also need to allow for variations in the PMT geometry as the muon system will consist of both new PMTs and recycled Macro PMTs.

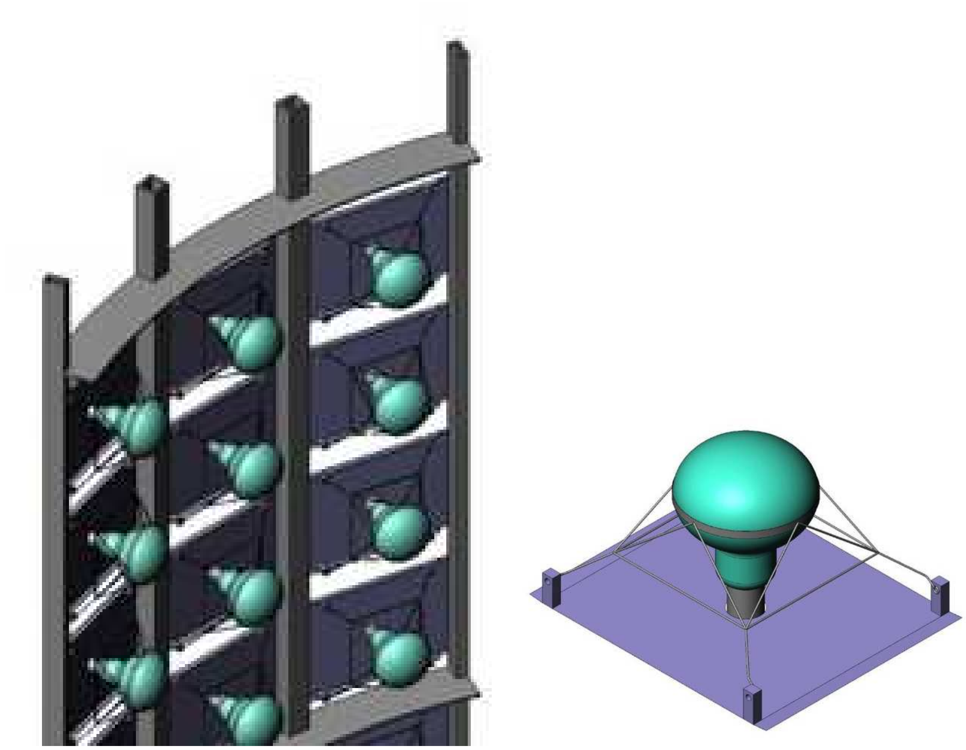

Fig. 6.27. *Left:* Detail of one section of the PMT support structure. *Right:* Individual PMT mount based on a wire frame construction similar to the one used in the MiniBOONE experiment. The PMTs are mounted perpendicular to the wall of the antineutrino detector.

6.4.3 PMT Magnetic Shielding

The effect of the Earth's magnetic field, whose typical strength is 0.3–0.5 Gauss, on the performance of a PMT is twofold:

- The trajectories of photoelectrons are affected such that the collection efficiency at the first dynode is a function of the orientation of the PMT relative to the magnetic field.
- The trajectories of secondary electrons in the dynode chain are affected such as to increase fluctuations in the PMT gain. This causes a lower "peak to valley" ratio for single photoelectrons, and increases the average transit time for the signal.

For example, an unshielded $8''$ Hamamatsu R5912 PMT showed $\pm 6\%$ gain variation as a function of orientation relative to the Earth's magnetic field in tests conducted by the Auger Collaboration [22–24]. An unshielded $10''$ Hamamatsu R7081 PMT showed a 30% lower peak-to-valley ratio and a 1-ns long transit time for single photoelectrons compared to a shielded PMT, in studies by the ANTARES Collaboration [25–27]. Note that the gain of a well-designed PMT such as the Hamamatsu R5912 is largely unaffected by magnetic fields larger than $\sim$1/3 of the Earth's field.

These effects are not large, so that many experiments, including LSND [28], and MiniBooNE [29] and the Pierre Auger Project [30], operate large PMTs with no magnetic shielding (since the classic technique of shielding a PMT with a μ-metal cylinder is awkward for large PMTs in tanks of liquids). Other experiments,

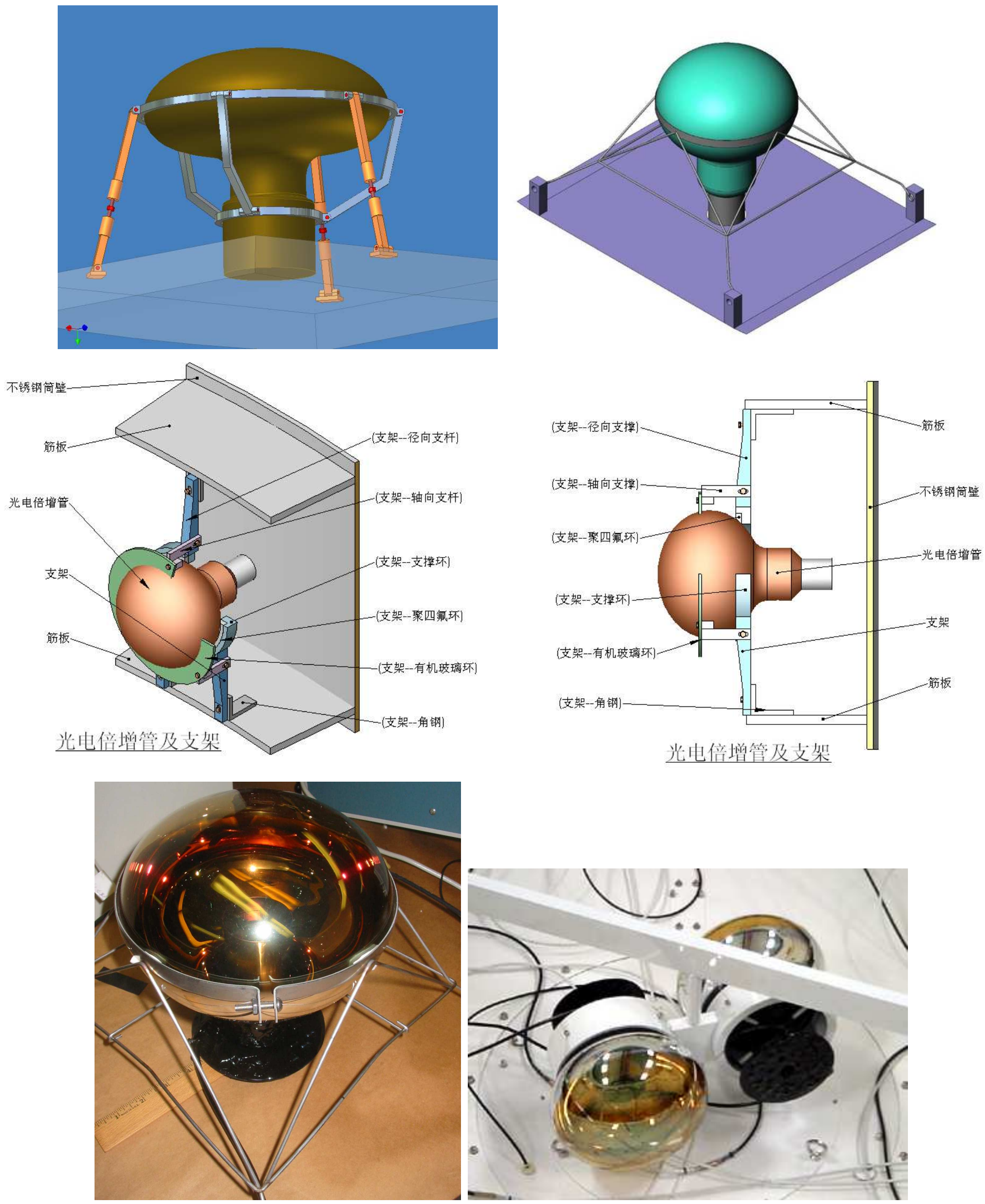

Fig. 6.28. *From top left:* A variety of conceptual design studies for mounting the PMTs onto the support structure. *Bottom row*: Pictures of the PMT mounts used in MiniBooNE.

including Super-Kamiokande [31], SNO [32], KamLAND [33] and BOREXINO [34], surround the entire detector with field-compensating coils to cancel some components of the Earth's field.

In the ongoing R&D and design studies we have considered a variant of the classic μ-metal shield that is well suited to large PMTs in liquid tanks, as pioneered by the DUMAND Collaboration [35] and also used in the NESTOR [36] and ANTARES [25–27] experiments. Namely, a quasi-spherical cage of $\sim$1-mm diameter wire, whose permeability is $\mu \sim 10^5$, encloses the PMT so as to block only $\sim$8% of the incident light (NESTOR), or $\sim$4% (ANTARES) as shown in Figure 6.29.

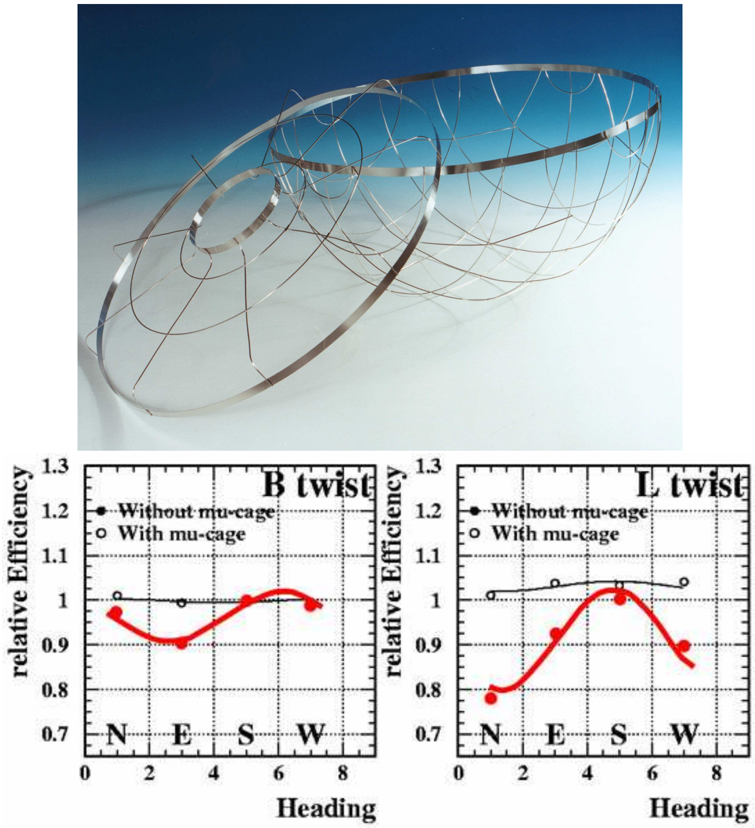

Fig. 6.29. *Top:* Quasi-spherical magnetic PMT cage shield. Image from [25]. *Bottom:* Variation of the PMT efficiency with and without mu-metal cage.

The ANTARES shield reduces the magnetic field strength on the PMT by a factor of ∼3 (and ∼8 for the NESTOR shield), with the resulting improvement in the single-photoelectron peak-to-valley ratio and transit time as shown in the figures at the top of the page. The variation of PMT gain with orientation is almost completely eliminated [25]. The suppression of the magnetic field by the wire-mesh shield is not fully effective at radii within about one mesh spacing of the mesh itself [37].

A simulation has been carried out by varying the collection efficiency as well as the SPE resolution of the phototubes according to previous measurements of the effect of the Earth's field (e.g. Auger). The results indicate that the impact of the Earth's field on the reconstructed energy resolution of the detector is negligible. The Daya Bay collaboration has reached the preliminary conclusion that it will not be necessary for the experiment to employ magnetic shields, and this element is not part of the baseline design and cost estimate. Additional simulations of the effect of magnetic shields on the PMT performance are underway.

6.4.4 PMT Testing and Characterization

Uniform performance, stable, reliable and lasting operation of the PMT system are essential to the successful execution of the experiment. While the two candidate PMTs, namely the Hamamatsu R5912 and the ET 9354KB have been studied for other experiments such as Auger, KamLAND, and IceCube the more stringent requirements of Daya Bay demand a comprehensive program of characterization, testing and validation conducted prior to installation and commissioning of the PMTs.

We will ask the selected manufacturer to provide certificates of acceptance for the PMTs. The certificates document measured results, compliant to our specifications, that typically include: cathode and anode luminous sensitivity, cathode blue sensitivity, anode dark current and dark counting rate, operating voltage for a gain of 10^7, charge response and transit time spread.

Testing and validation of the received PMTs will be conducted using a custom test-stand. Before testing the PMTs all PMT will be subject to physical inspection. This will be followed by a 4 week continuous burn-in period to stabilize the gain of the PMTs. During this period the new PMTs will be subjected to a 1kHz pulsed blue LED source with 500 p.e. equivalent pulses.

For the final testing and characterization of the PMTs a pulsed UV LED system will be used to stimulate a scintillator to generate a pulse of light. This scintillation light will be collected within optical fibers and transported to the PMT. This setup allows us to adjust the intensity and position (on the photocathode) of the light reaching the phototube. The purpose of this exercise is to gather a set of physical parameters for each PMT, such as gain vs. high-voltage, operating voltage at the nominal gain, relative quantum efficiency, dark rate, transition time spread, pre- and after-pulsing ratios, and linearity. The absolute gain of each photomultiplier as a function of the PMT HV will be measured using single photoelectron peak and the photostatistics methods and will be recorded in a database along with other characteristics.

In addition, tests of radio-purity will be made. A couple of randomly selected tubes from each batch will be radio-assayed non-destructively. If the K, Th, or U content exceeds the specified level of contaminations, additional randomly selected tubes from the same batch will be radio-assayed. If more PMTs exceed the specified contamination level, the whole batch will be rejected. The collected data will be used in simulation and analysis.

6.4.5 High-Voltage System

Due to the fact that we require the trigger threshold to be as low as 1/4 of a photoelectron level, the noise in the PMT system must be minimized. We have decided to use the low-cost CAEN SY1527LC high-voltage mainframe that has a proven record of low noise and excellent long-term reliability. Using the 48-channel A1932P modules with shared floating common each mainframe crate could accommodate up to a total of 384 independently programmable outputs. Voltage and currents will be controlled and monitored for each channel.

The SY1527LC are remotely controlled via the ethernet. We have experience with this type of power supply and will develop a LabView-based slow control and monitoring system for the antineutrino detector and muon Cherenkov system.

6.5 Monitoring and Instrumentation for the Antineutrino Detectors

This section outlines the proposed instrumentation for the antineutrino detector. The goal of this instrumentation is to:

- ensure the safety of the antineutrino detector and its acrylic vessels during transport, filling, and lifting
- evaluate the geometric identity of the antineutrino detectors
- preciselty measure the Gd-loaded liquid scintillator target mass during filling and monitor it during data taking
- monitor the environmental conditions of the antineutrino detectors

The requirements for the detector instrumentation and monitoring program are summarized in Table 6.14.

6.5.1 Survey of As-Built Detector Geometry

Purpose:

- To provide an as-built geometry of the steel tank, the acrylic vessels, and the position of the PMTs.

Item	Requirement & Justification
acrylic vessel geometry	- to determine fill volume prior to fill
fill level	- during filling and draining to avoid load on vessels
overflow tank volume	<1 l for target mass monitoring
fluid temperatures	to 0.1° C
cover gas monitoring	- integrity of dry N_2 supply
	- integrity of N_2 exhaust
	- O_2, H_2O, flow rate
acrylic vessel positions	- to determine change in γ-catcher thickness etc.

Table 6.14. Requirements on the instrumentation and monitoring of the antineutrino detector.

- To determine the volume of the as-built acrylic vessels prior to their fill.
- To be used as input to the detector simulations and to establish the geometric identity of the antineutrino detectors.

Instrumentation:

- laser-based optical survey device

We intend to precisely measure the dimensions of each acrylic tank and calculate the as-built volume from the data. Differences between tank volumes will impact the amount of scintillator required to fill each antineutrino detector. As discussed in Section 6.5.5 accurate knowledge of the filled target mass is obtained from the knowledge of the total mass filled into the detector and the liquid level monitoring in the overflow tanks. To fill the detector to a level within the allowable range in the overflow tanks it is necessary to determine the as-built volume of the target vessels. Furthermore differences in the geometry of the detectors also imply differences in the mass distribution. It must be recognized that sagging of the tank in air will impact the geometry. Loads to the acrylic walls and in particular to the top and bottom faces will be drastically different when the detectors are filled. Modelling calculations to estimate the sensitivity of the antineutrino detector to deflection induced geometry changes are in progress at Wisconsin. The results of this modelling will determine how much effort we must expend to keep track of deflection induced geometry changes.

6.5.2 Monitoring of Acrylic Vessel Positions

Purpose:

- To measure the concentric positioning of the nested vessels and to provide a monitor for possible lateral shifts of the acrylic vessels during transport, filling, and lifting.

Instrumentation:

- Viewport at top of antineutrino detector with camera looking vertically downward. Cross-hairs on viewport and on acrylic vessels to monitor relative shift of vessels with respect to each other and with respect to the steel tank.
- We may also employ designed calipers or other special tools for a mechanical inspection and measurement.

Ideally, we would like to track both translations and rotations if possible. Thus two such viewports are needed on top surface of outer stainless steel detector tank. Interpretation of the camera images will not be entirely straightforward. For example if the acrylic top surfaces are not perfectly normal to the camera line of site, then the relative position of cross hairs may change after tank filling even if there is no motion of any solids. Lighting may be provided by a ring of infrared LEDs around the camera. An interlock system and/or a lockout procedure on the PMT high voltage systems may be needed to protect PMTs. We consider the use of infrared cameras to provide an additional layer of safety for the PMTs.

6.5.3 Visual Monitoring

Purpose:

- To provide a visual monitor of the inside of the antineutrino detector and the behavior of the acrylic vessels during filling, transport, and lifting.
- To check visually the liquid levels during filling as they reach the critical acrylic boundaries between the oil and the γ-catcher and the γ-catcher and the inner target filled with Gd-loaded liquid scintillator.

Instrumentation:

- CCD camera at top looking into antineutrino detector (for general purpose inspection).
- CCD cameras on side of tank at height of interfaces between oil/γ-catcher and γ-catcher/target. These cameras can be installed inside the tank (radioactivity permitting) or outside looking horizontally into tank through windows (for monitoring liquid levels). This would require four windows and perhaps 2–4 removable CCD cameras (per tank) with infrared lighting.

It may be possible to use the cameras on top of the detector for multiple purposes. External viewports if needed can be realized by use of highly reliable and inexpensive CF flanges welded leak tight to the stainless tanks. Glass or quartz windows on CF can be sealed with copper or Viton gaskets. Several flange sizes are available and the choice will depend on the optics. With strategic positioning the support feet for the acrylic target vessels and the acrylic base structure may be observable from the lowest viewports or lowest internal cameras.

6.5.4 Motion Monitoring

Purpose:

- To provide a record of the motion of the antineutrino detector during its entire lifetime: From the assembly in the surface assembly building to the filling in the filling hall and the installation in the experimental halls. This will help us correlate any potential changes in the antineutrino detector with events during the transport, filling, or lifting.

Instrumentation:

- Accelerometers (on outside of antineutrino detector)
- Tilt sensors (on outside of antineutrino detector)

These devices must either be wireless or connected to a computer/DAQ moving with the detectors. The sensors can provide feedback to operators of the transporter and crane. They can be either removable or permanent and can be covered by the dry box if they are permanently attached to the outside of the detector.

6.5.5 Target Mass Monitoring During Filling and Operation

Purpose:

- To measure to an accuracy of $<0.1\%$ the mass of the Gd-loaded liquid scintillator target filled into the antineutrino detector and to monitor the mass inside the target volume during transport and data taking.

Instrumentation:

- Load cells on reference tanks (intermediate storage tanks used for filling detectors).
- Mass flow meters between reference tanks and antineutrino detector.
- Instrumentation for measuring the temperature and density of the liquid scintillator, Gd-loaded liquid scintillator, and mineral oil between reference tanks and the antineutrino detector.
- Volume flow meters between reference tanks and antineutrino detector.
- Liquid level sensors for Gd-liquids scintillator and undoped liquid scintillator in antineutrino detector overflow tanks.
- Liquid level sensor in antineutrino detector mineral oil region during filling.

MASS: Control of the delivered mass will be achieved with a combination of flow meters and load cells. Two competing methods of mass measurement are under consideration and described in Section 6.6. LEVEL during filling: Accurate knowledge of the liquid levels is crucial during the filling process. Potentially destructive load forces can be generated if the three tank levels are not precisely controlled. The instrumentation for the detector filling is designed under the assumption that liquid levels must be matched to ± 1 cm during filling but this number may change as engineering of the acrylic tanks progresses. The oil level during fill is the easiest and least expensive to monitor because direct insertion of a probe into the oil is acceptable. Monitoring of the GD-LS and the LS levels is likely to require the use of non-contact solutions such as sonar or radar based measurements. Internal CCD cameras or the viewports described above will be essential to calibrate and verify all three level sensors. LEVEL during data taking & transport: Temperature variations or tank distortions will cause fluid to enter and leave the overflow volumes. A 100 l overflow tank constrained to be less than 300 mm high will rise about 1 mm for every 2 l of added fluid. Thus we require a Teflon covered contact sensor accurate to 1 mm or better with a dynamic range of 300 mm DENSITY: The relative density of the three loaded fluids critically influences loading forces on the acrylic tanks and therefore their geometry. We will use Coriolis flow meters to accurately measure the fluid densities. However we must point out that it is not to sufficient to simply measure the as-delivered fluid densities. It will be necessary for the collaboration to specify the fluid densities ahead of time and use density measurements as one of several criteria for acceptance or rejection of the fluid deliveries.

6.5.6 Gas Supply Monitoring (dry N_2 and ambient)

Purpose:

- Maintain a continuous nitrogen cover gas to the detector and the calibration domes.
- Monitor the pressure, flow, and quality of the dry N_2 purge gas provided to the detectors
- Monitor the pressure, flow, and quality of the dry N_2 purge gas exiting the detectors and detect any leaks into the gas purge system.

- ○ Monitor the gas pressure above/in each overflow tank and calibration dome
- ○ Verify that tank purging is complete prior to filling of the antineutrino detector
- ○ Protect personnel and detect any leaks of flammable liquids from inside the antineutrino detector

Instrumentation:

- ○ Pressure monitors: supply line, above each fluid type, in calibration domes, and in detectors exit line.
- ○ Gas flow monitors: supply line, calibration & flow volumes, exit line.
- ○ O_2 sensors trace amounts: N_2 supply and exit lines
- ○ Humidity sensors on exit line: check for water leaks into dry-box or cable tubes.
- ○ O_2 sensors ambient gas: Connected to oxygen deficiency hazard alarm.
- ○ Flammable liquid sensor: Ambient gas. Connected to alarm.
- ○ Humidity sensor: ambient gas.
- ○ Differential pressure sensors between calibration and overflow volumes to protect against pressure surges and between the three detector fluids to protect against tank bulging.
- ○ Gas pressure in cover gas, in calibration boxes, and in overflow tanks.
- ○ Smoke/heat sensor.

A continuous flow of dry N_2 must be provided to every gas space in the antineutrino detector. Numerous strategies can be devised to accomplish this, but to protect the acrylic vessels all solutions must strictly restrict the possibility of differential pressure developing between the three antineutrino detector fluids. A failsafe design that is based on gas conductances and self equalization of pressure is preferred. Separated flow systems require some type of interlock system and are not desirable.

Regulation of the N_2 supply based on pressure and/or flow measurements will be required. Trace O_2 sensors are needed to monitor the quality of supply gas. Leaks into the purge system can be detected by trace O_2 sensors and water sensors in the exit gas. Flammable liquid sensors are desirable for the ambient gas but if LAB type scintillator is used the vapor pressure may be too low for typical sensors to detect. Differential pressure monitors will be required across the isolation gate valve between tank liquids and calibration dome to prevent pressure surge upon opening. If a gate valve is used some form of interlock will be required to protect against untimely closure when the calibration hardware is lowered into scintillator. Both the mineral oil and LAB scintillator are flammable. Smoke and heat sensors above and downwind from the detectors are needed for safety.

6.5.7 Temperature Monitoring

Purpose:

- ○ To monitor the temperature of the antineutrino detector and provide warning if the external temperature of the antineutrino detector exceeds the pre-defined specs of the detector environment.
- ○ To measure the temperature gradient (top vs bottom) of the buffer oil inside the detector as an input to convection calculations of the detector liquids.
  - – temperature at bottom of antineutrino detector (outside antineutrino detector and thermally isolated from the stainless steel tank)

- temperature at top of antineutrino detector (outside antineutrino detector and thermally isolated from the stainless steel tank)
- temperature of buffer oil inside antineutrino detector at top and bottom

The temperature sensors must either be compatible with ultra-pure water or they must be demountable.

6.5.8 Monitoring of LS Leaks

Purpose:

- To provide early warning to filling and transporting operators in case of a scintillator leak

Instrumentation:

- Resistive Wet Pads: under pumps and selected fittings during filling & transport

Resistive pads can provide invaluable early warning in case of a water leak. Tests will be required to see if this simple method works with LAB scintillator, or if a more sophisticated technology will be necessary.

6.5.9 In-Situ Monitoring of Attenuation Lengths

Purpose:

- To monitor in-situ and independent of the calibration sources the attenuation lengths and optical quality of the liquids in the antineutrino detector.

Instrumentation:

- laser-based attenuation length measurement

The method is not fully developed. A test apparatus using a broad spectrum light source, a reference arm, a chopper wheel, and a solid state light sensor has been demonstrated to work. The method is insensitive to fluctuations in light source intensity.

6.5.10 Gd-LS Liquid Sampling

Purpose:

- To provide the possibility to extract on a regular basis during data taking small (100 mL) samples of Gd-loaded liquid scintillator for analytic analysis and optical measurements without drawing down the water pool.

Instrumentation:

- Since the antineutrino detectors will operate under water there is no good idea yet for how to access the inner volumes of the detector and extract samples on a regular basis. A significant problem to be overcome is the height difference between the overflow tanks and the top of the water pool

6.6 Filling the Antineutrino Detectors and Measuring the Target Mass

The Daya Bay experiment requires the construction of eight multi-ton detector modules. Each module utilizes 20 ton of Gd-doped scintillator filled into a centrally located sub-tank. That sub tank forms the center of a system of three concentric nested tanks each filled with a different fluid. The detector modules are to be constructed as matched pairs so that one detector of each pair can be deployed at one of the near sites while the other one will be deployed at the far site. One of the requirements of the matching is that the amount (weight) of Gd doped scintillator fluid in a matched pair be equal to within $M_1/M_2 = 1 \pm 0.0005$ or better, where M_1 and M_2 denote the target mass of detectors 1 and 2. The module filling process requires that three concentric tanks be filled with different liquids simultaneously and that during the filling process the column levels of the three tanks match to within a well-specified tolerance of ± 1 cm or so. The tolerable level difference will be determined from the ongoing engineering calculations. Only the central tank has the strict mass balance requirement stated above. It is desirable to match the mass and volume of the γ-catchers similarly but the requirements are less stringent.

Two of the fluids to be filled are flammable and sensitive to air exposure and temperature excursions. During the filling process the detector and the fluids cannot be exposed to mine air. The entire system is to be kept in a nitrogen atmosphere at all times to avoid radon exposure. Ideally, the detectors will only be filled once. Draining the system and starting from scratch in the case of a filling error is not acceptable. We only envision draining the detectors (or pumping them out) if it a major repair of the detectors became necessary or at the end of the experiment.

At the required level of accuracy the experimental risk is significant if a single methodology is employed. A number of redundant techniques are being studied to ensure the precise mass measurement of the Gd-LS target:

1. Weighing of the Gd-loaded liquid scintillator
2. Mass flow meters
3. Volume flow meters + temperature + density measurements
4. Geometry surveys of the target volume + density measurement of the Gd-loaded liquid scintillator

Specifically, commercial Coriolis mass flow meters are stated to have the required accuracy but in cases of interrupted flow, power outages or trapped gas, their performance is questionable. Because they integrate a rate over time, they must operate flawlessly during the entire filling process which is expected to take on the order of one to several days. We therefore require a system that is robust against power interruptions and gas bubbles, both microscopic and macroscopic.

Our goal is to develop a methodology that

1. allows the precise, simultaneous filling of pairs of detectors
2. provides a way to measure or limit the variation of the target mass between pairs of detectors
3. is redundant and repeatable over a time period of months or years

The two methods described here, the I) balanced tank method, and the II) single reference tank method employ the instrumentation listed above and meet the requirements of such a fill system.

6.6.1 The Filling Process

To understand the complexity of the filling process we first consider some hydrostatic issues of the nested fluid design. The acrylic tanks have thin walls and therefore will flex considerably in response to unequal hydrostatic pressure between the inside and outside of each tank. Figure 6.30 illustrates the (imaginary) situation where all three tanks are filled so that the overflow levels are equal and the inner tanks are in their neutral (undistorted) positions. This is a stable condition only for all three liquids having the same density. If mineral oil is more dense than scintillator with a specific gravity 1% greater than scintillator, then the outer acrylic vessel would float and must be held to the bottom of the stainless tank against a buoyant force of ~ 400 kg. At the same time the entire outer acrylic vessel would experience a compression which varies with height. The bottom surface sees the largest force, about 450 kg for every 1% specific gravity

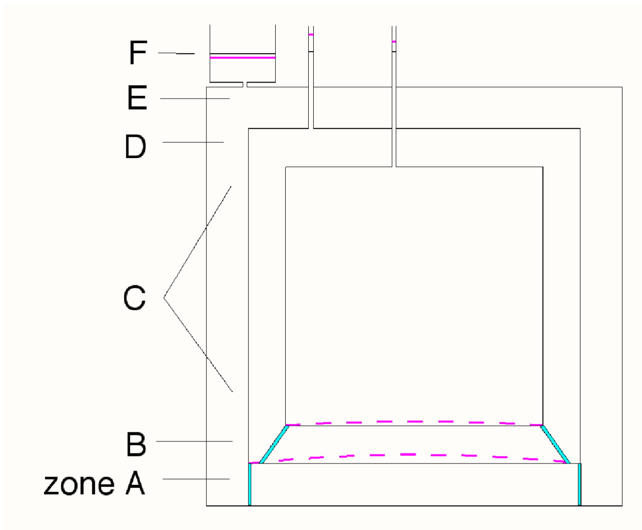

Fig. 6.30. Schematic of the different liquid zones in an antineutrino detector.

difference. The top sees about 50 kg. The cylindrical wall will also deform but this effect is undoubtedly smaller than the deflection of the flat bottom surface. The outer acrylic deflection reduces its volume and its overflow level rises. In response to the outer acrylic's higher overflow level, the inner acrylic experiences additional compressive force and its overflow level also rises. The final resting levels for the three overflow volumes in this imaginary exercise depend sensitively on the strength of the acrylic vessels, on the particular specific gravity of the fluids and on the diameter of the overflow columns. A small correction is required to account for the acrylic density which will differ from the liquid densities. In the case that mineral oil is less dense than scintillator the argument is the same but the scintillator overflow level drops.

In practice we expect to fill all three vessels simultaneously. At first only mineral oil is filled (zone A in Figure 6.30) until its level reaches the bottom of the outer acrylic vessel. At that point filling of the outer acrylic begins (zone B). Liquid delivery rates must be matched to keep the two column heights close to each other. If the two column heights are not equal the force generated on the bottom surface of the outer acrylic vessel is 106 kg for every cm of column mismatch where we assume liquid densities of 0.85 gm/cc and a face diameter of 4 m. The same consideration requires that the liquid level of the inner acrylic be close to the outer acrylic level as filling enters zone C. The force on the inner acrylic bottom face is 64 kg for every cm of column mis-match assuming an inner face diameter of 3.1 m. Liquid flow profiles are shown in Fig. 6.31.

As filling proceeds past the top of the inner acrylic (zone D) the situation becomes more complicated. In Fig. 6.30 we assume that the overflow column diameter of the inner acrylic in the region of penetration through the other two vessels (zones D and E) is relatively small, about 5 cm. One might expect that at the lower boundary of zone D, flow to the inner acrylic should be dramatically reduced but should not be zero. In fact, if at this point all filling were temporarily stopped and an amount was added to the inner vessel sufficient to raise the overflow column 10 cm there would only be a temporary rise in the column height; the increased hydrostatic pressure would expand the inner vessel and the level would return to almost the same as before the fluid addition. The stiffness of the inner acrylic vessel determines how much additional liquid would be required to raise the inner column height one cm. In effect, this geometry is equivalent to a huge hydraulic cylinder.

We can assume that in zone D no additional liquid is added to the inner tank. As the filling in zone D proceeds, the inner acrylic column level will rise so that the pressure caused by the deflection of the inner

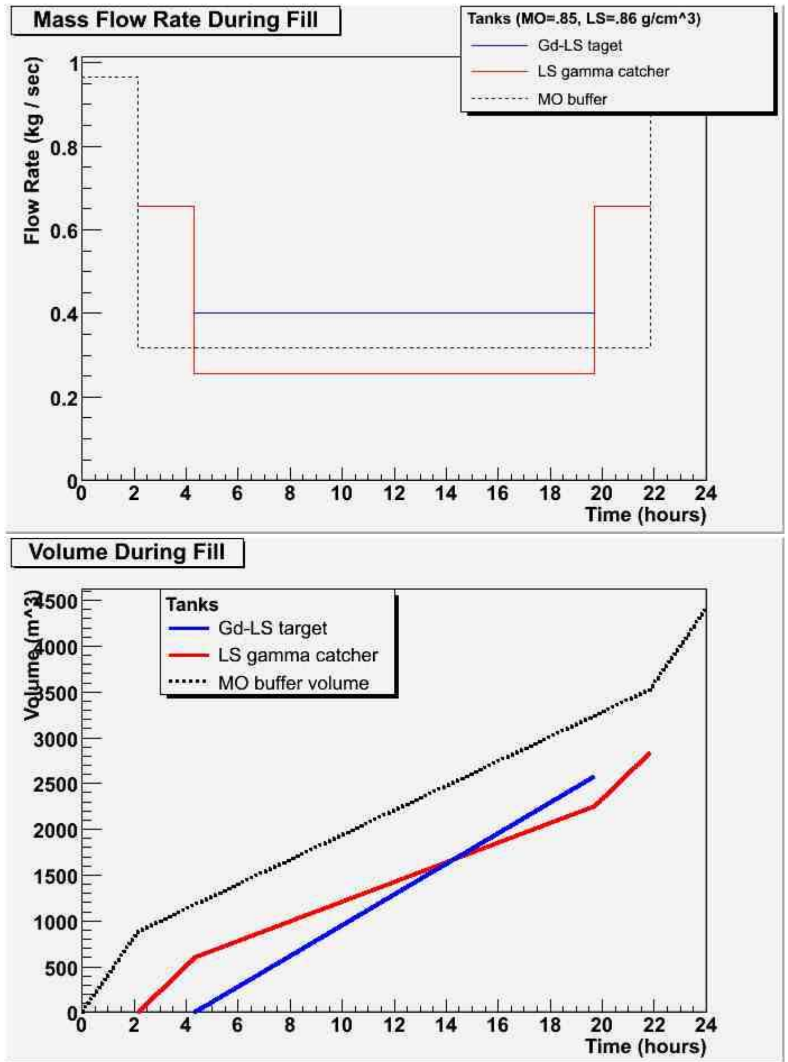

Fig. 6.31. *Top:* Mass flow rate of the three different detector liquids for a detector fill with a total duration of 24 hrs. The discontinuities indicate the points where the liquids reach acrylic vessel boundaries. *Bottom:* Cumulative liquids volumes during the detector fill. Again, we assume a total fill duration of 24 hrs.

tank equals the difference between the inner and outer scintillator columns. If the inner tank is not very stiff then the two scintillator levels will be similar even though no liquid was added to the inner tank. If the acrylic overflow columns have small diameter only small tank deflections are needed to adjust the column height to the equilibrium levels. The smaller the diameter of the column the stiffer the acrylic vessel appears to be. A similar effect on the outer acrylic column will be seen as the filling enters zone E. An intuitive explanation can be found by imagining two water filled balloons. One is connected to a 3 cm diameter glass tube and the other to a very tall capillary tube. The static force required to squeeze out 100 cc of liquid is different for the two cases.

Once the detector is filled, temperature drifts will cause changes in the fluid densities. Away from thermal equilibrium the outer layer of mineral oil will respond first because of its contact with outside conditions and the metal vessel it is in. The mineral oil thermal expansion is expected to be larger than scintillator expansion. We estimate 17 l expansion per 1° C temperature rise for scintillator.

As for the filling, we conclude:

- The two acrylic vessels should be thought of as highly elastic structures.
- To fill the three liquid volumes to equal overflow heights with a pre-specified mass we need to know more than the geometry of the three tanks. We also need to know the precise density of the three fluids and we need the stiffness of the acrylic vessels. Assuming the outer steel tank has no load deflection introduces only a small error.
- The stiffness of the acrylic vessels and their ability to deform (ΔV/V at failure) is a critical design issue. In turn, the requirements on these two parameters depends critically on difference in the three liquid densities.
- It could be possible to fill the acrylic tanks to the point that they fail by expansion even though the column heights are not excessively different. This threat is most likely if the mineral oil is less dense than scintillator. We should consider monitoring the curvature of the acrylic bottom surfaces during filling.
- Unstiffened acrylic tank bottoms have a disadvantage that during filling they could be flexed beyond their elastic limit. But they have the great advantage that, because of their ability to flex, the active volume of scintillator is stable against changes in mineral oil density. However if the ratio of scintillator density to mineral oil density differs from 1 by more than about 2% the forces on the bottom face might be excessive and ribbing or adding a pre-formed dome shape could be required. If mineral oil and/or scintillator of specified density could be manufactured this would greatly simplify the design of the acrylic tanks.
- To first order, the change in active scintillator mass as a function of detector temperature is inversely related to scintillator overflow column diameter. On the other hand a large mineral oil overflow column is desirable.
- Liquid level monitoring to an uncertainty of ± 1 cm is required for all three fluids during the filling process. Active regulation of the filling rates based on measured fluid levels should be employed. Level differences of only a few cm could damage the acrylic vessels. Interlocks and visual access to fluid levels are recommended.

6.6.2 Measuring the Target Mass

We are considering two competing methods to control the target mass. The balanced tank method relies on the repeatability of the filled mass ratio of two interconnected tanks. The other method of using a single reference tank relies on accurate measurement of the weight of a single reference tank with class C6 load cells.

6.6.3 Single Reference Tank Method

Although the balanced tank method described in Section 6.6.4 is capable of matching two detector target masses to a precision higher than required by the experiment it has the disadvantage of high complexity and cost. As a result we describe first the use of a single reference tank for filling detectors. A single 10 ton tank would be mounted on a platform and instrumented with load cells. In this case primary emphasis would be placed on the accuracy of the load cells so that cells of the best commercial accuracy grade would be used. For example accuracy class C6 with a stated accuracy of 0.008% is commercially available in the required load range. This corresponds to an accuracy of 2 L.

Two detectors would be filled at the same time. The reference tank would be filled four times and emptied into alternating detectors. In this way any difference in the properties of the first and last scintillator drawn from the underground master tank would be averaged across the detector pair.

The mass of delivered fluid would be determined by the difference between load cell readings. Thus it is not necessary to fully empty the reference tank to know the delivered mass. This flexibility would allow us to terminate or extend fluid delivery to accommodate variations in acrylic tank volume due to construction variation. For example a 3 mm deviation in the inner acrylic tank diameter from its nominal 3100 mm corresponds to a relative volume error of 2×10^{-3} or 45 L.

For redundancy and for precise measurement of the fluid densities we will include Coriolis flow meters on the delivery lines. These meters will also permit accurate regulation and monitoring of the filling rate.

Short term drift of load cells. Short term zero drift can be a significant source of weighing error. Generally, the problem is minimized by reducing the time been zeroing the scale and the measurement. In our case filling the reference tank may take as much as a half day. The time between zeroing and measurement can be reduced to about 10 minutes by use of hydraulic bottle jacks as shown in Fig. 6.32.

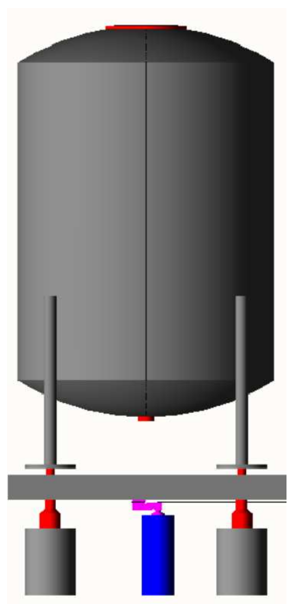

Fig. 6.32. Model of a single reference tank on a platform with load cells.

One issue of concern is the long-term stability of load cells. It is highly desirable for the experiment that the mass of all eight detectors be as close to each other as possible. The time between filling the first and last detector pairs could be as long as two years. To protect against drift of the target pair mass fill over this length of time it will be necessary to periodically calibrate the load cells. Commercial certified NIST traceable calibration services are available for this purpose.

A single 10 ton tank would be mounted on a platform and instrumented with load cells. In this case primary emphasis would be placed on the accuracy of the load cells so that cells of the best commercial accuracy grade would be used. For example accuracy class C6 with a stated accuracy of 0.008% is commercially available in the required load range. This corresponds to an accuracy of 2 L.

Two detectors would be filled at the same time. The reference tank would be filled four times and emptied into alternating detectors. In this way any difference in the properties of the first and last scintillator drawn from the underground master tank would be averaged across the detector pair.

The mass of delivered fluid would be determined by the difference between load cell readings. Thus it is not necessary to fully empty the reference tank to know the delivered mass. This flexibility would allow us to terminate or extend fluid delivery to accommodate variations in acrylic tank volume due to construction variation. For example a 3 mm deviation in the inner acrylic tank diameter from its nominal 3100 mm corresponds to a relative volume error of 2×10^{-3} or 45 L.

For redundancy and for precise measurement of the fluid densities we will include Coriolis flow meters on the delivery lines. These meters will also permit accurate regulation and monitoring of the filling rate.

Short term drift of load cells. Short term zero drift can be a significant source of weighing error. Generally, the problem is minimized by reducing the time been zeroing the scale and the measurement. In our case filling the reference tank may take as much as a half day. The time between zeroing and measurement can be reduced to about 10 minutes by use of hydraulic bottle jacks as shown in Fig. 6.32.

One issue of concern is the long-term stability of load cells. It is highly desirable for the experiment that the mass of all eight detectors be as close to each other as possible. The time between filling the first and last detector pairs could be as long as two years. To protect against drift of the target pair mass fill over this length of time it will be necessary to periodically calibrate the load cells. Commercial certified NIST traceable calibration services are available for this purpose.

6.6.4 Balanced Tank Method

Figure 6.33 shows a scheme that utilizes a balanced two-tank filling system in conjunction with load cells and Coriolis flow meters. In this design the flow meters and scales provide redundant measurement of total mass delivered and the balanced tanks ensure near equality of the filling.

The balanced tanks are connected with liquid and vapor phase equalization lines to eliminate differences in hydrostatic pressure. The balanced tank volumes should be similar but need not be identical. The procedure relies on the cancellation of the balanced tank volume difference by filling both detectors with both tanks.

The balanced volumes are filled to 5 ton each giving a total of 10 ton as measured by the sum of four strain gage scales. Commercially available load cells in this range have a stated repeatability of 0.015% (1.5×10^{-4}). Higher accuracy is available but as will be shown is unnecessary. After filling the balanced tanks, the equalization valves (one each for liquid and gas phases) between the tanks remain open until equilibrium is reached. Let us suppose that the balanced tank volumes differ by 2% after closing the equalization valves

Figure 6.33 shows a scheme that utilizes a balanced two-tank filling system in conjunction with load cells and Coriolis flow meters. In this design the flow meters and scales provide redundant measurement of total mass delivered and the balanced tanks ensure near equality of the filling.

The balanced tanks are connected with liquid and vapor phase equalization lines to eliminate differences in hydrostatic pressure. The balanced tank volumes should be similar but need not be identical. The procedure relies on the cancellation of the balanced tank volume difference by filling both detectors with both tanks.

The balanced volumes are filled to 5 ton each giving a total of 10 ton as measured by the sum of four strain gage scales. Commercially available load cells in this range have a stated repeatability of 0.015% (1.5×10^{-4}). Higher accuracy is available but as will be shown is unnecessary. After filling the balanced tanks, the equalization valves (one each for liquid and gas phases) between the tanks remain open until equilibrium is reached. Let us suppose that the balanced tank volumes differ by 2% after closing the equalization valves

$$M_b = 1.02 \times M_a \tag{30}$$

The balanced volumes are filled again to the same 10 ton weight as determined by the strain gage scales and equalized. This time their contents are pumped into the opposite tank (a into detector 2 and b

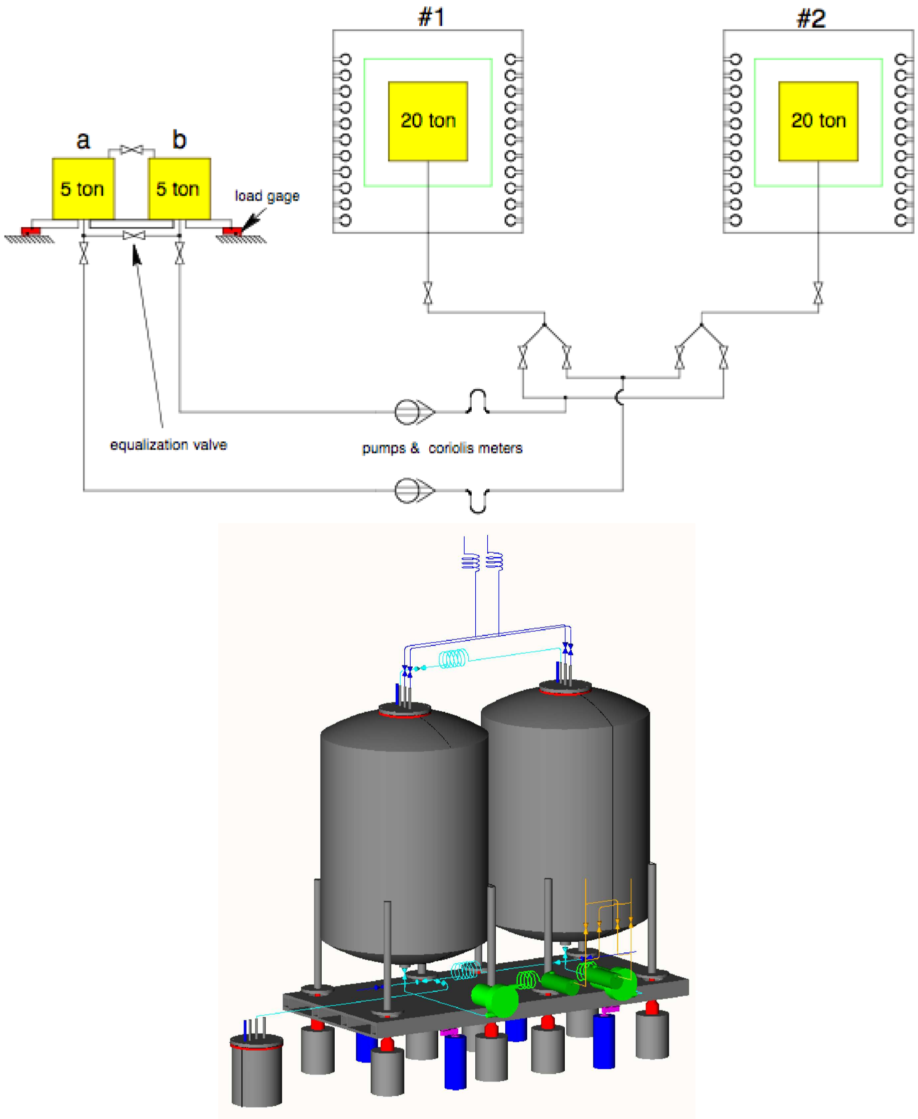

Fig. 6.33. Top: Schematic of the pipes and connections in the balanced tank assembly. Bottom: Model of the balanced tank assembly.

into detector 1). After four batches the detectors are filled to 20 ton each. Note that the Coriolis meters are positioned so that their readings are distributed onto both detectors. The mass ratio between detectors 1 and 2 can then be calculated as

$$\frac{M1}{M2} = \frac{2M_a(1 + 0.9994 \times 1.02)}{2M_a(0.9994 + 1.02)} = 1 - 6 \times 10^{-6} \tag{31}$$

where we have assumed pessimistically that the 0.015% non-repeatability of four strain scales add linearly (0.06%) and that the gages all read low when tank a fills detector 2 but read normally when a fills detector 1. If the 3000 division resolution of the load cells is included, the repeatability could degrade to about 0.15%. In that case one obtains

$$\frac{M_1}{M_2} = 1 \pm 1.5 \times 10^{-5} \tag{32}$$

The most likely error in this scheme, apart from someone forgetting to close an equalization valve or not reversing the fill assignment, is the possibility of over or under filling of the balanced tanks. If an operator overfills, say, the last batch by 2% and the balanced tanks differ by 2% the imbalance introduced into matched detector masses is 4×10^{-4}. But this error is *known* if records are kept and may be applied as a correction. To avoid this kind of problem a provision for trimming the balanced tank contents could be devised.

Other sources of error include unequal plumbing lengths for the different circuits but this is easily dealt with by careful design work. A relative error of 1.5×10^{-5} corresponds to a volume difference of 0.35 L. This corresponds to about a meter of 2 cm diameter tubing. To achieve this level of filling accuracy will require meticulous control of the plumbing system and represents an optimistic estimate of achievable filling accuracy.

The balanced tank procedure does not ensure that the total doped scintillator mass of one matched pair equals the mass of subsequent pairs. It is highly desirable for the experiment that the mass of all eight detectors be as close to each other as possible. The time between filling the first and last detector pairs could be as long as two years. To protect against drift of the target pair mass fill over this length of time it will be necessary to periodically calibrate the load cells. Commercial certified NIST traceable calibration services are available for this purpose.

6.6.5 Cost Considerations

The design of the reference tank or balanced tanks will follow the specifications and design requirements of the liquid scintillator storage tanks. These are described elsewhere in this document. One possibility is to line the balanced tanks with fluoropolymer coating. Reliable 1 mm thick coatings are available. See for example Fisher-Moore at http://www.fluoropolymer.com or http://www.edlon.com. Some cost could be saved by constructing the tanks from steel instead of stainless. Even more savings are possible if the use of glass lined tanks is acceptable. Figure 6.33 shows two 4000 L tanks on a platform with four load cells. Mild steel, glass-lined tanks are usually 50% of the cost of stainless steel tanks.

6.7 Antineutrino Detector Prototype

Valuable data on the performance of the antineutrino detector has been obtained from a scaled down prototype at the Institute of High Energy Physics, Beijing, China. The goal of this R&D work is multifold: 1) to verify the detector design principles such as reflectors at the top and the bottom, uniformity of the response in a cylinder, energy and position resolution of the detector, etc.; 2) to study the structure of the antineutrino detector; 3) to investigate the long term stability of the liquid scintillator; 4) to practice detector calibration; 5) to provide necessary information for the Monte Carlo simulation.

6.7.1 Prototype Detector Design

As shown in Fig. 6.34, the prototype consists of two cylinders: the inner cylinder is a transparent acrylic vessel 0.9 m in diameter and 1 m in height with 1 cm wall thickness. The outer cylinder is 2 m in diameter

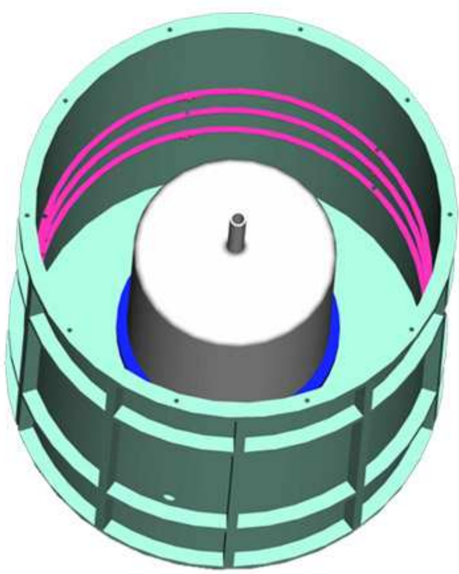

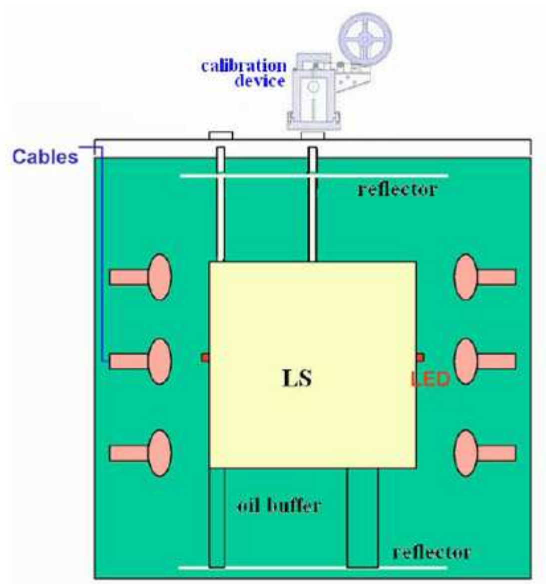

Fig. 6.34. Sketch of the antineutrino detector prototype (Left) Top view, (Right) Side view.

and 2 m in height made of stainless steel. Currently, the acrylic vessel is filled with 0.54 ton of normal liquid scintillator, while Gd-loaded liquid scintillator is planned for the near future. The liquid scintillator consists of 30% mesitylene, 70% mineral oil with 5 g/l PPO and 10 mg/l bis-MSB. The space between the inner and outer vessel is filled with 4.8 ton of mineral oil. A total of 45 8” EMI9350 and D642 PMTs, arranged in three rings and mounted in a circular supporting structure, are immersed in the mineral oil. The attenuation length of the LS is measured to be 10 m and that of the mineral oil is 13 m.

An optical reflector of Al film is placed at the top and bottom of the cylinder to increase the effective coverage area from 10% to 14%. The scintillator light yield is about 10000 photons/MeV, and the expected detector energy response is about 200 p.e./MeV.

The prototype is placed inside a cosmic ray shield with dimensions of 3 m$\times$3 m$\times$3 m. It fully covers five sides (except the bottom). The top is covered by 20 plastic scintillator counters (from the BES Time-of-Flight system), each 15 cm wide $\times$ 3 m long. The four side walls are covered by 36 1.2 m$\times$1.2 m square scintillation counters from the L3C experiment. Figure 6.35 shows a photograph of the prototype test setup, before and after the muon counters were mounted.

Fig. 6.35. The antineutrino detector: before (left) and after (right) the muon detectors were mounted.

The readout electronics were designed as prototypes for the antineutrino detector, according to the requirements discussed in Section 9.1. The trigger system, DAQ system and online software are all assembled as prototypes for the experiment (see Chapter 9).

6.7.2 Prototype Detector Test Results

Several radioactive sources including ^{133}Ba (0.356 MeV), ^{137}Cs (0.662 MeV), ^{60}Co (1.17+1.33 MeV) and ^{22}Na (1.022+1.275 MeV) are placed at different locations through a central calibration tube inside the liquid scintillator to study the energy response of the prototype. The gain of all PMTs are calibrated by using LED light sources, and the trigger threshold is set at 30 p.e., corresponding to about 110 keV.

Figure 6.36 shows the energy spectrum after summing up all PMT response for the ^{137}Cs and ^{60}Co sources located at the center of the detector. A total of about 160 p.e. for ^{137}Cs is observed, corresponding to an energy response of 240 p.e./MeV, higher than naive expectations. The energy resolution can be obtained from a fit to the spectra, resulting in a value of about 10%. A detailed Monte Carlo simulation is performed to compare the experimental results with expectations, as shown in Fig. 6.36. Very good agreement is achieved, showing that the detector behavior is well understood.

All of the sources were inserted into the center of the detector; the energy response is shown in Fig. 6.37 (left). Good linearity is observed, although at low energies non-linear effects are observed which are likely due to light quenching and Cherenkov light emission. The energy resolution at different energies is also shown in Fig. 6.37 (right), following a simple expression of $\sim 9\%/\sqrt{E}$, in good agreement with Monte Carlo simulation as shown in Fig. 6.36.

The energy response as a function of vertical depth along the z-axis is shown in Fig. 6.38. Very good uniformity (better than 10%) over the entire volume of the liquid scintillator shows that the transparency of the liquid is good, and the light reflector at the top and the bottom of the cylinder works well as expected. The fact that the data and Monte Carlo expectation are in good agreement, as shown in Fig. 6.38, demonstrates that the prototype, including its light yield, light transport, liquid scintillator, PMT response, and the readout electronics is largely understood.

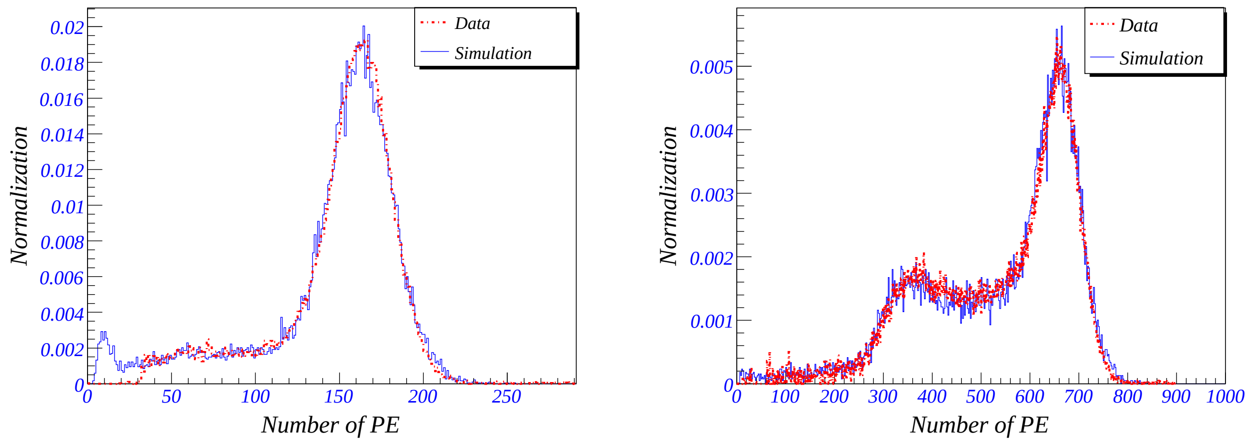

Fig. 6.36. Energy response of the prototype to ^{137}Cs (left) and ^{60}Co (right) sources at the center of the detector with a comparison to Monte Carlo simulation.

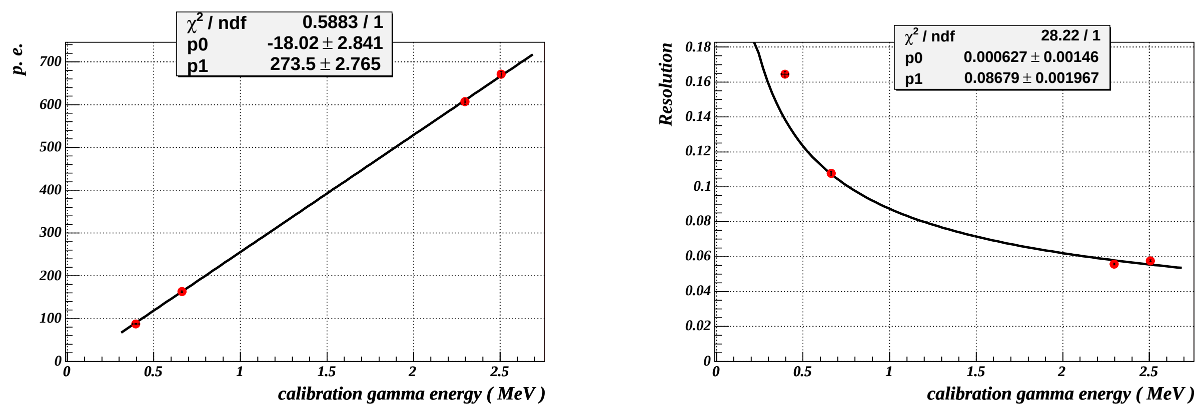

Fig. 6.37. Linearity of energy response of the prototype to various sources at the center of the detector (left), and the energy resolution (right).

6.8 Risk Assessment

The design of the antineutrino detector is based on liquid scintillator technology and photomultipliers. This technology has been used in similar form in previous reactor antineutrino experiments such as KamLAND, Chooz, and others. New in this experiment is the concept of a 3-zone design with nested acrylic vessels that contain the γ-catcher and the target mass. Also, the long-term stability of the Gd-loaded liquids scintillator is of concern. To achieve the required statistical precision we require the experiment to operate for at least 5 years. To facilitate the construction of eight identical detector modules and to allow for the possibility of swapping the detectors will be transported to the experimental halls after they have been assembled and transported. The detector systems and design issues that pose the highest risk are:

- **Acrylic Vessels:** The construction of eight nested acrylic vessels to contain the detector fluids with penetrations for calibration sources and other instrumentation is a non-trivial task. The acrylic vessels must meet stringent geometric and cleanliness specifications and be leak tight during detector filling and the entire duration of the experiment. *The construction of these vessels poses a schedule, cost, and physics risk to the experiment.*

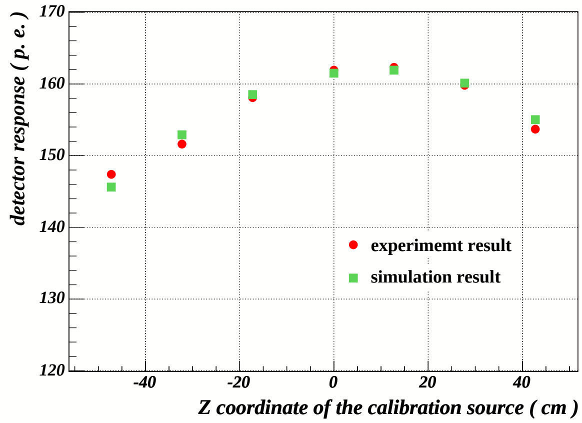

Fig. 6.38. Energy response of the prototype to a ^{137}Cs source as a function of z position, and a Monte Carlo simulation.

- **Liquid Scintillator:** The experiment will use a Gd-loaded and non-loaded liquids scintillator. Both must have good optical properties for the duration of the experiment. R&D is underway to define the recipe for the Gd-loaded scintillator and to develop a production process that allows the production of 200 ton of Gd-loaded liquids scintillator. The long-term stability and compatibility with materials in the antineutrino detector is of particular concern. *The production of the liquids scintillators is mostly a schedule and physics risk to the experiment.*

- **Transportation and Lifting:** A novel concept of this experiment is the transport of the fully-assembled and filled detectors over distances of up to 2 km to the experimental halls. It is critical not to damage or alter the detector during this process. While engineering studies have established the feasibility of this approach it is an unproven concept. Much of the ongoing R&D is dedicated towards understanding the detector response during transport and developing instrumentation to monitor the detector during the movement. *We consider the transport and lifting mainly a physics risk.*

- **PMT, Bases and Cables:** The risks involved in the delivery schedule are minimal. The main risk is the delay in availability of funding. The production work will not start without the funding. In addition there is a minor risk due to the fact that 50% of the initial production effort coincides with holidays in the US. This could reduce the initial delivery to about 250. Every effort will be made to start the fabrication as early as possible in FY08 to avoid these delays. Additional risks involve failure of a certain percentage of the PMT/base assemblies due to improper sealing or breakage of PMT bulbs. Based on past experience we expect these to be at a level of less than 0.2%. Please note that the PMT failures, while rare, will be detected before the bases are glued in permanently. This detection will be done in two distinct stages:

    1. During the initial physical inspection stage after the delivery of the PMTs
    2. During the PMT burn-in process. During this period each PMT/base will be tested with LED pulsers for a duration of 2–4 weeks.

Our proposed R&D in 2007 will address these critical issues and focus on mitigating the risks associated with the above described detector elements.

6.9 R&D Plan

6.9.1 PMT System

The photomultiplier tube is one of the critical elements of the detector system. Therefore it is important to understand its performance in the antineutrino detector as well as the muon Cherenkov system to the required systematic precision of the experiment. To improve our knowledge of these PMTs, we have implemented an extensive R&D program develop or measure the following:

- Study the characteristics of the PMT that are the most important to Daya Bay (i.e., Single photoelectron response of the PMTs - peak to valley ratio, absolute gain, dark current/pulse rate vs. high voltage, linearity vs. pulse height, stability, absolute quantum efficiency, variation of quantum efficiency vs. position, effect of magnetic field on SPE and gain.
- Measure the radioactivity of materials used in the PMT (radioassay for the candidate PMTs).
- Develop and optimize PMT bases: optimize linearity in the required dynamic range of the experiment. reduce internal ringing due to dynode capacitance and minimize external reflections due to the base.
- Study the effect of prolonged exposure of PMT glass to the highly purified water and mineral oil under pressure.
- Develop a reliable, low-radioactivity, water-proof base to be used in the water Cherenkov detector.
- Develop several automated large-scale PMT test setup (about 50 PMTs at time) for onsite PMT testing and characterization based on pulsed UV LEDs.
- Develop a signal-HV decoupler system.
- Characterize coaxial cables for underwater/oil operations, signal attenuation and low-noise operation.
- Develop and optimize a mu-metal shield for the PMTs.
- Develop support structures for the PMTs to allow easy installation and alignment of the PMTs in the antineutrino detector and muon systems. While we do not foresee prototyping a complete PMT support structure, we plan to build individual PMT mounts and test them with selected PMTs.
- Develop and test a waterproof cable feedthrough or suitable cable patch panel for all PMT cables coming out of the antineutrino detector.
- Develop QA procedures for final onsite testing and characterization of the PMTs.

Some of these tasks are currently underway and preliminary results will be available in the near future.

6.9.2 Acrylic Vessels

The antineutrino detector uses a pair of nested acrylic vessels to contain the target mass and provide high-efficiency for the detection of antineutrinos. The design, fabrication, and assembly of the nested acrylic vessels is a unique technical challenge. It requires precision and tight tolerances as well the flexibility to accommodate the dynamics of a moving detector. The collaboration plans to prototype the critical elements of the vessels and test them for structural strength, integrity, and leak tightness. This R&D program will be performed jointly between the US, China, and Taiwan. The University of Wisconsin and the Physical Sciences Laboratory plans to design the critical and high-risk elements shown below. In parallel, collaborators from National Taiwan University will work closely with Nakano Ltd. in Taiwan to prototype these parts, seek their engineering input, and test the manufacturing process of these items.

- Fabricate and test a full-size, bolted acrylic flange with O-ring seal for the connection of calibration ports.
- Fabricate and test a full-size acrylic penetration of a calibration pipe through the top of a vessel with a suitable (double?) O-ring or U-seal.
- Design, prototype, and test alternative seals such as U-seals, silicone seals, etc.
- Develop and test of a flexible coupling between the acrylic tanks and the steel tank such as a composite coupling using corrugated Teflon tubing.
- Design and construct a full-size prototype overflow tank with ports for liquid monitoring instrumentation.
- Machine and test a prototype flange for a removable lid to the acrylic vessels.
- Test the machining capabilities for a conical top/bottom to the acrylic vessel.
- Test the structural strength and properties of acrylic ribs, feet, or vessel support structure.
- Fabricate a prototype reflector using a sandwiched construction of highly reflective film between two acrylic plates. The adhesive to bond this structure and risk of possible air gaps needs to be studied.
- Perform extensive materials compatibility tests of acrylic with Gd-loaded liquid scintillator and undoped liquid scintillator studying both the optical as well as the structural properties.
- Characterize the optical properties of possible acrylic supplies through a series of systematic and well-characterized transmission measurements.

6.9.3 Instrumentation&Monitoring

Measurement of the target mass and monitoring of the state of the antineutrino detector during assembly, filling, and operation is key to understanding the systematics of the experiment. We plan to test individual units of all key instrumentation of the antineutrino detector prior to their installation in the detector. Key instrumentation tests will include the following:

- Accuracy and long-term stability of load cells and flowmeters for target mass measurements.
- Accuracy, reliability, and materials compatibility of liquid level sensors in overflow tanks.
- Test laser surveying method for determining the as-built geometry of the acrylic vessel.
- Test leak tightness of windows in tank against oil for visual monitoring.
- Characterization of accelerometers and motion monitor for detector transport and lifting.

6.9.4 Assembly&Integration

The antineutrino detector will consist of a pair of nested acrylic vessels inside a steel tank surrounded by a structure of photomultipliers. The nested geometry and multiple zones of the detector pose unique challenges to the assembly and integration of all subsystems. During the R&D phase in 2007 we will develop a procedure for the assembly of the detector paying particular attention to the mitigation of assembly risks and the reduction of labor intensive steps which could pose risks for human errors and schedule. A small-scale, simplified mockup model of the detector may be built to develop and practice the assembly sequence of the Daya Bay antineutrino detector and better understand the assembly sequence.

6.10 Manufacturing Plan

The antineutrino detector is jointly designed and built between the China, Taiwan, Russian, and US groups of the Daya Bay collaboration. In this subsection we outline the manufacturing plan for the detector and its subsystems:

- **Detector Tank:** The detector tank is a stainless steel construction that provides the outer support for the inner acrylic vessels and liquids. The detector tank will be designed and manufactured in China. A manufacturer close to the Daya Bay site may be chosen. We assume in this CDR that the steel tank will be welded and constructed at the manufacturer and shipped to the Daya Bay site as a complete assembly. Once it arrives on-site the tank will be cleaned and prepared for the detector assembly in the cleanroom of the surface assembly building. If the tank is to be constructed on-site at Daya Bay additional infrastructure beyond what is described in this CDR may be necessary. Preparations of the tank prior to the assembly of the detector include:
  - cleaning of the tank's inside
  - survey of inner and outer tank dimensions
  - lubrication of all threads on the inside with compatible, clean mineral oil
- **Acrylic Vessels:** The design of the acrylic vessels will be done by the US together with engineering support from China and Taiwan. We foresee the fabrication of the acrylic vessels at Nakano, an acrylic manufacturer in Taiwan. This company will fabricate the acrylic vessel and related acrylic fixtures such as support ribs and pipes. The acrylic hardware will be cleaned to specifications and shipped to the Daya Bay site where they will be received in the surface assembly building. Specialized acrylic hardware including acrylic bolts, flanges, and overflow tanks may also be fabricated elsewhere. In this case the same supplier of the UV transmitting Lucite will be chosen. The detailed design of the acrylic vessels and their manufacturing process are under study. It has not been decided yet whether the nested acrylic vessels will be assembled at the manufacturer and shipped in one piece or assembled at the Daya Bay site. Also, two different designs are under consideration. A fully bonded vessel design or a design based on a modular structure that can be taken apart and dismantled. If bonding of the acrylic vessels is done at Daya Bay expert personnel from the acrylic manufacturer may be needed on-site for this work. The acrylic vessels are a critical item of the detector system. We are exploring the possibility of backup vendors in China and in the US for a comparison of price and technical quality.
- **Overflow Tanks:** Overflow tanks outside the antineutrino detector are needed to accommodate the expansion of detector fluids during temperature variations. These tanks may be made out of stainless coated with Teflon or acrylic. They are to be instrumented with liquid level sensors and temperature sensors to precisely monitor the target mass inside the detector and the overflow volumes. The overflow tanks and related instrumentation are designed by the University of Wisconsin and PSL together with IHEP. Their design is closely related to the design of the acrylic vessels and the steel detector

tank. They have to interface with the stainless steel tank, th calibration systems, and connect to the inner acrylic vessels. The place of fabrication is not yet decided. It depends on the choice of materials and the final design. R&D and design studies will continue at the University of Wisconsin and the Physical Sciences Laboratory. We also plan to perform final tests and instrument the overflow tanks at the University of Wisconsin before they are shipped to China and installed in the antineutrino detector at Daya Bay.

- **Liquid Scintillators:**
  - 0.1% Gd-loaded liquid scintillator for inner antineutrino target: Daya Bay will prepare 20 ton of concentrated (1%) Gd-LS first either remotely or locally, which has not yet been decided, and then dilute this concentrated batch to 200t of 0.1% Gd-liquid scintillator on-site. Two synthesis recipes for Gd-loaded liquid scintillator are successfully developed at IHEP and BNL. The scale-up technologies for both recipes are undertaken at both institutes. We expect to select one as the production recipe with another one as the back-up recipe in September 2006. With the current schedule of filling the first pairs of detector modules in summer 2007, the production time of 20t of 1% Gd-LS is anticipated to be six months, starting in January 2007.
  - Unloaded LS for γ-catcher: Two linear-alkyl-benzene (LAB) manufacturers, Fushun in China and Petresa in Canada, have been inquired by IHEP and BNL. Both suppliers are capable of providing $\sim$400 ton of LAB in a short turn-around time (for example, the yearly production of Petresa LAB is $\sim$120,000 ton) and working closely with Daya Bay scientists. Drums of LAB samples provided from both companies have been tested at IHEP and BNL. The chemical qualities of LAB from both vendors are rather similar and proven to be satisfactory. Daya Bay will select the final supplier in October 2007.
  - Mineral oil for buffer region: mineral oil will be purchased from China and delivered to Daya Bay site without any further chemical processes. The batch-to-batch variation of chemical property and quality for mineral oil is well known. IHEP and BNL will impose quality-assurance criteria for the acceptance of mineral oil from the vendor. We expect to accumulate 400 ton of mineral oil in six months, starting in January 2007.

- **PMT Support Structure:** The PMT support structure will be designed by the US and fabricated in China. The University of Wisconsin, UCLA, and Berkeley are currently working together on a design that meets the PMTs specifications and installation requirements for the antineutrino detector. This work is done in close collaboration with the IHEP group in China to define the interface points with the stainless steel tanks. The current plan is for the Physical Sciences Laboratory to oversee the final design of the PMT support structure and its fabrication. Fabrication will be done in China. A manufacturer is yet to be identified.

- **PMTs and Cables:** The PMTs will be procured by UC Berkeley/LBNL and tested by Berkeley, UCLA, and other institutions. Some of the testing work will be done in China in collaboration with university groups. The bases for the PMTs will be designed and manufactured at UCLA. The potting of the PMT bases will be performed in China.

  The mechanical parts of the water-proof, potted PMT base housings will be designed and fabricated at UCLA. The design will be developed as part of the ongoing Daya Bay R&D and start in April 2007. We expect to complete the design and prototyping of these bases by the end of July 2007. Based on similar designs, the UCLA machine shop has estimated that the production of each mechanical housing will take $\sim$2.5 hours. Assuming availability of founding by Oct 1 2007, we expect to produce

100–200 housings per month after an initial setup period of 1 month. This will result in delivery of 100–200 units per month starting early January 2008.

The PMT base printed circuit fabrication and the assembly will be done by external vendors. Based on past experience we expect that by January 2008 we will have 500 PMT bases tested and available for shipment to China. The remaining bases could be delivered at a rate of 200–400 units per month following the initial delivery.

The PMT base printed circuit boards and the housings will be assembled in China mainly by the Chinese members of the Daya Bay collaboration. The assembly process involves attachment of the PMT bases to the PMTs and injecting the housings with potting compound. This will result in a sealed PMT assembly. The procedures and quality assurance steps to pot and seal the PMT-base assemblies will be developed during the initial design and prototyping of the bases. Therefore, an initial 100% underwater testing program of the first 20–50 assemblies followed by a random sample testing of 5% of the assemblies should suffice to insure the integrity of the seals.

- **Reflector:** The reflectors increase the light collection and energy resolution. They consist of a reflective foil sandwiched between acrylic plates. China will design and fabricate the reflectors for the antineutrino detector and ship them to Daya Bay.

- **Monitoring Instrumentation:** The monitoring instrumentation for the antineutrino detector is mostly commercially available. R&D and testing of this instrumentation is currently being performed at the University of Wisconsin and the Physical Sciences Laboratory. UW-PSL plan to oversee the design of the instrumentation package and coordinate its procurement and integration into the detector design. After an appropriate suite of tests at the University of Wisconsin the instrumentation will be shipped to Daya Bay where it can be integrated into the antineutrino detector

The assembly, filling, and installation of the antineutrino detectors is described elsewhere.

6.11 Quality Assurance During Fabrication and Assembly

The detector will be built in a worldwide collaboration. Fabrication of subsystems is likely to take place in the US, China, and Taiwan. Some materials may also be procured from Russia. To ensure the quality and performance of the assembled antineutrino detector a few guiding principles will be followed. We distinguish between the fabrication and assembly phase. During the fabrication phase the manufacturers carry the responsibility to meet the specifications of the collaboration. The Daya Bay managers will oversee the manufacturing process and enforce quality assurance. In the assembly phase, however, the Daya Bay collaboration carries the overall responsibility of defining the assembly process and finding a team of scientists, engineers, and technicians with the right set of skills to perform the assembly. The ultimate responsibility for the successful detector assembly will be with the L2 managers.

Fabrication of Subsystems

- During the design and R&D phase the Co-L2 managers of the detector will visit potential vendors, establish working relationships, and personal contacts. Local collaborators preferably at the L3 level will be the point of contact and responsible person for overseeing the fabrication of a part or subsystem in a respective country. In some cases design and fabrication will be done in different countries. In this situation it is important for the groups responsible to understand the manufacturing capabilities in advance and vice versa. The R&D phase will be used to develop a manufacturing plan and establish working relations between the design groups and manufacturing facilities.

- ○ The fabrication of all parts and subsystems of the detector will follow detailed written specifications and milestones in English. If specifications in languages other English are required a translated document will be prepared with the same level of technical detail. Translation services may be used for translating the technical documents.
- ○ Procedures and quantitative measures for the quality assurance of all parts and subsystems will be developed by the L2 and L3 managers.
- ○ For each part or subsystem a set of milestones will be developed during the R&D phase and written into the manufacturing plan.
- ○ During the fabrication the L2 detector managers together with local L3 contacts will regularly visit the fabrication sites to review quality assurance and fabrication progress. Regular phone conferences will aid in updating the task groups on progress and discussing manufacturing and quality problems as they arise.
- ○ A document summarizing the as-built characteristics and results from all quality assurance tests will be prepared for all subsystems and made available to the collaboration.

Assembly of the Antineutrino Detector

- ○ The assembly of the antineutrino detectors will follow strict written procedures that are developed by the detector group and approved by the L2 managers and the collaboration prior to the assembly on-site.
- ○ Electronic and paper check sheets will be used to organize the assembly effort.
- ○ A Daya Bay collaborator with scientific and technical experience (preferably the L2 managers or designated representative) will be present on-site during the entire assembly process for the antineutrino detector to discuss and approve any change in the assembly procedure. It is unavoidable that certain decisions regarding the assembly have to be taken in real-time and cannot first be discussed via phone or video conference. In addition, we require that L3 managers (or designated representative) will be on-site and available for discussion when their respective subsystem is integrated into the antineutrino detector.
- ○ Regular phone and video conferences will be used to monitor the assembly progress and inform the collaboration.

6.12 ES&H

An extensive discussion of the hazards and safety consideration for the antineutrino detector systems is given in the separate document "Daya Bay Project: Hazards & Safety Considerations".

REFERENCES

1. M. Apollonio *et al.* (Chooz Collaboration), Phys. Lett. B420, 397 (1998); Phys. Lett. B466, 415 (1999); Eur. Phys. J. C27, 331 (2003).
2. http://www.detectors.saint-gobain.com/
3. http://www.texloc.com/corrugated.html
4. Boehm *et al.* (Palo Verde Collaboration), Phys. Rev. Lett. 84, 3764 (2000) [arXiv:hep ex/9912050]; Phys. Rev. D62, 072002 (2000) [arXiv:hep-ex/0003022]; Phys. Rev. D64, 112001 (2001) [arXiv:hep-ex/0107009]; A. Piepke *et al.*, Nucl. Instr. and Meth. A432, 392 (1999).

5. H. Back *et al.* (LENS-Sol Collaboration), Proceedings of the 5th International Workshop on Neutrino Oscillations and Their Origin (NOON 2004), World Scientific Publishing Co., Eds. Y. Suzuki, M. Nakahata, S. Moriyama, Y. Koshio (University of Tokyo, Japan), June 2005.
6. C. Kraus, *et al.* (SNO+ Collaboration), Prog. Part. Nucl. Phys. **5 7** (2006) 150–152.
7. M. Yeh, R. L. Hahn, A. Garnov, and Z. Chang, AIP Conf. Proc. **785** (2005) 209.
8. M.Yeh, A. Garnov and R. L. Hahn, Gadolinium-Loaded Liquid Scintillator for High-Precision Measurements of Antineutrino Oscillations and the Mixing Angle, θ_{13}, submitted to Nucl. Instr. and Meth. **A** (2006)
9. R. L. Hahn, Progress in Particle and Nuclear Physics, **57** (2006) 134–143.
10. K. Eguchi *et al*. (KamLAND Collaboration), Phys. Rev. Lett., **90** (2003) 021802 [arXiv:hep-ex/0212021]; **94** (2005) 081801 [arXiv:hep-ex/0406035].
11. http://www.hamamatsu.com/.
12. http://www.electrontubes.com/.
13. J. Boger *et al.* (SNO Collaboration), Nucl. Instr. and Meth. **A449**, 172 (2000).
14. http://www.emcohighvoltage.com/.
15. http://www.analog.com/en/prod/0,,AD7247,00.html.
16. http://www.3m.com/product/information/Vikuiti-Enhanced-Specular-Reflector.html
17. Gold Aqua, http://www.goldaqua.com
18. Nakano Ltd. http://www.nakano.com.tw
19. Reynolds Polymer Technology, Inc. http://www.reynoldspolymer.com
20. http://www.aviantechnologies.com/products/coatings/
21. http://www.aviantechnologies.com/products/coatings/highreflectance.html
22. P. Ranin *et al.*, *Study of the Influence of the Earth's Magnetic Field on PMTs for Pierre-Auger Surface Detectors* UCLA-Cosmic/2001-02 (May 3, 2001)
23. A.K. Tripathi *et al.*, *Effect of Earth's Magnetic Field on Production Photonis PMTs* UCLA-Cosmic/2001-04 (Dec. 1, 2001)
24. A.K. Tripathi *et al.*, *A systematic study of large PMTs for the Pierre Auger Observatory*, Nucl. Instr. and Meth. **A497**, 331 (2003), Nucl. Instr. and Meth. **A504**, 1 (2003)
25. P. Vernin and J.-P. Schuller, *The Eyes of ANTARES* (Mar. 8, 2002)
26. P. Amram *et al.*, *The ANTARES Optical Module*, Nucl. Instr. and Meth. **A484**, 369 (2002)
27. J.A. Aguilar *et al.*, *Study of large hemispherical photomultiplier tubes for the ANTARES neutrino telescope*, Nucl. Instr. and Meth. **A555**, 132 (2005)
28. C. Athanassopoulos *et al.*, *The liquid scintillator neutrino detector and LAMPF neutrino source*, Nucl. Instr. and Meth. **A449**, 172 (2000)
29. I. Stancu *et al.*, *The MiniBooNE Technical Design Report* (May 14, 2001), http://puhep1.princeton.edu/m̃cdonald/dayabay/MiniBooNE/detector_tdr.pdf
30. J. Abrhaman *et al.*, *Properties and performance of the prototype instrument for the Pierre Auger Observatory*, Nucl. Instr. and Meth. **A523**, 50 (2004)
31. S. Fukuda *et al.*, *The Super-Kamiokande detector*, Nucl. Instr. and Meth. **A501**, 418 (2003)
32. J. Boger *et al.*, *The Sudbury Neutrino Observatory*, Nucl. Instr. and Meth. **A449**, 172 (2000)
33. A. Suzuki (for the KamLAND Collaboration), *Present Status of KamLAND*, Nucl. Phys. B (Proc. Suppl.) **77**, 171 (1999)
34. A. Brigatti *et al.*, *The photomultiplier tube testing facility for the Borexino experiment at LNGS*, Nucl. Instr. and Meth. **A537**, 521 (2005)
35. S. Matsuno *et al.*, *Single photon light detector for deep ocean applications*, Nucl. Instr. and Meth. **A276**, 359 (1989).
36. E.G. Anassontzis *et al.*, *The optical module for the NESTOR neutrino telescope*, Nucl. Instr. and Meth. **A479**, 439 (2002)
37. M. Taiuti, *Wild Ideas on Photon Detection* (Oct. 8,2003), http://www.vlvnt.nl/talks/P5/P5.5-Taiuti.pdf
38. A. Mager *Magnetic Shields*, IEEE Trans. Magn. **6**, 67 (1970)
39. R. Fitzpatrick, *Magnetic Shielding*

7 Calibration and Monitoring Systems

The measurement of $\sin^2 2\theta_{13}$ to a precision of 0.01 in the Daya Bay experiment will require extreme care in the characterization of the detector properties as well as frequent monitoring of the detector performance and condition. The physics measurement requires that the neutrino flux be measured with *relative* precision that is substantially better than 1%. This is accomplished by taking ratios of observed event rates in the detectors at near and far sites to separate the oscillation effect. This will require that differences between detector modules be studied and understood at the level of $\sim$0.1% and that changes in a particular detector module (over time or after relocation at another site) be studied and understood at $\sim$0.1%. Achieving these goals will be accomplished through a comprehensive program of detector calibration and monitoring, as described previously in Section 3.2.2.

7.1 Radioactive Sources

The response of the detectors at the far and near sites may have small differences, and these minute differences can lead to slight differences in efficiency and/or distortion in the measured energy spectra of the antineutrinos. Therefore, it is necessary to characterize the detector properties carefully before data taking and monitor the stability of the detectors during the whole experiment. Calibration sources must be deployed regularly throughout the active volume of the detectors to simulate and monitor the detector response to positrons, neutron capture gammas and gammas from the environment.

Sources that will be used in the calibrations are listed in Table 7.1. These sources cover the energy range

Sources	Calibrations
Neutron sources: Am-Be, ^{252}Cf , Pu(C)	Neutron response, relative and absolute efficiency, capture time
Positron sources: ^{22}Na, ^{68}Ge	Positron response, energy scale trigger threshold
Gamma sources:	Energy linearity, stability, resolution spatial and temporal variations, quenching effect
^{137}Cs	0.662 MeV
^{54}Mn	0.835 MeV
^{65}Zn	1.351 MeV
^{40}K	1.461 MeV
H neutron capture	2.223 MeV
^{22}Na	annih + 1.275 MeV
^{60}Co	1.173 + 1.333 MeV
^{208}Tl	2.615 MeV
Am-Be	4.43 MeV
^{238}Pu-^{13}C	6.13 MeV
Gd neutron capture	$\sim$8 MeV

Table 7.1. Radioactive sources to be used for calibrations.

from about 0.5 MeV to 10 MeV and thus can be used for a thorough energy calibration.

The Am-Be source can be used to calibrate the neutron capture detection efficiency by detecting the 4.43 MeV gamma in coincidence with the neutron. The ^{238}Pu-^{13}C source will similarly provide a 6.13 MeV gamma in coincidence with the neutron. The absolute neutron detection efficiency can be determined with a ^{252}Cf source, because the neutron multiplicity is known with an accuracy of about 0.3%. In addition, neutron sources allow us to determine the appropriate thresholds of neutron detection and to measure the neutron capture time for the detectors.

The positron detection can be simulated by a ^{22}Na source. When a ^{22}Na source emits a 1.275 MeV gamma, a low energy positron will be emitted along with the gamma and then annihilate. The primary gamma and the following annihilation gammas mimic the antineutrino event inside the detector.

The sources must be encapsulated in a small containers to prevent any possible contamination of the ultra-pure liquid scintillator. They can be regularly deployed to the whole active volume of the detectors and the γ-catcher.

7.2 LED Calibration System

LEDs have proven to be reliable and stable light sources that can generate fast pulses down to ns widths at similar wavelengths (470 nm) to the light propagating in liquid scintillator from ionizing radiation. They are therefore ideal light sources for checking the optical properties of the liquid scintillator, the performance of the PMTs and the timing characteristics of the data acquisition systems. LED controllers will control the pulsing of the individual LEDs which are coupled through optical fibers to diffuser balls installed in the automated deployment system which shall be described in Sec 7.5. The diffuser balls and optical fibers will have to be fully compatible with liquid scintillators. The features of the LED calibration system are described briefly below.

1. T_0: The diffuser ball on the central axis of the detector module will be lowered to the level of each ring of PMTs and then light pulses of around 2 ns are emitted to set the t-zero of events for that ring of PMTs.

2. Optical attenuation length: The calibration PMTs at the top/bottom of the detector will measure the light intensity emitted from the descending central diffuser ball to monitor the light attenuation length of the Gd-LS. Similarly the diffuser ball and calibration PMT in the γ-catcher will monitor the light attenuation length of the LS in the γ-catcher. (see Fig. 3.3.)

3. PMT gains: The quantum efficiency and gain of the PMTs are monitored by lowering the central diffuser ball to the appropriate rings of PMTs and then flash the light pulses to give single p.e. at the PMTs.

4. Timing characteristics of DAQ: Double flashes of different intensities from the diffuser ball can mimic the inverse beta decay. The pulses can be triggered by the muon system and the pulse separation can be generated randomly or stepped gradually for checking the performance of the data acquisition system.

5. The controller can be triggered by the muon system to test the detector response following muon events.

7.3 In-situ Detector Monitoring

Each detector module will be equipped with a suite of devices to monitor in-situ some of the critical detector properties during all phases of the experiment. The in-situ monitoring includes load and liquid sensors for the detector mass, attenuation length measurements of the Gd-LS target and the LS γ-catcher, a laser-based monitoring system for the position of the acrylic vessel, accelerometers, temperature sensors, and pressure sensors for the cover gas system. A sampler for routine extraction of a LS sample complements this multi-purpose suite of monitoring tools.

The purpose of these tools is to provide close monitoring of the experiment during three critical phases of the experiment:

1. detector filling

2. data taking
3. detector transport and swapping

During filling of the modules the changing loads and buoyancy forces on the acrylic vessels and the detector support structure are carefully monitored with load and level sensors to ensure that this dynamic process does not exceed any of the specifications for the acrylic vessels.

Most of the time during the duration of the experiment the detectors will be stationary and taking data. Experience from past experiments has shown that the optical properties of detectors will change over time due to changes in the attenuation lengths of the liquid scintillator or changes in the optical properties of the acrylic vessel. It is important to track these characteristics to be able to explain any possibly changes in the overall detector response as determined in the regular, automated calibration. In-situ monitoring of the LS attenuation length and regular extractions of LS samples from the detector modules will help monitor some of the basic detector properties.

The transport of the filled detectors to their location and the swapping of detectors over a distance of up to $\sim$1.5 km is a complex and risky task that will require close monitoring of the structural health of the detectors modules during the move. The proposed swapping scheme of the detectors is a novel method without proof-of-principle yet. While conceptually very powerful, extreme care has to be taken in the calibration and characterization of the detectors before and after the move to be able to correct for all changes in the detector response or efficiencies. The accelerometers, pressure sensors, and the monitoring of the acrylic vessel positions will provide critical real-time information during this procedure to ensure that the detectors — and in particular the acrylic vessels and PMTs — are not put at risk. Recording any changes in the detector modules will also help us understand possible differences in the detector response before and after the move. The acrylic vessel position monitoring system will use a laser beam and reflective target on the acrylic vessel surfaces. By measuring the angular deflection of the laser beam over the length of the detector, transverse displacements of the acrylic vessel can be monitored quite precisely.

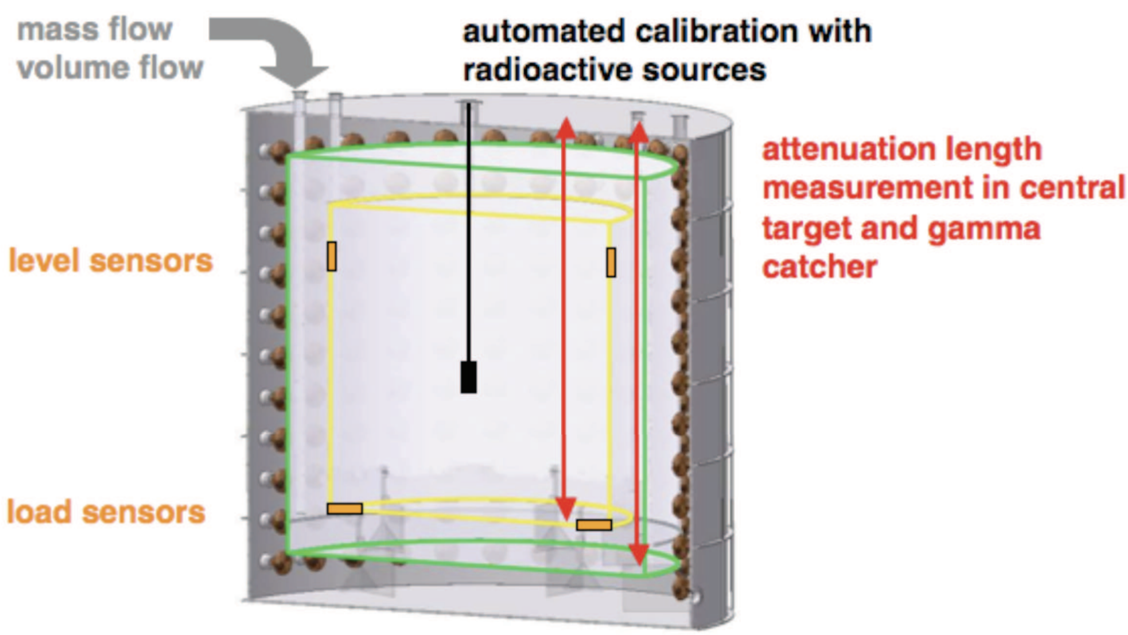

Fig. 7.1. Diagram illustrating the variety of monitoring tools to be integrated into the design of the antineutrino detector modules.

7.4 Detector monitoring with data

Cosmic muons passing through the detector modules will produce useful short-lived radioactive isotopes and spallation neutrons. These events will follow the muon signal (detected in the muon system as well as the detector) and will be uniformly distributed throughout the detector volume. Therefore, these provide very useful information on the full detector volume which is complementary to the information obtained by deploying point sources (see Sections 7.5 and 7.6). For example, such events are used by KamLAND to study the energy and position reconstruction as well as to determine the fiducial volume. As with KamLAND, the Daya Bay experiment will use primarily spallation neutron capture and ^{12}B decay ($\tau = 29.1$ ms and $Q = 13.4$ MeV). The rates of these events for Daya Bay are given in Table 3.5.

Regular monitoring of the full-volume response for these events, compared with the regular automated source deployments, will provide precise information on the stability (particularly of optical properties of the detector, but also general spatial uniformity of response) of the detector modules. With the addition of Monte Carlo simulations, this comparison can be used to accurately assess the relative efficiency of different detector modules as well as the stability of the efficiency of each module.

7.5 Automated Deployment System

Automated deployment systems will be used to monitor all detector modules on a routine (weekly, perhaps daily) basis. Each detector module will be instrumented with three identical automated deployment systems. Each system will be located above a single port on the top of the detector module, and will be capable of deploying four different sources into the detector volume (see Fig. 7.2). This will be facilitated

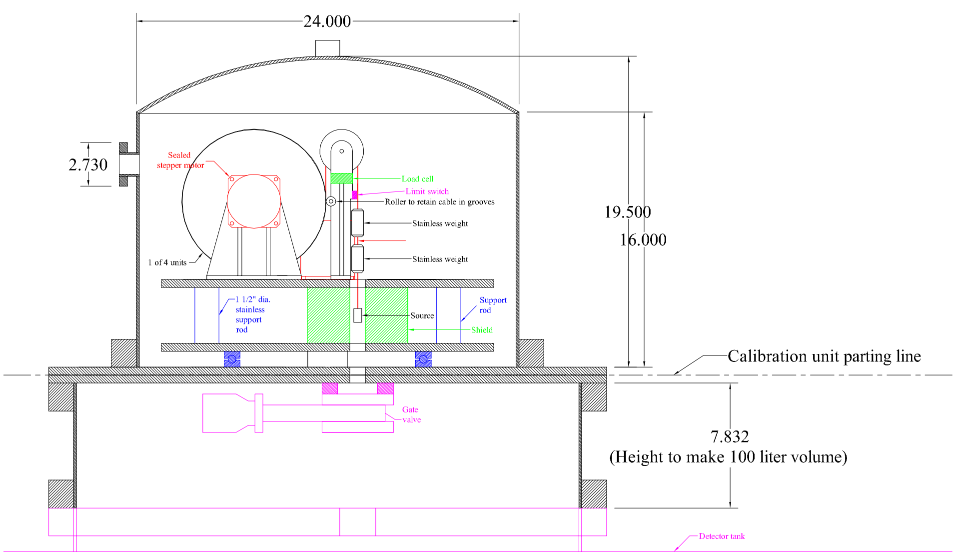

Fig. 7.2. Schematic diagram of the automated deployment system concept. Dimensions are in inches.

by four independent stepping-motor driven source deployment units all mounted on a common turntable. The turntable and deployment units will all be enclosed in a sealed stainless steel vessel to maintain the isolated detector module environment from the outside. All internal components must be certified to be compatible with liquid scintillator. The deployment systems will be operated under computer-automated control in coordination with the data acquisition system (to facilitate separation of source monitoring data from physics data). Each source can be withdrawn into a shielded enclosure on the turntable for storage. The deployed source position will be known to about 2 mm.

At present, we anticipate including three radioactive sources on each deployment system:

- ^{68}Ge source providing two coincident 0.511 MeV γ rays to simulate the threshold positron signal,
- ^{60}Co source providing a γ signal at 2.506 MeV
- ^{252}Cf fission source to provide neutrons that simulate the neutron capture signal.

The fourth motor unit will be used to deploy a LED diffuser ball into the detector. A conceptual diagram of the LED coupling to the diffuser ball is shown in Fig. 7.3.

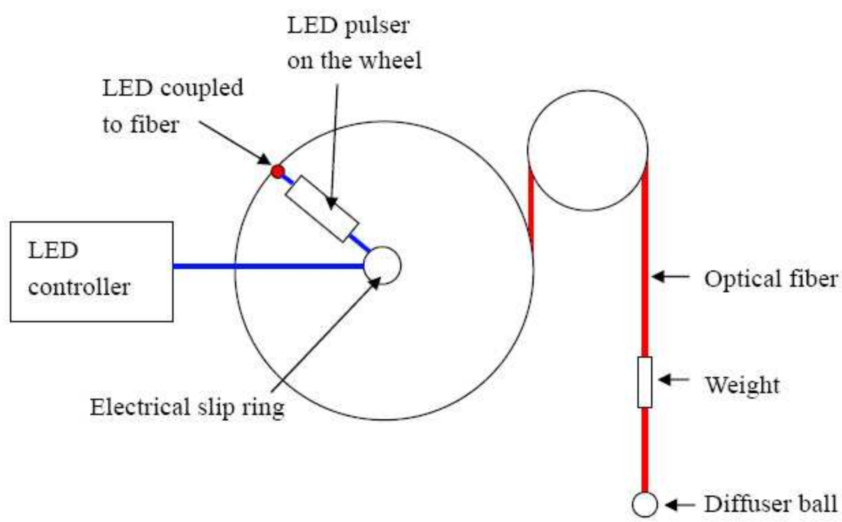

Fig. 7.3. Conceptual diagram of the LED deployment system.

These sources can be deployed in sequence by each of the systems on each detector module. During automated calibration/monitoring periods, only one source would be deployed in each detector module at a time. Simulation studies are in progress to determine the minimal number of locations necessary to sufficiently characterize the detector (in combination with spallation product data as discussed in section 7.4). At present we anticipate that three or four radial locations will be sufficient with at least three as follows:

- Central axis
- A radial location in the central Gd-LS volume near (just inside) the inner cylindrical acrylic vessel wall
- A radial location in the γ-catcher region.

An additional radial location may be instrumented if it is demonstrated to be necessary by the ongoing simulation studies.

Simulation studies indicate that we can use these regular automated source deployments to track and compensate for changes in:

- average gain of the detector (photoelectron yield per MeV)
- number of PMTs operational
- scintillation light attenuation length

as well as other optical properties of the detector system. Examples of these are detailed in Section 3.2.2.5.

7.6 Manual deployment system

A mechanical system will be designed to deploy sources throughout the active volume of the detectors. The source inside the detector can be well controlled and the position can be repeated at a level less than 5 cm. The whole deployment system must be treated carefully to prevent any contamination to the liquid scintillator. The system must be easy to setup and operate, tolerate frequent use and must have a reliable method to put sources into the detectors and to take the sources out as well. The space for operation should not be too large. Figure 7.4 shows a schematic view of the manual source deployment system. The philosophy of such a system is taken from the oil drilling system. The support pipe is separated into several segments. They can be connected one by one to make a long support pipe. This design would reduce the requirement for large space for operations.

The operation procedure will be the following: first, the support pipe and the source arm will be installed in line (vertical). Then, it will be put into the desired position inside the detector, by adjusting the number of segments. When it reach the measurement position, the source arm is turned to the horizontal. After this, the source position can be adjusted by the rope system. The rope system must be designed to insert and remove the sources easily and the position of the source must be accurately controlled. The whole system can be rotated around the axis of the pipe on the platform, thus it can deploy the sources to any position inside the detector.

7.7 Manufacturing Plan

The automated deployment systems will be fabricated in the Kellogg Laboratory at the California Institute of Technology (Caltech). Substantial components such as gate valves, stepping motors, slip rings, and stainless bell jar lids are commercially available. Many custom components such as the pulley wheels, turntable, and miscellaneous parts will be machined in shops at Caltech. The LED pulser units and fiber optics will be supplied by Hong Kong University and installed at Caltech. Each deployment system will be fully assembled and tested at Caltech prior to shipment to China. After arrival at the Daya Bay site, the units will be tested, installed and commissioned on the detector modules.

Radioactive sources will be procured, prepared, and tested at the China Institute for Atomic Energy (CIAE).

The manual deployment system will be fabricated at CIAE. CIAE is responsible for testing, installation and operation of the system.

7.8 Quality Assurance

The assembled automated systems will be fully tested at Caltech prior to shipment to China. Positioning accuracy of 2 mm, reliability, and fail-safety of interlocks will all be established during this testing program.

The manual system will be tested at CIAE prior to shipment to the Daya Bay site. Positioning accuracy of 2 mm, reliability, and fail-safety of interlocks will all be established during this testing program.

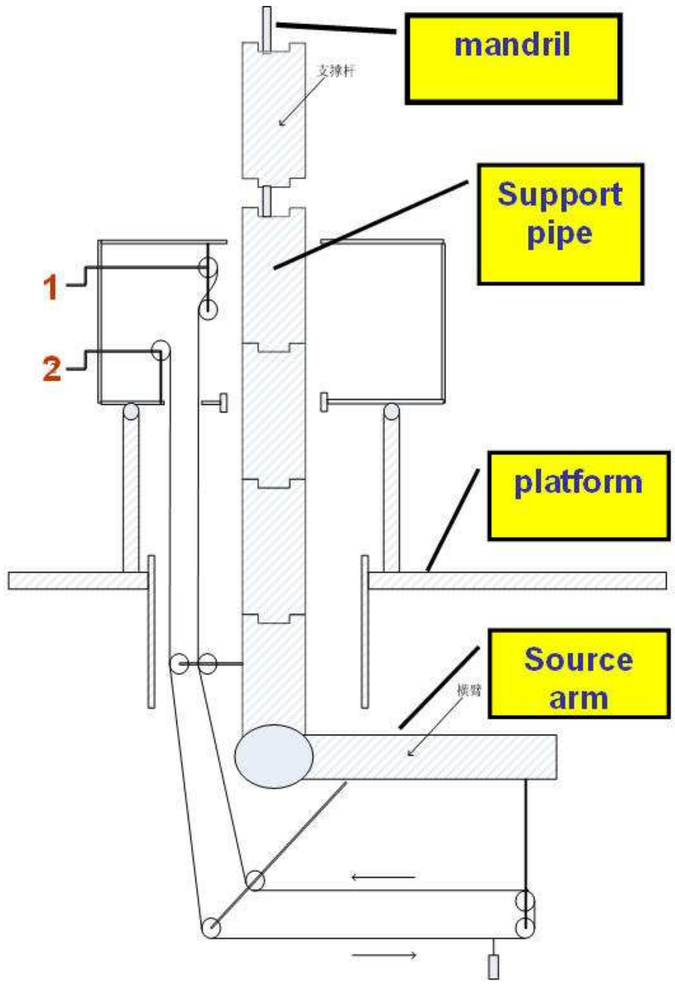

Fig. 7.4. Schematic diagram of the manual source deployment system.

Radioactive sources will be tested to certify that they are leak-tight. This will include soaking in acid or other solvent and counting the soak liquid. Absolute activity of each source will be measured and documented.

7.9 ES&H

The calibration systems do not involve flammable materials or gases, high voltage, or other hazards. The radioactive sources are of very low activity, typically 1000 Bq or less, and will be operated in a shielded environment so that they do not represent a hazard to humans. Personnel involved in the installation and testing of the sources will need to be properly trained and monitored, but the dose rates will be extremely low, of order μrem/hr.

7.10 Risk Assessment

The primary risk associated with the calibration systems is the interface with the detector module. Interlocks must insure that the pressure in the calibration system is equalized with the detector before opening the gate valve and deploying a source. The sources and materials must be tested to be compatible with the liquid scintillator to avoid contamination of the detector.

8 Muon System

The main backgrounds to the Daya Bay Experiment are induced by cosmic-ray muons. These backgrounds are minimized by locating the detectors underground with maximum possible overburden. Background due to muon spallation products at the depths of the experimental halls as well as ambient γ background due to the radioactivity of the rock surrounding the experimental halls is minimized by shielding the antineutrino detectors with 2.5 meters of water. Gammas in the range of 1–2 MeV are attenuated by a factor $\sim$10 in 50 cm of water [1]. Thus the 2.5 meters of water provides a reduction in the rock γ flux of roughly five orders of magnitude. This "water shield" also attenuates the flux of neutrons produced outside the water pool.

Events associated with fast neutrons produced in the water itself remain a major potential background. A system of tracking detectors will be deployed to tag muons that traverse the water shield. Events with a muon that passes through the water less than 200 μs before the prompt signal, which have a small but finite probability of creating a fake signal event, can be removed from the data sample without incurring excessive deadtime. By measuring the energy spectrum of tagged background events and having precise knowledge of the tagging efficiency of the tracking system, the background from untagged events (due to tagging inefficiency) can be estimated and subtracted statistically with small uncertainty. Our goal is to keep the uncertainty of this background below 0.1%.

The muon system will also have some ability to identify showering muons. Such muons have an enhanced likelihood to produce other cosmogenic backgrounds, of which ^{9}Li is the most important. This capacity supplements the ability of the AD to identify such muons. Although, as discussed in Section 3.3.3, we plan to measure and subtract this background, it may also be possible to suppress it without unacceptable deadtime by identifying likely parent muons and rejecting subsequent apparent signal candidates. While such tagging may help to suppress the ^{9}Li background, the working assumption is that no extra requirements are imposed on the muon system in order to reduce this background.

The current baseline configuration for meeting these challenges is shown schematically in Fig. 8.1. The antineutrino detectors are separated by 1 m from each other and immersed in a large pool of highly-purified water. The pool is rectangular in the case of the near halls and square in the case of the far hall. The minimum distance between the detectors and the walls of the pool is 2.5 m. The water shield is divided into inner and outer sections of the pool and instrumented with phototubes to detect Cherenkov photons from muons impinging on the water. The outer side and bottom sections of the pool are 1 m thick, read out by phototubes spaced periodically. The outer sections are separated from the inner pool by Tyvek film 1070D reflectors stretched over a stainless steel frame. The frame holds PMTs for both the inner and outer sections of the pool. The muon tracker is completed by four layers of Resistive Plate Chambers (RPCs) above the pool. The top layers extend 1 m beyond the edge of the pool in all directions, both to minimize the gaps in coverage and to allow studies of background caused by muon interactions in the rocks surrounding the pool.

Expected rates of cosmic ray muons in the components of the muon system can be found in Table 9.3.

8.1 Muon System Specifications

Note that it is not envisioned that this system will act as an online veto. This will allow ample opportunity for careful offline studies to optimize the performance of the system.

Requirements of the muon system are summarized in more detail in the following subsections.

8.1.1 Muon Detection Efficiency

The combined efficiency of the muon system has to exceed 99.5%, with an uncertainty $<$0.25%. This is driven by the need to reject the fast neutron background from muon interactions in the water and to measure its residual level. As can be seen in Table 3.11, without suppression, our simulations predict this background would otherwise be $\sim$50 times that of the fast neutron background from muon interactions in

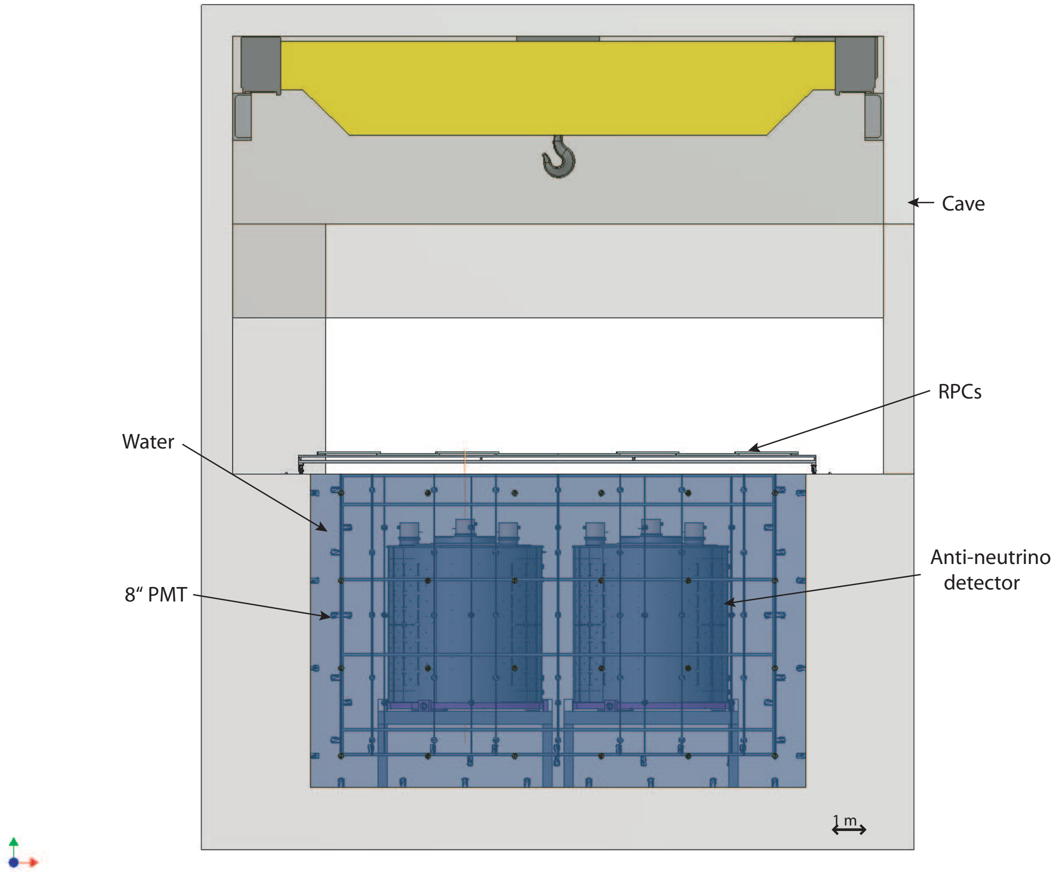

Fig. 8.1. Elevation view of an experimental hall, showing the baseline design for the muon system. This includes a layer of RPCs above a water pool with at least 2.5 m of shielding for the antineutrino detectors, two layers of 8" photomultipliers in the water, with compartmentalization of the outer 1 m of water for position resolution and redundancy.

the surrounding rock, *i.e.* at a level roughly 2% of that of the signal. According to our simulation, a factor of 200 reduction in this rate brings the fast neutron background from the water safely below that from the rock, and the total residual fast neutron background down to the 0.1% level. The requirement on the uncertainty in the efficiency brings the systematic due to the uncertainty on the fast neutron background from the water to a level at which it is small compared with other systematics.

8.1.2 Muon System Redundancy

It is difficult to achieve the requisite efficiency with only one tagging system. Moreover it is necessary to have a method of determining the residual level of background after the imposition of the muon rejection cuts. Therefore it is desirable to have two complementary tagging systems to cross-check the efficiency of each system and allow detailed comparison with simulation.

As discussed below, the current baseline design is to instrument the water shield as a Cherenkov tracker by deploying 8" PMTs in the water with 0.8% coverage. Such systems are expected to have $>95\%$ efficiency. A second tracking system, in our baseline a combination of RPCs [2] [3] above and outer water sections at the sides and bottom of the water pool, can give an independent efficiency of $>90\%$. The two systems compliment each other, with the probability of a muon being missed by both systems below 0.5%.

8.1.3 Spatial Resolution

The fast neutron background due to muons interacting in the water shield falls rapidly with the distance of the muon track from the AD. The spatial resolution of the muon tracker should be sufficient to measure this falloff. Measurements from previous experiments show that the characteristic falloff distance is about 1 meter [4]. A spatial resolution of 50–100 cm in the projected position in the region of the antineutrino detectors is necessary in order to study this radial dependence. The technologies we are proposing are capable of achieving sufficient resolution in each coordinate.

8.1.4 Timing Resolution

There are several constraints on the timing resolution. The least restrictive is on the time registration of the muon signal with respect to that of the candidate event. To avoid compromising the veto rejection to a significant extent, this resolution need only be in the range of fractions of a microsecond. More stringent requirements are imposed by other, technology-dependent, considerations. The water shield PMTs need $\sim$2 ns resolution to allow spatial reconstruction of the muon trajectory.

If scintillator strips are used, 1ns time resolution will allow the random veto deadtime from false coincidences in that system to be held to the order of 1%. RPCs will need $\sim$25 ns resolution to limit random veto deadtime from false coincidences in that system to a similar level.

8.1.5 Water Shield Thickness

As mentioned above the shield must attenuate γ rays and neutrons from the rock walls of the cavern by large factors to reduce the accidental background in the antineutrino detectors. A minimum thickness of 2 m of water is required; 2.5 m gives an extra margin of safety.

8.1.6 Summary of Requirements

The requirements discussed above are summarized in Table 8.1

The overall inefficiency for the muon system for cosmic rays should be $\leq$0.5%.
The uncertainty on this quantity should be no greater than $\pm$0.25%.
Random veto deadtime should be held to $\leq$25% to avoid undue impact on our statistical precision
The uncertainty on the random veto deadtime should be no greater than $\pm 0.05\%$
The position of the muon in the region of the antineutrino detectors should be determinable to 0.5–1 m
Timing resolution of $\pm$1, 2, 25 ns for scintillator, water shield, and RPCs respectively
Thickness of the water shield of at least 2 m

Table 8.1. Muon system requirements

8.2 Water Shield

The antineutrino detectors will be surrounded by a shield of water with a thickness of at least 2.5 meters in all directions. Several important purposes are served by the water. First, fast-neutron background originating from the cosmic muons interacting with the surrounding rocks will be significantly reduced by the water. Simulation shows that the fast-neutron background rate is reduced by a factor 1.5–2 for every 50-cm of water. Second, the water will insulate the antineutrino detectors from the air, reducing background from the radon in the air as well as γ rays from surrounding rocks and dust in the air. With the low-energy γ ray flux reduced by a factor $\sim$10 per 50-cm of water, the water can very effectively reduce the accidental background rate associated with the γ rays. Third, the water shield can be instrumented with PMTs for observing the passage of cosmic muons via the detection of the Cherenkov light.

The active inner and outer water shield sections, together with the RPCs, form an efficient muon tagging system with an expected overall efficiency greater than 99.5%. The ability to tag muons with high efficiency is crucial for vetoing the bulk of the fast-neutron background. Finally, the large mass of water can readily provide a constant operating temperature for the antineutrino detectors at the near and far sites, eliminating one potential source of systematic uncertainty.

8.2.1 Water Shield Design

The schematics of the water shield is illustrated in Fig. 8.1 for the water pool configuration. The cylindrical antineutrino detector modules are placed inside a rectangular cavity filled with purified water, *i.e.* a water pool configuration. The dimensions of the water pool are 16 m$\times$16 m$\times$10 m (high) for the far site, and 16 m$\times$10 m$\times$10 m (high) for the near sites. The four detector modules in the far site will be immersed in the water pool forming a 2 by 2 array. As shown in Fig. 8.1, the adjacent detector modules are separated by 1 meter and each module is shielded by at least 2.5 meters of water in all directions. For the near sites, the two antineutrino detector modules are separated by 1 meter. Again, any neutrons or γ rays from the rock must penetrate at least 2.5 m of water in order to reach the antineutrino detector modules. The weight of water is 2170 ton and 1400 ton, respectively, for the far site and for each of the two near sites.

The water shield is divided into inner and outer sections separated by Tyvek partitions. The outer sections are 1 m thick covering the sides and bottom of the pools.

8.2.2 Water Shield PMT layout

In the baseline design the inner water shield will be instrumented with arrays of hemispheric 8” PMT as shown in Fig. 8.2. Inward-facing PMT arrays will be mounted on frames placed at the sides and on the

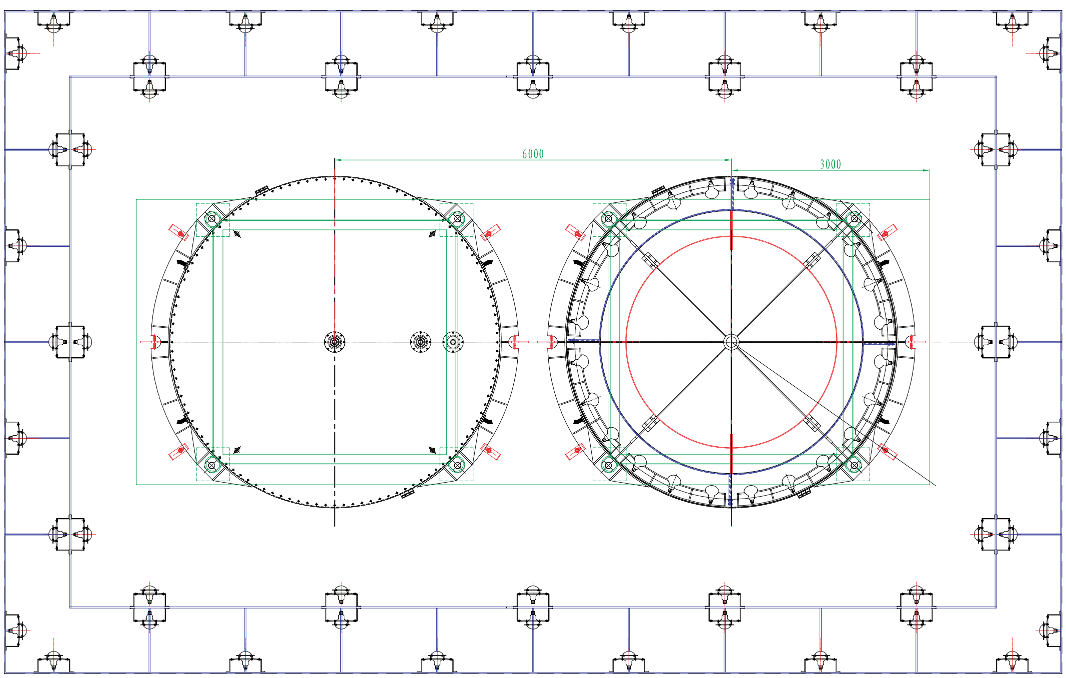

Fig. 8.2. Plan view of a near hall configuration.

bottom of the pool, abutting the inner surfaces of the outer sections (which will be covered with Tyvek). The PMTs will be approximately evenly distributed forming a rectangular grid with a density of 1 PMT per $\sim$4 m^2. This corresponds to a 0.8% areal coverage. The total number of PMTs for the far site and the two near sites is 415, as detailed in Table 8.2. bottom 23 The outer shield has inward-facing PMTs on the

Site	inner bottom	inner sides	inner total	outer in-facing	outer out-facing	outer total	grand total
DB Near	23	100	123	104	64	168	291
LA Near	23	100	123	104	64	168	291
Far	41	128	169	132	80	212	381
All three	87	328	415	340	208	548	963

Table 8.2. Number of PMTs for the water shield.

sides and bottom of the pool and outward-facing PMTs on the side partitions, all at densities of one per 6-7 m^2. The numbers are summarized in the same table. Bases for these PMTs will be custom designed and manufactured potted and encapsulated. The final design will completed after we choose a PMT. Figure 8.3 shows the design of a base with the required characteristics that is offered by Hamamatsu.

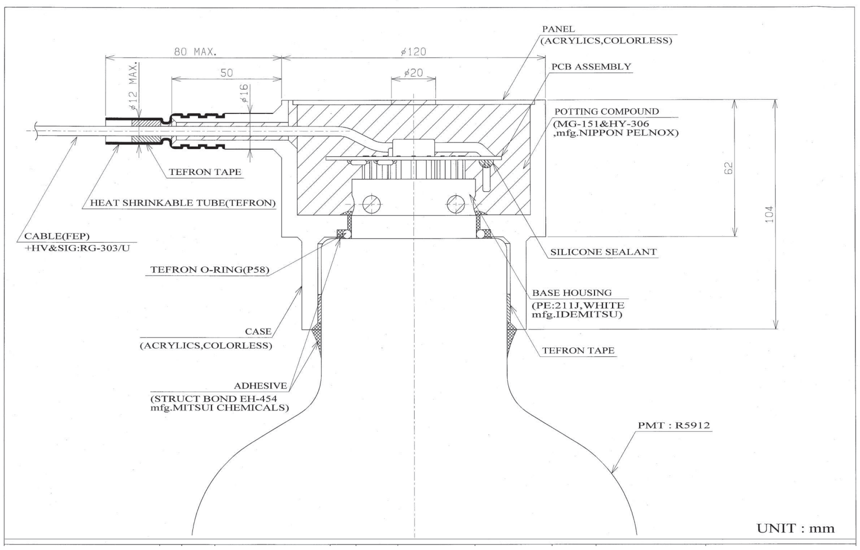

Fig. 8.3. Hamamatsu proposal for PMT base suitable for use in ultra-pure water.

The HV system will be very similar to that described in Section 6.4.5 for the antineutrino detector PMTs. One candidate PMT support scheme is shown in Fig. 8.4. The PMTs must be supported against their own weight in air but also against a much larger buoyant force when they are under water. In this scheme they are supported near the widest part of the bulb by pressure between a Teflon backing ring and a transparent PMMA pressure disk which themselves are affixed via three “legs” to the support frames. The pressure disk is attached to slotted bars at the three points. Bolts through the slots allow an adjustable attachment to the support legs. One leg is above and two below the PMT. There is also a cable support (not shown) to relieve stress on the base.

Efficiency, position resolution, timing resolution, etc. are being further optimized by Monte-Carlo simulations now in progress. The baseline and a number of other possible arrangements of PMTs have been studied so far.

8.2.3 Water Shield Front-End Electronics

Extrapolation of the curves in Figs. 8.9 and 8.17 indicates that although the number of photoelectrons per PMT has a long tail, only about 0.01% of the PMTs see more than 100 photoelectrons. Thus the per-

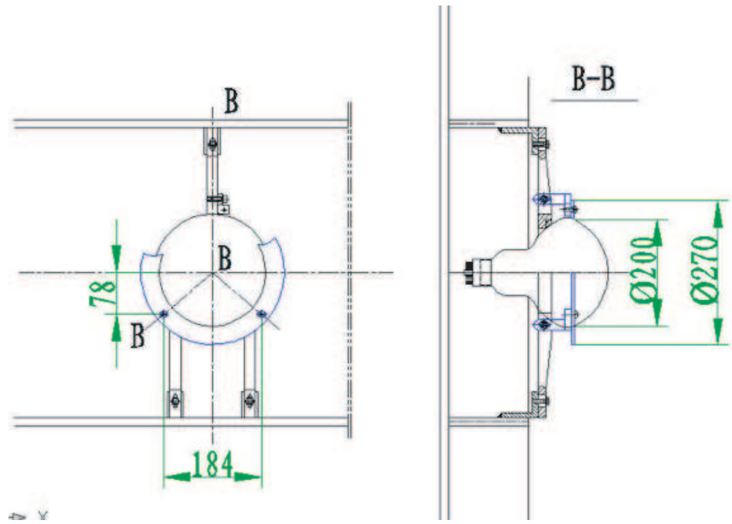

Fig. 8.4. PMT support scheme for water pool.

formance of the antineutrino detector electronics, as listed in Table 9.1, should certainly be adequate for the water shield readout. However the reduced dynamic range requirement may indicate that less expensive options should be considered for the pulse height measurement. In addition to the pulse height information, timing information will also be provided by the readout electronics. With 0.5 ns/bin TDCs, a timing resolution of 2 ns is readily achievable for a single PMT channel. The energy sum of the PMTs as well as the multiplicity of the struck PMTs will be used for defining the muon trigger (see Section 9.2.3).

8.2.4 Calibration of the Water Shield PMTs

The gain stability and the timing of the PMTs will be monitored by a system of LEDs similar to that for the antineutrino detectors as described in Section 7.2. In this case the diffuser balls will be permanently mounted at several locations within the water shields. No radioactive sources will be required.

8.2.5 Water Conditioning

The pool water needs to be conditioned to meet specifications necessary for acceptable performance. These include clarity, radioactivity, long term corrosiveness, and temperature. A preliminary design for the water conditioning system is shown in Fig. 8.5.

Our clarity specification is a requirement that the attenuation length for Cherenkov light be on the order of the pool dimensions or larger. For micron sized particles, this translates to a particle density of 10^{10}/m^3 or less. We expect to use a filter stage followed by reverse osmosis to meet many of our specifications. Such a system has been used to reduce suspended particles down to 1 nm and other dissolved solids in water to a level of 4 ppm [5], far lower than necessary for water clarity.

Most radioactive backgrounds will be carried on suspended particles and removed to a satisfactory level by the filters. Radon presents a particularly insidious background for the antineutrino detectors, however, and is dissolved in the water as a noble gas. Estimates of the effect of γ rays from the ^{214}Bi daughters indicate that radon needs to be reduced to a level less than 5 Bq/m^3 (3×10^6 atoms/m^3). The Super-Kamiokande detector [6] achieved a three order of magnitude lower concentration using reverse osmosis, followed by vacuum and membrane degasification stages, which are likely unnecessary for our specifications.

Water can act as a corrosive agent, given certain characteristics related to its “purity” and to the materials that are submerged in the pool. Of particular interest are the PMT glass [7] and bases, given their operational criticality and high voltage characteristics. One must also take care in the selection of materials used for

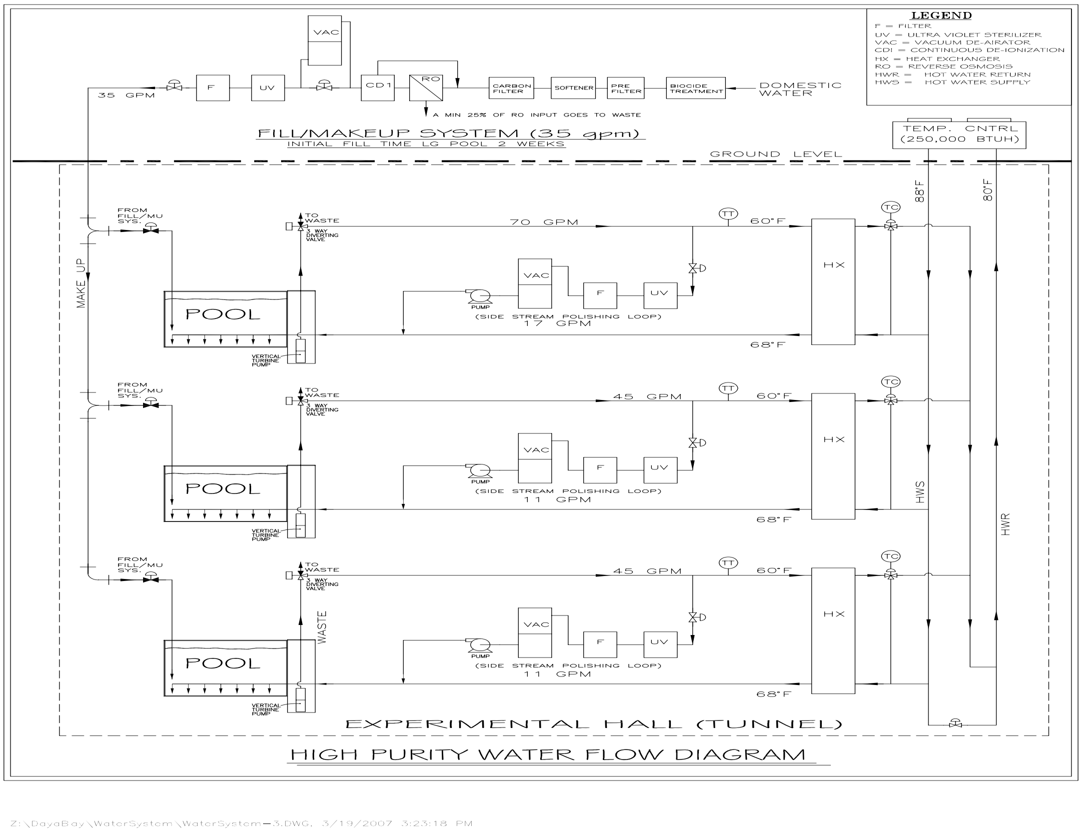

Fig. 8.5. Schematic diagram of a water conditioning system.

support and framing. Aside from potential compromising of their structural integrity, they could introduce dissolved solids which may violate other criteria. We are studying these aspects of the problem to understand if they need to be considered after the other specifications are met.

The water pool will effectively serve as a temperature stabilization medium for the antineutrino detectors. Keeping the temperature constant to $\pm 1^\circ$ C is required by the AD design and equalizing the temperatures between the near and far halls to the same level is necessary to achieve "identical" detector pairs. The cost and challenges of maintaining an overall temperature specification, with the water pool in contact with the cavern walls, is being investigated.

Bacterial growth in the water must also be minimized, at least for the sake of clarity. To first approximation, this is accomplished using an ultraviolet sterilization stage [6,8]. Gas removal, aimed at radon, will also be used to remove dissolved oxygen, and we will aim for as low an operating temperature as possible, given other constraints. We anticipate circulation of $\sim$70 gallons/minute in the Far Hall pool and $\sim$45 gallons/minute in the near hall pools which will allow one complete turn-around of the water in about 6 days.

8.2.6 Inner Water Shield

8.2.6.1 Inner Water Shield Simulation Studies

Figure 8.6 shows the simulated distribution of track length of cosmic ray muons in the water shield of the Far Hall. The mean distance traveled through the water is about 5.5 m. For full geometric coverage with

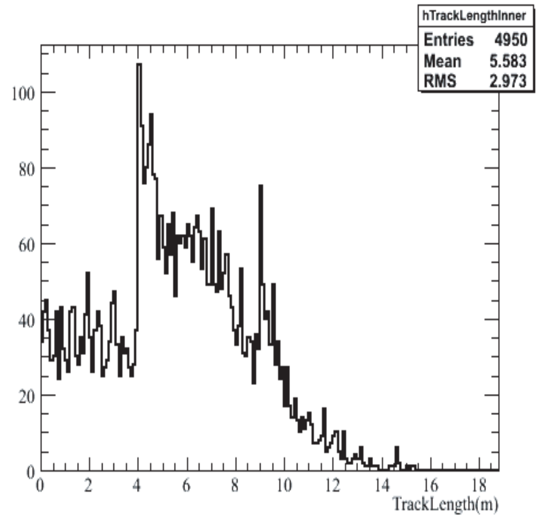

Fig. 8.6. Track length of muons in the inner water shield for the Far Hall. The edge at around 4.5 m is due to muons that penetrate the water and the ADs approximately vertically while the edge around 9 m is due to those that miss the ADs.

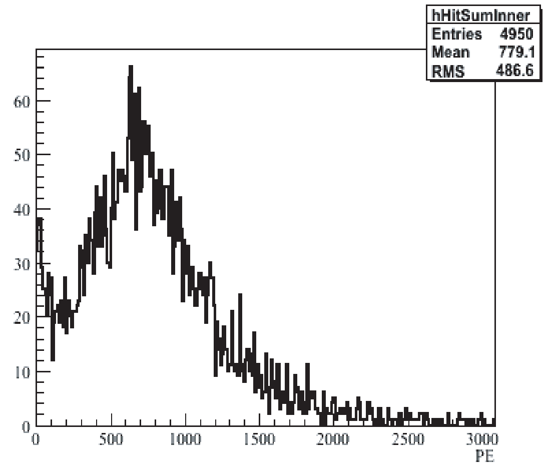

Fig. 8.7. Total number of photoelectrons observed in baseline configuration in the inner shield of the Far Hall.

a typical bialkali photo-cathode, one would expect about 16,500 photoelectrons from a track of this length. Taking into account the 0.8% PMT geometric coverage, these muons would produce ∼130 photoelectrons in the PMTs from photons collected directly. As can be seen in Fig. 8.7, our simulation shows that the average is actually ∼770 for the baseline configuration. Our simulation verifies that this is due to reflected photons. A photon collection time of 200 ns is assumed. We conservatively assume an attenuation length of 20 m. These photoelectrons are spread over an average of ∼97 PMTs as seen in Fig. 8.8, and the resulting distribution of photoelectrons in a single PMT is shown in Fig. 8.9. As expected the average for events with non-zero PMT counts is about 7 photoelectrons, although there is a long tail exponential tail.

Muons are identified in the Monte Carlo by demanding a minimum number of PMTs to fire. Results on efficiency of the inner water shield as a function of the number of PMTs demanded are shown in Fig. 8.10. In each case a threshold number of PMTs is determined by the requirement that the deadtime due to random coincidences be <1%. Conservatively an effective singles rate (dark current plus radioactivity) of 50 kHz/PMT was assumed for this calculation. For the baseline configuration described above, this level was reached at a threshold of 12 PMTs, yielding an efficiency of 98.6% as can be seen from the lower curve in Fig. 8.10*. The PMTs, bases, electronics and PMT support scheme for this region will be the same as those for the inner pool. However the outer shield will have its own front-end electronics and trigger.

8.2.7 Outer Water Shield

Combined with the RPCs to be discussed below, the outer water shield forms a nearly hermetic muon tagging layer that can determine the path of muons through the region of the antineutrino detectors. In addition, it can measure the efficiency of the inner water shield for muons.

As mentioned above, the water pool is divided into inner and outer sections by reflecting dividers

*Note that since virtually all muons entering the inner water shield must have penetrated the RPCs or the outer water shield, the overall efficiency is higher than this.

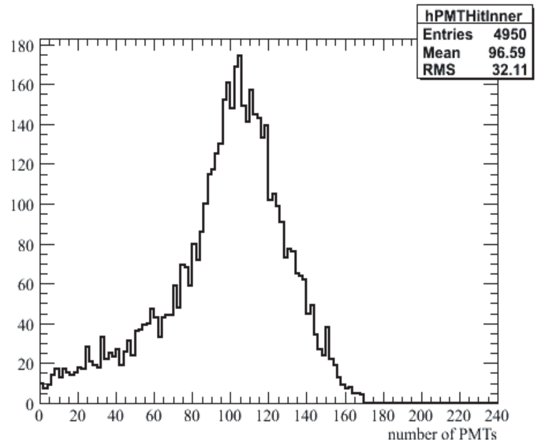

Fig. 8.8. Number of inner shield phototubes hit in baseline configuration of the Far Hall.

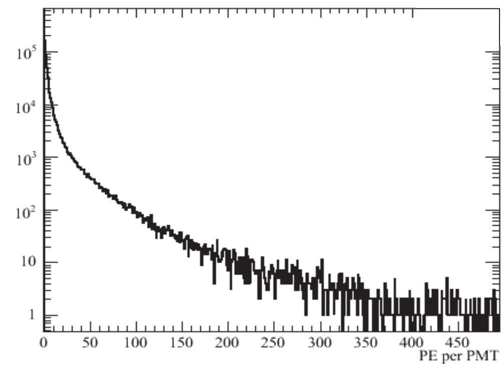

Fig. 8.9. Photoelectrons observed per inner shield PMT in baseline configuration of the Far Hall.

supported on stainless steel frames as shown in Fig. 8.11. The outer sections are 1 m thick. The dividers are multilayer films supported by stainless steel frames. Outer layers of Dupont Tyvek film 1070D sandwich an inner layer of thin white plastic. These films separate the inner and outer water pools optically. Figure 8.12 shows the scheme for constraining the separator panels, and Fig. 8.13 shows how the panels are attached to the frames. The frames are also used to support the inner water shield PMTs and some of the outer water section PMTs (the rest are supported on the pool side and bottom walls).

8.2.7.1 Performance of the Outer Water Shield

The distribution of track lengths in the outer shield is shown in Fig. 8.14. Here the average path length is about half that of the inner shield. However, as shown in Fig. 8.15, the number of photoelectrons collected is about 2/3 of that of the inner shield, because the overall density of PMTs is higher in the outer shield.

Figure 8.16 shows the number of phototubes excited by the passage of a muon through the outer shield. This is again about 2/3 of the case of the inner shield. The density of PMTs in the outer shield is being further optimized by simulation. Figure 8.17 shows the distribution of the number of photoelectrons per phototube for the outer shield. Once again as in the case of the inner shield there is a long tail. The upper curve in Fig. 8.10 shows the efficiency of the outer shield as a function of the number of PMTs required in the trigger. Using the same random rate criterion as for the inner shield, the threshold number of PMTs is 13 and the outer shield efficiency for tracks that hit the water is 98.8%. Note that the events missed by both systems are predominantly corner-clippers that have a very short path length in the water. This can be seen in Fig. 8.18. This implies that the muons missed by the water shield are those which are furthest from the ADs and therefore the least likely to cause fast neutron background.

8.3 Resistive Plate Chambers (RPC)

The RPC is an attractive candidate tracking detector for instrumenting large areas. RPCs are economical, and are simple to fabricate. The manufacturing techniques for both Bakelite (developed by IHEP for the BES-III detector [2]) and glass RPCs (developed for Belle [3]) are well established.

An RPC is composed of two resistive plates with gas flowing between them. High voltage is applied on the plates to produce a strong electric field in the gas. When a charged particle passes through the gas, an avalanche or a streamer is produced. The electrical signal is registered by pickup strips placed outside the plates and sent to the data acquisition system. In our case, the RPCs will operate in the streamer mode.

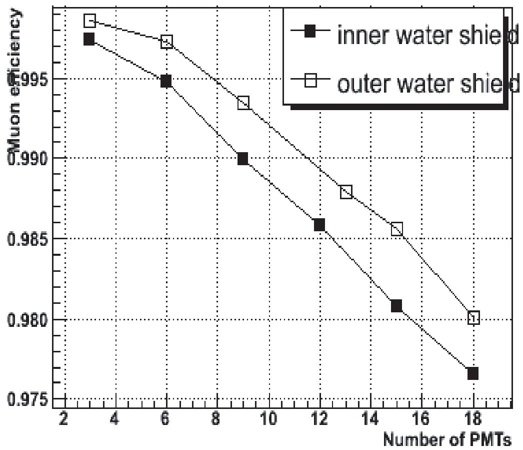

Fig. 8.10. Muon efficiency of the inner and outer water shields as a function of the number of hit PMTs demanded. For the inner shield the threshold level needed to reduce the random rate to 50 Hz is 12 PMTs, for the outer it is 13 PMTs. Approximately 7500 muons are simulated for each curve.

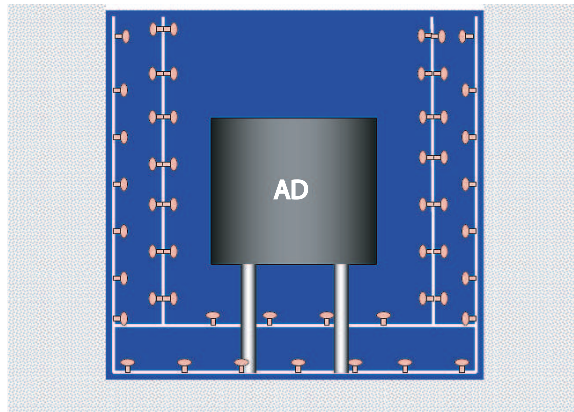

Fig. 8.11. Inner and outer sections of a near hall water pool.

We plan to use RPCs developed at IHEP for the BES-III muon spectrometer for the Daya Bay Experiment. These RPCs were constructed using a new type of phenolic paper laminate developed at IHEP. The surface quality of these plates is markedly improved compared to the Bakelite plates previously used to construct RPCs. The resistivity of the laminates can be controlled to any value within a range of 10^9–10^{13} Ω·cm. These RPCs can operate without linseed oil coating. Applying linseed oil to the Bakelite plates is a time-consuming step in the production, and presents a major risk factor in the long-term operation of the chambers.

About 1000 IHEP-style bare chambers ($\sim$1500 m^2) have been produced for BES-III. Tests show that the performance of this type of RPC is comparable to that of RPCs made with linseed oil treated Bakelite and glass.

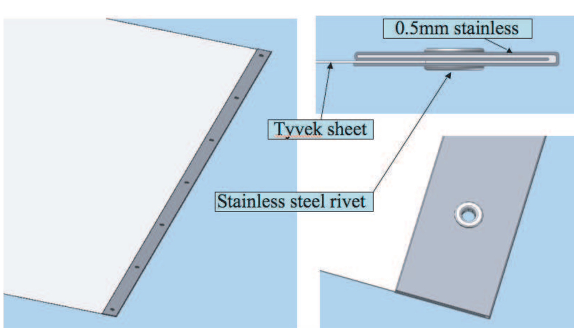

Fig. 8.12. Inner-outer pool separator panel.

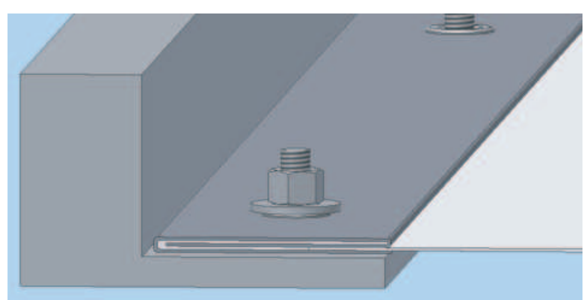

Fig. 8.13. Anchoring of separator panels.

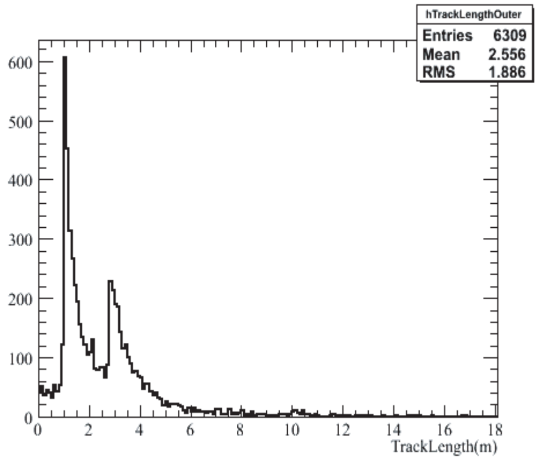

Fig. 8.14. Track length of muons in the outer water shield for the Far Hall. The structure starting just below 3 m is due to muons that enter the side and exit the bottom section of the outer shield.

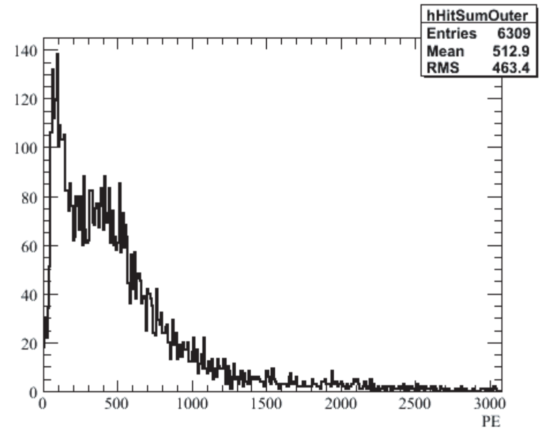

Fig. 8.15. Total number of photoelectrons observed in the outer shield PMT in baseline configuration of the Far Hall.

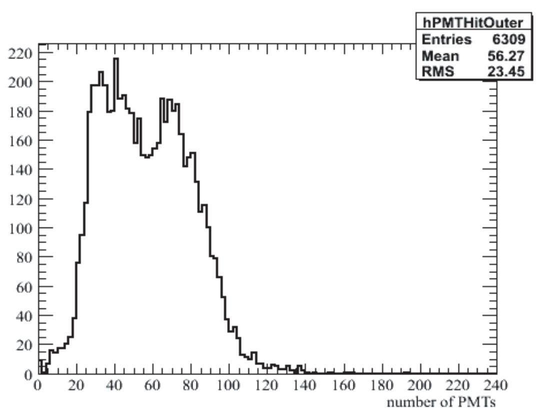

Fig. 8.16. Number of outer shield phototubes hit in baseline configuration of the Far Hall.

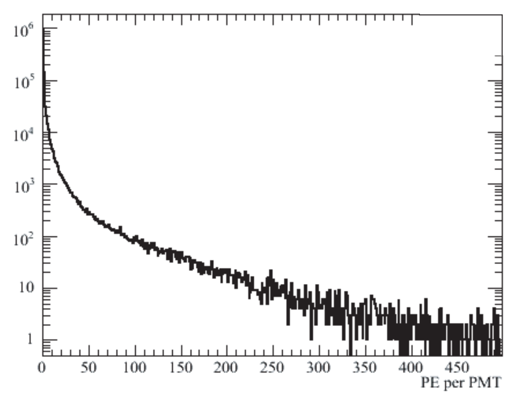

Fig. 8.17. Photoelectrons observed per PMT in baseline configuration of the outer shield of the Far Hall.

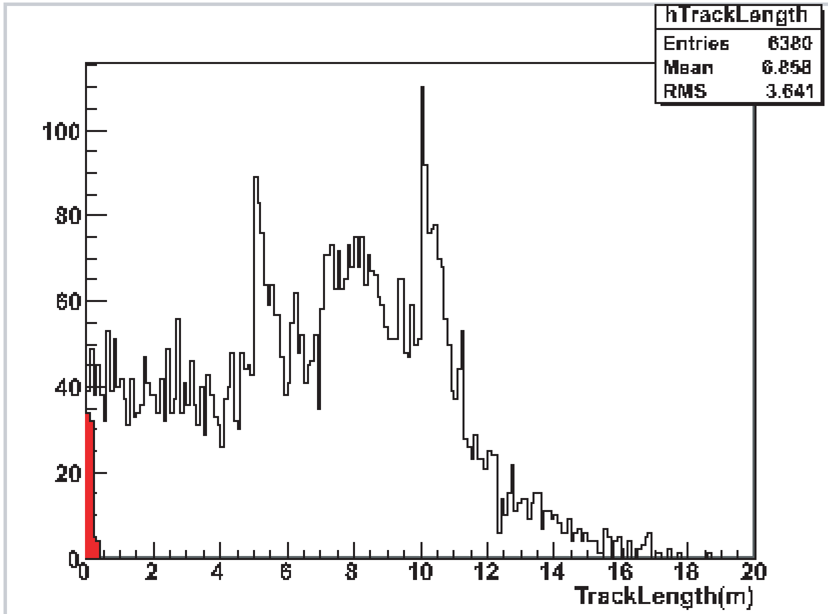

Fig. 8.18. Total track length of muons in the water shield for the Far Hall. Red histogram is events that were missed by both the inner and outer shields.

The efficiency and noise rate of the BES-III RPCs have been measured. In Fig. 8.19, the efficiencies versus high voltage are shown for threshold settings between 50 and 250 mV. The efficiency plotted does not include the dead area along the edge of the detector, but does include the dead region caused by the insulation gasket. This kind of dead area covers only about 1.25% of the total detection area. The efficiency of the RPC reaches a plateau at about 7.6 kV, and rises slightly to 98% at 8.0 kV for a threshold of 150 mV. There is no discernible difference in efficiency above 8.0 kV for thresholds below 200 mV.

It is a common practice to subject a new RPC to 10 kV high voltage in Argon for three or more days, a process known as "training", to burn off dust and corona points in the chamber. The singles rate of an RPC trained for three days is typically <0.1 Hz/cm^2. The singles rate will drop significantly below this if the training lasts for more than one month. Figure 8.20 show the singles rates at various thresholds of an RPC that had been trained for more than a month.

Although the typical singles rate after training is <0.1 Hz/cm^2 at thresholds above 150 mV, the noise rate, increases significantly when the high voltage is raised above 8 kV.

In cosmic-ray tests of $\sim$600 BES-III RPCs, the average efficiency was 97%, and only 2 chambers had an efficiency less than 92%. Figure 8.21a shows the efficiency distribution; the efficiency was obtained without excessive chamber noise. Figure 8.21b shows the singles rates of the RPCs. The most probable noise rate was $\sim$0.08 Hz/cm^2. Only 1.5% of these tested chambers had a noise rate higher than 0.3 Hz/cm^2.

8.3.1 RPC Design

The above measurements were made with one dimensional readout of the RPCs. For the Daya Bay Experiment, we are planning to use RPCs with readout in two dimensions in order to get both the x and y coordinates of the cosmic muons. Four gas gaps will be combined to form a module. Each gas gap will be read out by x or y strips such that each module provides two x and two y measurements of a cosmic muon. The four layers (a layer is defined as a gas gap with a x or y strip readout) are electrically shielded from one another to avoid cross talk. The structure of a single 4-layer module is shown in Fig. 8.22.

Plastic spacers are placed at regular intervals in the gas gap to precisely maintain the gap distance.

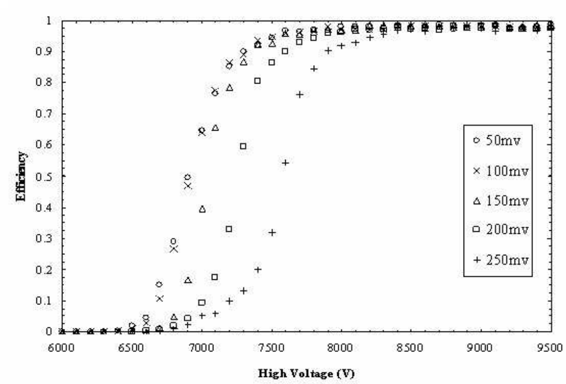

Fig. 8.19. Efficiency of the BES-III RPC versus high voltage for different thresholds.

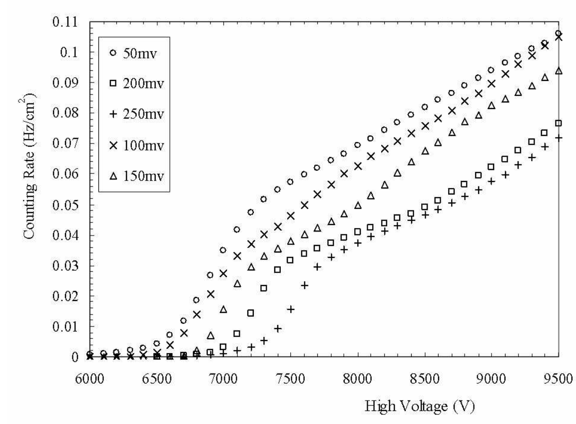

Fig. 8.20. Noise rate of the BES-III RPC versus high voltage for different thresholds.

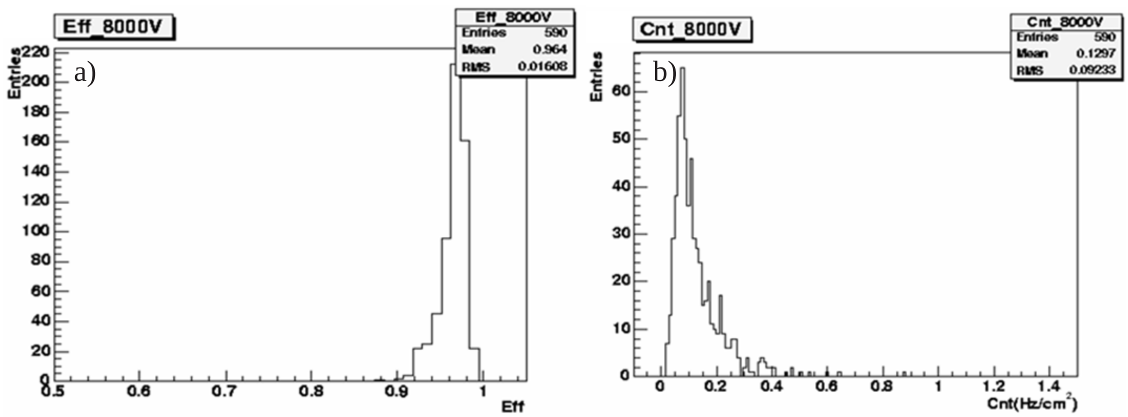

Fig. 8.21. Distribution of tested RPC a) efficiencies and b) singles rates.

These spacers are a source of dead space. Therefore, within each module, spacers in different layers will be offset, resulting in no aligned dead space. Also, as discussed in Section 8.3.2, modules will overlap at the edges, so there will be no inter-module dead space.

Bakelite RPCs as large as 1 m$\times$2 m are straightforward to manufacture. Two of these will be bonded side by side to make a single 2 m$\times$2 m unit. The chambers will be read out by strips of $\sim$25 cm pitch. Thus each module will have 32 strip channels, a good match to the front-end cards (FECs) which have 16 channels per card. To provide adequate module overlap and extend the tracker an extra 1 m on all sides of the pool, it will be necessary to cover an area of 18 m$\times$18 m at the far hall and 18 m$\times$12 m at each of the two near halls. This will require a total of 189 modules, each slightly larger than 2 m$\times$2 m to provide adequate inter-module overlap, and a total of 6048 readout strips. Including spares we will manufacture a total of 200 modules and 6400 readout channels.

RPC front end electronics and trigger system are discussed in Section 9.1.3.

8.3.2 RPC Mounting

Figure 8.23 shows a candidate scheme for mounting the RPCs on a flat sliding roof over the water pool. The roof will be divided into two sections and the RPCs mounted in a way that allows the sections to slide

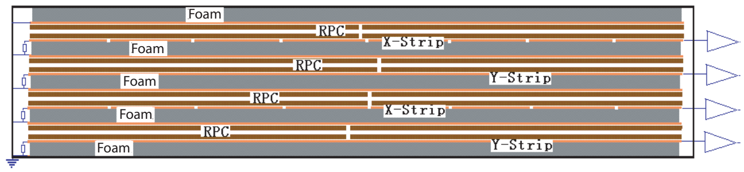

Fig. 8.22. Structure for a four-layer RPC module.

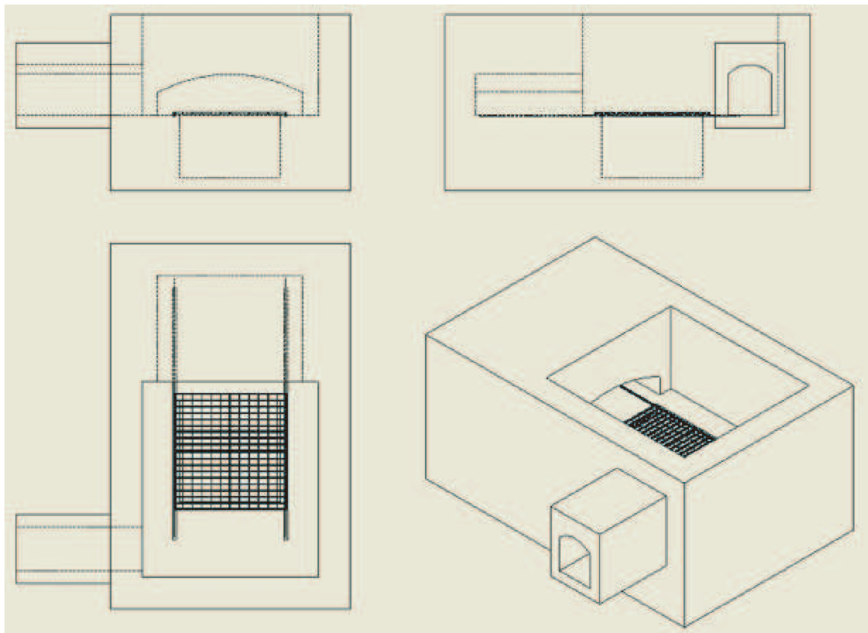

Fig. 8.23. Sliding roof mount for RPC modules above the water pool.

independently. A slot in the wall allows the back half of the roof to slide out of the way to allow access to the back AD(s) from above. If access to the front AD(s) is required, both sections of the roof are slid backwards. Figure 8.24 is a closeup of a roof section showing the wheels which are spaced about 1 m apart. The carriage holds the RPCs about 50 cm above the surface of the water. The RPCs extend 1 m beyond the edge of the pool in all directions. The primary support elements are HM300x200† steel I-beams spaced 1 m apart connected by cross-members. The 4-gap RPCs modules are overlapped to avoid dead regions associated with the chamber frames. The arrangement is shown in Fig. 8.25. Each module in a row is tilted to overlap its neighbor sufficiently that the dead regions of the two modules do not line up. Alternate rows are raised to overlap the intervening rows.

8.3.3 RPC Performance

Taking into account inefficiencies due to dead-spaces, we expect the overall efficiency of a single layer to be $\varepsilon \sim$96%. If we adopt the definition of a track as hits in at least three out of the four layers within an area of $\sim$50 cm$\times\sim$50 cm, the tracking efficiency is calculated to be at least 99.1%. Assuming a conservative bare chamber noise rate, r, of 1.6 kHz/m^2 (twice the BES-III chamber measurements), a signal overlap width τ, of 25 ns (40 MHz clock rate), and a coincidence area, A, of 0.25 m^2, the accidental rate would be about 6×10^{-5} Hz/m^2. For the far hall, this gives a total accidental rate of 0.02 Hz and a negligible contribution to the deadtime in the case that a muon signal is defined by a track in the RPCs alone (*c.f.* the cosmic ray muon

†These are similar to S12x50 I-beams.

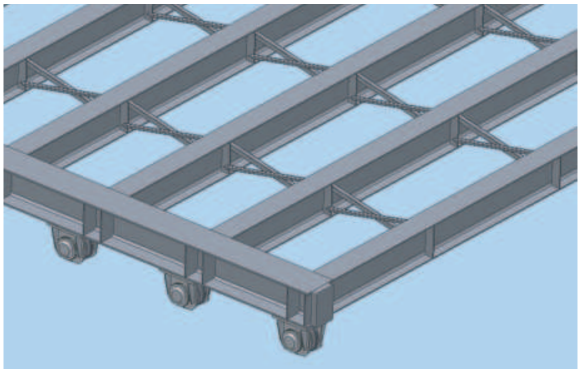

Fig. 8.24. Detail of sliding roof support over the water pool. Each section moves on multiple wheels.

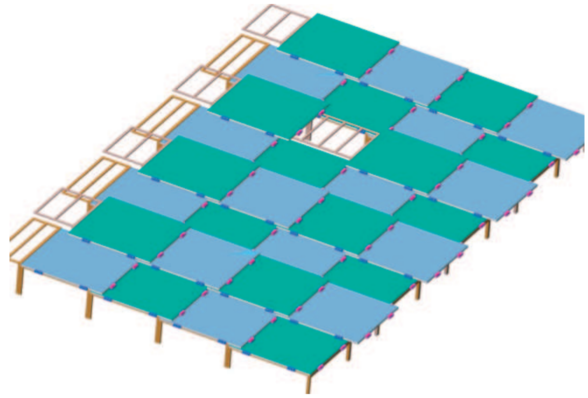

Fig. 8.25. Overlapping RPC modules.

rate of 16 Hz in the Far Hall). A test of a 3 layer configuration with prototypes of the Daya Bay chambers, using a track definition of two out of three planes hit, found a coincidence efficiency of 99.5$\pm$0.25%, which is consistent with that calculated. The efficiency curves are shown in Fig. 8.26.

Initial simulation results based on measurements of radioactivity in the Aberdeen Tunnel predict singles rates from radioactivity of $\sim$650 Hz/m^2

Note that when the RPCs are added to the simulation of the veto system efficiency, they raise the overall efficiency of the three components of the system in OR to 99.4%. When the probability of each muon to create a fast neutron background event as a function of distance of the muon trajectory to the nearest AD is taken into account, since the muons that are missed are those furthest from the ADs, the effective efficiency will meet the 99.5% requirement.

8.3.4 RPC Gas System

The RPC gas system will be similar to that used in the BELLE [3] and BABAR [9] experiments, in which a gas mixing systems distributes gas to the individual RPCs through simple "flow resistors", with the output flow from each chamber separately monitored by a low-cost electronics bubbler [10]. A high-level diagram of the system is given in Fig. 8.27.

Mixing of the chamber gases is performed with mass flowmeters, as sketched in Fig. 8.28. It will be advantageous to use "drop-in" modular mixing components recently developed for the semiconductor processing industry, such as the Integrated Gas System of Fujikin [12].

The electronic bubbler system [10] monitors the chamber gas flow by counting gas bubbles in a small oil bubbler as they pass a photogate, as indicated in Fig. 8.29. Detailed histories of the input and output gas flow will be available via the online slow-control system.

The gas will be input from multiple, switchable sources to minimize interruptions of the gas flow during chamber operation. However, the gas flow rate will be only $\sim$1 volume per day, so that short interruptions of the flow will be of little consequence.

An extensive safety system with status monitors and interlocks will be implemented via the slow-control system. For a recent example of a muon-chamber-gas safety system, see [11].

8.3.5 RPC High Voltage System

The RPC high voltage system is composed primarily of commercial parts from CAEN [15]. All gas gaps will be operated with an $\sim$8000 kV gap. This will be achieved by using $\sim$5.5 kV positive supply in conjunction with a $\sim$2.5 kV negative supply. The positive supply will be the A1526P model, which provides

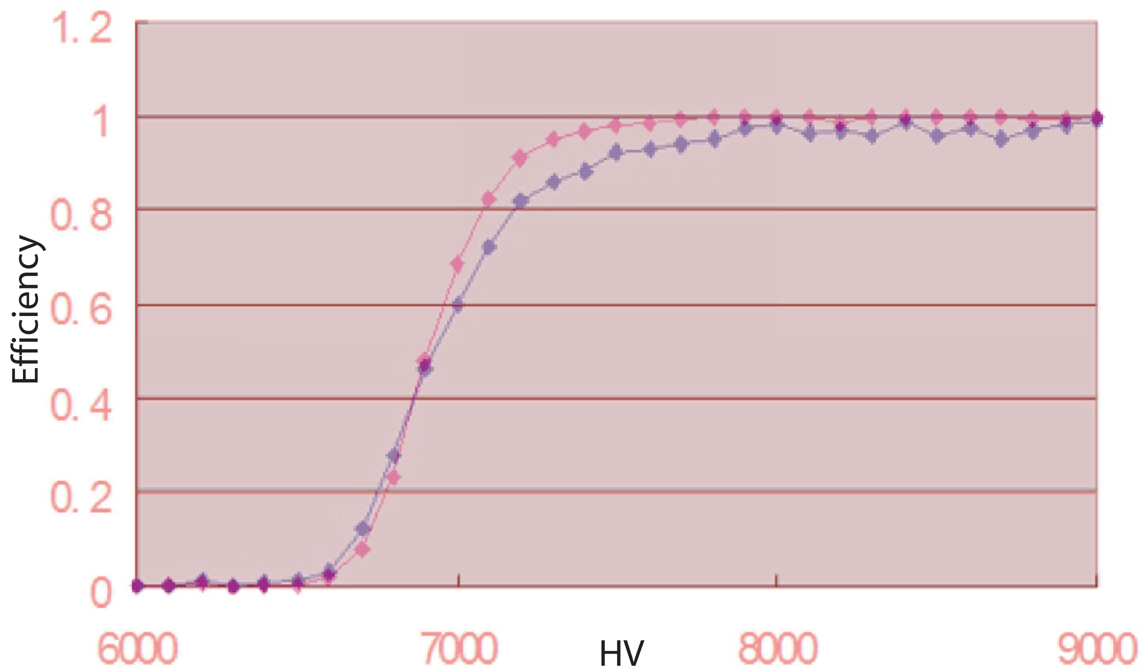

Fig. 8.26. Efficiency as a function of gap voltage for the individual modules of the Daya Bay prototype RPCs (blue) and for the system when two out of three hit modules are required (red).

up to 15 kV at 1 mA in each of six channels. Two cards will be used at each site. At the near sites each positive spigot will supply HV to 18 2 m by 2 m RPC planes with an expected current draw of less then 500 μA, while at the far site each channel will supply 28 gaps with a current draw of less then 700 μA. The negative supply will be the A1932AN, which has 48 channels at up to 3 kV and 0.5 mA. Again two cards will be used at each site and up to 4 RPC planes will be powered by each channel with a per channel current of less than 100 μA. At each site the high voltage will be powered and controlled by a CAEN multichannel power supply mainframe (model SY1527LC) which will house both the positive and negative supply cards.

8.3.6 Plastic Scintillator Strip Backup Option

Plastic scintillator strips serve as a backup option for the top tagging system. We propose to use the extruded plastic scintillator strip technology developed by MINOS, OPERA and other previous experiments. The parameters of this system are shown in Table 8.3.

The scintillators would be arrayed in the manner described above for the RPCs, *i.e.* there would be four layers mounted on the sliding roof. In this case, as for the RPCs, a triple coincidence would be demanded.

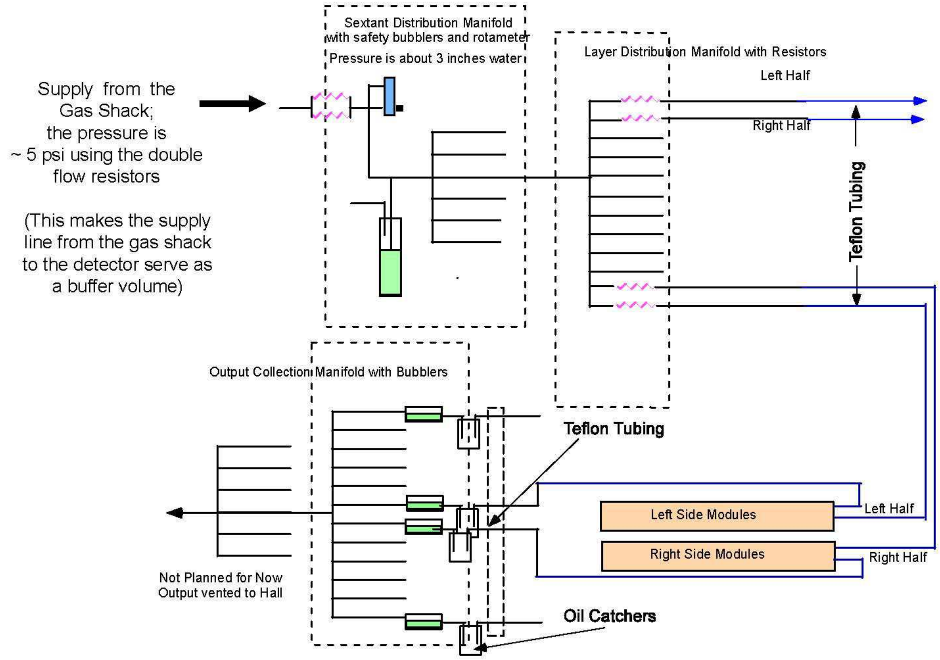

Fig. 8.27. Overall process diagram of the RPC gas system. From [11].

8.3.6.1 Scintillator Strip Design

All the scintillators will be of the same type: 6.02 m$\times$0.2 m$\times$0.01 m extruded polystyrene, co-extruded with a coating of TiO_2-doped PVC. Five 1 mm Kuraray Y-11(200) S-type wavelength-shifting fibers will be glued into 2 mm deep $\times$ 1.6 mm wide grooves in the plastic using optical glue [16]. Six such scintillators will be placed in a single frame and read out as one 1.2 m-wide unit. Figure 8.30 shows the cross section of one scintillator.

8.3.6.2 Scintillator Strip Photoreadout

A $1\frac{1}{8}$-inch photomultiplier tube such as a Hamamatsu R6095 or Electron Tubes 9128B will be used to read out 30 fibers on each end of the six-scintillator module. The PMTs will be run at positive HV, via a system similar to that discussed in Section 6.4.5. Calibration will be via thin-film ^{241}Am sources placed near the ends of the scintillators. The sources provide about 400 Hz of $\sim$0.5 MeV (visible) signals. Cosmic ray muons provide supplementary calibration signals. In the worst case, the Far Hall, the rate of these is 0.3 Hz/counter.

8.3.6.3 Counter Housing and Support

The counters will be mounted on a simple system of strong-backs supported by the sliding roof. Six scintillator strips will be read out together into two PMTs, one on each end. The fiber ends are dressed to have an equal length of $\sim$80 cm. They will be routed through a molded cookie, gathered into a single bundle, squared off and glued to a transparent cookie that is in turn glued to the PMT. Figure 8.31 shows the design of the routing cookie.

8.3.7 Scintillator Strip Performance

We base our expectation of performance on that of the prototype OPERA target tracker scintillators [18]. Figure 8.32 shows the yield of photoelectrons versus distance to the photomultiplier tubes. Note that our

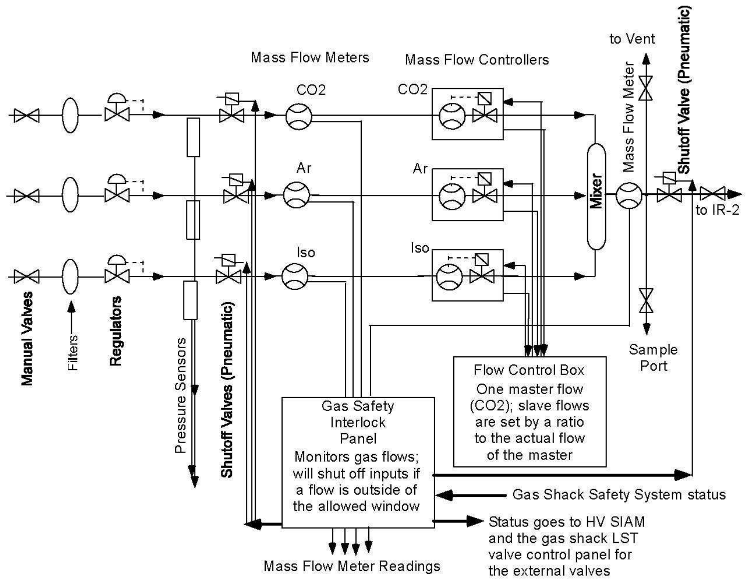

Fig. 8.28. Process diagram for the gas mixing subsystem. From [11].

counters are 6 m long, a point at which the OPERA strips yield about 6 p.e.

The OPERA strips are 26 mm wide by 10.6 mm thick. Our strips are 200 mm wide by 10 mm thick. The MINOS GEANT3 Monte Carlo was adapted to compare the two cases. For collection into the wavelength-shifting fibers, the fraction of OPERA light collection efficiency for 4, 5, and 6 fibers per 20 cm is 0.74, 0.89, and 1.02 respectively. OPERA uses Hamamatsu H7546-M64 PMTs, which have a photocathode efficiency about 80% as high as either of the single-anode tube we are planning to use. Thus any of the 4–6 fiber cases should achieve performance similar to that of OPERA. Tests on a short prototype indicate performance consistent with this estimate. We choose 5 fibers, which nominally should give 1.15 times OPERA performance in our system. The single photoelectron pulse height distribution will reduce the effective number of photoelectrons by a factor of (1 + the variance of the distribution). With PMTs of the type discussed, this will result in an inefficiency of $\sim$0.6% in the worst case (hit at one end of the counter) if a two-end coincidence is required. An upper limit on the position resolution is given by the granularity of the counters:

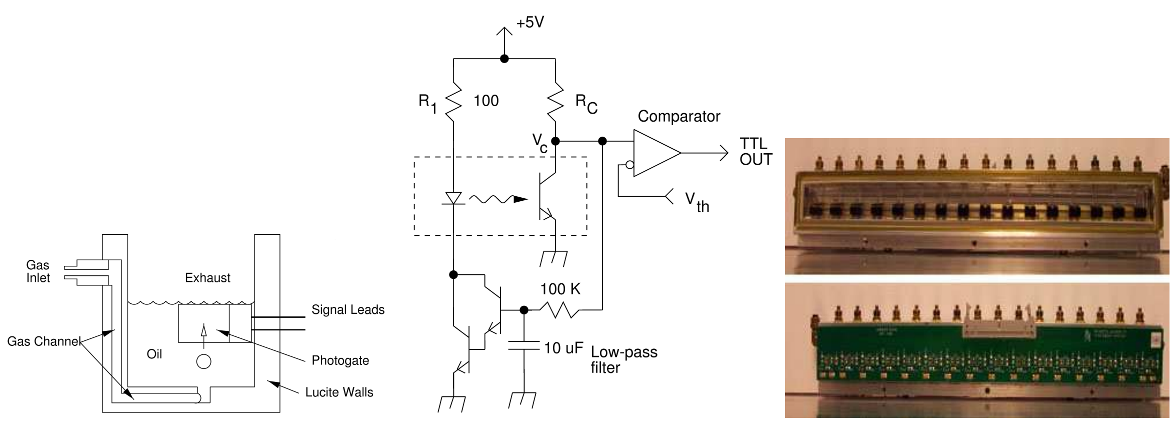

Fig. 8.29. concept, circuit diagram and photographs of the electron bubbler system. From [10].

Name	value	unit
number of strips	2520	
length of strip	6.02	m
width of strip	0.2	m
thickness of strip	1	cm
fibers/strip	5	
length of fiber	7.6	m
diameter of fiber	1	mm
strips/module	6	
modules	420	
phototubes	840	

Table 8.3. Parameters of scintillator strip detectors

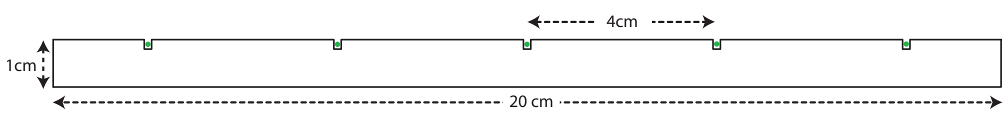

Fig. 8.30. Cross-section of a single scintillator strip.

$\sigma_x = 120\text{cm}/\sqrt{12} \approx 35\,\text{cm}$. For a muon that hits two sides of the pool, the resolution on the position at the center of its trajectory through the pool will be $\sim$25 cm. End-to-end timing and pulse height are expected to improve this. A timing resolution of 1 ns will contribute $\sim$15 cm to the resolution along the counter and $\sim$11 cm to the resolution at the center of the trajectory for through-going muons.

Plastic scintillators are sensitive to the ambient radioactivity from rock. Tests of these rates were carried out with a scintillator telescope in the Aberdeen Tunnel in Hong Kong [19], which has similar granite to that of Daya Bay. A GEANT4 simulation matched the singles and coincidence rates of the two 2.5 cm-thick counters to within a factor $\sim$1.5. The relative γ suppression versus cosmic-ray muon efficiency could then be predicted as a function of threshold for any configuration of scintillation counters. Several configurations were studied. Figure 8.33 shows the result for a configuration of four layers of 1 cm thick scintillators for a trigger demanding that three of the layers fire in coincidence. This arrangement matches the baseline RPC configuration in number of layers, trigger scheme, approximate weight and approximate cost. As can be seen, a threshold of 0.75 MeV on each counter (*c.f.* $\sim$2 MeV deposit by a muon), reduces the γ rate by a factor of more than 10^6. This would give a γ-induced rate of $\sim$10 Hz for the Far Hall, which is the worst case.

8.3.8 Scintillator Strip Front-End Electronics

Once again, the electronics and readout discussed in Section 8.2.3 would be adequate for this system. However since it is not necessary to measure energies above a few MeV, a smaller dynamic range would be acceptable. Whether it is worth it to develop separate electronics for this case is under study. In any case the readout would be similar to that discussed for the AD.

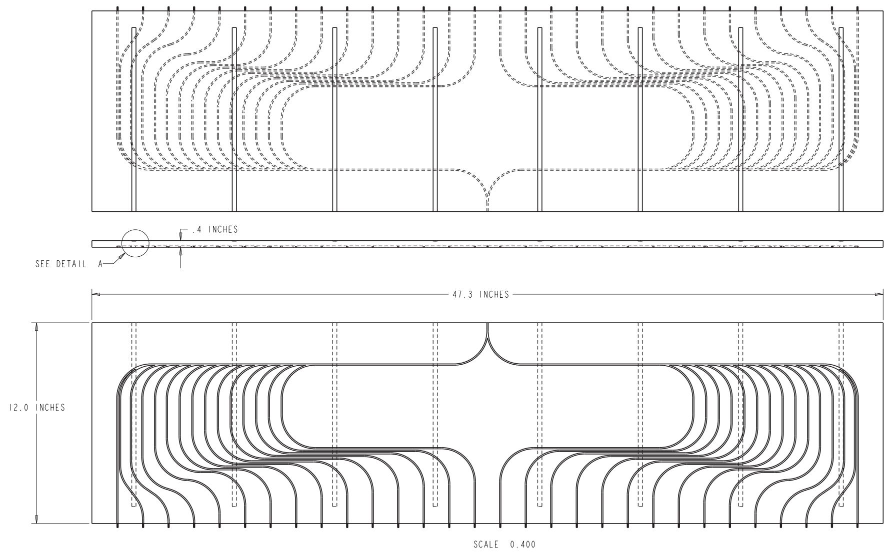

Fig. 8.31. Cookie for routing fibers to PMT.

Component	Number	Source
PMTs/bases	1400	Hamamatsu/ET/Photonis/in-house
PMT electronics	1400	IHEP
RPCs	800	IHEP
RPC FEEs	6400	USTC
PMT support structure		IHEP
RPC roof support		IHEP

Table 8.4. Components of muon system

8.4 Manufacturing Plan.

8.4.1 Commercial Components and Where to Get Them

8.4.1.1 Water Shield Commercial Components

The main commercial components are the $\sim$600 8-inch phototubes. We are considering the three manufacturers, Hamamatsu (R1512), Electron Tubes (9354KB), and Photonis (XP1806). In addition there approximately 500 legacy PMTs from the MACRO experiment, most of which can be used in the muon system. Bases may also be bought from the manufacturers although we are leaning toward fabricating them ourselves. We will test all the MACRO PMTs to determine how many new PMTs must be purchased. A decision on the type of new PMT to be purchased must be made by October of 2007. Since the PMT requirements of the AD system are more stringent than those of the veto, in order to minimize the overhead of having multiple PMT types and to get the benefit of possible volume discounts we will use the same PMTs as that system, unless these is a significant financial penalty for doing so. If we purchase the PMTs (R5912) and bases from Hamamatsu, they can deliver approximately 200/month to Daya Bay starting three months after the order is placed. Thus if the order is placed in October of 2007, PMTs will begin to be delivered in January of 2008. The complete order for the muon system and the ADs could be completed by April of 2009. Sufficient PMTs for both the ADs and the muon system of the Daya Bay Near Hall could be delivered by May 2008. The HV supplies will be commercial (probably from CAEN).

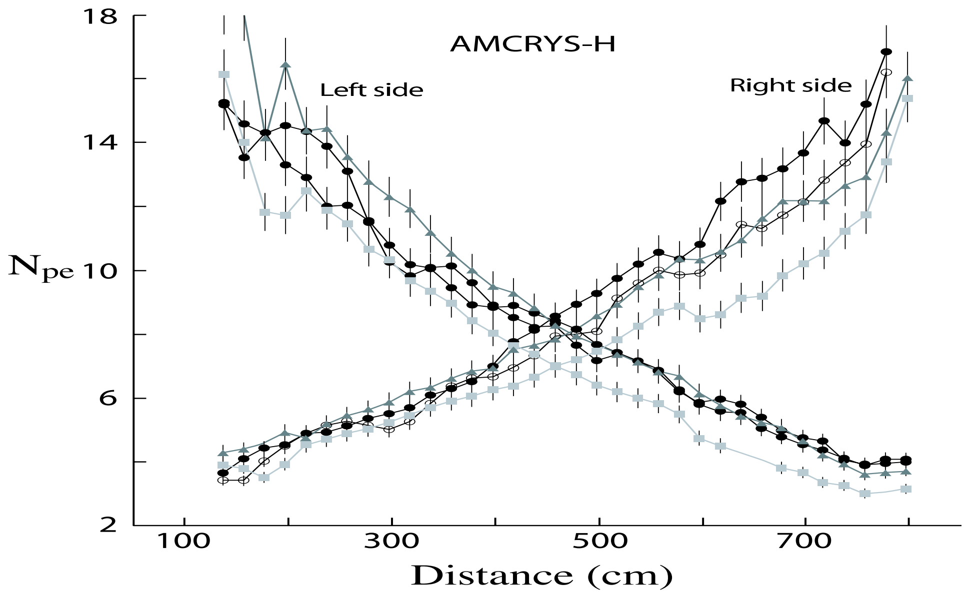

Fig. 8.32. Number of photoelectrons detected on each side of several AMCRYS-H plastic scintillator strips versus the distance to the photomultipliers (from Dracos *et al.*).

8.4.1.2 Commercial Components for RPCs

The production of the Daya Bay RPC chambers will take place in Beijing, China. A local company, called Beijing Gaonengkedi Science and Technology Co. Ltd. (GNKD), will be contracted to produce all the bare RPCs. This company has the experience of producing 1500 similar bare RPCs for the BESIII muon detector. The company has started the preparation work for the production of Daya Bay RPCs. A 2 m $\times$ 2 m RPC prototype module consisting of 4 gas gaps will be produced in March 2007.

GNKD will obtain its Bakelite sheets from an outside supplier. Right now, a few Bakelite production companies, including the one which produced the Bakelite plates for the BESIII RPC detectors, are under consideration. Once the Bakelite producer is selected, the production of all the Bakelite plates will take only about 20 days, tentatively scheduled from May to June 2007.

All the RPC bare chambers will be assembled in GNKD. The assembly procedure includes gluing the spacers between the Bakelite sheets and applying a graphite layer on top of each Bakelite sheet. All the production fixtures, including a large clean room, are in place. The staff at GNKD will test the chambers for gas tightness and HV integrity. The bare chambers which meet the acceptance criteria will be transferred to IHEP for further testing and assembly into modules. The RPC bare chamber production rate will be about 10 m^2 per day day (include the weekends). The Daya Bay muon tracker requires about 3500 m^2 of RPCs; the bare RPC production can be accomplished in about 1.5 years. (3500 m^2/10 m^2/day s = 350 days.)

8.4.2 Components to be Fabricated In-house

8.4.2.1 Components to be Fabricated In-house for Water Shield and Outer Water Sections

8.4.2.1.1 PMT base fabrication

The main components to be fabricated for the water shield are the PMT bases if we fabricate them ourselves. This fabrication will include the 40-m Teflon cables for transmitting HV and signals that are soldered to the bases - the other end has an SHV connector. The mechanical parts of the water proof potted

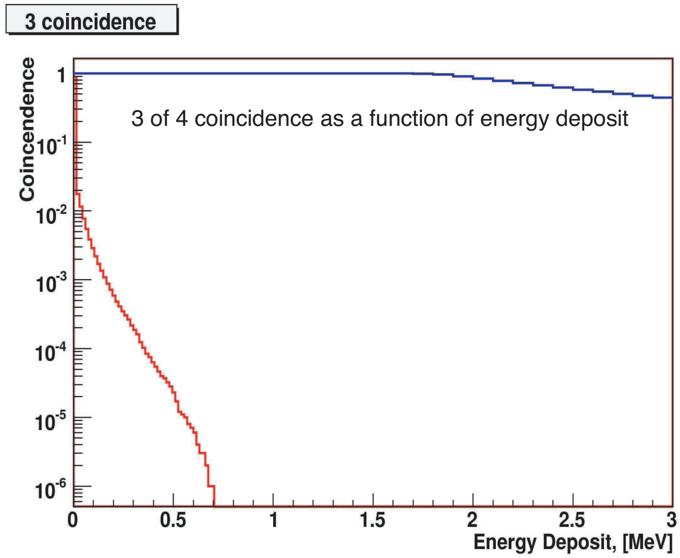

Fig. 8.33. The blue line is the efficiency for a cosmic ray muon as a function of the single counter threshold when 3 out of 4 layers of 1 cm scintillator are demanded. The red line is the suppression factor for ambient γ-rays in the same configuration and threshold.

PMT base housings will be designed and fabricated in UCLA. The design will commence in April 2007. We expect to complete the design and prototyping of these bases by the end of July 2007. Based on similar designs, the UCLA machine shop has estimated that the production of each mechanical housing will take 2.5 hours. Assuming availability of founding by October 1, 2007, we expect to produce 100–200 housings per month after an initial setup period of 1 month. This will result in delivery of 100–200 units per month starting early January 2008.

The PMT base printed circuit fabrication and the assembly will be done by external vendors. Based on past experience we expect that by January 2008 we will have 500 PMT bases tested and available for shipment to China. The remaining bases could be delivered at a rate of 200–400 units per month following the initial delivery.

The PMT base printed circuit boards and the housings will be assembled in China mainly by the Chinese members of the Daya Bay collaboration. The assembly process involves attachment of the PMT bases to the PMTs and injecting the housings with potting compound. This will result in a sealed PMT assembly. The procedures and quality assurance steps to pot and seal the PMT-base assemblies will be developed during the initial design and prototyping of the bases. Therefore, an initial 100% underwater testing program of the first 20–50 assemblies followed by a random sample testing of 5% of the assemblies should suffice to insure the integrity of the seals.

The risks involved in the delivery schedule are minimal. The main risk is the delay in availability of funding. The production work will not start without the funding. In addition there is a minor risk due to the fact that 50% of the initial production effort coincides with holidays in the US. This could reduce the initial delivery to about 250. Every effort will be made to start the project on October 1, 2007 to avoid these delays.

Additional risks involve failure of a certain percentage of the PMT/base assemblies due to improper sealing or breakage of PMT bulbs. Based on past experience we expect these to be at a level of less than 0.2%. Please note that the PMT failures, while rare, will be detected before the bases are glued in permanently. This detection will be done in two distinct stages:

1. During the initial physical inspection stage after the delivery of the PMTs
2. During the PMT burn-in process. During this period each PMT/base will be tested with LED pulsers for a duration of 2–4 weeks.

The main ES&H challenge of the base fabrication is the potting compound which needs to be handled under a hood. The bases need to be tested at high voltage, but the power supplies don't put out much amperage so the electrocution hazard is not high. In addition the connections made are only SHV and there is no exposure to open HV during the testing stage.

Since a single cable (RG-303U) will carry both (+) HV and signal, these must be splitters to separate the two. The components for these will be procured from an outside vendor and the machining of panels and installation of the electronics will be done at UCLA.

8.4.2.1.2 PMT supports

These will be nearly identical to those in the antineutrino detectors. See Chapter 6 for a discussion of manufacturing these.

8.4.2.2 Components to be Fabricated In-house for RPCs

8.4.2.2.1 RPC fabrication

The next level RPC assembly and testing will be done at IHEP. Four steps, each supervised by an IHEP staff member (or an experienced graduate student), and assisted by technicians and students, are planned:

1. Bare chamber training and testing: the bare chambers will be trained for 1–3 days. The trained RPCs will be tested for performance including dark current, singles rate, and efficiency.
2. RPC module assembly: the trained chambers, readout strips, readout electronics (mainly the front-end cards), and gas and HV connections will be assembled into 2 m $\times$ 2 m modules, each consisting of 4 layers of RPCs and readout strips.
3. Module testing: the performance of the fully assembled modules will be tested with full readout electronics.
4. Pre-installation module testing: simplified testing will be performed on the modules after transport from IHEP to the Daya Bay site.

The present manufacturing schedule does not pose any risk to the overall schedule of the Daya Bay Experiment which will start taking data in June 2010. The main time bottleneck is the bare chamber production. The other steps generally proceed faster than the chamber production, although the testing of chambers and modules may take some time to set up at the beginning.

The main ES&H challenges of the RPC manufacture will be the adhesive used in the chambers which must be handled under a hood, the isobutane component of the gas used for testing the chambers, and the HV needed in the QA tests. Single RPC panels when assembled weigh about 25kg so can be handled without cranes. Gases will be premixed in non-flammable proportions. The factory floor is level and the building is well-ventilated, minimizing ODH hazards. Routine testing will involve only one chamber at a time, reducing the electrical hazard. Open HV connections will be avoided and surge trips will be built into the circuits.

There are technical, cost and schedule risks associated with the RPC fabrication. We assume most of the technical risks (unacceptable efficiency, stability, noise rate) will be eliminated by R&D now in progress. The main cost and schedule risks are related to possible underestimates of the labor required to assemble and test the chambers. These are unlikely because of the recent and very relevant experience of GNKD in RPC fabrication.

8.4.2.2.2 RPC support manufacture

The RPC support structure will be designed at IHEP and fabricated by an outside vendor.

REFERENCES

1. Hubbell, J.H. and Seltzer, S.M. (2004), "Tables of X-Ray Mass Attenuation Coefficients and Mass Energy-Absorption Coefficients" (version 1.4). [Online] Available: http://physics.nist.gov/xaamdi [2006, August 2]. National Institute of Standards and Technology, Gaithersburg, MD.
2. J. W. Zhang *et al.*, Nucl. Instr. Meth. A **540**, 102 (2005).
3. A. Abashian *et al.*, Nucl. Instr. Meth. **A449**, 112 (2000).
4. M. Aglietta *et al.* [LVD Collaboration], "Measurement of the neutron flux produced by cosmic-ray muons with LVD at Gran Sasso," arXiv:hep-ex/9905047.
5. R. Becker-Szendy *et al.*, "IMB-3: A Large water Cherenkov detector for nucleon decay and neutrino interactions," Nucl. Instr. Meth. A **324**, 363 (1993).
6. Y. Fukuda *et al.*, "The Super-Kamiokande detector," Nucl. Instr. Meth. A **501**, 418 (2003).
7. R. Aleksan, P. Bourgeois, G. Vasseur, A. Cormack, R. McAlpine and R. Sequira, "Ageing of the DIRC phototubes in ultra pure water," Report DAPNIA-00-10, http://dphs10.saclay.cea.fr/Doc/Publications/Archives/dap-00-10.pdf
8. J. Boger *et al.* [SNO Collaboration], "The Sudbury Neutrino Observatory," Nucl. Instr. Meth. A **449**, 172 (2000) [arXiv:nucl-ex/9910016].
9. S. Foulkes *et al.*, *Gas system upgrade for the BaBar IFR detector at SLAC*, Nucl. Instr. Meth. A **538**, 801 (2005).
10. M. Ahart *et al.*, *Flow Control and Measurement for RPC Gases*, Belle Note 135 (Aug. 26, 1996), http://wwwphy.princeton.edu/m̃arlow/rpc/gas/flow.ps
11. R. Messner, *The LST Gas Mixing System* (Oct. 4, 2004), http://puhep1.princeton.edu/m̃cdonald/dayabay/BaBar_gas_system/messner_LST_gas_system.pdf
12. *Fujikin Integrated Gas System Brochure*, http://www.technofittings.com/pdf/igs/igsbroc.pdf
13. G. Benelli *et al.*, *The* BaBar *LST Detector High Voltage System: Design and Implementation*, IEEE Nucl. Sci. Symp. Conf. Rec. **2**, 1145 (2005), http://www.slac.stanford.edu/cgi-wrap/getdoc/slac-pub-12069.pdf
14. Extensive documention of the BaBar LST high voltage system is available online at http://www.physics.ohio-state.edu/k̃laus/LST/HV/osu/OSUHV.htm
15. CAEN Short Form Catalog 2007.
16. SHELL EPON 815C with hardener TETA @ 13%.
17. C. James, private communication.
18. M. Dracos *et al.* Phys. At. Nucl **67** (2004) 1092-1096 (Yadernaya Fizika, **67** (2004) 1120-1124).
19. K. Luk et al., Daya Bay Internal Document, Nov 2005.

9 Electronics, Trigger, and Data Acquisition Systems

The readout electronics and the trigger event selection, with estimated rates, are presented along with the timing synchronization between all of the electronic elements. The processing of the trigger data from the front-end modules through data storage is discussed, along with the detector control system. Each detector module (AD, inner muon, outer muon, RPC) is designed to have a readout system independent of the other modules, except for a common clock signal. We are building into the system the capability to readout a module based on information within an adjoining module (cross triggers).

9.1 PMT Front-End Electronics

The Front-End Electronics (FEE) readout system is designed to process PMT output signals. Even though the requirements for the muon system are not as stringent as those for the AD, we plan to use the same FEE electronics for both systems. The essential functions are as follows:

- Provide fast information to the trigger system
- Determine the charge of each PMT signal to measure the energy deposit in the liquid scintillator or water. This will enable us to identify muon events, select neutrino events, reject backgrounds, and deduce the antineutrino energy spectrum.
- Provide precision timing information (PMT-to-PMT) that can be used to reconstruct the location of the interaction within the detector, to study and reject potential backgrounds, and increase the precision of the measured trigger signals.

9.1.1 Requirements for the PMT Front-End Electronics

When a reactor antineutrino interacts within the target volume, its energy is converted into ultraviolet or visible light, some of which will ultimately be transformed into photoelectrons (p.e.) at the photocathodes of the PMTs. Monte Carlo simulations predict (for a given PMT) that the number of p.e. produced per antineutrino event will range from 0 to 50, depending on the location of the interaction within the detector. The passage of cosmic muons through the detector may produce as many as 2000 p.e. in individual PMTs. It seems prudent to provide sufficient headroom to accommodate more photo-electrons than the current simulation predicts; as such, we choose a full dynamic range from 1 to 4000 photoelectrons. This range is more than sufficient to accommodate the needs of the Cherenkov water shield. In order to maintain precision below 400 p.e., two pairs of amplifiers and ADCs will be used, resulting in a fine range from 0–400 p.e., and a course range from 0–4000 p.e.

The intrinsic energy resolution for a single p.e. is typically about 40% with some variation from PMT to PMT, while the threshold for a PMT signal is constrained by the dark noise, typically at the level of about 1/3–1/4 of a p.e. The electronic noise and charge resolution of the readout electronics should not further contribute to these limitations. Therefore, we require the RMS noise due to the electronics to be less than 10% of a p.e., and the charge resolution of the electronics to be better than 20% of a p.e.

In addition to measuring the pulse size and shape, we can determine (with precision) the arrival time of the signal from the PMT relative to a common stop signal, for example, the trigger signal. The time jitter of a PMT for a single p.e. is about 1–2 ns, caused by the PMT transit time jitter, the PMT rise time, and the time walk effect of the discriminator. The design goal for the time resolution of the readout electronics should therefore be better than 1.0 ns. The dynamic range of the time measurement depends on the trigger latency and the maximum time difference between the earliest and the latest arrival time of light to PMTs. Guided in part by simulations, this range is chosen to be from 0 to 500 ns. By comparing the arrival time at various PMTs, we can roughly reconstruct the event within the detector. Although such a method is more suitable for large detectors similar to KamLAND, it provides an independent measurement which complements the charge-gravity method for small detectors with diameters of several meters. Hence it offers a cross-check of systematic uncertainties and an additional handle for studying backgrounds.

The requirements for the electronics used to read out the PMTs are summarized in Table 9.1.

Quantity	Requirement	Primary Justification
Dynamic Range	0–4000 p.e.	large enough to accept the signals from cosmic muons
Bit Resolution	$<$ 0.1 p.e. @ 1 p.e.	sufficiently fine to resolve 1 p.e. distribution
Noise	$<$10% @ 1 p.e.	electronics should not contribute to overall noise
Time range	0–500 ns	allows for trigger latency and photon propagation
Time resolution	$<$1 ns	reconstruction of event vertex
Sampling rate	$\geq$40 MHz	accurately determine PMT pulse shape
Channels/module	$\geq$16	can fit each AD into one VME crate
VME standard	VME64xp-340 mm	DAQ architecture requirement

Table 9.1. Requirements for the electronics used to read out the PMTs.

9.1.2 PMT Front-End Electronics (FEE) Boards

The PMT readout electronics for each detector module is housed in a single 9U VME crate with up to 16 FEE boards, one trigger board, and one or two fan-out boards. In such an arrangement, moveable boards can be easily realized, and correlations among modules can be minimized. In order to make the readout electronic system simple and easy to maintain, the same front-end electronics (FEE) boards will be used for both the Antineutrino Detectors and Water Shield PMTs.

Each FEE board accepts 16 PMT signals and performs the time and charge measurements. The number of channels over threshold and the total charge observed by the FEE board is fed to the trigger system for a fast trigger decision. After collecting information from all readout boards, a trigger signal may be generated and distributed to each FEE board and used as a common stop for the TDCs. It also initiates readout of the ADC and TDC data.

The input PMT signal is immediately amplified and used to drive three distinct circuits, a discriminator (threshold decision and TDC start pulse), an energy summing circuit (for the energy sum trigger), and a pulse shaping circuit whose output is used to measure the size and shape of the pulse. A simplified circuit diagram of the electronic readout system, showing its main functions, is given in Fig. 9.1.

A stable threshold is set using a 14-bit DAC (AD7247) [15] controlled from the VME processor. This level of precision is required in order to achieve the required TDC time resolution. The rising edge of the discriminator output signal is used to start the TDC. The TDC is realized by using internal resources of a high-performance Field Programmable Gate Array (FPGA) with key components of two ultra high speed Gray-code counters. The first counter changes at the rising edge of an internal 320 MHz clock, while the second one changes at the falling edge. Each time bin is 1.563 ns. The RMS of the time resolution is less than 0.5 ns. The FPGA also uses the discriminator output to increment the NHIT counter.

To measure the charge of the PMT signal, an ultra low-noise FET input amplifier (AD8066) is selected for the charge integrator. A CR-(RC)^4 shaping circuit is used to obtain a smooth signal peak after shaping. An RC time constant of 25 ns is chosen, corresponding to an output signal width (1% amplitude to 1% amplitude) of about 325 ns. The RC implemented using discrete surface mount components. The shaped signal is sent into two amplifiers with different gains, a gain of $\times$10 for the fine range and a gain of $\times$1 for the coarse range. These two analog signals are digitized using two 12-bit Flash ADCs (AD9222) with a 40 MHz sampling rate (one for the course range and one for the fine range). The digitized samples go directly into the FPGA, in which all data processing (*e.g.* range selection, peak finding, data pipelining, pedestal

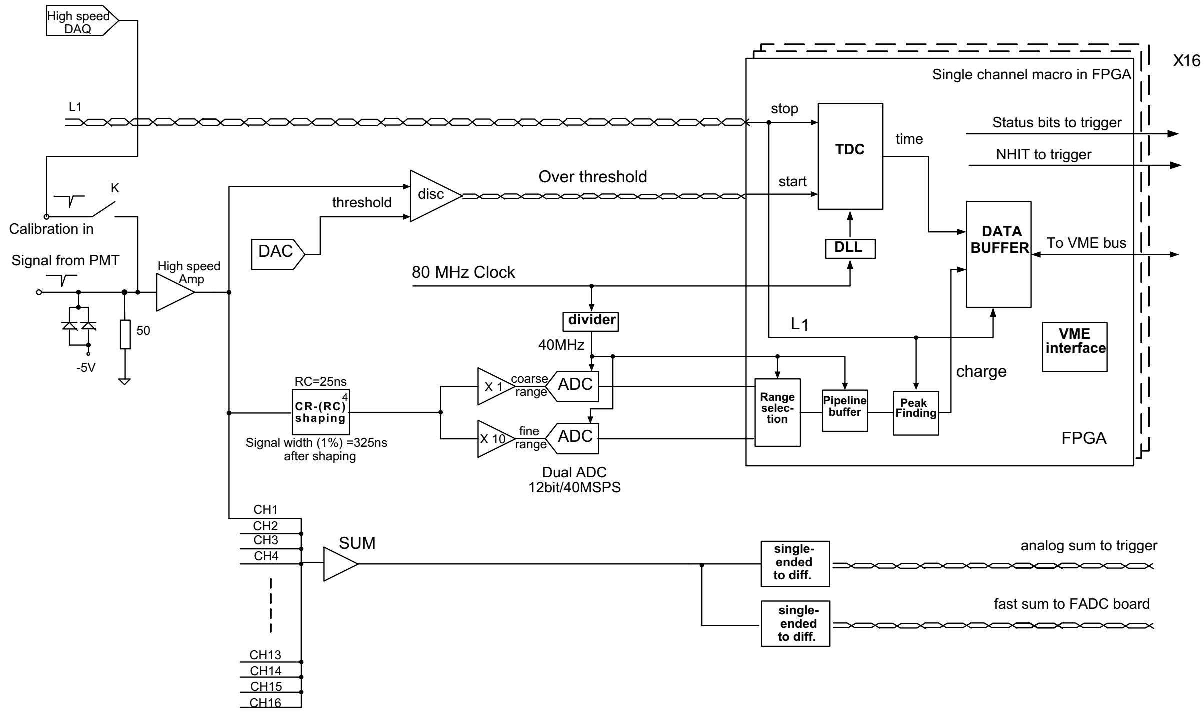

Fig. 9.1. Block diagram of front-end electronics module for PMT readout.

subtraction, nonlinearity corrections, and data buffering) will be implemented. Since data manipulation takes place within the FPGA, we maintain flexibility in choosing how best to record the size and shape of the pulse. At this moment, we anticipate saving between 3 and 5 samples of each waveform, with full digitization an option which would certainly be implemented (at minimum) for a pre-scaled set of pulses.

We also anticipate saving the time-ordered ADC data inside a buffer for up to a few hundred microseconds. This data can be accessed and retrieved on command should we wish to examine the activity within a given detector module prior to, for example, a signal from a different detector module (something we call a cross trigger). Cross triggers will be used to study backgrounds (primarily muon induced backgrounds).

The FEE board has a standard VME A24:D32 interface. Both ADC and TDC data of the triggered event are saved in a buffer, which can store a maximum of 256 events. The data will be readout through the VME backplane by the DAQ system within a reasonable time span.

The last branch is for the energy sum trigger. Signals from all 16 channels are sent into an analog sum circuit. The result is converted into differential signals, one for the trigger board and the other for a 200-MHz Flash ADC board.

The NHIT information is generated every 100 ns according to the number of PMTs over threshold in the current 100 ns period. The NHIT can be from 0 to 16, which is encoded in a five bit binary word that is sent to the trigger board through five pairs of twisted cable. This information is used to form a multiplicity trigger. Overlapping time bins will be employed.

Self testing is accomplished using a programmable pulse generated by a fast on-board DAC chip and sent as a calibrated input to every channel on the board. This may also be used as a calibration.

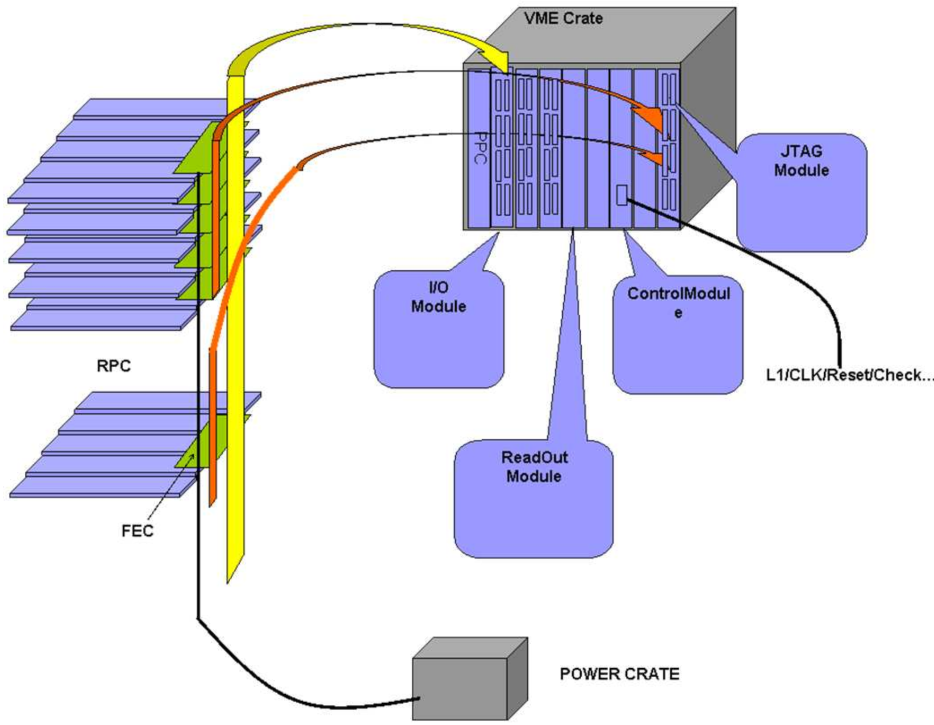

Fig. 9.2. Configuration of the RPC electronics & readout system.

9.1.3 RPC Front-End Electronics

We plan to modify the BESIII RPC readout system for Daya Bay RPC readout. The BESIII RPC readout system consists of a readout subsystem, a threshold control subsystem, and a test subsystem. The readout system, shown in Fig. 9.2, contains a 9U VME crate located above the detector, which holds a system Control Module, a Readout Module, an I/O Module, and a JTAG Module. The system clock will operate at 40 MHz.

The Control Module receives the trigger signals (L1, Clock, Check, and Reset) from the trigger system and transmits them to the Front-End Card (FECs) through the I/O Modules. It also receives commands (such as setting thresholds, testing, etc.) and transmits them to the FECs. The Control Module is also a transceiver which transfers the FULL signal between the Readout Module and FECs.

The VME crate contains several I/O Modules, each of which consists of 12 I/O sockets connected by a data chain. The I/O Module drives and transmits the signals of the clock and trigger to all the FECs, and transmits control signals between the Readout Module and the FECs.

The Readout Module is responsible for all the operations relative to data readout. It not only reads and sparsifies the data from all the data chains (it can read 40 of them in parallel), constructs the sub-event data to save into the buffer, and requests the interrupt to the DAQ system to process the sub-event data, but also communicates the FULL signals to the FECs to control the data transmission. The Readout Module checks and resets control signals to the trigger system and the counting and resetting of the trigger number.

The FECs are located on the RPC detector. Their task is to transform signals from the strips into a bit map, store the data in a buffer and wait for a trigger signal. Events with a trigger will be transmitted in a chain event buffer in the VME readout modules. Data without a trigger are cleared. Analog signals from groups of 16 strips are discriminated and the output read and stored in parallel into a 16-bit shift register, which is connected to a 16-shift daisy chain. A total of 16 FECs compose one FEC Daisy-Chain, which covers 256 strips. The data from each chain, as position information, are transferred bit-by-bit to the readout module in the VME crate through the I/O Modules using differential LVDS signals. Each datum of the chain will be stored temporarily in the relative data chain buffer of the Readout Module. After the data sparsification, the whole data chain will be stored into the sub-event data buffer awaiting DAQ processing.

The JTAG Module gets the FPGA setting command from the VME BUS, transforms the command into the JTAG control timing, and sends it to the FECs. Each of the JTAG Modules has 12 slots on the front-panel of the module, enough to satisfy the requirements of the entire readout system.

When a test command is received by the Control Module, it uses the Test Signal Generator to send timing signals through an I/O Module to a DAC on each FEC. This chip then delivers a test signal to each channel's comparator.

The threshold-setting system consists of the threshold-setting control module in the VME crate, and a threshold-setting generator on the FEC. The principle of the threshold setting circuit is the same as the test circuit. The timing pulses are generated by the threshold controller in the Control Module and sent to the DAC to generate the threshold level at each of the input ports of the discriminators in the FEC.

9.2 The Trigger System

The trigger system of the Daya Bay experiment makes trigger decisions for the antineutrino and muon detectors to select neutrino-like events, muon-related events, periodic trigger events and calibration trigger events. The primary trigger will be based on the multiplicity of PMTs over threshold within a defined coincident window. The trigger will have high efficiency for events which deposit more than 0.7 MeV in the AD enabling a complete energy spectrum analysis that increases our sensitivity to θ_{13}. We will also implement an energy sum trigger. The following sections will describe the requirements and technical baseline for the trigger system.

9.2.1 Trigger System Requirements

The signature of a neutrino interaction in the Daya Bay antineutrino detectors is a prompt positron with a minimum energy of 1.022 MeV plus a delayed neutron. About 90% of the neutrons are captured on Gadolinium, giving rise to an 8 MeV γ cascade. The lifetime of a thermal neutron in the Gd-doped liquid scintillator is about 28 μs. The main backgrounds to the signal in the antineutrino detectors are fast neutrons produced by cosmic muon interactions in the rock or the water, ^{8}He/^{9}Li, which are also produced by cosmic muons, and accidental coincidences between natural radioactivity and neutrons or beta emitters produced by cosmic muons. All three major backgrounds are related to cosmic muons. Since an antineutrino event is a coincidence of the prompt positron followed by a delayed neutron capture, the time interval between these signals is a crucial parameter for the physics analysis. The precision of this interval is linked to the trigger signal which is synchronized to the 80 MHz system clock. The following are the main trigger requirements imposed by the physics goals of the Daya Bay experiment:

The requirements for the trigger system are summarized in Table 9.2.

Quantity	Requirement	Primary Justification
Efficiency	$>$99%	reduce systematic uncertainties
Time of Trigger	known to 13 ns	measurement of neutron capture time
Energy Threshold	$\sim$0.7 MeV	high acceptance for prompt signal
Flexibility	dynamic algorithms	functionality under a variety of conditions
Reproducibility	$<$ a few ns	consistency between AD modules
Redundancy	$>$1 algorithm	ability to measure trigger efficiency

Table 9.2. Requirements for the trigger system.

Trigger efficiency: In the early stages of the experiment, the trigger efficiency is required to be as high as possible for both signal and background, provided that the event rate is still acceptable and will not introduce dead time. After an accurate characterization of all the backgrounds present has been achieved, the trigger system can then be modified to have more powerful background rejection without any efficiency loss for the signal. To measure the efficiency variation, the system should provide a parallel trigger algorithm (energy sum trigger) as well as a random periodic trigger (with no requirement on the energy threshold). A precise spectrum analysis also requires an energy-independent trigger efficiency for the whole signal energy region.
Trigger time stamp: Since neutrino events are constructed offline from the time correlation between the prompt positron signal and the neutron capture signal, each readout crate must be able to accurately time-stamp events with consistency from one crate to the next. The trigger board must provide a local system clock and a global time-stamp to the DAQ and FEE readout boards in the crate. The trigger board in each crate will receive timing signals from a global GPS based master clock system as described in Section 9.3. Events recorded by the antineutrino detectors and muon systems can thus be accurately associated in time offline using time-stamps. It may be possible to use the PMT TDC data to further increase the precision of the trigger time measurement.
Energy dependence: The trigger is required to independently trigger on both the prompt positron signal ($E \geq 1.022$ MeV) and the delayed neutron capture on Gd (photon cascade of $\sim$8 MeV) with very high efficiency. In order to avoid potential bias, we intend to use a multiplicity trigger as our primary trigger (as opposed to an energy sum trigger). The multiplicity trigger must have high efficiency for events with an energy of 0.7 MeV and above. This low threshold requirement fulfils two trigger goals, allowing the DAQ to record all prompt positron signals produced from neutrino interactions, and for background, it allows the DAQ to register enough uncorrelated background events due to either PMT dark noise or low energy natural radioactivity to enable a detailed analysis of backgrounds offline.
Flexibility: The system must be able to easily implement various trigger algorithms using the same basic trigger board design for different purposes such as

- Using different energy thresholds to adapt to the possible aging effect of liquid scintillator, or for triggering on calibration source events which have lower energy signatures.
- Using different hit multiplicities to increase the rejection power due to the uncorrelated low energy background and for special calibration triggers.
- Implementing different pattern recognition for triggering on muon signals in the different muon systems.
- Using an OR of the trigger decision of different trigger algorithms to provide a cross-check and cross-calibration of the different algorithms as well as a redundancy to achieve a high trigger efficiency.

Independence: Separate trigger system modules should be used for each of the antineutrino detectors and components of the muon system. This is to reduce the possibility of introducing correlations between triggers from different detector systems caused by a common hardware failure.

9.2.2 The Antineutrino Detector Trigger System

Neutrino interactions inside a detector module deposit an energy signature that is converted to optical photons which are then detected by a number of the PMTs mounted on the inside of the detector module. Two different types of triggers can be devised to observe this interaction:

- A multiplicity trigger.
- An energy sum trigger.

In addition to physics triggers, the antineutrino detector trigger system needs to implement several other types of triggers for calibration and monitoring:

- Calibration triggers of which there are several types:
  1. Triggers generated by the LED pulsing system that routinely monitors PMT gains and timing.
  2. Special energy and multiplicity triggers used to test detector response using radioactive sources
- A periodic trigger to monitor detector stability and random backgrounds.
- An energy sum and/or multiplicity trigger (prescaled with looser threshold and multiplicity requirements) generated in individual antineutrino detector modules which is initiated by a delay trigger from the muon system. This trigger records events to study muon induced backgrounds.
- A specialized readout of a detector module based on information from a different detector module.

A VME module with on-board Field Programmable Gate Arrays (FPGA)s is used to implement the antineutrino detector trigger scheme outlined in Fig. 9.3 based on experiences gained at the Palo Verde [1] and KamLAND experiments. We will use a multiplicity trigger or an energy sum (or both) to signal the

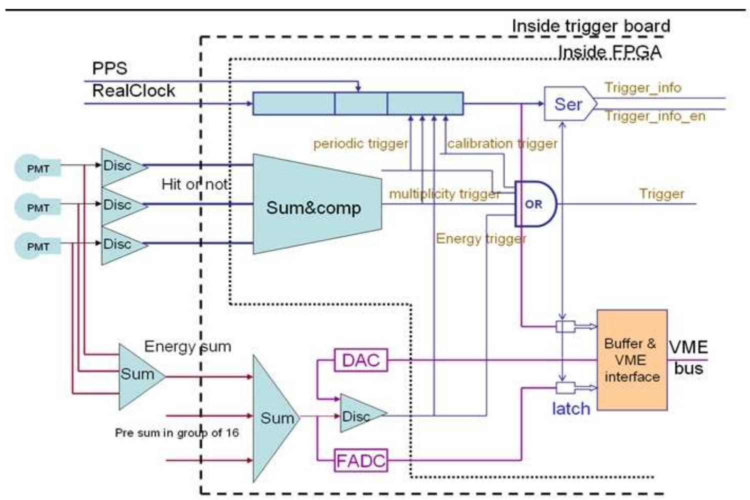

Fig. 9.3. A simplified trigger scheme.

presence of neutrino interactions in the antineutrino detector. These two triggers provide a cross-check and a cross-calibration of each other.

The multiplicity trigger is implemented with FPGAs which can perform complicated pattern recognition in a very short time. FPGAs are flexible and can be easily reprogrammed should trigger conditions change. If necessary, different algorithms can be downloaded remotely during special calibration runs which make use of customized radio-active sources or LED based flashers. As described in Section 9.1, each FEE board delivers to the trigger board a count of the total number of PMTs over threshold. While the trigger board FPGA is capable of complicated pattern recognition algorithms, we expect to begin by implementing a simple multiplicity trigger decision. The dark current rate for the low activity PMTs is typically around 5 kHz at 15° C. For a detector with N total PMTs, a dark current rate of f Hz, and an integration time of

τ ns, the trigger rate R given a multiplicity threshold m is

$$R = \frac{1}{\tau} \sum_{i=m}^{N} i C_N^i (f\tau)^i (1 - f\tau)^{N-i}, \quad f\tau << 1 \tag{33}$$

where C_N^i are the binomial coefficients.

To be conservative, we will assume a PMT dark current rate 10 times larger than expected (50 kHz) when estimating the multiplicity trigger rate due to dark current. A coincidence window of 100 ns will also be used. The rate thus calculated using Eq. 33 as a function of the number of coincident PMTs is shown in Fig. 9.4. We expect that multiplicities of 10 or more PMTs within a 100 ns coincidence window should occur due to dark currents with a rate less than about 1 Hz.

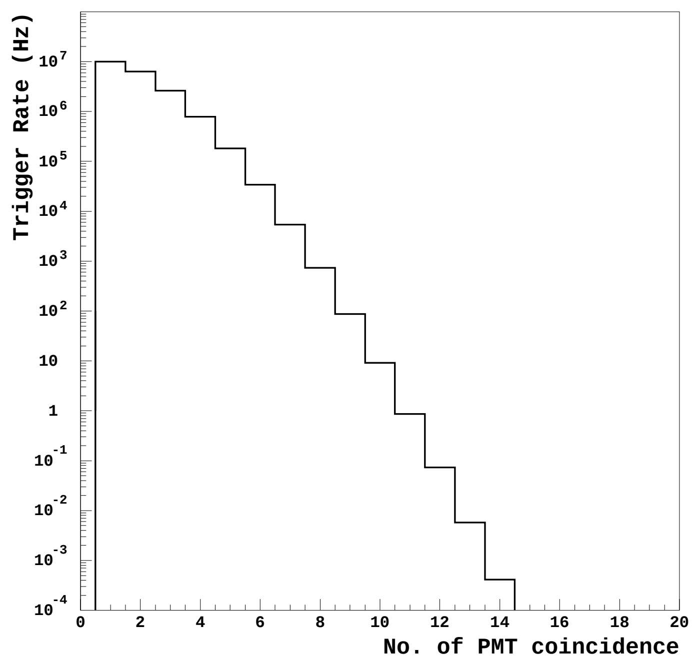

Fig. 9.4. Calculated trigger rates caused by PMT dark current as a function of the multiplicity threshold. For this study, we assumed that the maximum number of PMTs was 200. The PMT dark current rate used was 50k with a 100 ns coincidence window.

The energy sum trigger is the sum of charges from all PMTs obtained from the FEE boards with a 100 ns integrator and discriminator. The threshold of the discriminator is generated with a programmable DAC which can be set via the VME backplane bus. The energy sum is digitized using a 200 MHz flash ADC (FADC) on the trigger module. We plan to have an energy trigger threshold of 0.7 MeV or less, which is about 3σ below the positron energy threshold (based on simulations). At such low energy thresholds, the trigger will be dominated by two types of background: one is natural radioactivity originating in the surrounding environment (shown to be less than 50 Hz in Section 3.3.4), and the other is from cosmic muons (negligible at the far site). At this threshold, the energy sum trigger rate from the PMT dark current with a 100 ns coincidence window is negligible.

Tagging antineutrino interactions in the detector requires measuring the time-correlation between different trigger events. The time-correlation will be performed offline, therefore each triggered event needs to be individually time-stamped. It may become necessary to have a correlated event trigger in case the background rate is too high. A periodic trigger to monitor the PMT dark-current, background activity, and detector stability will be included.

9.2.3 The Muon Trigger System

The muon system will utilize three separate trigger and DAQ VME crates, one for each of the muon detector systems: 1) The inner water shield Cherenkov detector, 2) the outer water shield Cherenkov detectors - which cover the sides and bottoms of the water pool - and, 3) the system that tracks muons coming through the top of the water pool. Two different technologies are being considered for the muon tracker system: four layers of RPCs on top of the water pool, or Four scintillator strip layers on top of the pool.

The presence of a muon which goes through any of the water Cherenkov detector regions can be tagged with energy sum and multiplicity triggers using a similar scheme and hardware modules as used for the antineutrino detector. In addition, a more complicated pattern recognition scheme using localized energy and multiplicity (e.g. localized to one segment of the outer water shield) information may be used. The trigger rate in the water Cherenkov detector from cosmic muons is estimated to be $<$16 Hz in the far hall and $<$300 Hz in the near halls (see Table 9.3). The PMTs used in the water Cherenkov detectors are assumed to have a singles rate of 50 kHz per PMT from noise and radioactivity. The trigger rates from PMT singles in the water Cherenkov systems can be controlled by adjusting the multiplicity trigger requirements. The requirement for the water Cherenkov detector systems is $<$1% trigger deadtime due to radioactivity and PMT noise. The multiplicity thresholds required for the various proposed PMT configurations in the inner water shield system are discussed in detail Section 8. The random coincidence rate in the water Cherenkov systems is thus expected to be kept at $<$50 Hz in each of the detector halls.

In addition to the segmented water shield Cherenkov detector triggers, muons could also be tagged by a system of multiple-layer RPCs or scintillator strip detectors placed above the water pool.

The FPGA trigger logic used for the RPC muon tracking system forms muon “stubs” from coincident hits in three out of four layers of RPC modules. Although the readout electronics of RPC is very different from that of the PMT, the RPC trigger decision board design can still be similar to the other trigger board since most of the differences will be implemented in the FPGA logic. As we discussed before, each FEC of RPC readout electronics can provide two fast OR signals for the trigger, one for each 8 channels. All the fast OR signals will be fed into the trigger board for further decision by FPGA chips. The principal logic is to choose those events with hits in three out of four layers within a time window of 25–50 ns set by the 40 MHz clock rate, in a localized region of typically 0.25 m^2. The noise rate of the single gap BES-III RPC chamber is measured to be about 0.8 kHz/m^2. Therefore the accidental rate in an area 0.25 m^2 within a 50 ns time window is $\mathcal{O}(10^{-5})$ Hz/m^2. The accidental rate requiring coincident signals in three out of four single gap layers is therefore negligible.

The RPC response to radioactivity was measured using several BES-III modules placed in the Aberdeen tunnel (see Section 8.3.3), which is expected to have similar ambient radioactivity levels as that in the Daya Bay site. A simulation of the three out of four layer coincidence rate in the RPC system due to radioactivity based on the Aberdeen tunnel measurements was carried out. The trigger rate from radioactivity is thus estimated to be $\leq$1 Hz/m^2. This corresponds to a radioactivity trigger rate of about $<$300 Hz in the far hall.

An alternative to the RPC tracker system on top of the water pool is discussed in Section 8: four layers of extruded scintillator strips mounted above the water pool in a similar configuration to the four layer RPC modules. Multiple wavelength shifting fibers embedded in the scintillator strips collect the light signals and are readout by PMTs. The AD PMT front end readout electronics are well suited for use with the scintillator strip PMTs. Each scintillator module is readout by two PMTs at each end. The scintillator PMTs noise rate is $<$2 kHz at 15° C. To reduce the accidental rate from PMT noise the scintillator trigger logic should be flexible enough to allow several schemes for determining if an individual scintillator module is hit: 1) A single ended hit with a higher PMT threshold required or 2) a coincident hit on both ends of the scintillator strip. The muon stub trigger requirement for the scintillator strip muon tracker is similar to the RPC tracker system: localized coincident hits in three out of four layers are required within the 100ns coincidence time window. This requirement reduces the fake trigger rate from the scintillator strip PMT noise to a negligible level. Measurements of the radioactivity rates in plastic scintillators were carried out in the Aberdeen tunnel. A GEANT4 simulation in reasonable agreement with the Aberdeen tunnel measurements was used to estimate the trigger rate from radioactivity. The suppression factor of ambient γ rays requiring a coincidence of 3 out of 4 layers as a function of single counter energy threshold is shown in Figure 8.33. A requirement of 0.75 MeV visible energy in each counter suppresses the γ rate by a factor of more than 10^6, this corresponds to a radioactivity induced trigger rate of $\sim$10 Hz in the Far Hall. In principal, the same trigger module design can be used for both RPCs and scintillator strips with different FPGA software to handle the stub formation in the different geometries.

The global muon trigger decision is an OR of the three muon detector trigger systems: RPC/scintillator strip muon tracker, inner water Cherenkov and outer water Cherenkov systems. The muon trigger decision may be used to launch a higher level delay trigger looking for activity inside the antineutrino detector at lower thresholds and/or multiplicities for background studies.

9.3 The Timing System

The design of the trigger and DAQ system is such that each antineutrino detector and muon detector system has independent DAQ and trigger modules. In this design it is necessary to synchronize the data from the individual DAQ and trigger systems offline. This is particularly important for tagging and understanding the backgrounds from cosmic muons. A single cosmic muon candidate will be reconstructed offline from data originating in three independent systems: the inner and outer water shields and the RPCs. Cosmic muon candidates reconstructed in the muon detector systems have to then be time correlated with activity in the antineutrino detector to study muon induced backgrounds. To this end, the Daya Bay timing system is required to provide a global time reference to the entire experiment, including the trigger, DAQ, and front-end boards for each module (AD, inner and out water shield detectors, and RPC tracker) at each site. By providing accurate time-stamps to all components various systematic problems can easily be diagnosed. For instance, common trigger bias, firmware failure, and dead time can all be tracked by looking for time-stamp disagreements in the data output from each component. Furthermore, by having multiple sites synchronized to the same time reference, it will be possible to identify physical phenomena such as supernova bursts or large cosmic-ray air showers.

The timing system can be conceptually divided into four subsystems: the (central) master clock, the local (site) clock, the timing control board, and the timing signal fanout.

9.3.1 Timing Master Clock

The global timing reference can easily be provided by a GPS (Global Positioning System) receiver to provide a UCT (Universal Coordinated Time) reference. Commercially-available units are typically accurate to better than 200 ns relative to UCT [2,3].

This GPS receiver can be placed either at one of the detector sites (most conveniently the mid hall) or in a surface control building. A master clock generator will broadcast the time information to all detector sites. If the master clock is located underground, the GPS antenna may require an optical fiber connection to the surface, which again is commercially available. One such possibility is illustrated in Fig. 9.5

The master clock will generate a time reference signal consisting of a 10 MHz clock signal, a PPS (Pulse Per Second) signal, and a date and time. These signals can be encoded onto a one-way fiber optic link to be carried to each of the detector halls where they are then fanned-out to individual trigger boards as shown in Fig. 9.6

Additionally, the GPS receiver will be used to synchronize a local computer. This computer can then be used as a Tier-1 network time protocol (NTP) peer for all experiment computers, in particular the DAQ,

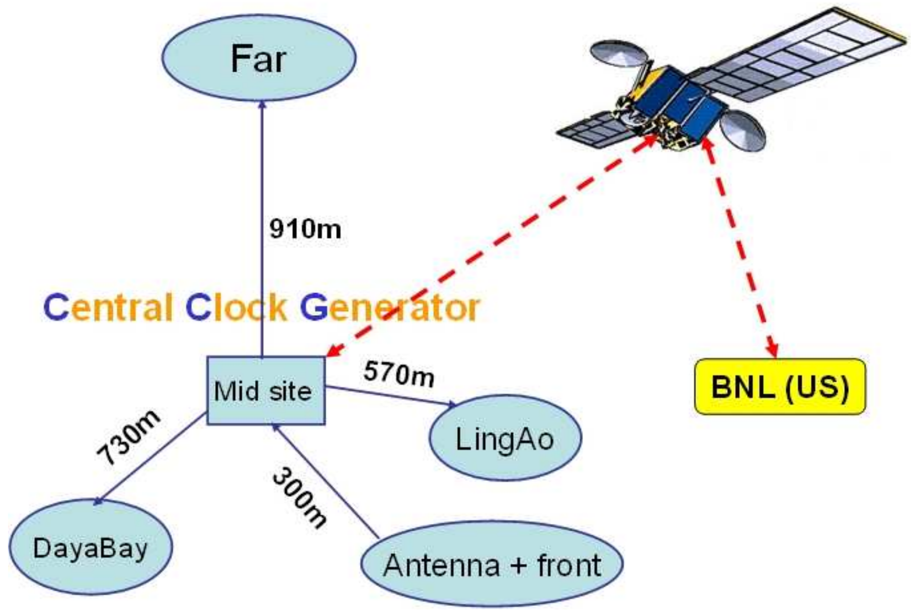

Fig. 9.5. Schematic layout of the global clock.

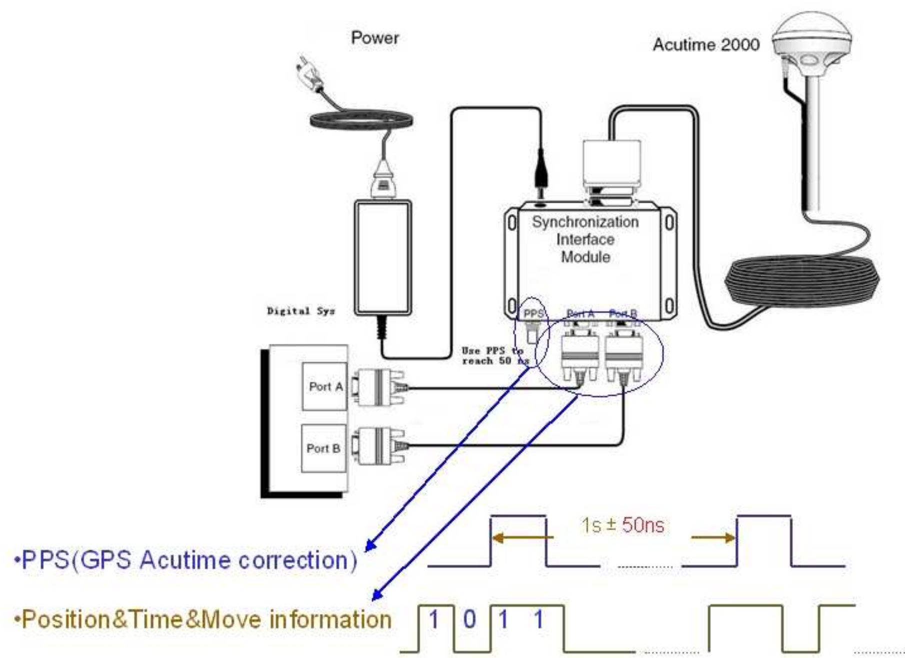

Fig. 9.6. Block diagram of the Daya Bay clock system.

Each site will receive the signals from the master clock and use them to synchronize a local 80 MHz quartz crystal oscillator via a phase-locked loop. This local clock can then be used as the time reference for that site. This method allows each site to operate independently of the master clock during commissioning or in the case of hardware failure, but in normal operation provides good time reference. This clock could be used to multiply the 10 MHz time reference to the 40 MHz and 80 MHz required for the front ends. This clock will reproduce the PPS, and 10 (or 40/80) MHz signals and supply them to the timing control board.

9.3.2 Timing Control Board

The timing control board will act to control the local clock operations (i.e. to slave it to the master clock or let it run freely) and to generate any timing signals required by the trigger, DAQ, or front end that need to be synchronously delivered. Typical examples include buffer swap signals, run start/stop markers, and electronic calibration triggers. In addition, this board could be used to generate pulses used by optical calibration sources. This board would be interfaced to the detector control computers.

9.3.3 Timing Signal Fanout

The signals from the timing control board need to be delivered to the individual detector components: every FEE board, DAQ board, and trigger unit. This will allow each component to independently time-stamp events at the level of 13 ns.

This fanout system could work, for example, by encoding various signals on a serial bus, such as HOTLink. The trigger board in each FEE and DAQ VME crate could then receive the serial signal and distribute it via the crate backplane. The crate backplanes will then carry the 40 MHz clock, the PPS signal (to reset the clock counters), and the other timing signals (run start/stop marker, calibration, etc).

Individual components of the trigger, DAQ, and front end can employ counters and latches to count seconds since start of run and clock ticks since start of second. These will provide sufficient data to assemble events and debug the output data streams.

9.4 The Data Acquisition System

The data acquisition (DAQ) system is used to:

1. Read data from the front-end electronics.
2. Concatenate data fragments from the FEE boards into a complete event, crate by crate.
3. Perform fast online processing and event reconstruction for online monitoring and final trigger decisions.
4. Record event data on archival storage.

A brief review of the DAQ design requirements is followed by a discussion of the system architecture, DAQ software, and detector control and monitoring system. The BESIII DAQ acts as the starting point for development of the Daya Bay DAQ.

9.4.1 Requirements

The Daya Bay DAQ system requirements are listed in Table 9.3. The total data throughput rate for all 3 sites is estimated to be about 3000 kB/s. For these calculations, we have assume that the trigger rate due to radioactivity and noise equal the largest estimated value. We also assume that the only other significant contribution is due to cosmic muons, as the rate of anti-neutrino interactions is negligible. The four layer scintillator muon tracking system alternative to the RPCs would have 240/360 PMTs at the near/far sites with the same muon trigger rate as the RPC system and $<$10 Hz of noise from radioactivity. The data throughput from the scintillator strip muon tracker option is thus estimated to by 90 kB/s.

1. **Architecture requirements:** The architecture requires separate DAQ systems for the three detector sites. Each antineutrino detector module will have an independent VME readout crate that contains the trigger and DAQ modules. In addition, the inner and outer water Cherenkov detectors and the

Detector	Description	Trigger Rates (Hz)			Occ	Ch size	data rate
		DB	LA	Far			(kB/s)
$\bar{\nu}$ module	cosmic-μ	36×2	22×2	1.2×4	100%	192×112 bits	325
	Rad.	50×2	50×2	50×4			1075
RPC	Rad.	160	160	256	10%	$1728/2592 \times 1$ bit	160
	cosmic-μ	186	117	11			74
Inner water shield	Rad & noise	50	50	50	10%	$138/189 \times 64$ bits	35
	cosmic-μ	250	160	15	70%		590
Outer water shield	Rad & noise	50	50	50	10%	$280/364 \times 64$ bits	67
	cosmic-μ	250	160	15	30%		512
site totals	(kB/s)	1216	894	736			2850

Table 9.3. Summary of data rate estimations. kB/s = 1000 bytes per second.

RPC/Scintillator muon tracking detectors will also have their own VME readout crates. The trigger and DAQ for the antineutrino and muon detector modules are kept separate to minimize correlations between them. The DAQ run-control is designed to be operated both locally in the detector hall during commissioning and remotely in the control room. In addition, run-control will enable independent operation of individual antineutrino and muon detector modules.

2. **Event rates** The trigger event rates at the Daya Bay, Ling Ao and Far site from various sources are summarized in Table 9.3. The rate of cosmic muons coming through the top of a detector are calculated using Table 3.10. To turn this into a volumetric rate, we use a MC simulation to calculate the ratio of muon rates entering the top to all muons entering the detector's volume. The total rates from cosmic muons in the inner and outer water shield muon detector systems are shown in Table 9.3. At the far site, the trigger rates in the ADs are dominated by natural radioactivity ($<$50 Hz/detector) and at the near sites both cosmic and natural radioactivity contribute.

   The trigger rate in the water shield detectors caused by the singles rate from PMT noise and γ rays will be adjusted to be $\leq$50 Hz ($<$1% deadtime requirement) by varying the multiplicity and energy trigger requirements.

   The RPC noise rates are scaled from the BES chamber measurements in Section 8.3.3. The RPC noise rate when requiring a localized co-incidence in three out of four layers is considered negligible. The singles rates shown in Table 9.3 are the natural radioactivity rates in the RPC systems at the various sites.

   While the trigger rate in the antineutrino detectors at each site is of order a few 100 Hz, an OR of the three muon trigger systems could produce a maximum trigger rate of 1 kHz. The Daya Bay trigger and DAQ system will be designed to handle a maximum trigger rate of 1 kHz. In addition, to trigger on the correlated neutrino and fast neutron signals in the antineutrino detector, the DAQ needs to be able to acquire events that occur $\geq$300 ns apart.

3. **Bandwidth**

   Table 9.3 summarizes the trigger rates, channel counts and data throughputs required at each site and for each detector system. We have assumed that the largest data block needed for each PMT channel is 14 bytes. The PMT data thus assumed (for the water shield) would be:
   Address: 8 bits
   Timing: TDC + time stamp: 32 bits

Charge: 6 ADC samples @ 12 bits/sample: 72 bits
For the RPC readout, we assume 1 bit/channel + header (64 bits) + global time-stamp (64 bits).

For our estimates, we assume zero suppression will occur for the inner and outer water Cherenkov shields, as shown above. We anticipate reading out all AD PMTs for each AD trigger. The expected data throughput from each site is estimated by combining the number of readout channels with the trigger rates and occupancies as shown in Table 9.3, and includes a 128 bit header word for each subsystem per trigger, but does not include trigger words or additional time-stamps (as necessary) which add only a small overhead. We estimate that the expected data throughput rate is $<$1.5 MBytes/second/site. These estimates would increase should we decide to implement full waveform digitization or additional triggers.

4. **Dead-time:** The DAQ is required to have a negligible readout dead-time ($<$0.5%). This requires fast online memory buffers that can hold multiple detector readout snapshots while the highest level DAQ CPUs perform online processing and transfer to permanent storage. It may also require some low level pipelines at the level of the PMT FADCs.

9.4.2 The DAQ System Architecture

The main task of the DAQ system is to record antineutrino candidate events observed in the antineutrino detectors. In order to understand the background, other types of events are also recorded, such as cosmic muon events, low energy radiative backgrounds... etc. Therefore, the DAQ must record data from the antineutrino and muon detectors (inner and outer water Cherenkov detectors and RPC tracker), with precise timing information. Offline analysis will use timing information between continuous events in the antineutrino detector and in both the muon and antineutrino detectors to select antineutrino events from correlated signals or study the muon related background in the antineutrino detectors.

The DAQ architecture design is a multi-level system using advanced commercial computer and network technology as shown in Fig. 9.7. There should be three sets of DAQ systems: one for each of the three

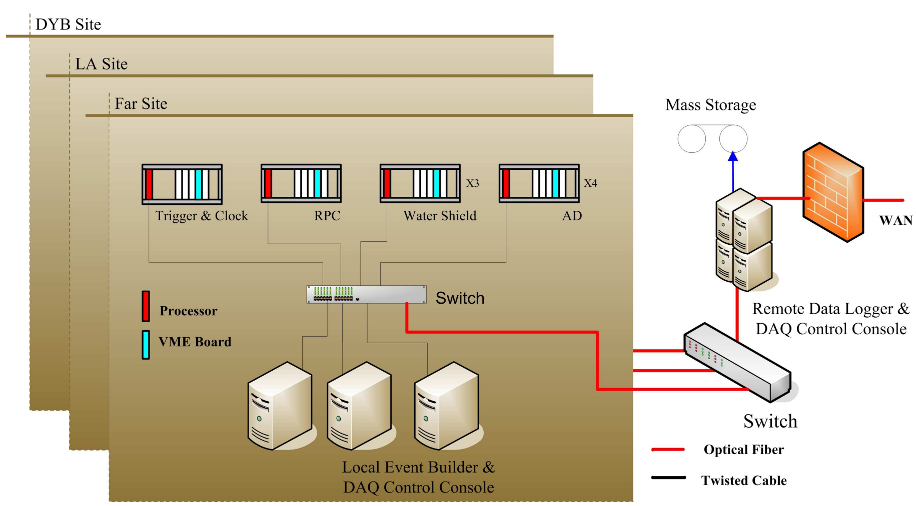

Fig. 9.7. Block diagram of data acquisition system.

detector sites. The DAQ system levels shown in Fig. 9.7 are as follows:

1. **VME front-ends:** The lowest level is the VME based front-end readout system. Each VME crate is responsible for one detector or muon system. Each module of the antineutrino detector will have its

own independent VME crate. Therefore, The lowest level VME readout system of the far detector hall will consist of the trigger boards for each system, the front-end readout boards from three muon systems, and the four antineutrino detector readout boards. All readout boards are expected to be 9U VME boards.

The Far and Near detector halls, will have the same DAQ architecture but with different number of VME readout crates to accommodate the different number of readout channels in the Far/Near halls. Each VME crate holds a VME system controller, some front-end readout (FEE) modules and at least one trigger module which supplies the clock signals via the VME backplane to the FEE modules. The VME processor, an embedded single board computer, is used to collect, preprocess, and transfer data. The processor can read data from a FEE board via D8/D16/D32/MBLT 64 transfer mode, allowing a transfer rate up to 80 MB/s per crate which is sufficient to meet the bandwidth requirement. All readout crates of the entire DAQ system at a single site are connected via a fast asynchronous Ethernet switch to a single local event builder computer.

2. **Event Builder and DAQ control:** At each site an Event Builder computer collects the data from the different VME crates for the different detectors and concatenates the FEE readout to form single antineutrino or muon events. The data stream flow can work in two ways, depending on the requirements of offline analysis. One scheme is to send muon events and antineutrino events out into one data stream on the readout computer. Another scheme is that each type of sub-event, muon events, or antineutrino events, have a different data stream and will be recorded as separate data files in permanent storage. The second scheme is simpler from a DAQ design viewpoint and complies with the DAQ system design principal of keeping each detector system completely independent for both hardware and software. The Event Builder computer at each site also allows for local operation and testing of the DAQ system.

3. **Data Storage and Logging:**

   Data from the Event Builder computer at each site are sent via fast optical fiber link through a dedicated switch at a single surface location where it is then transferred to local hard disk arrays. The hard disk arrays act as a buffer to the remote data archival storage or as a large data cache for possible further online processing. Each day will produce about 0.3 Terabyte of data that needs to be archived. Although implementation of data logging has not yet been finalized, there are two obvious options:

   (a) Set up a high bandwidth network link between Daya Bay and the Chinese University of Hong Kong, China, and distribute the data via the GRID (high bandwidth computing network and data distribution applications for high energy physics experiments). This is the preferable scheme.

   (b) Record the data locally on disk (or tape) and deliver to Hong Kong by car, where they would be copied and distributed via the GRID.

   Whichever option is realized, the local disk array should have the capability to store a few days worth of data in the case of temporary failures of the network link or the local tape storage.

Since the DAQ system is required to be dead time free, each DAQ level should have a data buffer capability to handle the random data rate. In addition, both the VME bus and network switches should have enough margin of data bandwidth to deal with the data throughput of the experiment.

The DAQ control and monitoring systems should be able to run both remotely from the surface control room computers and locally on the Event Builder computer in each detector hall. The run control design should be configurable allowing it to run remotely for data taking from all systems and locally. Run control should allow both global operation of all detector systems simultaneously, and local operation of individual detector systems for debugging and commissioning.

9.4.2.1 Buffer and VME Interface

For each trigger, the event information (including the time stamp, trigger type, trigger counter) and the snapshot of the FADC values should be written into a buffer that will be read out via the VME bus for crosscheck.

The global event information which includes absolute time-stamps and trigger decision words will be read out from the trigger board, while individual channel data are read out from the FEE boards. In this case the event synchronization between the FEE boards and the trigger board is critical, and an independent event counter should be implemented in both the FEE boards and the trigger boards. The trigger board in each crate provides the clock and synchronization signals for the local counters on each FEE board. The global timing system is designed to enable continuous synchronization of the local clocks in different crates and at different sites.

The event buffers are envisioned to be VME modules that are in the same crates as the FEE boards. Data from the trigger and FEE boards is transfered via the VME bus to the VME buffers. An alternative design is to have the VME buffer modules in separate crates and have data transfered from the FEE modules via fast optical GHz links (GLinks) to the VME buffer modules. We envision VME buffers with enough capacity to store up to 256 events.

9.5 Detector Control and Monitoring

The detector control system (DCS) controls the various devices of the experiment (e.g., high voltage systems, calibration system, etc.), and monitors the environmental parameters and detector conditions (e.g., power supply voltages, temperature/humidity, gas mixtures, radiation, etc.). Some safety systems, such as rack protection and fast interlocks are also included in the DCS.

The DCS will be based on a commercial software package implementing the supervisory, control, and data acquisition (SCADA) standard in order to minimize development costs, and to maximize its maintainability. LabVIEW with Data logging and Supervisory control module is a cost effective choice for the DCS. The BESIII system will act as a model from which the Daya Bay system is developed.

The endpoint sensors and read modules should be intelligent, have digitalized output, and conform to industrial communication standard. We will select the minimum number of necessary fieldbus technologies to be used for communication among the SCADA system and the readout modules.

9.6 Manufacturing Plan, Quality Assurance, ES&H (Environment, Safety and Health) and Risk Assessment

9.6.1 Manufacturing Plan

The PMT readout electronics (*e.g.* FEE boards), are being designed by IHEP and will be manufactured in China. Front end electronics for the RPCs will be manufactured and tested at the University for Science and Technology in China. Final stage testing of all components together with the RPCs will take place on site at Daya Bay. The trigger and clock systems are being designed by Tsinghua University in Beijing in concert with the electronics group at IHEP. These systems will use a mixture of commercial electronics (including GPS receivers) and custom made boards either purchased or manufactured in China. The DAQ software is being designed and developed at IHEP, with some support from the US. The VME crates, power supplies, processors, cables and other miscellaneous. components are available from commercial vendors, as are electronic racks and cooling systems. The crates and rack hardware will be acquired in Asia. Computer systems are readily available from numerous sources. The monitoring and control system will use a mixture of commercial hardware and software, and some custom software. University resources (students and post-docs) will be used to develop both hardware and software components of the electronic systems. Testing and integration of the system will be done by physicists, primarily in Asia, but also within the US.

9.6.2 Quality Assurance

The electronic designs will be thoroughly reviewed by experienced electronic engineers not directly involved with the design effort prior to prototyping and production of electronics boards. Prototypes will be tested both in China and in the US. Custom electronics boards will use commercial off-the-shelf components and products that are available in China. Furthermore, ADCs and FPGAs will be selected from pin-compatible family lines allowing for unanticipated upgrades. Full production will occur only after a complete system integration test involving all parts. Software will be exercised by several groups during development to identify problems and bugs, both in China and within the US. Responsibility for maintenance and repairs (as needed) will remain with the original design team during installation and commissioning. Finally, a programmable calibration pulse can be generated by a fast DAC chip on-board the PMT FEE which is sent to the input of every channel on that board. We will use this feature as a reliable self test and calibration for the full readout system.

9.6.3 Environment, Safety, and Health

The principle hazard is exposure to electrical power (220 VAC and various high-current, low-voltage DC power lines). Local standards and regulations will be followed for installation of AC power into the electronics racks. Appropriate commercial class-2 cable, outlets, and plugs will be used throughout. High current DC power supplies will be mounted inside the racks. Voltage distribution will use appropriate high current cables, with all connectors properly covered to prevent accidental human contact or short-circuits. Custom PCBs will be fused to prevent/reduce fire hazards. Cooling fans will have appropriate covers to limit contact with spinning fan blades. Sensors mounted within the rack will automatically shut-off power in emergency situations. Hazard and hazard mitigation plans will be reviewed internally by engineers not directly involved with the original design. Written procedures will be drafted to advise people working with Daya Bay electronics on proper safety procedures.

9.6.4 Risk Assessment

There is a risk that experimental conditions will be different than those experienced during integration testing. A sample of possible risks include:

1. excess noise
2. unanticipated cross talk
3. failure of the GPS clock system
4. trigger rates larger than anticipated
5. detector response outside original design expectations
6. environmental conditions outside expectations

Mitigation:
To mitigate these risks, designs are being kept as simple and flexible as possible with built-in redundancies (*e.g.* using a precision oscillator as a backup clock), where possible. We will require that about 50 percent of the FPGA resources on each module remain available to accommodate upgrades and modifications for both the readout and trigger systems. Isolation transformers will minimize the impact of external sources of electronic noise. The rack environmental design will be flexible enough to allow for improvements and upgrades should any aspect prove inadequate.

REFERENCES

1. G. Gratta *et al.*, Nucl. Instr. and Meth. A**400**, 54 (1997).
2. Trimble Navigation Ltd. http://www.trimble.com/acutime2000.html.
3. TrueTime Ltd, http://www.truetime.net/software-winsync.html

10 Offline

This section describes the Daya Bay Offline Software and Computing Project. The project covers all developments of offline software for the Daya Bay experiment, the definition of the computing environment, the provision of hardware and manpower resources, and the operation of the offline computing systems.

In particular, the Daya Bay Offline Software and Computing Project is responsible for the provision of the software framework, computing infrastructure, data management system, and external software as well as provision of the hardware and networking required for offline processing and analysis of Daya Bay data.

The development of detector-specific algorithmic code for simulation, calibration, alignment, trigger and reconstruction is under the responsibility of each detector subsystem, but the Software and Computing Project plans and coordinates these activities across detector boundaries and supplies and supports the non-detector-specific software and tools that the detector subsystems use.

10.1 Offline Requirements

Daya Bay is still in the relatively early stages of the project, and the offline requirements will change over time. Current requirements for offline focus on the simulation of detector designs and physics signatures, and software development. As data taking begins, all software, hardware, and networking components must be in place to ensure calibration of the detectors and rapid first results from data. Once data taking reaches steady-state, the offline requirements will shift towards data management, data processing and ease of access for the data and software to all Daya Bay collaborators.

10.1.1 Networking, Computing and Software Distribution

Computing hardware, archival storage, and networking requirements for Daya Bay are not extraordinary for modern physics experiments. However, the international and distributed aspect of the collaboration impels special attention to networking and data archiving, as well as strong coordination of US and Chinese resources and ease of access to experiment resources for all collaborators.

Offline software must be easily distributable, installable, and usable for collaborators at Daya Bay institutions. Software and infrastructure must require a low level of long-term maintenance effort. Offline software must run on all validated and supported platforms and must allow integration of Daya Bay collaborator-written code specific to the experiment with generic tools and packages such as Geant4 and ROOT.

1. **Steady-state Network Bandwidth:** End-to-end network bandwidth from the DAQ disk cache at the Daya Bay reactor site to the data archives in Beijing and Berkeley must be able to deliver an aggregate of $>$200 TB/year of recorded raw data. Sufficient additional bandwidth is required for remote access by Daya Bay scientists to the on-site computers as well as normal incidental use by researchers at the reactor site (e.g. email, web access).

2. **Recovery Network Bandwidth:** End-to-end network bandwidth from the DAQ disk cache at the Daya Bay reactor site to the data archives in Beijing and Berkeley must be sufficient to recover from periodic network outages or interruptions. Surplus bandwidth for such recovery should be approximately 50% of the steady-state data rate, sufficient to drain the DAQ disk cache without interfering with nominal data transfer. This model drains the DAQ disk cache over a time-period twice the length of the network outage.

3. **Network Connectivity:** The maximum time to recovery and mean time between failures of the end-to-end network connectivity from the DAQ disk cache at the Daya Bay reactor site to the data archives in Beijing and Berkeley must not overflow the DAQ disk cache. The DAQ disk cache will be 20 TB, which is sufficient for $\sim$1 month of recorded raw data. In theory, this implies that the maximum time to recovery of the network must be less than 1 month, and that the aggregate down-time of the end-to-end network connectivity must not exceed 33%. In practice, the maximum time to recovery should

be less than 1 week, and the aggregate availability should be greater than 96% (i.e. 2 weeks aggregate outage per year).

4. **Computing Power:** Dedicated, validated computing resources must be sufficient to allow 2 full production passes through a year's worth of raw data per year using less than 50% of the total compute power. The remaining 50% will be dedicated to user-level analysis and simulation.

5. **Software Releases and Distribution:** Daya Bay software releases must be installed on each of the three official clusters (BNL, IHEP, LBNL). Software releases must be available for download and installation on other institutional resources running supported operating systems and software loads (i.e. suite of loaded external software versions).

10.1.2 Simulation

Daya Bay simulation, like most modern physics experiments, is done using Geant4 [1]. Daya Bay requires specific physics processes be properly implemented in the physics engine, the ability to easily compare alternate detector designs, configurations, and options, and that the output of the simulations permit the development of offline algorithms well before detector turn-on. Other simulation packages exist (e.g. Geant3 and Fluka) currently. Some early simulation (e.g. neutron background simulation) is done with a Geant3 program inherited from Palo Verde experiment. But Daya Bay will officially support only Geant4 as the central simulation engine. Other simulation packages will serve as validation tools.

10.1.3 Data Processing and Analysis

Daya Bay offline analysis of data will be mostly done using the ROOT object-oriented data analysis framework [2]. Daya Bay collaborator-written software must integrate easily with ROOT's data analysis, graphics, and I/O capabilities.

We do not want to preclude the use of other analysis engines and/or tools, so tight coupling between user code and ROOT classes will be minimized. However, we expect the use of other frameworks and/or tools (e.g. PAW, JAS, Excel) will not be officially supported by Daya Bay Offline.

Some visualization capability is needed for single events. This will either use an adopted visualization framework or a light-weight custom-built framework tailored to Daya Bay's simple geometry and detector data requirements.

Daya Bay's data stream is not triggered like an accelerator detector's. Hence, the typical HEP analysis pattern of independent events is not applicable. Instead, analysis will be predicated upon sliding windows on data within an Anti-neutrino Detector (AD) and between ADs and the veto system. The offline framework must provide a natural interface to this kind of data analysis and allow users to configure the time-window size and other appropriate parameters without recompiling.

1. **ROOT Integration:** For the immediate future, ROOT is the most capable analysis toolkit available to Daya Bay. ROOT must be supported by the offline analysis framework permitting researchers to fill with Daya Bay data and manipulate ROOT ntuples, histograms, and other analysis objects from within the framework and/or allowing direct access to Daya Bay data from ROOT.

2. **Data Externalization:** Daya Bay data should be accessible from non-ROOT analysis tools and environments.

3. **Data Processing Model:** The offline analysis framework must read Daya Bay raw data format as defined by the final stage of DAQ merging and permit the time-window data processing model required by Daya Bay raw data processing. Other data processing models required by subsequent analysis must be supported.

4. **Database for Important Quantities:** Offline analysis requires efficient access to important but typically slowly changing data. Examples calibration and reactor power data.

10.1.4 Data Movement and Networking

Daya Bay data will initially be distributed to a few collaboration-funded computer clusters to be calibrated, processed, and archived. The processed data are then made available to all collaborators for analysis at these official clusters or at local, institutional machines (e.g. local desktops and/or university clusters). The Offline subsystem must provide tools for the automatic and manual movement and management of data coming out of the data acquisition (DAQ) system. Offline must also provide the tools for management of data provided by the utility company (e.g. reactor power levels, etc).

10.1.5 Online Interface

The online system will be responsible for merging the data streams from all detector subsystems (e.g. ADs, Water Cherenkov and RPCs) and slow controls in a single detector hall into a single, time-ordered stream for subsequent offline analysis. Past this point of the experiment's data processing, the management of data files, tools for data transfer and accounting, and software for I/O and processing are the responsibility of the Offline group. Before this point in the data flow, responsibility resides with the Online group.

1. **Slow Control Data:** Detector slow control data are those data which monitor detector and trigger state and/or configuration. These data change slowly over time and will be recorded in the main data stream. The offline analysis must provide all salient detector state information for detector events in the data stream.

10.2 Data Management, Networking and Computing

Daya Bay is an international collaboration with commensurately international hardware resources and globally distributed scientists requiring access to Daya Bay data, compute resources, and software. All managed data transfers are made via national and international networks. We expect to make use of Grid resources and tools for data transfer and job submission where appropriate. However, the modest data volumes and compute requirements of Daya Bay simulation, processing, and analysis as well as the limited manpower available suggest that more than a small investment in customizing Daya Bay software and/or hardware resources to a specific Grid is not cost-efficient. Therefore, we do not expect to fully Grid-enable our system, rather use a subset of easily adopted tools.

10.2.1 Data Movement

During steady-state data taking mode, data taken by the detectors are transferred by network from the reactor site in China to two permanent data archives (one in China, one in the US). The first stage of data processing (i.e. calibration, reconstruction, and event filtering) will occur at one or both clusters, using validated production Daya Bay software running in the Daya Bay offline analysis framework. We may want to replicate processing at both clusters as a QA measure (i.e. process twice and compare results to ensure reproducibility). Results from each stage of data processing and subsequent data analysis steps are centrally archived and available to all collaborators for local and/or remote processing. Full data archiving, data processing, and data analysis will be done at the LBNL and IHEP clusters. Data processing and analysis will also be done at the BNL cluster and data analysis will be done at other institutional compute resources.

Daya Bay data are recorded by the DAQ system at the Daya Bay reactor site and stored on a local disk cache large enough to hold $\sim$1 month's worth of recorded raw data (see Data Rate Estimate in Section 9.4.1). Data are transferred by network concurrently to two major Daya Bay data archives on NERSC's HPSS system at LBNL in Berkeley, CA, and on IHEP's Castor system in Beijing, China. Integrity of the network data transfers are checked by comparing checksums of the data at either end. Failure of the integrity check triggers a retransmit of the data file.

Once data are transferred and validated, the original master copy at the Daya Bay reactor site on the DAQ disk cache is marked as redundant and deleted using a high-watermark/low-watermark algorithm. This scheme can accommodate temporary outages of the network and/or data migration tools without impact on the science output of the experiment.

Most of the data migration effort will be either automated or use tools which minimize the manual effort involved and reduce the likelihood of human error. Examples of this are: Bookkeeping for the disk cache at the Daya Bay site will be done by a database loaded programmatically, rather than manually, from a spyder-like service which will keep watch on well-defined file system directories on the disk cache. All data migration and high-watermark/low-watermark processes will work from this bookkeeping database.

10.2.2 Networking

Daya Bay depends upon several externally funded national and international networks and upon one network link funded specifically for use by Daya Bay.

The network connection from Daya Bay (dubbed DayaNet) will be provisioned in Fiscal Year 2007 at 155 Mbps which will be dedicated to Daya Bay data transfers and site access. This will be more than sufficient for the Daya Bay steady-state data taking rate (up to 600 GB/day), leaving headroom for recovering from data migration and/or network interruptions and providing access to the site for remote monitoring of the experiment for researchers offsite.

The maximum data rate estimated for Daya Bay is 600 GB per day (see Data Rate Estimate in Section 9.4.1). Assuming that $<66\%$ of the total bandwidth to the site should be reserved for recorded raw data transfer and that the aggregate network availability is $>90\%$, this requires provisioning connectivity with effective instantaneous bandwidth of $\sim$100 Mbps.

From China to the United States, Daya Bay will rely on two R&E (Research & Education) networks. Gloriad [3], which connects to ESNet in Chicago is currently 10 Gbps across the Pacific and already in use by Daya Bay. TransPAC2 [4], which connects to Internet2 in Los Angeles, is part of the NSF's IRNC (International Research Network Connections) program. This international diversity of connection ensures that no single trans-Pacific network outage will interrupt data flow to the US.

Once in the US, the DOE-funded Energy Science Network (ESNet) [5] provides a high-reliability 10 Gbps IP backbone to all DOE Office of Science facilities including the NERSC PDSF cluster at LBNL and to BNL where the Coop Cluster is located.

Networking within China and connection to IHEP in Beijing relies on the Chinese national network (CSNet) [6] which provides a 10 Gbps backbone and 1 Gbps connectivity to IHEP.

The final network topography for Daya Bay is not yet settled. The connection from the Daya Bay reactor site may land in Hong Kong (CUHK) or connect directly to CSTNet in Shenzhen, or even to the alternate Chinese national R&E network, CERNet at Zhoushan University. This will depend upon final negotiations and costs, but we have vendor quotes for the direct connection to CUHK. Likewise, the second trans-Pacific network connection via TransPAC2 has not been tested. We are in discussions with the Internet2 and IRNC network operation centers to ensure the connection.

10.2.3 Data Archiving

All Daya Bay data (raw data, calibrations, reactor data, processed data, and collaboration analysis objects) will be archived at two locations. At LBNL's National Energy Research Scientific Computing (NERSC) [7] Facility we will store our raw data on the HPSS (High Performance Storage System) mass store. This system has a current total capacity of 8.8 PB and is allocated via the normal NERSC allocation process. At IHEP, the Castor system in use for LHC experiments will be replicated to provide a dedicated archival storage for Daya Bay.

Data from these two archives will be available to all collaborators via the use of standard data transfer tools such as FTP, scp, and/or GridFTP. A bookkeeping database will allow users to query all centrally managed data files.

10.2.4 Database

A single, central database will be used to hold auxiliary data needed to analyze the detector data. The data includes items not in the detector data stream such as reactor power or values derived from the detector stream such as calibration constants. Certain, important slow control data may also be stored in this database.

The main role this database provides is efficient time based random access to its data. Every entry of a particular type of data has an associated range of time when it is considered valid. Given a specific point in time, the software interface to the database will select the correct entry. When entries have overlapping validity ranges the entry with the most recent creation date is selected. This versioning mechanism allows improved quantities to be entered without the need to delete values and provides a way to reproduce past results.

10.2.5 Computing Resources, Operations, and Data Processing

The offline computing resources needed for simulation and for data management, processing, and analysis will be met at three officially supported computing clusters at BNL, IHEP, and LBNL and at two tape archives at IHEP and LBNL. The manpower required to administer and operate the resources will be supplied by the host institutions. Daya Bay operational manpower will be required to manage data files and batch jobs on the systems, as well as installing and validating the official Daya Bay software load.

We are currently making use of the BNL's Coop Cluster, LBNL's PDSF, and smaller clusters and/or resources at IHEP and other institutions for detector design and simulation efforts.

Because of our limited manpower, we will be officially support only one platform (i.e. operating system + compiler versions) in Daya Bay. ”Officially support” in this context means 1. Data Bay software will not be considered releasable until it runs and has been validated on the supported platform, 2. bug reports on the supported platform take priority. The officially supported platform will be a variant of Linux and will change over time. The initial supported platform is not yet chosen, but Scientific Linux 3 (SL3) is an obvious initial candidate as this is currently a widely used and supported version of Linux in HEP (e.g. CERN and FNAL officially support SL3). As a general principle, Daya Bay will adopt new platforms as required, external software become well tested and supported. (e.g. CERN plans to retire SL3 in favor of SL4 by the end of 2007, we would follow when we are assured that SL4 has reached sufficient stability.) We expect that the official platform will the default installed on Daya Bay clusters or alternatively, that the cluster managers will take responsibility for porting releases to their non-standard platform.

In accord with Computing Science Engineering (CSE) best practices, all Daya Bay produced software will be intentionally written as portable as possible. Likewise, external dependencies should not unnecessarily constrain e.g. our choice of Linux operating system + gcc compiler version. i.e. No artificial barriers should be erected to porting Daya Bay software to other Linux/gcc platforms. Of course, any other platform may be supported for the collaboration by a motivated volunteer who takes responsibility for porting software and responding to bug reports and support requests. Any additional platforms' releases can be made available by that volunteer from the official Daya Bay software source. Any sensible code changes to accommodate additional platforms shall be acceptable in the CVS repository.

10.2.5.1 BNL Cluster

The BNL Cooperative Cluster (coop) [8] is a relatively small ($>$50 CPU, $\sim$8 TB disk) AMD Opteron based Debian Linux cluster serving the MINOS, Daya Bay and other contributing experiments. US Daya Bay will add $\sim$40 CPU and 10 TB disk to this shared cluster for use in Daya Bay data analysis and offline processing.

10.2.5.2 IHEP Cluster and Tape Archive

IHEP has several medium and large Linux clusters for experiments including CMS, ATLAS, BESIII, Argo, and HXWT (Hard X-ray Modulation Telescope). The BESIII experiment includes a Castor tape archive system of 4.8 PB capacity.

CAS will standup another cluster of $\sim$100–200 CPUs with $\sim$20 TB of disk and another Castor system with $\sim$200–500 TB tape capacity dedicated to Daya Bay. This system will be managed in parallel with the other clusters, initially running Scientific Linux 3.

10.2.5.3 LBNL Cluster and Tape Archive

At LBNL, the Parallel Distributed System Facility (PDSF) [9] is used by approximately 20 different nuclear physics and high energy physics experiments. These experiments are able to pool their resources allowing a much larger and professionally managed central resource than they could realize individually. PDSF supplies currently approximately 600 processors, 150 TB of shared disk space, and 150 TB of local disk space. All CPUs are running Linux operating system and allow the user to specify at run time the software load (via the modules facility) and operating system (via chos), which allows simultaneous usage by the widest variety of applications.

US Daya Bay will add another 100 processors and 20 TB of shared disk to the PDSF system. This will guarantee a minimum fairshare of the overall resources. Additional CPU resources are available depending on usage by other stakeholder experiments.

PDSF is part of the NERSC facility and well coupled to the HPSS mass storage system [10]. The NERSC HPSS system consists of 8 large STK tape robot silos with an aggregate capacity of 8.8 PB and a large (100 TB) disk cache. The maximum throughput for the system is 3.2 GB/sec. Users can access the system through a variety of clients such as hsi, htar, ftp, pftp, and grid clients.

The NERSC facility is operated for the Department Of Energy (DOE) as an open resource for DOE's Office of Science researchers. Allocations of NERSC computer time and archival storage are awarded by DOE to research groups whose work reflects the mission of DOE's Office of Science. The allocations are administered by NERSC and managed by DOE. The research groups are awarded project accounts, known as repositories, from which they draw resources throughout the allocation year.

Requests to use NERSC resources are submitted annually via a web form known as the ERCAP (Energy Research Computing Allocations Process) Request Form. ERCAP is accessed through the NERSC Information Management (NIM) web interface and is available year-round.

Daya Bay currently has mass storage allocation of 25 TB on NERSC's HPSS system and will apply annually for additional storage up to a maximum of $\sim$500 TB to archive all raw and processed data sets.

PDSF and HPSS are administered by computing professionals and adhere to defined metrics for availability, uptime, and performance. The only Daya Bay operations manpower necessary is that required to submit and manage jobs and data files.

10.3 Offline Core Software and Infrastructure

Like most current generation High Energy Physics experiments, Daya Bay has adopted an object-oriented approach to software based primarily on the C++ programming language and relies on common C++ tools, software tools, and programs such as Geant4 and ROOT as obvious examples.

Offline core software includes frameworks, databases, infrastructure, and services which are either not specific to Daya Bay or are not an explicit step in the physics analysis or simulation of data. Core software is often differentiated from Physics software which contains details of the detector and/or data analysis and are typically written by research scientists in the collaboration specifically for the experiment at hand.

We categorize core software effort into three general areas:

1. **Simulation:** Software frameworks, databases, and tools needed to simulate the detector and data both in the design and the data processing and analysis stages of the experiment. This is by necessity tightly coupled to Geant4 as the main simulation engine for Daya Bay.

2. **Processing and Analysis:** Software frameworks, databases, and tools needed to calibrate and filter recorded data, reconstruct events, produce processed event data and common experiment-wide analysis objects, allow scientists to explore data and produce final physics results.

3. **Infrastructure:** Software services, databases, build systems, and other tools for software development, building, testing, and deployment and for data management and movement.

The development of software for detector and trigger studies, and of algorithmic code for calibration, reconstruction and analysis is not covered by the core effort, as it is thought that these activities fit naturally into what is expected from all physicists who are members of the collaboration. These activities are nevertheless necessary, therefore they are coordinated by the Offline Computing project.

10.3.1 Simulation Software

The Geant4-based simulation framework (g4dyb) currently being used by Daya Bay allows researchers to investigate different detector configurations, but with a relatively awkward combination of hard-coded constants and external XML files. We plan to move to a system in which the detector geometry, material properties, particle properties and physical constants are easily configurable in a manner which allows comparison of alternate designs and assumptions and which can be easily maintained and referenced over the course of the detector design. These configuration constants must be available to both the Geant4 simulation engine, and to user code which analyzes simulated data.

10.3.2 Processing and Analysis Software

The primary component of the core software for offline processing and analysis is the offline framework. The framework provides a common software environment in which user codes run and cooperate. It is the software which controls what code gets called on which data and when.

There are several analysis frameworks in HEP which are well established and supported within a single experiment. There are very few that are used across multiple experiments. One of those supported across multiple experiments is the Gaudi [11] framework used by LHC experiments ATLAS [12] and LHCb [13], as well as non-LHC experiments like GLAST [14], Harp [15], and BES III [16].

We are currently evaluating the Gaudi framework for application to Daya Bay software. Arguments in favor of using Gaudi:

1. **Reduced Developer Burden:** Gaudi is an existing and well supported framework which has been developed and tested in large collaborations with much more manpower than Daya Bay can bring to bear on development of our own framework.

2. **Collaboration Expertise:** Gaudi is used by Chinese collaborators in BES III and has been used by US collaborators and potential collaborators in ATLAS. Hence, we are able to draw upon technical expertise. This is especially compelling if we are able to incorporate other ATLAS and/or BES III collaborators into Daya Bay.

3. **Reduced User Burden:** Gaudi minimizes user coding. Users generally only have to write Algorithms that interact with the transient event store for data access and automatic data I/O.

4. **Geant4 and ROOT:** Gaudi is well integrated with Geant4 and ROOT, respecting the data object ownership models of both and integrating seamlessly with ROOT's introspection and PyROOT interface.

5. **Services:** Gaudi provides integrated access to many generic services including: Particle properties, random number generators, ROOT and AIDA histograms and ntuples, ROOT and POOL persistency (Data I/O), error and message logging.

Our evaluation of Gaudi is focusing on several aspects of usability and applicability to Daya Bay including:

1. **Build, Install, Distribute:** We have successfully built Gaudi on the IHEP cluster under Scientific Linux 3.0.4. We must be assured that Gaudi-based Daya Bay software will be simple to build, install and distribute to collaboration clusters.

2. **Event Processing Model:** The processing models for accelerator-based experiments are typically based upon separate, uncorrelated triggers which are processed one-by-one. Daya Bay data processing will involve analyzing together distinct event records within the data stream.

3. **Support and Upgrades:** Daya Bay is a small experiment relative to ATLAS and LHCb (the main developers of core Gaudi). We will need assurances that we can expect some level of support from these authors when we find bugs and request or contribute feature additions.

4. **Geometry:** We are developing Daya Bay geometry definitions based on AGDD. We will need to be able to easily incorporate this work with the integrated Gaudi/Geant4.

Pending final evaluation of the Gaudi framework, we are not certain we will adopt it or develop a Daya Bay specific framework. If we do adopt Gaudi, we will certainly want to adopt several of the ATLAS extensions. Specifically, using Python rather than text-based job options files (i.e. program configuration), and the StoreGate transient data store. The Python configuration language allows much greater flexibility, capability, and stability. The StoreGate transient data store allows Daya Bay to develop software which uses any valid C++ class for data object rather than forcing a inheritance dependency on the Gaudi IObject interface.

10.4 Risk Assessment

Offline computing does not pose environmental, health or safety risks.

10.4.1 Schedule

Offline software by its nature is heavily front-loaded in the schedule. In order for scientists to bring up, debug, and characterize detectors as they are installed into the Daya Bay site, the software for reading and processing detector data must be in place before detector installation. This requires that researchers develop, test, and debug detector-specific code, define data structures and data I/O formats, and are familiar with processing and analyzing simulated detector data using the offline framework and data analysis tools. This implies that the offline framework and analysis tools themselves (the matrix in which researchers develop, test, and debug their own code) have already been developed, tested, debugged, and deployed to the collaboration.

Schedule Pipeline: The front-loading of offline software carries risk to the overall schedule for detector specific software and consequently to the ability of the experiment to be prepared at turn-on to bring the experimental hardware up in a timely fashion.

Mitigation:

- ○ We are leveraging work done by other experiments with far more resources than Daya Bay, evaluating adopting the HEP Gaudi framework with targeted ATLAS extensions. We are drawing upon Gaudi expertise of LBNL Computing Science Engineers (CSEs) currently working on ATLAS.
- ○ We are concurrently prototyping event data model structures with an option to build a framework specific to Daya Bay data analysis or incorporate those data model structures to the Gaudi-based framework.

10.4.2 CyberSecurity

Cybersecurity risks posed to the Offline Software and Computing Project relate to the experiment's information and information systems. Much of the computing and data is housed at US or Chinese national labs.

Those in the US are subject to the Federal Information Systems Management Act (FISMA). Compliance with FISMA entails, among other things, enumeration of risks in terms of their effect on the confidentiality, integrity and availability of the information and information systems. Risks must be mitigated through security controls and any residual risk must be accepted by the lab's DOE representative. Currently one lab (BNL) has completed the Certification and Accreditation process under FISMA. LBNL is still in the process but has gotten good evaluations from past security audits.

The IHEP cluster also is managed with explicit attention to cybersecurity best practices for WAN-accessable Linux clusters and is part of the IHEP security enclave. IHEP cybersecurity practices are subject to the classified criteria for security protection of computer information system (GB 17859-1999). In order to understand the current status of the information security programs and controls to make informed judgments and investments that appropriately mitigate risks to an acceptable level, IHEP has completed the Security Self-Assessments Compliance with GB 17859-1999 entails. IHEP uses defence in depth to elevate cybersecurity above that required by GB 17859-1999.

Besides the general risks in covered by the above there are specific risks posed to this project.

Data transfer: Raw data from the detectors must be transferred from the DAQ disk array to offsite locations at IHEP and LBNL for initial processing and subsequent distribution. There is a risk of data loss or corruption during this transfer.

Mitigation:

- ○ File checksums are computed before transferred. The cached file is removed only after it is confirmed that the copied files have matching checksums. A corrupt or lost file is retransmitted.
- ○ Copies at IHEP and LBNL provide redundancy against loss or corruption after the initial transfer.

Malicious code insertion: The offline software is developed by many people in parallel and used on information systems at many institutions. In principle, malicious code can be included that could alter results or provide avenues to attack collaboration computing systems.

Mitigation:

- ○ Committing code requires username and password authentication unique to each contributor.
- ○ The contents of each commit is monitored by the offline group through email notifications.
- ○ If malicious code is found it can easily be excised from the repository.
- ○ Elevated privileges are not required to run the software so a local vulnerability must exist for any attack to spread beyond the account running the code.
- ○ Individual institutions have general mitigations against malicious software affecting their computing systems.

REFERENCES

1. http://cern.ch/geant4/
2. http://root.cern.ch/
3. http:www.gloriad.org/
4. http://www.transpac.org/
5. http://www.es.net/
6. http://www.cstnet.net.cn/
7. http://www.nersc.gov/
8. http://www.phy.bnl.gov/coop/doc/coop.html
9. http://www.nersc.gov/nusers/resources/PDSF/
10. http://www.nersc.gov/nusers/resources/HPSS/
11. http://proj-gaudi.web.cern.ch/proj-gaudi/
12. http://atlas.web.cern.ch/Atlas/index.html
13. http://lhcb.web.cern.ch/lhcb/
14. http://www-glast.slac.stanford.edu/
15. http://harp.web.cern.ch/harp/
16. http://bes.ihep.ac.cn/

11 Installation, Testing and Deployment

Careful logistical coordination will be essential for the receiving, staging, assembly, installation, and testing of all detector components and subsystems. This chapter discusses some of the basic considerations in the installation process and outlines a plan for the assembly, filling, and deployment of the antineutrino detector modules.

The installation of subsystems, system testing of experimental equipment and deployment of detectors in their appropriate locations begins as beneficial occupancy of facilities under civil construction are completed. Well-coordinated activities underground and on the surface are essential for the timely start of the experiment. While the civil construction of the underground tunnels and halls is being completed the assembly and testing of the first detectors will be started above-ground so that they can be deployed as early as possible.

The Collaboration has a wide range of experience in the installation and operation of large detector systems including underground installations at SNO, KamLAND, GALLEX (at the Gran Sasso Laboratory), IceCube (at the South Pole) and STAR. Members of the Daya Bay Collaboration have also been involved in the engineering and installation activities at MINOS, and Chris Laughton is directly involved in the evaluation of the tunnel design and specification for the civil construction at Daya Bay.

All of the assembly work of the antineutrino detector modules except for the filling will be performed above-ground in a Surface Assembly Building (SAB), as described in Section 11.1.1 below. This will provide a facility for the assembly and testing of two antineutrino detector modules at a time. The SAB will also include staging and testing facilities for other subsystems such as the muon system, the calibration system and PMTs as well as some storage and mixing facilities for the antineutrino detector liquids (see Section 6.3.) A Storage Building (SB) for storage of arriving equipment will likely be provided by the power plant. If not, we would plan to lease such a building. Some elements, such as the mineral oil storage tanks, will arrive ready for installation on the surface or in the tunnel. Other elements, such as the RPCs will require brief retesting to ensure that no damage occurred during shipping. However, elements such as the antineutrino detector vessels will require assembly under cleanroom conditions and system testing prior to transportation underground and filling.

The logistics of assembly and installation of the antineutrino detector include:

1. All detector modules will be fully assembled and tested with inert gas under cleanroom conditions in the surface assembly building.
2. Only empty detector modules will be moved down the portal access tunnel to the underground facilities. During initial transport from the surface to the underground filling hall the antineutrino detectors are unfilled and weighing about 20 ton, or 20% of their final weight.
3. All detector liquids will be transported underground to the filling hall in special ISO liquid containers to ensure clean and safe handling of all liquids (see Section 6.3).
4. The detector modules will be filled in pairs in the underground filling hall to ensure “identical” target mass and composition for each pair.
5. Once a pair of detector modules has been filled, the detectors are ready for deployment in one of the experimental halls.
6. Once a module is filled with liquid it will only be moved in the horizontal tunnels ($<0.5\%$ grade) between the experimental halls.
7. The filling hall is designed to allow for the draining of all detector modules at the end of the experiment.

The logistics of assembly and installation of the other detector systems (muon, calibration, electronics) include:

- Testing of components and subsystem assemblies in the SAB.
- Preparation of components and subsystem assemblies in the SAB for transport underground.
- System assembly in underground halls.

The effort of WBS 1.7 supports the overall planning, staging, control and execution of the final assembly and installation of the experimental hardware on site at Daya Bay. It includes labor, materials and universal (not including any custom installation and test hardware required for individual detector elements) equipment required to perform these functions. It includes all technician, trades, supervisory and engineering labor required to install the detector elements, but not the physicist and engineering efforts from the subsystems supporting the installation and test activities.

The effort of WBS 1.1, 1.2, 1.3 and 1.4 will provide system experts and cognizant engineering oversight along with relevant procedures and installation documentation for assembly and installation of the subsystem elements while in the Surface Assembly Building, in the experimental halls and subsequent in-situ system testing.

11.1 Receiving and Storage of Detector Components

The logistics of receiving, storing, staging, assembling, and testing components for the Daya Bay experiment requires the construction of suitable surface facilities including the SAB and SB. As detector subsystem elements arrive at the Daya Bay site, they will be delivered to one of these buildings. Special arrangements will be made for the handling of the detector liquids: the unloaded LS, Gd-LS, and mineral oil. The major elements of the experiment (antineutrino detector outer vessel, acrylic vessels, calibration systems, muon detectors, PMTs and liquid storage tanks) will arrive on a well coordinated timeline to avoid space problems and to allow the assembly of two detector modules at a time in the SAB. The space required for the storage of all components would otherwise quickly overrun the available storage space. The storage building will be of sufficient size to hold the large elements of the antineutrino detector and muon systems, but only for a few of these elements and for short periods of time before they are moved into the surface assembly building. Space for two steel outer vessels plus two sets of nested acrylic vessels as well as several large muon detector panels and boxes of PMTs will be sufficient. This requires a building of roughly 200 m^2 area and a crane with a 20 ton minimum capacity. A possible layout of the on-site storage and assembly facilities is shown in Fig. 11.1.

The logistics underground also requires special consideration: the storage tanks for Gd-LS, LS and mineral oil will need to be in place prior to the arrival of antineutrino detector elements to avoid delay in filling the antineutrino detectors.

11.1.1 Surface Assembly Building

A surface assembly building of the scale of 25 m$\times$50 m (1250 m^2) is required to assemble, survey, and test two antineutrino detectors at once. This building will be large enough to house two detector tanks and their associated inner acrylic vessels. The rest will be stored in the storage building. It will also have a 20-T crane to assemble the nested vessels and to lift the completed (but dry) antineutrino detectors onto their transporter. The surface assembly building will require clean assembly space for working on the open vessels to maintain the appropriate surface cleanliness. Once the detector modules are assembled and tested as required, they will be moved underground for filling and subsequent installation in the experimental halls.

In parallel with the assembly of the antineutrino detectors, the muon detectors will be inspected and tested. A building of this size will allow us to set up several inspection and testing stations and have a station

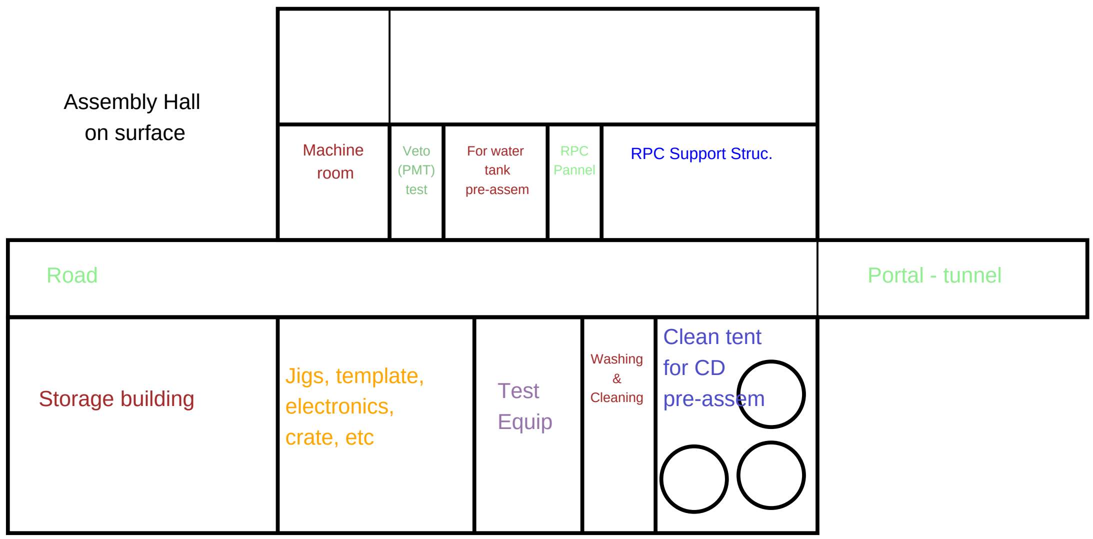

Fig. 11.1. Layout of the surface assembly building and storage facilities along the road to the tunnel portal.

for survey and alignment. It is sized to handle the assembly of two antineutrino detectors in parallel plus a short incoming RPC panel test station. If the building is arranged in a long (50 m), orientation, a single 30 ton bridge crane with rails along the building and a smaller 5–10 ton crane utilizing the same rails are sufficient. This allows for the manipulation of partially or fully completed (dry) antineutrino detectors while moving muon detector panels or staging other structures in parallel.

To accomplish these multiple testing, assembly, and QA tasks, appropriate test stations will be assembled. We plan to provide appropriate gases and high and low voltage power as well as a low-noise test environment with suitable electrical shielding and grounding. Mechanical noise is expected to play a minor role in these tests.

The surface assembly building will be designed to ensure several levels of cleanliness control. Detector components arriving on site will be stored under sealed conditions in the surface assembly building. During the assembly of the detector modules stringent cleanliness requirements apply. Both the level of particulates and the environmental air will have to be monitored. Cleanrooms of class 1000–10000 inside the surface assembly building or movable clean tents with HEPA filters to cover the detector modules can be used to provide the appropriate environment for the detector assembly.

11.2 Detector Assembly, Testing and Transport

11.2.1 Assembly of the Antineutrino Detectors

The major components of the antineutrino detectors will be fabricated at different places worldwide and shipped to the Daya Bay site for assembly and testing. The tasks involved in the assembly of the detector modules include:

1. Cleaning and inspection of stainless steel tank
2. Installation of the PMTs and cabling inside the detector tank
3. Installation of monitoring equipment in tank
4. Cleaning and inspection of the acrylic vessel.

5. Lifting the acrylic vessels into the detector tank
6. Connecting all fill lines, calibration, and instrumentation ports
7. Precision survey of tank and acrylic vessel geometry
8. Final cleaning throughout the entire assembly process.
9. Pressure/leak testing of acrylic vessels and detector tank after assembly
10. Test installation of automated calibration systems (to be removed before transport underground)

The entire assembly of the detector modules will be performed in class 1000–10000 cleanroom conditions. This complex assembly and integration task will require close coordination of several working groups (detector design, engineering, calibration, monitoring) and the on-site presence of key scientific and technical personnel. The detector assembly is shown in Fig. 11.2.

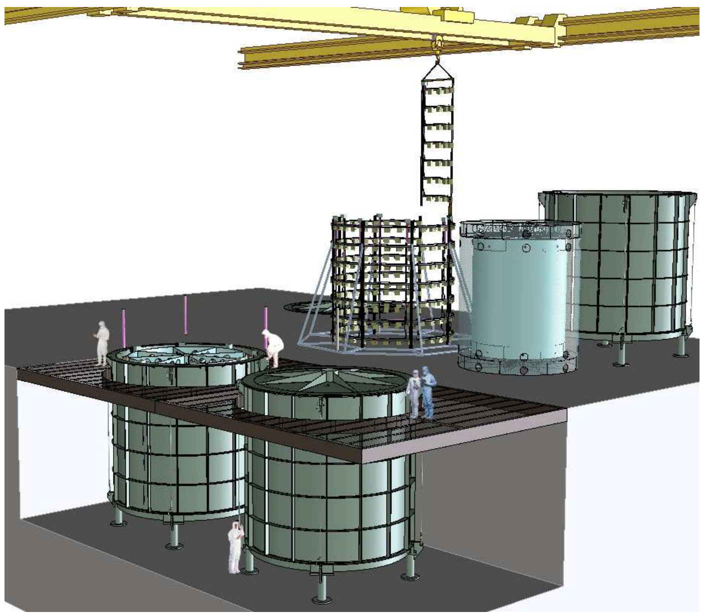

Fig. 11.2. Illustration of the envisioned detector assembly process in the Surface Assembly Building outside the underground tunnel at Daya Bay.

11.2.2 Precision Survey of the Antineutrino Detectors

Before transporting the antineutrino detector modules underground the geometry of the detector modules will be surveyed to high precision using modern laser surveying techniques. The precision commonly achieved in modern equipment over the scale of the antineutrino detector ($\sim$5 m) is of the order of $<$100 μm in both the radial and the longitudinal direction. This will serve as a baseline reference for the as-built detector geometry. In-situ monitoring equipment inside the detector modules will then be used to track any changes during the transport or filling of the modules. Relating internal system geometries to external fiducial points in the experimental halls will ultimately allow a precise relative understanding of detector geometry to the experimental hall and the outside world. This task will be the responsibility of the AD subsystem.

11.2.3 Antineutrino Detector Subsystem Testing

Following the assembly of detector modules and subsystems, testing becomes a critical task to ensure a smooth turn on and commissioning of the detectors underground. The collaboration's quality assurance (QA) and quality control (QC) experience, such as from IceCube and SNO, will be invaluable in preparing subsystems, getting them ready, and finally installing them underground with a high success rate.

All incoming equipment will be inspected for obvious damage. For system elements that are completely assembled and tested to meet specifications at far away sites (the US and Beijing, for example) we require a limited retest to ensure that no internal damage occurred during shipment, such as for the PMTs and calibration modules. Appropriate test stations will be assembled and utilized in the surface assembly building. Appropriate infrastructure including low- and high-voltage, laboratory gases, and other supplies will be provided for the on-site system tests.

Once the antineutrino detectors have been assembled in the surface assembly building we plan to perform a suite of tests of their mechanical integrity and functionality including:

1. pressure and leak tests of the detector tank and acrylic vessels with an inert gas
2. running the PMTs and all cabling with a gas fill inside the detector zones
3. testing the functionality of all ports, calibration, and monitoring equipment

Once a detector module passes these tests it is ready for transport underground. It will be moved down the access tunnel into the underground filling hall on transporters at very low speed.

11.2.4 Antineutrino Detector Transport to Experimental Halls

Detector modules and related systems will be transported to the filling hall and experimental halls from the surface assembly building using a self-propelled transporter. There are several issues associated with this task that make it somewhat more difficult than simply using conventional transportation equipment:

1. Due to cost and construction constraints the tunnel itself is not very large.
2. Entrance to the underground laboratory is through an access tunnel with an incline of 9.6%.
3. Transport systems have to be compliant with ventilation and underground safety requirements.

Because of this, the transport mechanism should:

1. have a low bed height ($\leq$0.5 m).
2. be powered by an electric drive or by some very clean burning fuel such as propane gas.
3. be capable of accurate tracking along an electric, mechanical or magnetic guide

Note that the detector modules will be filled in the underground filling station and they will only be transported in the horizontal tunnels between experimental halls after they have been filled. During the transport to the experimental halls the antineutrino detectors are filled and have a total mass of $\sim$100 ton. We have identified a suitable transportation system that meets these requirements. Figure 11.3 shows an illustration of the transporter we are considering for use at Daya Bay.

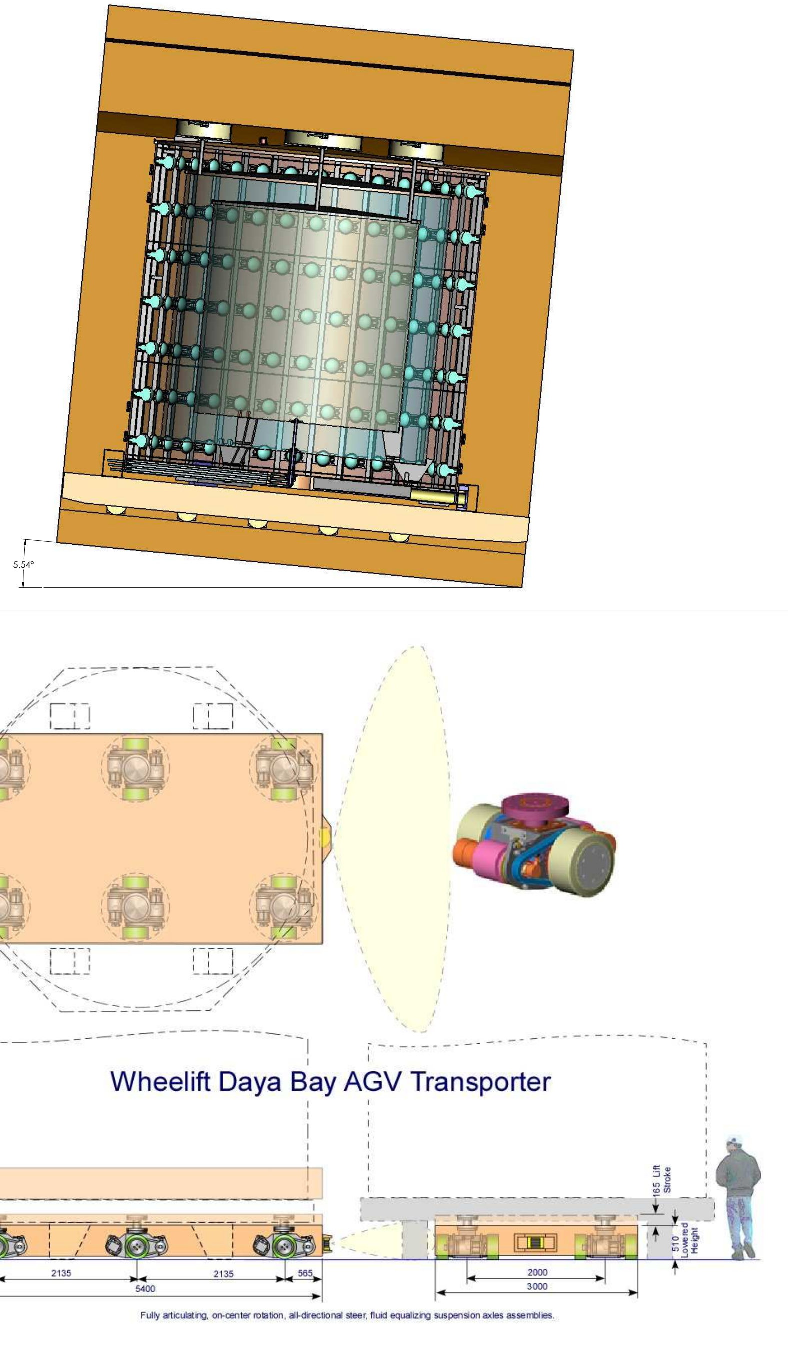

Fig. 11.3. *Top:* Antineutrino detector on transporter during transport down the access tunnel. *Bottom:* Illustration of the Wheelift transporter we consider for the transport of the antineutrino detectors [1].

11.2.5 Filling the Antineutrino Detector Modules

The underground filling station in Hall 5 is designed to allow the precise filling of the antineutrino detectors to the required precision of $\leq 0.1\%$ in target mass. Hall 5 is designed to accommodate up to two detector modules during the filling process. It has not been decided yet if the detectors will be filled in parallel or sequentially. The three components: Gd-LS, LS for the γ-catcher, and mineral oil will be filled simultaneously into each detector module. All three regions of the detector modules will be filled simultaneously while maintaining equal liquid levels in each vessel to minimize stress and loads on the acrylic vessels. The goal is to fill at least two detector modules from the same batch of liquids to ensure the same target mass and composition in pairs of detectors. Having one uniform batch of each type of liquid will further ensure the identical nature of the different detectors. The detectors can then be deployed, either both at the same near site for a check of the relative detection efficiency, or one at the near and the other one at the far site for a relative measurement of the antineutrino flux.

The filling process of the antineutrino detectors and required instrumentation are described in detail in Section 6.3.10. The filling station will be equipped with a variety of instrumentation on the storage tanks and the fill lines for a precise and redundant measurement of the target mass and composition. In addition, all fill lines will be equipped with the necessary filtration and liquid handling systems. After filling, the detector modules will be deployed in the appropriate experimental halls using the transporter system.

11.2.5.1 Antineutrino Detector Transport from the Filling Hall to the Experimental Halls

Once the detector has been filled in Filling Hall it is ready for transport to the experimental halls. In preparation for the transport to the experimental halls the following steps will be taken:

1. Review expected temperature in tunnel and experimental halls compared to Filling Hall. Discuss impact of temperature variation on detector. Apply insulation to outside of antineutrino detector if necessary.
2. Program transporter for virtual path magnetic guide from Filling Hall to experimental hall.
3. Wrap detector in clean plastic foil to prevent dust and environmental contamination.
4. Move transporter into Filling Hall and under the antineutrino detector.
5. Raise antineutrino detector from floor using transporter. Monitor the inside of the antineutrino detector with all available detector instrumentation during this initial lift and the subsequent transport.
6. Move detector out of hall 5 into tunnel.
7. Move detector along tunnel to experimental hall.
8. Move detector into experimental hall paying attention to minimizing the environmental contamination of the experimental hall from the tunnel.
9. Remove dust cover from detector.
10. Lower detector onto floor in experimental hall.
11. Move transporter out of experimental hall.

An antineutrino detector transport team consisting of the following people with appropriate communication devices will be needed during this operation:

- operators for transporter
- scientific project leads for the antineutrino detector
- personnel for observing the move of the detector through the tunnel
- personnel for monitoring the detector instrumentation including cameras of acrylic vessels, accelerometers, etc.

11.2.6 Assembly and Testing of Other Subsystems

The logistics of assembly and installation of the other detector systems (muon, calibration, electronics) include:

- Testing of components and subsystem assemblies in the SAB.
- Preparation of components and subsystem assemblies in the SAB for transport underground.
- System assembly in underground halls.

All incoming equipment will be inspected for obvious damage. For system elements that are completely assembled and tested to meet specifications at remote sites (the US and Beijing, for example) we require a limited retest to ensure that no internal damage occurred during shipment. Testing for broken channels or shorts in RPC chambers, PMTs, and calibration systems will all be required. To accomplish these tasks, appropriate test stations will be assembled and utilized in the surface assembly building. The test stations will be manned by technicians, grad students, post-docs and scientists and will utilize a small set of simple electrical tests performed to written test specification. Appropriate infrastructure including low- and high-voltage, laboratory gases, and other supplies will be provided for on-site system tests.

The pre-assembly and testing of the calibration system will include:

- Mount calibration boxes on AD overflow tank.
- Test functionality and operation of calibration system in the dry AD by moving the sources up and down.
- Test automated calibration sequence in SAB with dry detector (running all three boxes simultaneously, go through the sequence of different sources at different positions).
- Perform visual check of motion of calibration system with cameras inside AD.
- Test for gas leak tightness.
- Test flow and overpressure control of N_2 cover gas system with calibration box and gate valve.
- Install calibration PMTs in AD

11.3 Detector Installation in the Experimental Halls

The Daya Bay experiment consists of several detector subsystems:

1. Muon veto pool and RPC system
2. Antineutrino detectors

The installation procedures of these detector systems are outlined below following a possible time ordered sequence of this installation task.

11.3.1 Installation of the Muon Veto System

The installation of the muon system begins with a number of parallel efforts both in the surface assembly building and after civil construction beneficial occupancy of access tunnels and experimental halls.

A. Water pool systems require the following tasks:

1. With access to empty water pool, clean and prep wall surfaces and apply spray on sealant coating as per manufacturer's specification.
2. Deliver water system filtration skids to the SAB, transport underground to experimental halls, pour concrete pads and anchor skids, then connect electrical utilities. Install surface feed water skid system near portal entrance. See Fig. 8.5 which shows a conceptual design schematic of the overall system.
3. Install supply and return water piping through tunnels between surface feed water skid and experimental hall skids. Install localized experimental hall piping between filtration skid and water pool.
4. Fill pool with water and run/test filtration systems. Then empty pool for detector systems installation.

B. PMT test and assembly in parallel with item "A".

1. Setup PMT testing area in SAB.
2. Start phased delivery and testing of 8" PMT in SAB.
3. Transport to experimental halls for storage and assembly to support structure as required.

C. Install muon support structure after completion of item "A".

1. Deliver pool floor anchors, bulk PVC piping and fittings, and Tyvek material and frames to experimental halls.
2. Layout, survey and install structural support floor anchors in water pool flooring. Re-seal around anchors and floor as required.
3. Assemble and glue-up PVC support substructures, attach PMT supports, install PMTs in supports and attach Tyvek sheet frames to form a complete substructure unit.
4. Lower by crane support scaffold into water pool onto floor anchors and roll personnel access bridge across pool span for scaffold access.
5. Lower by crane and stack bottom course of substructure units onto floor anchors around pool circumference.
6. Continue to stack remaining courses of substructure units to the top elevation of water pool.
7. Roll personnel access bridge off of pool and remove by crane the support scaffold from pool.
8. Lower by crane and install lower central course of substructure units onto floor anchors.
9. Fill pool with water and begin system testing of water muon detector.

D. RPC support structure installation in parallel with item "C".

1. Deliver disassembled structural framing and rails to the experimental halls and offload to far end of hall off of the pool.
2. Install rails, level, anchor and grout on either side of pool.
3. Erect individual 4 m wide RPC support frames and set on rails off far end of pool.
4. Connect drive units and test roll each 4 m wide structural span across the pool and back. Structure is ready for RPC panel installation.

E. Install RPC on structural supports after completion of item "D".

1. Deliver RPC panels to the SAB for storage and testing.
2. Run and test RPC panels then deliver to experimental halls when complete structural support is complete.
3. With structural supports off the far end of the pool, install individual RPC panels.
4. Complete a 4 m wide structure and roll over pool for storage and systems testing.
5. Complete all (4) individual structures with panels and prep for complete muon system test with water in the pool item “C-9”.

11.3.2 Installation of the Antineutrino Detectors

After the antineutrino detectors have been filled they will be slowly transported through the tunnels to the appropriate experimental hall where they will be deployed into the drained water pool and onto their stands. The default plan is to lift the detectors from the transporter into the water pool by crane. We assume that the installation of the muon veto system is essentially complete at this point. The installation of all detector systems in the experimental halls is a complex procedure that requires good coordination between the various subsystems. Detailed check lists and procedures will be developed for this task. We also suggest to practice the steps in the lifting and installation procedure with a lightweight mockup frame that resembles the antineutrino detector and has the same dimensions. This will help prepare everyone for the lifting process and test the procedures developed for this task. The installation process is illustrated in Fig. 11.4, Fig. 11.5

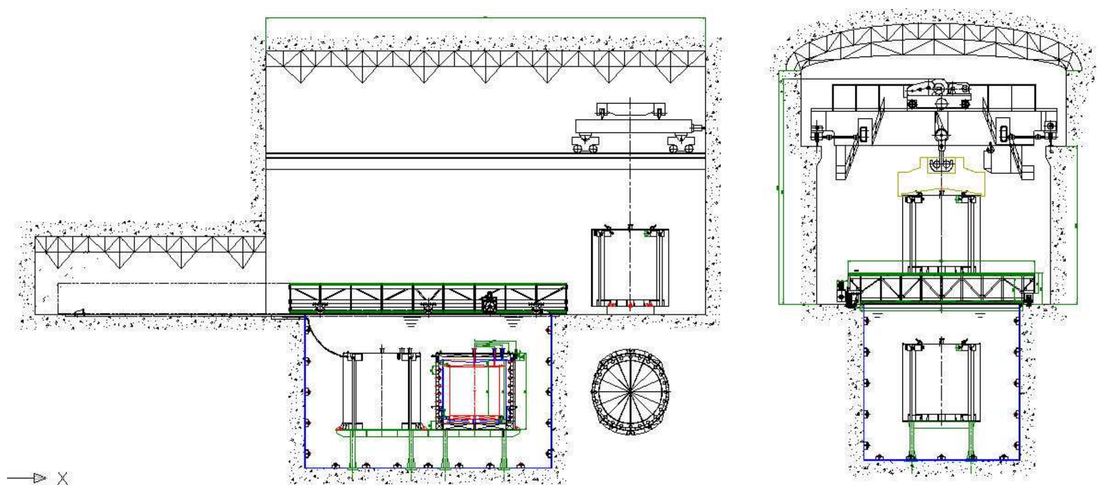

Fig. 11.4. Side views of one of the experimental halls with detectors inside the water pool and above the floor of the experimental hall with the overhead cranes above. In this deployment scheme the detectors will be suspended on stands or a platform inside the water pool. The overhead crane lifts the detectors from the transporter near the entrance area and lifts them into to the water pool.

and Fig. 11.6.

The installation of the antineutrino detector will include the following steps. Estimates for the time it will take to perform each step are given.

1. Setting the antineutrino detector down on the floor in the entrance area of the experimental hall by lowering the transporter. Removing the transporter from the experimental hall.

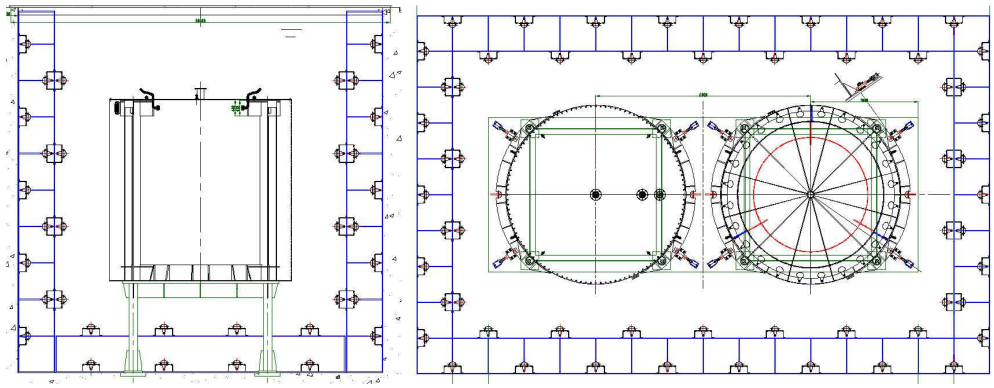

Fig. 11.5. Side view (left) and top view (right) of the detectors inside the water pool. In this default deployment scheme the detectors are suspended from stands or a platform inside the water pool. The left figure shows support stands for the antineutrino detectors while the right figure shows the outline of a support platform. The advantages and disadvantages of such a support structure are being evaluated and the detailed design of the detector support is under development. Also shown is the schematic structure and position of the PMT support in the water pool.

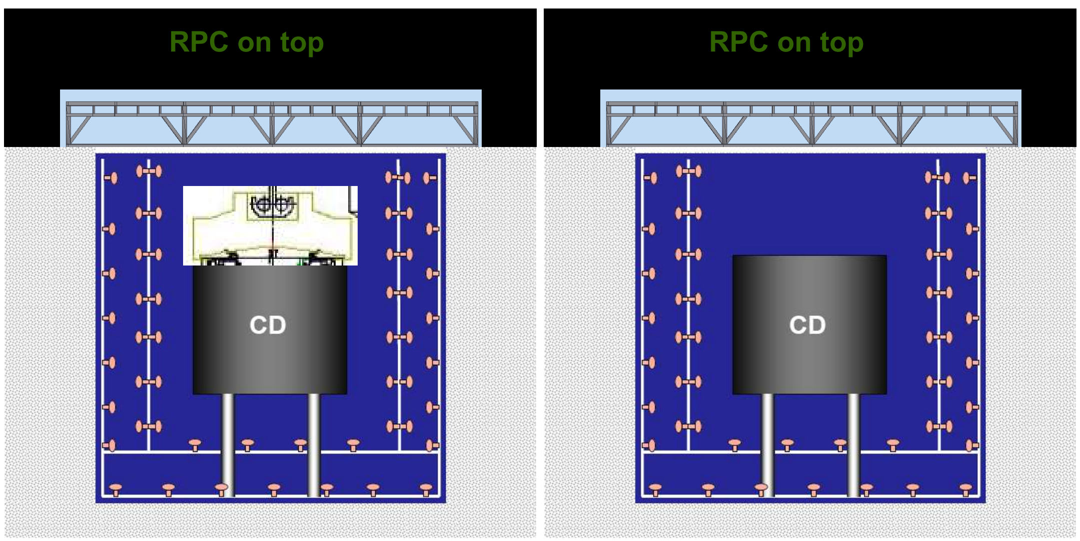

Fig. 11.6. *Left:* Side view of one of the antineutrino detectors in the water pool with the lifting beam of the overhead crane attached to the detector. The lifting beam needs to be manually attached and detached prior and after all lifting. The water of the pool needs to be drained for this operation. *Right:* Schematic side view of the detector submersed in water and supported from stands or a platform. The support structure for the antineutrino detector needs to be integrated with the PMT structure of the water pool. The support stands will penetrate the Tyvek layers separating the various regions of the water pool veto.

2. Install scaffolding or secure ladder structure around antineutrino detector to attach the lifting fixture to the stainless steel tank. Attach the lifting fixture to the stainless steel tank of the antineutrino detector

paying particular attention to safe work practices 5 m above the floor. *(1 day)*

3. Prepare the water pool for the installation of the antineutrino detector. *(1 day)*
   - Drain pool.
   - Complete work on other subsystems and stop any unnecessary activities.
   - Clear unnecessary personnel and equipment from the water pool and verify that there is no obstruction in the lifting path of the antineutrino detector. (We may want to practice the steps in the lifting procedure and the installation of the antineutrino detector with a lightweight mockup frame that resembles the antineutrino detector and has the same dimensions.)
   - Position a few trained people in the water pool to observe and guide the lifting of the antineutrino detector. Provide good communication with 2-way radios.
4. Lifting the antineutrino detector into the water pool: *(1–2 days)*
   - Raise the antineutrino detector vertically off the ground, and move it over the water pool.
   - Lower the antineutrino detector onto the support platform in the empty water pool. A mechanical system for guiding the antineutrino detector into place will be needed.
   - Manually secure the antineutrino detector to the stand in the water pool. This will require a specially designed work platform to access the bottom of the antineutrino detector and the top of the support stands or platform.
5. Install scaffolding or a work platform to access the top of the antineutrino detector. *(1 day)*
6. Using the work platform or scaffolding make all the necessary connections to the top of the antineutrino detector. During this work all personnel will be secured with a fall-arrest harness and protected by helmet and appropriate other gear. *(2 days)*
   - Disconnect lifting fixture from antineutrino detector and raise it out of the way.
   - Lower the automated calibration boxes (200 kg each) from the entrance to the experimental into the water pool above the antineutrino detector. A special crane for small equipment may be needed to avoid use of the large 100 ton crane.
   - Install automated calibration boxes with sources, N_2 gas supply lines, and calibration control cables. Perform a leak and functionality check on each calibration box.
   - Lower bundle of PMT HV and signal cables from floor of experimental hall and make connection at patch panel of antineutrino detector.
   - Lower readout cables for all other instrumentation of the antineutrino detector and make connection to antineutrino detector.
   - Install dry boxes around cable bundles and covering selected instrumentation and cable ports on the antineutrino detector.
   - Perform leak check of dry box areas by using either helium and a leak detector or by simply pressurizing the dry box and watching for a slow pressure drop with time.
7. With scaffolding or work platform in place perform a system check of the antineutrino detector: *(3 days)*
   - Deployment of all calibration sources into the different regions of the antineutrino detector using all three automated calibration boxes.

   - PMT HV test.
   - Test readout of all other instrumentation of the antineutrino detector.

8. Once the antineutrino detector has been determined to be functional, the scaffolding or work platform can be dismantled and lifted out of the water pool *(1 day)*

We estimate that it will take at least 1–2 weeks to install a detector in the experimental hall. This estimate assumes that the work is not manpower limited.

Special equipment will be needed for the installation of the antineutrino detectors. We assume that all of this equipment will be provided by the civil construction or integration tasks. This includes:

- concrete, flat pad for antineutrino detector in entrance area of experimental hall where detector can sit until it is lifted into the experimental hall
- large 100 ton crane for lifting of full antineutrino detector into water pool
- small 5 ton crane for lifting equipment such as calibration boxes and scaffolding into water pool
- (re)movable scaffolding or work platform in experimental hall to attach lifting structure
- removable scaffolding or work platform in water pool to detach lifting structure, install calibration boxes, and make connections for cables and gas lines
- mechanical system that guides the antineutrino detector into the correct position on the support platform in the water pool.
- safety harness and support systems for personnel working at heights of 4–8 m above floor of experimental hall or water pool
- secure ladders or scaffolding for personnel and workers to enter the 10 m deep water pool from the experimental hall.
- rescue cage and other provisions to lift injured worker out of empty water pool

One of the important elements in this deployment procedure is a work platform that provides access to the bottom of the detector for securing it to the support stands and at the top of the detector for making all required cable and pipe connections and for performing the necessary system checks. A couple of different options for such a work platform have been considered (see Fig. 11.7): One is a mechanical structure supported from the detector itself. The other one is a floating platform on the water in the half-filled pool of the muon veto. Such floating work platforms have been used in other experiments such as Super-Kamiokande and SNO. The water level can be adjusted to allow access to the detector at any height inside the water pool. The water and platform would help protect the PMTs but access to several levels of the detector at the same time is difficult. The operational issues for these solutions still need to be evaluated in detail.

Special training and trained personnel is needed for the entire lifting operation of the antineutrino detector including the attachment of the lifting fixtures. The safety considerations and hazards of the installation of the antineutrino detectors is described in a separate document. During the installation and final testing of the antineutrino detectors in the experimental hall we require the presence of a number of subsystem experts. The personnel needed during this complex installation process includes:

- operators for the transporter and cranes
- lifting and hoisting experts

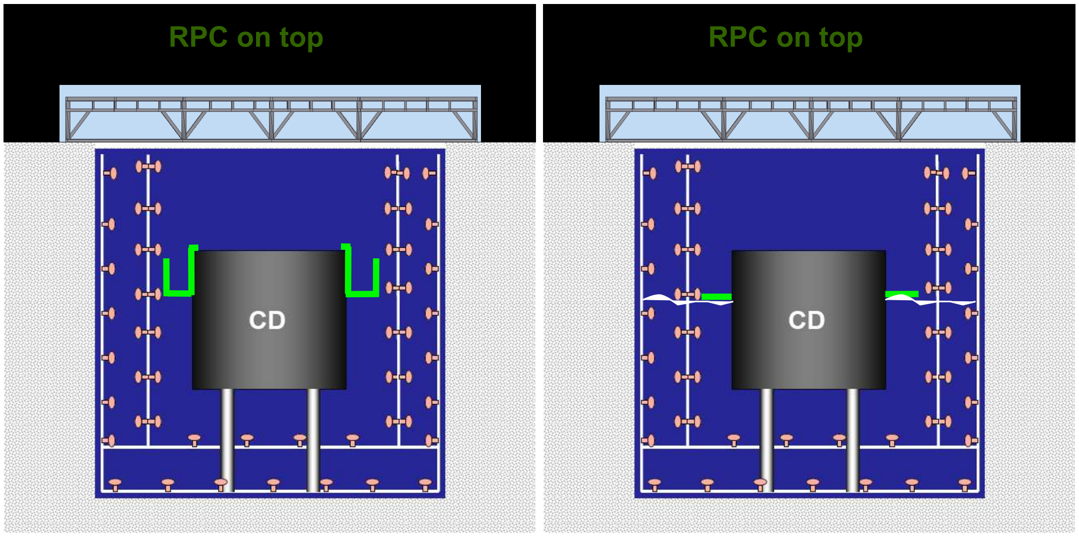

Fig. 11.7. *Left:* Schematic sketch of a mechanical work platform suspended from the detector itself. It can provide access to the top of the detector during the installation for connecting cables, the automated calibration system, and for performing the final antineutrino detector system checks. *Right:* Schematic of a floating work platform around the antineutrino detector. The height of this platform can be adjusted by raising and lowering the level of the water in the pool.

- engineering and scientific project leads for the antineutrino detector
- calibration subsystem experts for installation and final testing
- instrumentation subsystem experts for installation and final testing
- PMT and HV subsystem expert for final testing
- general technician support
- support for installation of work platforms and scaffolding

The open issues in this deployment method include:

- An installation plan for a work platform in the muon veto water pool without the risk of damaging the PMTs in the water pool or its reflective structure.
- A procedure for the removal of the detector from the far site of the experimental hall while the detector in the location near the entrance is still deployed in the water pool. We might want to replace only the far module without disturbing the near module. All utilities, cables, etc. for the near detector would have to be located to provide clearance for lifting the far detector out of the water pool. Some of this clearance problem will also exist for the alternative concept using movable platforms.
- A support platform for the detector in the water pool offers structural and technical advantages over support pillars. However, such a platform blocks more light in the muon veto. Further muon veto simulations are required to evaluate the impact of a detector support platform or detector stands on the performance of the muon veto.

11.3.3 Precision Alignment and Survey

Precise knowledge of the ‘global’ location of each hall with respect to the reactor cores is important for the accurate determination of the distances between the reactor cores and each neutrino detector. Permanent survey markers in each experiment hall will serve as reference marks for the positioning of the detectors. These survey markers will be placed and known to a precision of better than tens of centimeters, with respect to the outside world, even though the halls are hundreds of meters inside underground tunnels. This precision is commonly achieved in the construction of tunnels and in mining.

Within the experimental halls the position of the detectors can be determined quite precisely. The antineutrino detectors will be placed and anchored in precisely known location on their stands at the bottom of each water pool. The knowledge of the location of each antineutrino detector, with respect to the fiducial markers in the halls, will be at the sub-mm level. The location of the muon system elements also can be surveyed and understood at the same sub-mm level. This is both with respect to the antineutrino detectors and the experimental hall.

With this information the distance between the detector modules and the reactor cores will be known to the required precision of better than 30 cm. A summary of the required positioning accuracy is provided in Table 11.3.3.

Element of Experiment	Positioning Accuracy
experimental hall	$\mathcal{O}(10\ \mathrm{cm})$
detector position in experimental hall	<1 mm
acrylic vessels within detector tank	<1 mm

Table 11.1. Positioning accuracy of the principal elements of the Daya Bay experiment.

The Muon System will require survey of PMT locations within each water pool as well as a survey of the location of each RPC. The positioning requirements are not as severe as for the ADs.

.

REFERENCES

1. Wheelift Systems Group, ultraheavy capacity transporters, http://www.wheelift.com/

12 Integration

The scope of effort for this subsystem is to assist experimental subsystems and their managers in developing, defining, and controlling the mechanical systems, electrical systems, experimental assembly, safety systems, and civil construction interface between each subsystem. To this end the Integration Group will act as liaisons between each subsystem to coordinate and document efforts in resolving all physical interface issues. Engineering and design effort is being devoted to ensure that subsystem hardware can fit together, be assembled and serviced, and have minimal negative impact on other subsystem performance. This group will communicate integration issues and their resolution based on change control policy to L2 managers, project management and the collaboration in general on interface issues. The integration group must approve and process all Engineering Change Request and Engineering Change Notice (ECR/ECN) dealing with subsystem interface, experimental assembly and physical envelope related issues. To accomplish this effort the subsystem has been subdivided into five WBS L3 subcategories: WBS 1.8.1: Mechanical Systems Integration, WBS 1.8.2: Electrical Systems Integration, WBS 1.8.3: Experimental Assembly, WBS 1.8.4: Safety Systems Integration and WBS 1.8.5: Subsystem Management.

12.1 Mechanical Systems Integration

The primary goal is subsystem mechanical hardware interface coordination, by assisting in defining and developing subsystem component hardware geometry. It is important to develop 3-D envelope drawing documentation of the maximum dimensional subsystem mechanical hardware, and its operational location within the experimental complex. Subsystems nominal dimensional detail and assembly drawings will likely differ as their designs evolve and mature due to manufacturing and alignment tolerances. These integration drawings will differ as they represent simple geometric volumes that bounds a subsystem dimensional hardware limits and stay clear zone. It will also define and document mechanical hardware interfaces between subsystems where mechanical support connections are required.

An early project effort will be the civil construction of the Daya Bay experimental complex, with its access tunnels, experimental halls, surface assembly building and utility requirements. The integration group will assist in defining these areas and the development of experimental requirements as they pertain to the civil construction. We will interact formally with the civil contractor in defining and documenting civil and experimental interfaces. We will maintain as-built documentation and 3-D envelope drawings of the civil complex when the facilities are complete, and will update the drawings whenever modifications are made.

The integration group will assist in specifying and documenting the experimental mechanical utility requirements for detector installation and operation. Below ground tunnel and experimental hall ambient temperature, humidity and air exchange requirements will help determine the appropriate HVAC system to be installed. Overhead crane requirements in the experimental halls and surface assembly building will be specified. Antineutrino Detectors (AD), each weighing 100 tons full, will have to be transported from Liquid Scintillator (LS) filling station to each experimental hall. The AD transporter to be used for this operation will have to be specified and an appropriate vendor found that can deliver this specialty equipment. The Muon system water pools require highly filtered water with excellent clarity. The water filtration and pumping system for each experimental hall pool will be specified along with determination of capable vendors. Discussions are underway with CGNPG over the use of ultra-pure water from the reactor. Experimental gas systems will need to be defined and documented within each experimental hall and surface support building along with compressed gas bottle and dewar storage racks. Mechanical utilities (piping and ducting) routing for experimental needs through the complex will be defined and documented by the integration group along with interface mounts to the facility and interconnection points to subsystems.

12.2 Electrical Systems Integration

Electrical power requirements will be divided into two parts; facility electrical power and experimental electrical power. Facility electrical power is defined as the supply and distribution network extending from the main feeder lines down to and including distribution panels and wall receptacles as provided in the civil construction of the complex. This network will supply both conventional (rotary equipment) and isolated clean power for experimental use. The integration group will assist in determining conventional power requirements for water systems, gas systems, LS filling station, and experimental HVAC systems as required.

Detector electronics systems used to collect data are adversely affected by the electrical noise generated by conventional electrical equipment. Therefore an isolated clean power distribution network is required to supply power for all subsystem electronics. In conjunction with this network a grounding plan for all AC power systems must be developed and implemented to eliminate clean power ground loops and minimize electrical noise on the system. The experiment is responsible for this network and grounding plan, and the integration group will assist in determining and documenting this network capacity and distribution.

To minimize operational downtime and loss of data caused by electrical utility power dips and short term disruptions ($<$30 minutes), uninterruptible power supplies (UPS) will be used on the isolated clean power network. Integration will assist each subsystem in determining and documenting the need and capacity throughout this network.

Emergency power requirements will be needed for the facility electrical power network to maintain life safety system during long term disruption of utility power. At this time it is not clear if the isolated clean power network has the same emergency power needs, possibly during LS filling, but the integration group will work with each subsystem to make this determination.

Electrical utilities (tray and conduit) routing for experimental needs through the complex will be defined and documented by the integration group along with interface requirements to both facility and specific subsystems.

12.3 Experimental Assembly

Each subsystem is responsible for the delivery to the Daya Bay surface assembly building of fully or partially assembled component hardware for installation. It is the installation subsystem that provides the resources needed to complete subsystem assembly and final operational installation in the complex. The integration group will assist individual subsystems in defining and documenting a hand-off interface with the installation group. This interface will specify the deliverable hardware configuration, quantity, timeline, and initial staging of the hardware when delivered. It should include any requirements for use of surface assembly building floor space for additional hardware assembly or component testing.

The integration group will assist in the development of an overall experiment installation plan. This plan will be documented in solid model drawings showing the assembly flow of subsystem hardware through the complex in a timeline sequence starting at beneficial occupancy of the surface assembly building. The time interval will be directly coupled to installation milestone dates through to project completion.

12.4 Safety Systems Integration

Environmental, Safety, Security and Health issues for the project will fall within those policies established by the host country, China, and must meet minimum standards, as negotiated, for all collaborative members working at the experimental complex. These polices will include life safety concerns for radiological controls, chemical inventory controls (MSDS), emergency egress and access controls, fire protection and suppression systems, laser operation, cryogens, oxygen deficiency hazards, fall protection, personnel protective equipment, electrical and mechanical hazards, and liquid spill confinement and cleanup controls. The integration group will assist in evaluating, defining and documenting these life safety hazards as they pertain to this project and will work with each subsystem on engineered solutions and/or procedures required to mitigate these hazards.

Equipment protection systems will also be incorporated into the experimental operational safety envelope. A system will be developed using a programmable logic controller (PLC) as the heart of a safety interlocks system to alarm subsystem fault conditions and automatically bring experimental hardware to a preprogrammed safe state. These fault interlock conditions will automatically valve off liquid and gas sources and/or turn off electrical power to designated hardware based on cooling water leak detection and/or detection of flammable gases and liquids. It will also alarm and interlock AC power for smoke detection near electronics, and alarm and ventilate for ODH and flammable gas conditions. The integration group will assist in developing and documenting these equipment protection and life safety interlock systems, and provide guidance in the implementation of hardware and logic for system operation.

12.5 Subsystem Management

The integration group will provide the necessary management, engineering, design, and administrative effort needed to assist all subsystems in fulfilling our project interface objectives, as outlined herein. To this end there will be two L2 subsystem co-managers from both the China and United States collaborative groups whose primary responsibilities will be to ensure subsystem goals and objectives are successfully accomplished. They will report directly to project management their subsystem tracking of schedule and cost progress. They will work with project management and L2 subsystem managers as members of the Technical Board in reporting, resolving, and documenting all subsystem interface issues through the engineering change control process. They will hire and manage the engineering, design and administrative resources needed to develop and maintain this subsystem effort.

The integration group will develop general standards and controls that include engineering document standards to be used project wide for CAD file exchange, engineering drawings and design notes, specifications and procedures, engineering change request and engineering change notice (ECR/ECN) process, and a document numbering system. Engineering design standards will be developed outlining analytical methods and factors of safety, along with industry standards and codes to be applied in the design, fabrication or procurement of both mechanical and electrical experimental components. The integration group will assist in defining an experimental component reference name and coordinate system standard to identify, by unique name, designation subsystem components and their operational location in the complex. The integration group will develop and maintain a project wide cable/fiber/connector database with unique name designation along with from-via-to location information. Integration will also maintain all documentation related to alternative value engineering design studies used in the development of the baseline project experimental hardware.

13 Value Engineering

The Integration Office oversees the value engineering program of Daya Bay. This group provides high level systems and value management oversight over all technical aspects of the Project. A number of value management studies have been undertaken, including an overall detector design with the ADs in air (rather than water), studies of alternatives to large (150 ton) cranes and studies of alternative layouts for servicing ADs in the SAB.

13.1 Alternative Designs of the Water Shield

We have chosen a water pool as the baseline experimental design (see Fig. 2.3). The two near detector sites have two antineutrino detector modules in a rectangular water pool, whereas the far site has four antineutrino detector modules in a square water pool. The distance from the outer surface of each antineutrino detector is at least 2.5 m to the water surface, with 1 m of water between each antineutrino detector.

Our primary alternative to the baseline design is the "aquarium" option. A conceptual design, showing a cut-away side view is provided in Fig. 13.1. Several views are shown in Fig. 13.2. The primary feature of

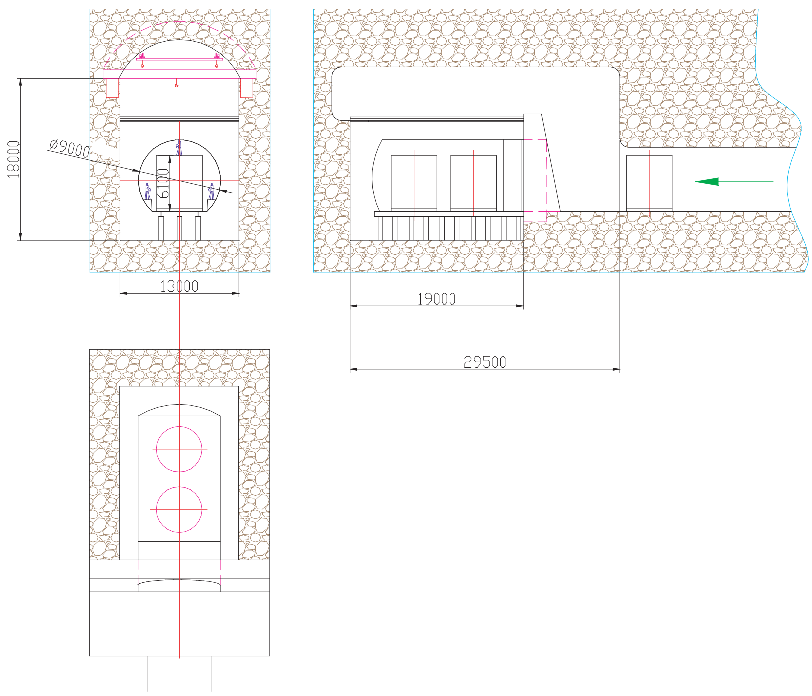

Fig. 13.1. Side cutaway view of a near detector site aquarium with two detectors visible.

this aquarium design is that the antineutrino detector modules do not sit in the water volume, but are rather in air. The advantages of this design are ease of access to the antineutrino detectors, ease of connections to the antineutrino detectors, simpler movement of the antineutrino detectors, more flexibility to calibrate the antineutrino detectors and a muon system that does not need to be partially disassembled or moved when the antineutrino detectors are moved. The primary disadvantages of this design include the engineering difficulties of the central tube and the water dam, safety issues associated with the large volume of water above the floor level, cost and maintaining the antineutrino detectors free of radon and radioactive debris. This design will be retained as the primary option for a "dry detector" and serves as our secondary detector design option. Other designs that have been considered include: ship-lock, modified aquarium, water pool

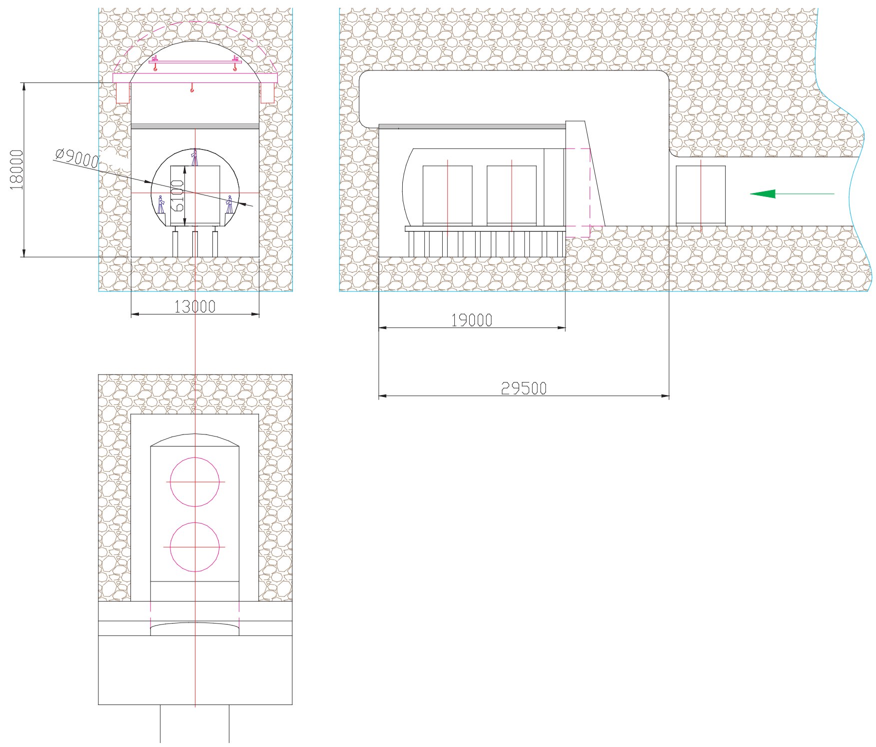

Fig. 13.2. End, side and top views of the conceptual design of a near detector site aquarium. All distances are in mm.

with a steel tank, shipping containers, and water pipes, among others.

The cost drivers that we have identified for the optimization of the experimental configuration include:

- Civil construction
- Cranes for the antineutrino detectors
- Transporters for the antineutrino detectors
- Safety systems in the event of catastrophic failure
- Storage volume of purified water
- Complexity of seals in water environment

The physics performance drivers that we have identified include:

- Uniformity of shielding against γ rays from the rock and cosmic muon induced neutrons
- Cost and complexity of purifying the shield region of radioactive impurities
- Amount and radioactivity level of steel near the antineutrino detectors (walls and mechanical support structures)
- High efficiency of tagging muons and precise measurement of that inefficiency

The primary parameters that we have investigated in the optimization of the detector design are the thickness of the water shield, the optical segmentation of this water Cherenkov detector, the PMT coverage of this water Cherenkov detector, the size and distribution of the muon tracker system, the number of PMTs in the antineutrino detector, the reflectors in the antineutrino detector. The existing work favors the water pool.

13.1.1 Alternate Surface Assembly Building Design

An alternative design for the Surface Assembly Building (SAB) is presented. This design like the present baseline design is located at the portal entrance to the underground access tunnel. It is a surface assembly building of the 25-m by 50-m scale as required for the staging, assembly, survey and test of the larger subsystem components. The building will have the capacity for the in-parallel staging, cleaning and assembly of two antineutrino detectors composed of outer vessels, acrylic vessels, PMT array structure and calibration system. To accomplish this effort in this alternative design, the AD outer vessels will be staged in an access trench that runs partially through the length of the SAB and inline with the tunnel portal entrance (see Fig. 13.3). The vessels will be staged atop support stanchions off the trench floor to allow access of the

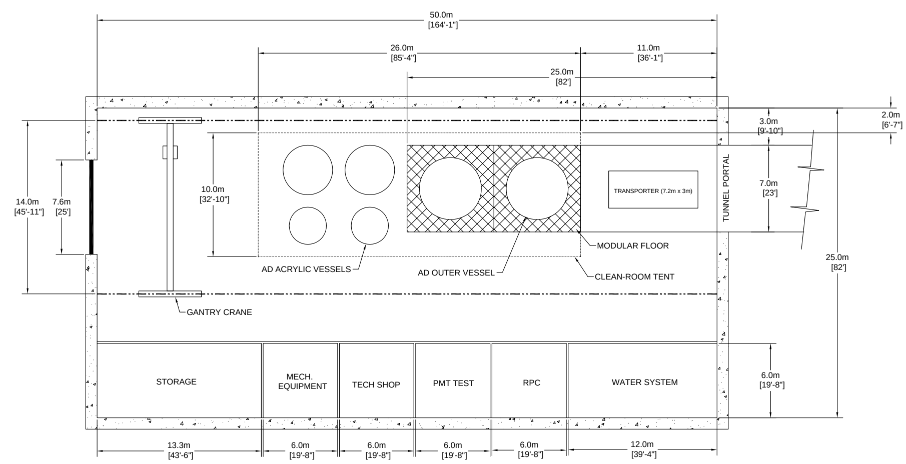

Fig. 13.3. Plan view of alternative SAB design.

transporter from below to lift and transport an AD. These AD support stanchions should be used throughout the facilities where ever an AD must be delivered (filling hall, experimental halls). The depth of this access trench is approximately 5.5-m so that the top of an AD is level with the SAB floor (see Fig. 13.4). This will allow for appropriate personnel access walkways/railings, and a clean room tent to be erected above the top opening of the AD outer vessels at SAB floor height. The width of the access trench is approximately 7-m and will allow for appropriate scaffolding to be erected around the AD outer vessel for access from either above or bellow. The outer vessel can be cleaned and prepped in this area and waste solutions easily contained and removed.

A roll-up door is located opposite the tunnel portal entrance inline with the trench. This will allow delivery of large experimental components into the SAB under the gantry crane for easy offloading. The 20-ton floor gantry crane that spans the access trench will be used, not only for AD assembly, but to offload materials, equipment, transporter and experimental components from SAB floor level to the lower trench at the tunnel portal for transport below ground. For the AD assembly, the acrylic vessels, PMT support

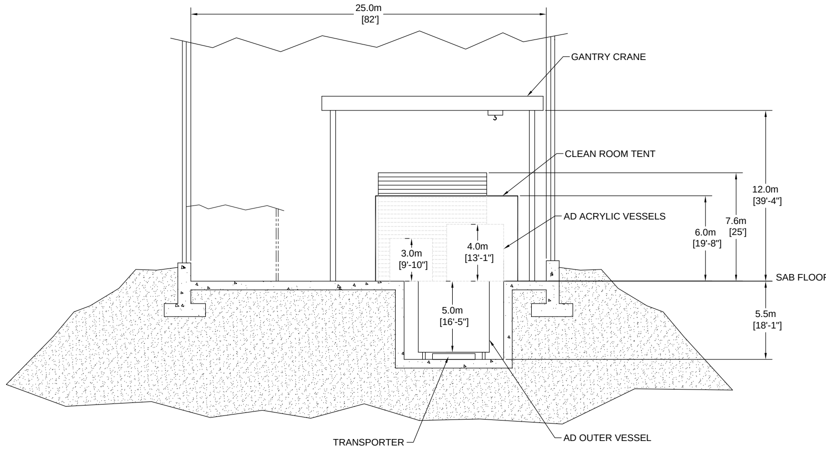

Fig. 13.4. Elevation View shows AD staged in trench with clean room above.

structure and top cover can be staged on the SAB floor in the clean room tent beyond the end of the trench and then rigged with the gantry crane to an AD vessel located below in the trench. A fully assembled and tested, but dry AD, will be picked up by the transporter and brought from the tunnel portal access trench, below ground for filling with liquid and subsequent installation in an experimental hall.

Stairs from the SAB floor to the bottom of the trench will allow for personnel access to electric powered vehicles to be used in the transport of personnel and tools from the trench portal to experimental halls below ground. During civil construction of the complex the tunnel entrance portal can be fully ramped to the surface for ease of entry and removal of civil construction materials, but should then be modified for the trench alternative SAB design.

Advantages to this alternative design are:

- The trench, starting 5.5-m below the ramp design, will reduce the grade of the access tunnel to something less than the 9.6% slope reducing the tilt of an unfilled AD during transport.
- This alternative SAB design is not symmetrically located about the portal entrance, but shifted to one side allowing for larger shop areas and not interfere with an existing on-site hospital structure.
- The floor gantry crane should be less costly than a longer span overhead bridge crane that must be incorporated into the building structure. It also requires less clearance height since the top of the outer vessel is at SAB floor height when installing inner acrylic and PMT structures.
- AD modules are completely assembled in a common clean room area and then transported below for filling and delivery to experimental halls, requiring only one crane lift in the entire process, at the experimental hall.

13.1.2 An Alternative Deployment Method for the Antineutrino Detectors

An alternative deployment method for the antineutrino detectors is the use of lifting platforms that lower and raise the antineutrino detector in and out of the water pool, as shown in Fig. 13.5. The idea is to use

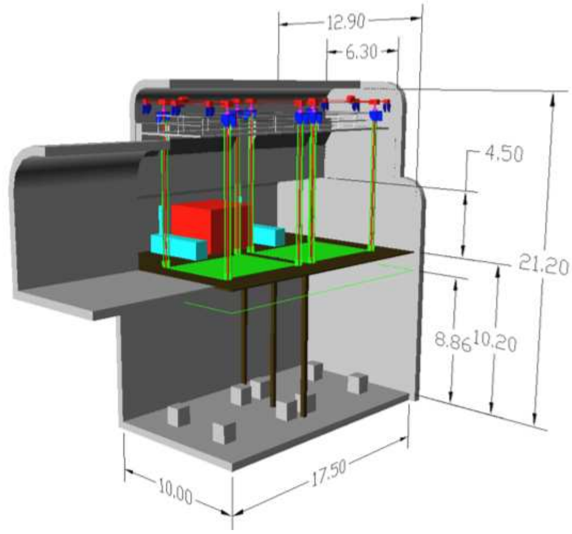

Fig. 13.5. Model of the movable detector platforms in the experimental halls. The platforms are shown in green. All the drive components are shown in red. The blue parts are supports for the gear boxes and attached to the walls. The water pool is underneath the green support platforms. Only the green platform and its vertical hangers enter the water. The screws (in red) and the nuts (small but visible in magenta at the top of the hangers) stay well above the final water level.

platforms which are moved by a vertical gear system to lower and raise the detectors in the water pool. This system is specifically designed to lower and raise the detectors in and out of the water pool. This method offers some operational advantages and also eliminates the need to drain the water pool. The lifting platform can be made from stainless steel plates in an all-welded construction. To save costs the platform can also be made of out steel with a coating against the ultrapure water in the veto pool. We estimate the mass of the platform to be $\sim$12 ton. The lift drive system that is used to lower and raise the platform consists of commercially available motors, reducers, right-angle drives, and power screws. The parts inside the water pool can be enclosed so that the moving parts would not come in contact with the ultra-pure water. It is not necessary to enclose the drive components as they never enter the water.

The lift screws are special items but commercially available. They are 4.5” acme thread power screws with a dynamic capacity of 445 kN. The load on each screw would be about 300 kN. The torque required to lift the antineutrino detector is about 2900 N-m per screw. The system can be designed for a 1–2 hrs lift time.

The main gear box in this system is a double-enveloping right angle worm gear reducer which provides the highest possible torque capacity. This gear box would provide all the required speed reduction so that lower torque components can be used in the drive components. A miter box can be used to drive 90 degrees with bevel gears at a 1:1 ratio. A double-ended worm gear motor box can be used for the initial reduction. With such an assembly a motor power of $\sim$30 kW is sufficient. Spherical roller thrust bearings with a thrust capacity of 800 kN can be used. They do not overconstrain the system so that the resulting loads are strictly vertical.

We estimate that the cost of this system is similar to the baseline plan of installing the detectors by crane once all aspects are taken into account. The cost of this movable platform system is to be compared to the total of a.) the overhead crane, b.) the lifting structure or beams above the antineutrino detectors, c.) the platform at the bottom of the pool, d.) the larger experimental hall required for the overhead crane, and e.)

all other special access equipment including the work platform or floating platform.

The basic procedure for the deployment of the antineutrino detectors with such a platform is illustrated below:

1. The transporter moves the antineutrino detectors into the experimental hall and places them on the platforms shown in green in Figure 13.6. As the platform covers the entire opening to the water pool personnel can easily work on the transporter and the detector. The antineutrino detectors will be secured to the platform and prepared for submersion in the water.

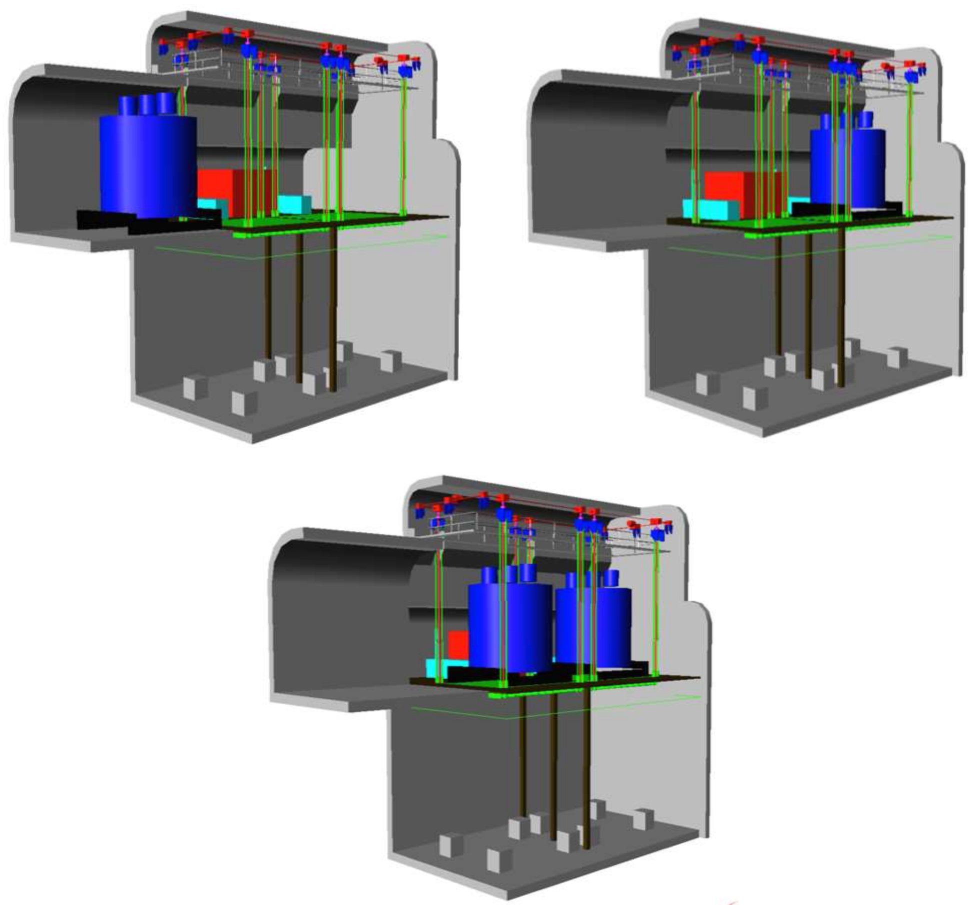

Fig. 13.6. Transport of antineutrino detectors into the experimental hall. Both detectors can be moved into the hall above the water pool before they are lowered into the water pool. Alternatively, the detectors can be moved into the hall one-by-one and lowered individually into the pool. During this time the muon veto pool can already be filled with water. Only the transporter is needed to move the detectors.

2. The detectors will then be lowered one by one into the water pool, as shown in Fig. 13.7. When the detector is half submerged into the water a temporary walkway or platform can be placed across the opening to access the top of the antineutrino detector. Using this temporary work platform the calibration boxes can be installed and all cable connections made.

3. As the detector is lowered into the water pool the HV, signal, and control cables are given out. A dry box enclosure around the cable can be assembled as the detector is lowered into the water pool.

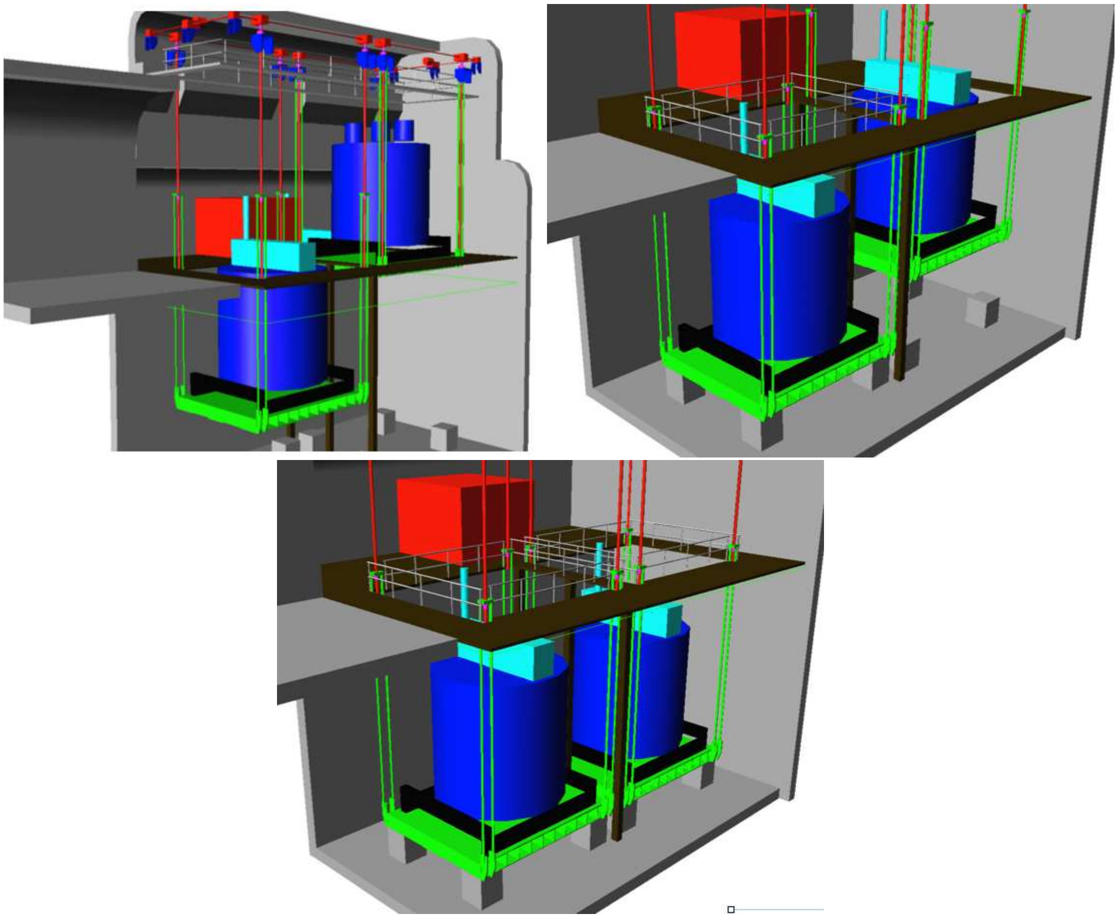

Fig. 13.7. Illustration of the main steps of lowering the detectors into the water pool. First, the detector is lowered far enough that the top of the antineutrino detector is at a comfortable working height for personnel on the floor of the experimental hall. The calibration boxes can be installed and all cable connections made. At this point all system checks for the calibration system can be performed. While we continue to lower the detector into the water pool the dry boxes and waterproof enclosures are installed around the cables, penetrations, and other instrumentation.

During this entire time the installation team and personnel will be working at the floor level of the experimental hall. At no point during the installation procedure is the installation team required to enter the water pool. The risk of damage to the PMTs in the muon veto is minimized.

4. After the detector is lowered into its final position the top of the water pool is closed to be light and leak tight. The RPC system can now be moved over the water pool. One possibility is to integrate the RPC system into this movable detector platform so that it is raised and lowered with the antineutrino detector. One can envision suspending it $\sim$5.5 m above the green platform so that the RPCs close the top of the water pool as the detector is lowered into the pool.

For the maintenance of detectors or the swapping of detectors it may be necessary to remove the detector at the far end of one of the experimental halls while the detector near the entrance area is still deployed. This requires a procedure for the removal of the detector from the far site of the experimental hall without disturbing the near module. One approach is to use a portable bridge with a capacity in excess of 100 ton for the transport vehicle and far detector. It would span from the near side of the far platform to the near edge of the water pool, at least 6 meters. In addition, all utilities, cables, etc. for the near detector would have to be located to provide clearance for the exiting detector and for the temporary bridge. The same clearance problem will also exist for the default concept of installation with a crane. Another, simpler approach is to integrate a platform above the near detector in the movable platform. By adding a second floor to the platform as shown in Figure 13.8 one creates a flat floor over the near detector when it is in the pool. During

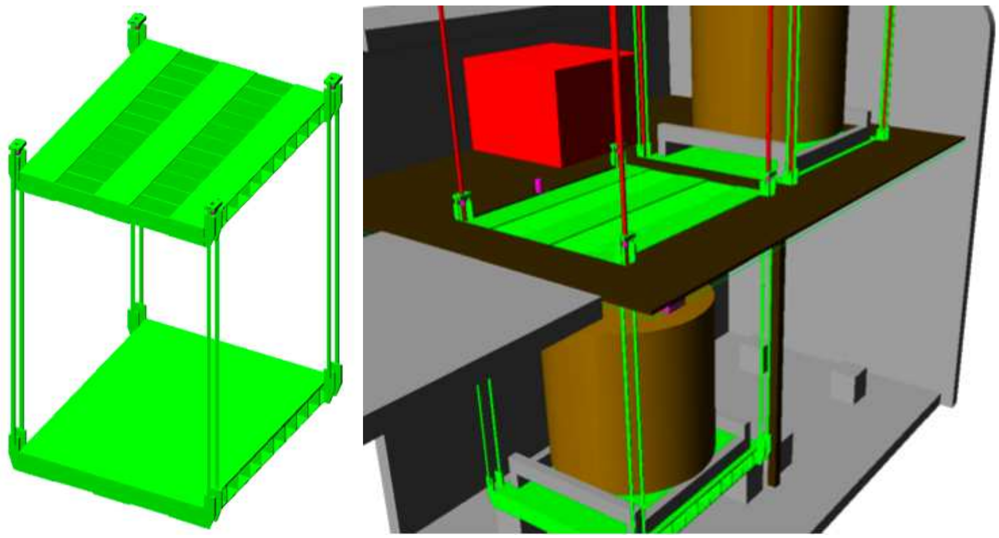

Fig. 13.8. *Left:* Near platform with two levels, one for the AD and one as a bridge across the pit for the near detector. *Right:* Engineering model illustrating the removal of the far detector across the upper platform covering the near detector. The near detector is in the pool with a flat floor covering it. In this situation the weight of the near detector is on the pool bottom. The weight of the far detector is supported by the near platform during the move.

the removal of the far detector the near detector is in the pool with a flat floor covering it. In this situation the weight of the near detector is on the pool bottom. The weight of the far detector is supported by the near platform during the move. Cables, dry boxes, and other service installations are offset to the side to avoid any “holes” in the muon water shield. At the same time this will allow the far detector to move across the platform and exit the hall without interference with the cable installation.

The cost of this system of movable platforms still needs to be compared in detail to the cost of deploying the detectors by crane but this system offers some operational advantages:

- Safe and repeatable operation with minimum number of expert personnel.
- No need for cranes, rigging, and heavy equipment.
- No need for lifting the antineutrino detector. The detector will be supported from its base plate and feet at all times.
- No need to drain and re-fill waterpool to install or service the antineutrino detectors. No extra water purification or storage tanks are needed to allow for the radon to be removed or decay away. The pool can already be filled with water as the antineutrino detectors are prepared and moved into the experimental hall.

- During the installation of the antineutrino detector all personnel will be working at the floor level of the experimental. There is no need to enter into the water pool. The risk of damaging the PMTs in the muon veto is minimized.

- All cable connections to the top of the antineutrino detector can be made at a comfortable working height. The calibration boxes can be installed at the floor level of the experimental hall.

- All dry boxes and enclosures to the cables and cable penetrations can be installed as the detector is lowered into the water pool.

- Such a deployment platform would likely minimize the dimensions of the experimental as no extra overhead room for the cranes are needed.

The open issues in this deployment method include:

- Integration of the RPCs into the platform assembly. They can be supported above the antineutrino detector so that they move into position when the antineutrino detector is lowered into the water pool.

- Method for making the opening of the water pool light and leak tight. The light tightness can also be achieved by switching off the lights in the experimental halls. The leak tightness is required to maintain a nitrogen cover gas above the water pool.

We will continue to explore the design of this alternative deployment system as R&D funds and the project schedule permit.

14 Operations of the Daya Bay Experiment

Operation of the Daya Bay Experiment requires a variety of tasks including:

1. Underground transport of filled detector modules and deployment into the experimental halls.
2. Data taking with the detector modules in the experimental halls.
3. Frequent automated calibration of each detector module.
4. Full-volume calibration of the detector modules as needed.
5. Monitoring of the state of the detector modules and the underground lab conditions.
6. Monitoring and maintenance of the muon system.
7. Maintenance and repair of the calibration systems.
8. Monitoring, maintenance, and repair of electronics and data acquisition system.
9. Monitoring the target liquid and and performing regular chemical assays on the liquid scintillator samples.
   (It would be invaluable to be able to do chemical assays on a regular basis of the Gd-loaded liquid scintillator and the unloaded liquid scintillator in the antineutrino detector. Such assays would complement in-situ measurements with a lasers or calibration sources to check optical transparency and light yield. These assays would have to be done offline in a remote laboratory. Sampling ports on the inner vessel containing the Gd-loaded liquid scintillator and the intermediate vessel containing the liquid scintillator would be required. However, it is very difficult to access the target liquids in the detector when they are installed in the water pool and we are currently studying the feasibility of such sampling ports in the design of the antineutrino detector.)

The routine monitoring of the experiment and daily maintenance work will be performed by the scientific members of the collaboration with support from technical personnel. A control room will be set up in the vicinity of the access portal for monitoring and data taking. Daily walk-around checks in the underground facility, in addition to regular remote monitoring, will ensure the safe operation of all underground systems. The training of the shift personnel will meet the safety requirements of underground work in the vicinity of the Daya Bay power plant.

The operations of the detector will consist of monitoring the detector performance and data quality, routine calibration, and online data analysis. The calibration procedure will include automated calibration runs to be performed by shift members operating the detector. Special manual calibration runs are to be performed by expert personnel.

All shift duties related to data taking and monitoring will be shared between the members of the Daya Bay Collaboration. On-site shifts as well as remote, off-site shifts will be part of running the Daya Bay experiment. Groups responsible for specific subsystems will make arrangements for the maintenance of detector subsystems.

The scientific and technical team of the Daya Bay experiment will have support from the China Guangdong Nuclear Power Group (CGNPG) which operates the Daya Bay reactor complex, and which is a collaborator on the experiment.

Operation of the Daya Bay experiment includes data taking with the detector modules in different configurations. The default configuration as well as other optional configurations are outlined in the following section. A variety of alternative operations plans are currently being evaluated with varying frequency of detector swaps.

14.1 Configurations of Detector Modules

This section describes the different possible detector configurations of the Daya Bay experiment and their possible use during different phases of the experiment. The different deployment options and run scenarios are currently being evaluated from the point of view of logistics, cost and physics reach:

1. **Initial Detector Deployment:** The eight detector modules are built, assembled, and filled in pairs to ensure that their characteristics and target mass and composition are as identical as possible. Once a detector pair has been filled underground there are two options:

   (a) the detectors can either be deployed together at the Daya Bay near site for a commissioning run and check of their relative detector efficiencies, or

   (b) one of them can be installed at the near site and the other one at the mid or far site to immediately start data taking with two detectors of the same pair at different distances

   A commissioning run of both detectors at the near hall is a unique opportunity to test the operation of each detector module before one of them is deployed at the mid or far site. The intrinsic detector background, the cosmogenic background at the near site, and the relative detection efficiency of the detector modules can be checked during this commissioning phase. This step is trivial for the first detector pair, as the default plan for the Daya Bay near site allows for the installation of two detector modules. Commissioning of the other detector pairs at the near site requires deploying the detectors to the other experimental halls immediately after the commissioning run. A drawing of the detector configuration is shown in Fig. 14.1.

Fig. 14.1. Optional commissioning runs of pairs of detectors at the Daya Bay near site. With sufficient runtime of several months, systematic checks of the detectors and a relative comparison of the detector response is possible.

   Including the time for detector installation and start-up, the total time for such a commissioning run is likely to be $\sim$6 months. The collaboration may decide to skip this initial commissioning step and immediately deploy the two detectors from each pair at the near and far (or mid) sites to expedite the overall experiment. In this second scenario two detectors are assembled and filled at the same time and then one of them is deployed at a near site and the other one is immediately moved to the far site. Data taking and a relative measurement of the neutrino flux between these two detectors can then commence immediately.

2. **Using the Mid Site:** If sufficient funding can be obtained a mid-site will be constructed at a distance of 1156 m from the Daya Bay cores and 873 m from the the Ling-Ao cores (as discussed in Section 2.1). Civil construction of this site would finish earlier than the excavation of the tunnel to the far site. By deploying two 20-ton detector modules at the mid-site along with two 20-ton detectors at the Daya Bay near-site it may be possible to make a first, "fast" measurement of $\sin^2 2\theta_{13}$ at this intermediate distance. See Chapter 11 for a discussion of the logistical and construction issues relating to early occupancy of the near and mid sites. A drawing of this detector configuration is shown in Fig. 14.2.

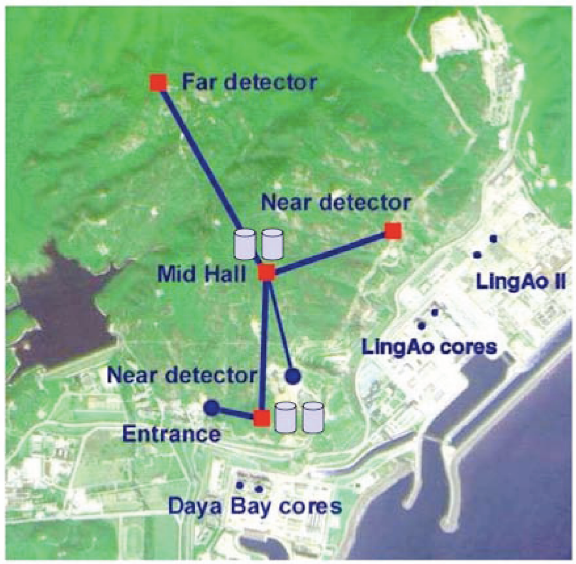

Fig. 14.2. Optional near-mid configuration of the Daya Bay experiment for an early physics run. With two 20-ton detectors at the near and mid sites a sensitivity of $\sin^2 2\theta_{13}$ <0.035 can be achieved in $\sim$1 year of data taking.

One can also envision using the mid-site for systematic cross checks. By running the experiment in the mid-far configuration it is possible to probe the θ_{13} oscillation with a different combination of distances. The ultimate sensitivity of the experiment is somewhat reduced but the ratio of the energy spectra from the mid and far site provide a different oscillation signature as a function of energy.

3. **Default Configuration of Full Experiment:** To achieve the best sensitivity in the Daya Bay experiment two 20-ton detector modules are deployed at both the Daya Bay and Ling-Ao near sites along with four 20-ton detector modules at the far site. The total active target mass at the far site is 80 tons. In the default scenario, the mid-site is unused. It is possible to operate in this configuration either with or without the swapping of pairs of detectors. A drawing of this detector configuration is shown in Fig. 14.3.

4. **Optional Swapping in the Daya Bay Run Plan:** Swapping of detector modules is an option but not a necessity in the Daya Bay experiment. The target sensitivity of $\sin^2 2\theta_{13} < 0.01$ at 90% C.L. can be

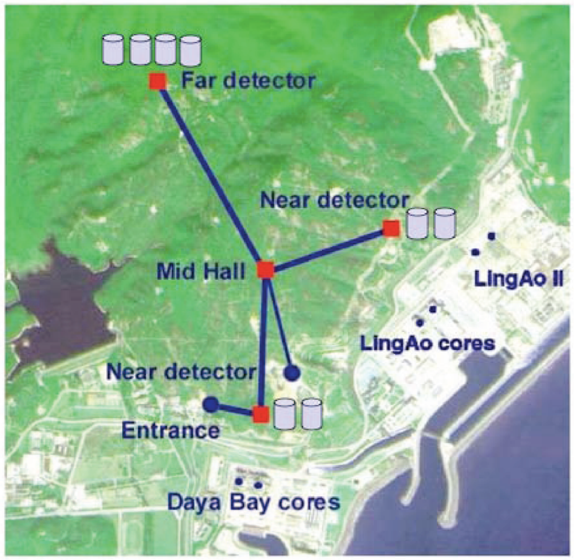

Fig. 14.3. Default configuration of the Daya Bay experiment, optimized for best sensitivity in $\sin^2 2\theta_{13}$. Data taking can occur in a static configuration or with swapping of detectors.

achieved without swapping detectors. The design of the Daya Bay experiment provides the option of swapping detectors for systematic checks and to ultimately increase the sensitivity of the experiment to about $\sin^2 2\theta_{13} < 0.006$ (see Table 3.16). After all detectors are commissioned and located at their initial sites swapping of detectors can occur either:

(a) throughout the experiment in regular 6-months intervals for the optimal cancellation of the experimental systematics (as described in Table 3.9), or

(b) after an initial static experiment with data taking for 2-3 years that reaches the design goal of $\sin^2 2\theta_{13} < 0.01$

The collaboration has not decided yet which approach to choose. It will depend on the outcome of the design studies of the antineutrino detectors, their transportation system, and R&D on the calibration and monitoring of the detector response. In addition, the timeliness and potential impact of a first measurement of θ_{13} at Daya Bay will drive the detector deployment and run plan.

14.2 Early Occupancy of the Experimental Halls

The civil construction of the underground laboratory including the experimental halls and tunnels will take about 24 months. The time scale is set by the excavation of the tunnels between the experimental halls. The Daya Bay near site (and mid site if it becomes part of the baseline option) will be completed before the tunnels to the Ling Ao and far site are finished. Completion of experimental halls at the Daya Bay near site and the mid site suggests the implementation of an early experiment utilizing these two sites. Early occupancy of these sites would provide the opportunity to commission the detector modules at the near site and to make a first, "fast" measurement with a sensitivity of $\sin^2 2\theta_{13}$ <0.035 (see Chapter 3).

The use of these experimental halls during the ongoing excavation and construction of the tunnel to the far site poses significant but not insurmountable logistical challenges for the work underground. Shared underground occupancy is generally undesirable because of safety issues (traffic, blasting, explosives, fumes etc..) and general interference. Other experimental facilities such as KamLAND in the Kamioka mine have demonstrated that data taking with a sensitive neutrino experiment is possible while a new underground hall is excavated some few hundred feet away. In the case of KamLAND, a new underground hall for a liquid scintillator purification system was built in 2006. The experiment continued data taking and access to the experimental facilities for scientists was arranged on a specific schedule together with the mining and construction crews. A similar situation can be found at SNOLab in the Creighton mine in Canada which is being constructed during the active phase of the Sudbury Neutrino Observatory.

The possibility of commissioning the detector modules at the near site and making an early measurement of $\sin^2 2\theta_{13}$ with detector modules at the near and mid sites may be worth the additional logistical challenge of coordinating the underground construction work and the installation of the first detector modules. In this case, the experiment may start commissioning detector modules 18 months after the start of civil construction and collecting the first neutrino oscillation data about two years after breaking ground.

The planning for this scenario requires that

1. the necessary infrastructure for the operation of the detector modules (power, air, etc) can be installed at the near and mid sites while the construction of the tunnel to the far site is ongoing.
2. a plan for the installation of the detector modules will be developed that does not impact the day-to-day mining operation
3. safety issues with respect to escape routes and personnel underground are addressed

This possibility requires further discussion and negotiations with the contractors for the underground construction of the tunnel and experimental halls.

14.3 Servicing and Maintenance of the Antineutrino Detector

Once the antineutrino detectors are installed and the pools filled with water the detector cannot be easily accessed. Service or repair of the calibration boxes, instrumentation attached to the antineutrino detector, cables or gas lines requires that the water pool is at least partially drained and a work platform is installed. The basic steps required to access the antineutrino detector, perform the service, and ready it again for data taking are:

- Stop data taking and shut down HV.
- Slide RPCs to the side and open water pool. *(0.5 day)*
- Partially drain the water pool to uncover the top of the AD. *(2 days)*
- Install scaffolding or work platform in the water pool to access the top of the antineutrino detector *(1 day)*
- Remove dry covers from cables and cable penetrations.*(0.5 day)*
- Perform service or repair on calibration boxes, patch panels, gas lines, or instrumentation. *(1–2 days)*
- Perform leak check on dry box systems as described in the installation procedure. *(0.5 day)*
- Dismantle work platform and lift out of water pool.*(1 day)*
- Refill the water pool. *(2 days)*
- Move the RPCs back into place and close up water pool. *(0.5 day)*
- Ramp up HV and start data taking.

We estimate that the operational turn-around time for servicing the antineutrino detector from the time we stop data taking to the time we can resume data taking will be of the order of 10–14 days. This is based on the assumption that the water pool can be drained to a suitable level and filled in about two days respectively. The details of the purification system for the water pool are described in Section 8.2.5.

In this estimate we do not take into account the impact of the radon background in the water pool that will be introduced in the draining and refilling process. We are mainly concerned about the ^{214}Bi γ ray from the ^{222}Rn decay chain. The half life for ^{222}Rn is about four days, and ^{214}Bi is shorter. The specification for radon in the water is less than 5 Bq/m^3 (see Section 8.2.5). Radon in water varies greatly depending on its origin. In the Kamioka mine water the background can be as much as 1000 times larger. In this worst case limit we would have to wait about 10 half lives, or $\sim$40 days to meet the specification for the water in the pool. However, we expect that we will have a water supply that is well below 5000Bq/m^3 to start with. In addition, we can filter the radon from the supply water and also store water prior to filling the water pool to let the radon decay away.

14.4 Detector Swapping

The purpose of swapping detectors has been described in Sections 2 and 3. An overview of the steps involved in the swapping procedure is given below. Detector swapping will utilize the standard transportation methods developed for the underground movement of the detectors. As such, detector swapping uses all of the same techniques and procedures developed for the initial deployment of the detector. It is important to characterize any change in detector performance when swapping, so the detector must be carefully calibrated both before and after the swap.

14.4.1 Logistics of Detector Swapping

The total estimated time for detector swapping is several days. We anticipate that the transport of each detector module in the tunnel can be performed in less than a day. With a transportation speed of $\sim$5 m/minute a distance of 1500 m can be covered in less than 7 hrs.

Detector swapping includes the following sequence of steps:

1. Perform final detector calibration to establish detector response immediately prior to the move.
2. Shut down HV and DAQ.
3. Disconnect the RPC system as necessary and slide off away from pool.
4. Drain water pool to a level below the antineutrino detector module ($\sim$1000–1500 m^3). (Replace with fresh, filtered water when refilling.)
5. Install scaffolding to allow safe access to the top of antineutrino detector.
6. Disconnect PMT HV and signal cables, LS overflow plumbing, etc. as required to prepare for move.
7. Remove calibration system & piping as required from top of antineutrino detector.
8. Attach the lifting device to the antineutrino detector.
9. Using a 150 ton crane, lift the antineutrino detector vertically out of pool and translate it horizontally onto a transporter.
10. Transport the antineutrino detector to the new location.
11. Reverse the operation at the previously prepared new location.
12. Calibrate the detector in the new location to establish the detector response immediately after the move.

14.5 Maintenance and Operations Costs

At this time, just prior to the CD-1 review, it is approximately four years before the Daya Bay Collaboration begins operation of the experiment. As we have not yet fully finalized the US Project scope, cost, nor schedule, it is impossible to provide a formal pre-operations and operations scope and cost plan with any kind of accuracy. But, in the interest of providing some insight into what may occur, or one such scenario, we are preparing this initial concept for Pre-operations and Operations. It is expected that as we prepare a complete agreement (MOU) on scope, cost and schedule with the international Daya Bay community, we will improve our understanding of what this plan entails and the US cost of these items.

There are many assumptions in this conceptual pre-operations and operations plan. The biggest one is that the DOE base program will support the physicists, postdocs and grad students associated with Daya Bay to perform detector testing, commissioning and on-going data analysis. And, that their associated travel and living expenses will be covered as well. This means that the only labor and travel/per-diem costs included here are associated with technical and engineering resources.

14.5.1 Pre-operations

Pre-operations are expected to begin after assembly and initial check out, or commissioning, of a significant portion of the experiment. More specifically, we would like this to occur after initial commissioning of the two Antineutrino Detectors (AD) and Muon System (Muon) and their associated electronics and online system in the Daya Bay Near Hall. It is estimated that this will occur approximately nine months prior to CD-4 approval for operations of the entire three hall, eight AD experiment. Initial Pre-Operations could occur as early as late 2009 or early 2010.

At this point in time, we will begin taking physics data but with only a portion of the entire experiment. But, this will represent an end-to-end slice of the full technical detector. The offline system (hardware and software) will be in initial start-up mode and will be capable of sorting, time-ordering and processing the data making it ready for preliminary data analysis. The Daya Bay Project, because of its identical detector systems, in three experimental halls, lends itself nicely to this plan.

Initiating pre-operations could require the project to complete a CD-4a — initiate early operations — review.

Pre-operations will require funding for the items shown below. It is envisioned that the US will be responsible for maintenance and operations of at least the US scope deliverables or for a large (up to 50%) portion of the entire experiment.

1. Consumables (gasses, DI filter beds, etc)
2. Spares (breakage and failure of items like PMTs and CPUs)
3. Maintenance technician labor, travel and living expenses (for replacing consumables and repairing failed systems)
4. Pre-operations Planning and Management labor and travel/expenses
5. Pre-operations Safety personnel labor and travel/expenses
6. Computing and software
7. Office space, supplies and accommodations for US collaborators
8. Miscellaneous and unforeseen expenses

These preoperations costs listed above will be associated with the Daya Bay Research Program.

The expected monthly cost of these items is \$135k. This cost is roughly budgeted in the following manner:

1. $20k/mo. for consumables
2. $10k/mo. for spares
3. $40k/mo. for technical/engineering labor, travel and per-diem
4. $25k/mo. for planning and management labor, travel and per-diem
5. $15k/mo. for safety labor, travel and per-diem
6. $10k/mo. for computing and software
7. $5k/mo. for space and supplies
8. $10k/mo. for miscellaneous expenses

It is expected that pre-operations would last until the experiment begins full regular operations or approximately nine months ($1,215k).

14.5.2 Operations

Operations will begin after we have successfully completed DOE CD-4b review and approval — begin full experiment operations. At this time, we would have completed the construction, assembly, installation and initial check-out of all technical systems — the full, eight AD, three Hall, experiment — and the Daya Bay Research Program will begin. This could occur as early as July 2010. Steady-state operations will evolve over time. Initially, we will be able to leave the detectors alone except during maintenance and repair situations. But, after 2–3 years of operation, we may want to ‘swap’ ADs between halls to further reduce systematic uncertainties. In years where ‘swapping’ will occur, a somewhat larger Technical and Engineering labor force may be necessary. The cost estimate below is for a normal (non-swapping) maintenance and operations year. Steady-state operations (non-swapping year) will require funding for the following items:

1. Consumables
2. Spares
3. Maintenance tech and engineering labor, travel and per-diem
4. Operations Office labor
5. Safety Office labor
6. Computing and Software
7. Office space, supplies and accommodations for US collaborators
8. Miscellaneous and unforeseen expenses

The expected annual cost for these items totals between $1,650k and $2,400k per year. This is budgeted approximately in the following manner:

1. $200–300k/yr. for consumables
2. $150–250k/yr. for spares
3. $500–750k/yr. for maintenance tech and engineering labor, travel and per-diem

4. \$250–350k/yr. for operations office labor
5. \$200–250k/yr. for safety office labor
6. \$100–200k/yr. for computing and maintenance
7. \$50–100k/yr. for space and supplies
8. \$200k/yr. in miscellaneous and unforeseen expenses

At this point no considerations towards an upgrade R&D program have been developed.

14.6 Decommissioning of Experiment

A reverse of the procedures described in Section 14.3 will be used during the decommissioning phase of the experiment. During decommissioning special attention will be paid to the appropriate disposal of all liquids and materials involved.

15 Environment, Safety and Health

Protecting the environment and personnel safety is of the highest priority for the Daya Bay Project. This requires an adherence to safety regulations of both the host country and those of the U.S. The Project is integrating safety into all phases of project development and will work to assure a positive worker attitude towards safety.

The project has a U.S. Daya Bay Safety Officer who is responsible to assure that all relevant US safety guidelines are satisfied. The U.S. Daya Bay Safety Officer reports directly to the Project Manager and also serves as the L3 Manager for Safety in the Integration Office and draws upon the safety organizations at BNL and LBNL. The project has a Safety Liaison which is supported by WBS 1.9.1 to assist in collecting the necessary safety resources for reviewing the project and assisting with mitigation efforts. The international Daya Bay project has identified a Safety Officer who is also the liaison to the power plant. A chart showing the organization of the Daya Bay safety responsibilities is shown in Fig. 15.1. The Safety Officers run the Daya Bay Project Safety Office, which will evolve into the Operations Safety Office.

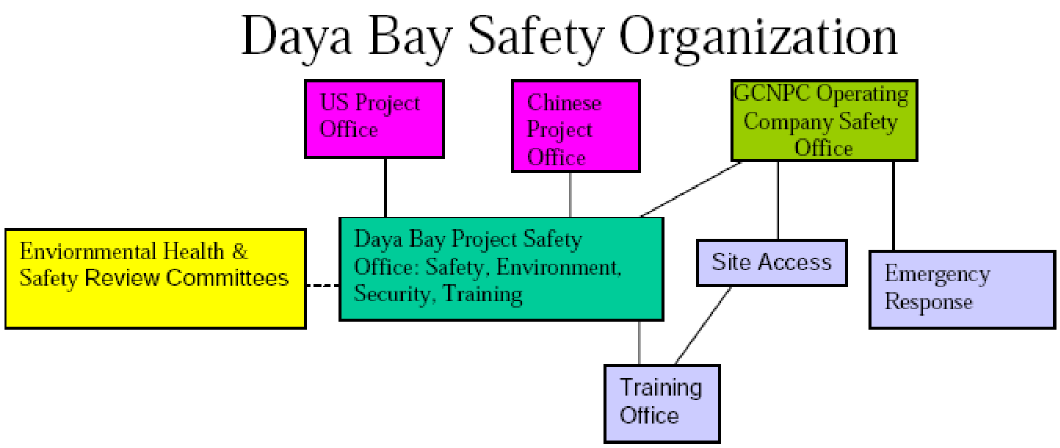

Fig. 15.1. Daya Bay Project Safety organization chart.

The Project's liaison to the power plant has begun discussions to determine the scope of support that the power plant will be able to provide to the Project through their existing safety organization during the construction and operations phases.

The project has three distinct phases. In the first phase of civil construction all funding is provided by China and all personnel working at the site will work safely under guidelines imposed by Chinese authorities, including the power plant, and overseen by the international Daya Bay Project Safety Officer. Special additional guidelines will be put into effect for visits by U.S. personnel associated with the project. During the second, detector construction phase, all safety guidelines established by Chinese and U.S. authorities will be applied to all personnel working at the site under the direction of the international and U.S. Daya Bay Safety Officers. Construction of detector components at Universities and Labs will be reviewed by the Project and will follow all appropriate local safety guidelines. Finally, during the operations phase the Operations Office will support the continued presence of the International and U.S. Safety Officers.

The Project has overseen the development of a hazard analysis document that includes an identification and analysis of safety hazards associated with the construction and operation of the Daya Bay Project. This document has been developed in conjunction with the appropriate L2 Managers and is summarized below (Section 15.1). The Project has consulted with a number of underground construction and safety experts as well as with conventional safety experts at BNL and LBNL. An Underground Safety Review Committee chaired by Howard Hatayama (EHS Division Director at LBNL) has been convened and has been offering advice to the Project on safety issues. A more detailed discussion of underground safety issues can be found in Section 15.3.

The Project will develop a Training Program and a Job Training Assessment program in conjunction with the power plant, which is very interested in cooperating with the Project. All personnel entering the facilities will have site training. Short-term access without training will only be allowed if the individuals are escorted by a qualified escort. The training will include how personnel should report and respond to emergencies, including egress to the safe areas. All personnel going into the underground facility are expected to sign-out and carry tokens, which are linked to the specific area where they will be working. In the event of an emergency the tokens will provide information on the personnel in the facility and their expected locations. The Training Program will likely be tied to the issuance of Identification Badges by the power plant to allow site access. All work will be planned, with appropriate considerations for "Skill of the craft" and specialized training as needed.

The experiment will have a designated local emergency coordinator (LEC). A qualified LEC will be required to be on site and be able to be immediately contacted if an emergency should arise. The LEC will be required to be trained in the appropriate response procedures and be fluent in the native language. The primary responsibility of the LEC is to provide information and coordination to the emergency response personnel.

We understand that the power plant will provide emergency response, including fire, police and emergency medical response. These forces are connected to the local government, but administratively report to the power plant. The Project will discuss issues regarding mine rescue training of the emergency response teams. We anticipate that the power plant will provide sufficient on-site security for the Project's needs.

15.1 Identification and Mitigation of Safety and Environmental Hazards

The Project's hazards analysis and mitigation strategy are described in the Preliminary Hazards Analysis Document (P-HAD).

15.2 Environmental Stewardship

The Project is committed to protecting the environment. All Project work that is performed in the U.S. will be performed in accordance with all applicable local, State and Federal laws and regulations. Project work performed at the Daya Bay site will conform to all applicable Chinese regulations. The primary environmental concerns are with releases of RPC gases, possible spills of liquid scintillator and mineral oil and the use of cleaning solutions. The filling hall, where LS and mineral oil are filled into the ADs, will have a secondary containment vessel to trap any spills. When the experiment is finished these fluids will be disposed of following Chinese regulations. The amount of RPC gas is small and we anticipate that it will be below Chinese regulatory concern. The amount of cleaning solution is also small. We do not anticipate any radiological issues, but all sealed sources will be inventoried and tracked and radon will be monitored.

15.3 Underground Safety

The Project is learning from the experiences of others in underground experimental physics work. Our underground safety committee has benefited from the experience of people working at Yucca Mountain, the Nevada Test Site and has consulted with others involved with safety issues in the NuMI tunnel, the Soudan mine and SNO.

Current priorities include:

- Preparing for a Review of the ongoing final Civil Design activities. We want to understand the safety standards implemented in the design and to what extent those design standards may be different than equivalent standards in the U.S. We will evaluate the design to assure ourselves that safety concerns are being properly addressed.

- Working with the power plant to understand the capabilities of the local emergency response and what will be needed to ensure appropriate mine rescue and firefighting training and equipment.
- Establishing the appropriate safety design and operational mitigation of safety risks associated with the use of flammable gases and liquids underground.

16 Manufacturing Plan and Quality Assurance

In this chapter, we disucss the approach to manufacturing each of the technical subsystems, the quality management system we will employ and the various kinds of tests planned for each subsystem as well as for the integrated Daya Bay detector. Section 16.2 provides an overview of the quality management approach, as well as the design codes and standards utilized, the drawing exchange and archiving system and our use of design, manufacturing and safety reviews throughout the life of the Project.

16.1 Manufacturing Plan

Initial detailed plans for manufacturing hardware elements of the technical subsystems are provided in each of the technical chapters of this CDR. These plans will continue to evolve as the designs firm up and optimal manufacturing approaches are decided.

16.2 Quality Assurance and Testing

The Daya Bay quality assurance program is designed to assure that the detector performs according to our specifications. Each institution's Quality Assurance program will be implemented for procurements from that institution; however, an overall quality assurance for the Daya Bay Project will also be applied. The standard for the Daya Bay quality assurance program will be comparable to that of the LBNL or BNL institutional standard (e.g., BNL-QA-101).

16.2.1 Quality Management Plan

The purpose of the Quality Management (QM) Plan is to implement quality management methodology throughout the various project management systems and associated processes in order to:

- Plan and perform project operations in a reliable and effective manner to minimize the impact on the environment, safety, and health of the staff and the public;
- Standardize processes and support continuous improvement in all aspects of project operations; and
- Enable the delivery of products and services that meet the Project's requirements and expectations.

This policy is applicable to all Daya Bay Project activities and items involving construction, operations, maintenance, and research, including the procurement of equipment for these activities. A graded approach to quality is used to place the most emphasis on and allocate proper resources to those items and/or processes that may have the greatest effect upon personnel, environment, safety, health, cost, data, equipment, performance, and schedule. The graded approach is a process for determining that the level of analysis, management controls, documentation, and necessary actions are commensurate with an item's or activity's potential to:

- Create an environmental, safety, or health hazard;
- Incur a monetary loss due to damage, or to repair/rework/scrap costs;
- Reduce the availability of equipment;
- Adversely affect the program objective or degrade data quality;
- Unfavorably impact the public's perception of the Daya Bay or DOE mission.

This provides a methodology for establishing a level of analysis, documentation, and actions commensurate with the programmatic and/or ES&H impact. The scope of the quality-related activities is a function of its risks and programmatic issues. Quality classification designations, A1 (Critical); A2 (Major); A3 (Minor);

and A4 (Negligible), may be used to aid in selecting applicable quality-related activities, as appropriate. The graded approach does not allow internal or external requirements to be ignored or waived, but allows the degree of controls, verification, and documentation to be varied in meeting requirements based on ES&H risks and programmatic issues. This policy can be found in the BNL Standards Based Management System (SBMS) in the subject area: “Graded Approach for Quality Management”.

16.2.2 Design Codes and Standards

Engineering design standards and guidelines that will be applied in the design of experimental hardware will be defined in a controlled project document as a collaboration wide policy. Conflicts between this policy and local institutional policies require the more stringent or conservative approach be taken. The policy defines design loads to be applied to structural analysis of experimental hardware, fixtures and tooling including applicable seismic codes. The policy suggests sources for data on materials selection, certification and their properties as defined in American Association and Society standards. The policy defines analytical methods to be used based on load application and failure criteria of the materials being selected. The policy defines Factor of Safety and gives specific guidelines for the application of factor of safety used in the design of project experimental hardware. Lastly it defines a method and format for documenting all engineering analysis performed in the design of project experimental hardware.

16.2.3 Drawing Exchange and Archiving

Engineering drawing control systems have been developed for use project wide and are defined in a project controlled document. The scope of this system details the engineering drawing standards for dimensioning and tolerancing, along with a system of units. It defines a common language for all notes and specifications, a system for revision, drawing format sizes to be used along with a global project title box. A method for handling, transferring and archiving electronic drawing files has been defined collaboration wide. A drawing number scheme along with WBS L2 drawing number assignments is detailed and the policy for released drawings is defined.

16.2.4 Design Reviews

To promote value added engineering in the design process and insure all experimental hardware meet or exceed minimum defined engineering design standards and safety policies, a series of engineering committee design reviews will be conducted on all experimental hardware designs prior to drawings release for procurement or fabrication. Each subsystem will undergo in total or in part a preliminary and final design review. The project office with chair these engineering reviews and form a committee of appropriate experts for this peer review process. The preliminary review will be early in the design process when conceptual designs have been firmed up based on scientific requirements, engineering analysis, conceptual design drawings, cost and schedule. The outcome of this review and the action items generated should promote and enhance the design process towards a finished hardware design. The final design review is conducted when subsystem hardware detailed design drawings and engineering analysis are complete and the L2 manager is ready to release drawings for procurement or fabrication. The charge for the final design review will insure that previous action items and issues have been satisfactorily resolved, meets the functional experimental requirements, is within the integration interface envelope, meets engineering design and drawing standards and policies, the hardware can be assembled, installed, tested and operated in a safe manor and it is within the project cost and schedule definition.

16.2.5 Test Plans

Each subsystem will provide a staged testing plan for all elements. This includes a QA test plan for the manufacturer, testing upon receipt of materials, testing prior to and after shipping to China and testing prior to and after installation, as appropriate. These plans will continue to be developed by each subsystem as design decisions are made. Preliminary versions or outlines of test concepts are described in some detail in each of the technical chapters of this document.

17 Risk Program and R&D Efforts

There are several key aspects of the Daya Bay Risk Program. First, there is the early identification of potential risks in each of the detector elements as well as the system as a whole. Second, there is an early R&D program that focuses on understanding, reducing or eliminating the identified risks. Third, there is the formal tracking of the remaining risks and mitigation strategies throughout the life of construction phase of the experiment. And lastly, there is an accounting for technical, cost and schedule risk in developing the contingency analysis for the experiment. These first three components (ID, R&D, tracking) will be discussed in in this chapter.

17.1 Risk Assessment and Tracking

Subsystem Managers have been asked to perform a risk assessment of their technical systems. These have been gathered by the Project Office and disseminated back out to the Subsystem Managers as well as the key engineering leads and the rest of the project leadership team. A list of the currently identified risks have been collected in our preliminary Risk Assessment and Mitigation Strategy document. This document also contains a further assessment of integrated or system level risks. At the end of the document, we include a summary list of what we believe to be the highest priority (a combination of probability and consequence) risks. In the future, the risk list will be reviewed and discussed regularly in subsystem and overall project meetings. Updates to the risk list and status will occur several times each year as more info is gathered or risk status changes.

17.2 Risk Mitigation

Several key project risks can be addressed in the current R&D phase of the project. Therefore, a sizable number of our current and planned R&D efforts are directed towards understanding and mitigating project risks. Other risk areas require design and the manufacture of prototypes. These are all elements of the risk mitigation strategy. We will apply the appropriate level of R&D, careful planning, and the judicious assignment of international labor resources within the Project to address all the projects technical, cost and schedule risks.

17.3 Relevant R&D plans

R&D efforts are focused on development of suitable technologies and helping the collaboration make wise technology and cost decisions in designing the Daya Bay experiment. These efforts are also very useful in understanding and reducing risk. The major R&D efforts are summarized below.

1. Detailed physics simulation of various detector geometries to optimize performance for science requirements while minimizing cost and risk

2. Engineering studies and analysis of various detector geometries and elements

3. AD: including the development of 3-D models of the AD (acrylic vessels, steel tank, drain and fill ports, overflow tanks), assembly and installation planning, prototypes (fill mechanism, overflow tanks, calibration ports, feedthroughs and seals), test instrumentation for the target mass measurement system, test survey equipment, conceptual design of filling station, planning for characterization of ADs, test instrumentation for safety systems (overpressure protection, cover gas, flammable gas/liquid detection)

4. PMTs: including PMT mount design, characterization and testing plan, supplier validation, optimization of PMT base and magnetic shielding design, production test stand, validation of cables and feedthroughs for use under water (and in oil/water interface)

5. Gd loaded LS: including recipe and process development and testing, materials compatibility testing, Gd-LS for prototype AD in Hong Kong, procedures for scaling up LS production to multi-ton quantities, radio-assay procedures and measurement capabilities.

6. Acrylic vessels: prototyping of acrylic vessel elements and full scale models, development of a viable vendor for the acrylic vessels

7. Water Cherenkov system: including materials compatibility testing in high purity water, water purity specification development (including attenuation length measurement), water purification system prototype tests and water systems design, optimization of PMT count and location with simulation and engineering studies, optical reflectivity studies of various materials, evaluation and characterization of MACRO PMTs, potted PMT base design and validation in water, PMT mount design (10 lb. buoyancy force vs. 1 lb. weight), water pool PMT structural support conceptual design, water pool cover systems design (cover and cover gas)

8. RPC system: including structural support conceptual design, operation in high humidity environment, design and optimization of strip size, gas system and HV system

9. Calibration system: including simulation of sources and spallation products, design development for automated source deployment system, design, construction and testing of prototype automated system, source design and testing, source shielding design, final automated system design, simulation studies for detailed calibration plan

10. Electronics: including design review of key electronics designed in China (FEE, Clock, Trigger), construction of a test stand to certify and verify prototype electronics

11. Software and Computing: including development of software framework, evaluation of pre-existing software framework packages, core software infrastructure and data management development, design and evaluation of network transfer and data archiving, software tutorials for collaboration users

12. Installation: including the development of as-built 3-D models of facilities and subsystems to assist installation planning and staging and to provide early identification of possible areas of interference, the creation and implementation of project controls and policies for engineering documentation and drawing standards, change control policies, analysis and design standards, QA and safety policies.

13. Integration: including the development of installation and test plan for the overall detector installation, with a timeline for delivery, storage, staging, assembly, transport, installation and testing, develop overall installation and test plan, based on plans from each subsystem, with resource loaded schedule and milestones

14. Project Development: including the development of overall project cost, schedule, risk, hazard analysis and the preparation for CD-1 and CD-2/CD-3a reviews

18 Organization and Management

The Daya Bay Project (the Project) will be international in scope, funding and organization. In this chapter, we present an overview of the international Project organization as well as some of the management approaches. We also present a summary of the planning and scheduling process as well as our proposed tools. While there will be oversight by many international agencies and many reviews of the Project, here we only summarize the planned function of the U.S. standing and ad-hoc committees and the technical review process. For example, the function of the Project Advisory Panel (PAP) as well as the expert ad-hoc technical reviews, are described.

A detailed project management plan has been included in the Preliminary Project Execution Plan (or P-PEP) document. In addition to the management organization and standing committees described here, this document further describes the management organization details, management processes, periodic technical reviews and change control.

18.1 Daya Bay Project Organization

The U.S. Project's reporting and decision making from the perspective of DOE is summarized in Fig. 18.1

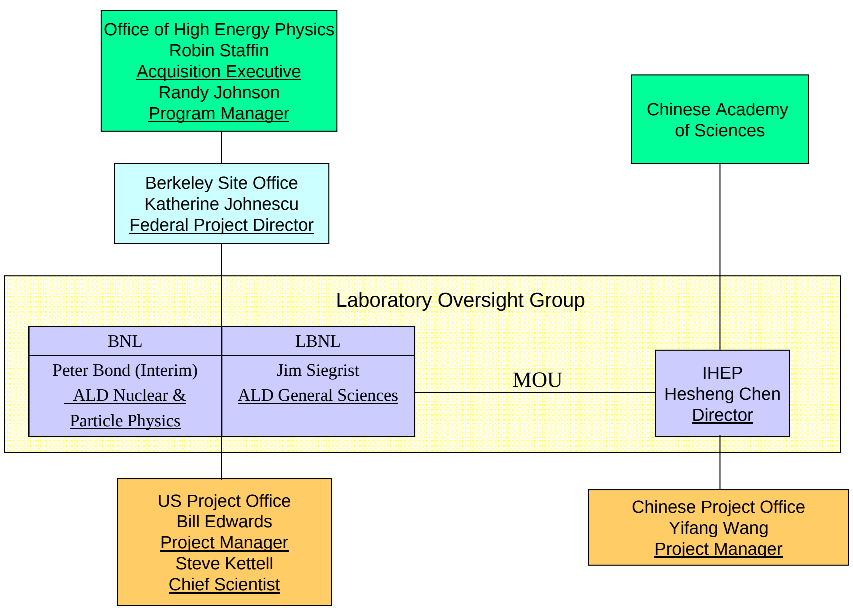

Fig. 18.1. U.S. Daya Bay Project reporting and responsibility organization chart, with an emphasis on the relationship to DOE.

The Daya Bay Laboratory Oversight Group (LOG) and International Finance Committee (IFC) will aid the international oversight of the Project. The IFC will meet at the regularly scheduled U.S.-China meetings.

The LOG has among its members Sam Aronson (Director, Brookhaven National Laboratory), Hesheng Chen (Director, Institute of High Energy Physics) and Jim Siegrist (Associate Lab Director for General

Sciences, Lawrence Berkeley National Laboratory). This oversight group will meet regularly with the leadership from the Daya Bay Collaboration and the Project leadership to assess progress and plans. They will report their views regularly to the U.S. DOE, Chinese Academy of Sciences (CAS), Chinese Ministry of Science and Technology (MoST), the National Natural Science Foundation of China, Guangdong Provincial Government, Shenzhen Municipal Government, China Guangdong Nuclear Power Group and the rest of the international funding agencies.

The IFC will have representatives from the international funding agencies and will meet annually to receive an overview of Project financial status and future funding requirements. Both of these groups will provide reports of project status to the multiple funding agencies.

Figure 18.2 highlights the internal organization of the Project and its oversight boards and panels. The

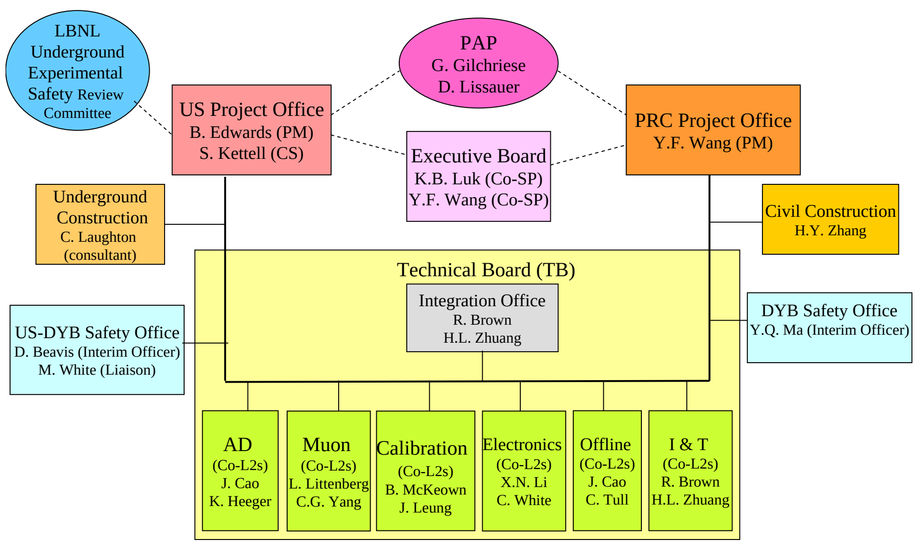

Fig. 18.2. Daya Bay Project organization chart.

Spokespersons are part of the Collaboration's Executive Board (Spokespersons are Yifang Wang and Kam-Biu Luk, the rest of the Executive Board is Bob McKeown [U.S.], Changgen Yang [China], Ming-Chung Chu [Hong Kong], Yee Bob Hsiung [Taiwan], Alexander Olshevsky [Russia]) which will help guide the Project organization in its goal of delivering the experimental apparatus and software that will meet the scientific goals/requirements of the Daya Bay Collaboration. The Project Officers are *ex-officio* members of the Executive Board.

The Project Advisory Panel (PAP) is a panel with expertise in large projects gathered from the relevant international community. This panel will provide valuable guidance and advice to the Project over the course of the construction lifecycle. The PAP is charged by and reports to the LOG.

18.1.1 U.S. and China Project Management Offices

Because there are two countries providing the major funding for Daya Bay (China and the U.S.), and because each country's funding agencies have their own project management and control requirements, the plan is to have two Project Offices, one in the U.S. and one in China. This way, each country has an organization overseeing, and reporting on, their portion of the construction effort to their funding agencies. The complication of splitting the project office in this way is obvious. The key to making this work is agreement between the two Project Offices on the project scope and goals as well as frequent communication of issues and plans. A Memorandum of Understanding (MOU) will be developed between the lead laboratories in the U.S. and China at CD-2 to define a mutually agreeable set of scope deliverables for each country.

The U.S. Project Office personnel includes: Project Manager Bill Edwards, Chief Scientist Steve Kettell, Chief Engineer Ralph Brown, Safety Officer Dana Beavis (interim) and Project Controls Officer Mike Barry. The Chinese Project Office personnel includes: Project Manager Yifang Wang, Deputy Project Managers Changgen Yang and Jun Cao, Chief Engineer Honglin Zhuang and Safety Officer YuQian Ma. This organization has been in place and functioning well together for more than six months now.

The Integration Group, shown in Fig. 18.2, is headed by the two Chief Engineers, Ralph Brown and Honglin Zhuang, and is responsible to make sure that the design efforts are well coordinated and that plans for the detector installation are clearly defined.

A Technical Board, composed of the Project Offices and L2 managers (see Section 18.1.2) is responsible for technical decisions regarding the detector design and construction.

The Daya Bay Collaboration holds 4–5 collaboration meetings per year at which status, issues and plans are discussed and agreed upon face-to-face. Additionally, the Collaboration's Technical Board meets by phone conference bi-weekly. This frequent high-level communication will provide the connection which binds the project together and enables joint decision making, problem solving and planning.

18.1.2 Project Subsystem Organization

The current roster of U.S. and Chinese Co-Subsystem Managers (at Level 2 of the WBS) are listed below in Table 18.1. This table also represents the makeup of our Technical Board.

WBS	Description	U.S. Manager	Chinese Manager
1.1	Antineutrino Detector	K. Heeger	J. Cao
1.2	Muon System	L. Littenberg	C.G. Yang
1.3	Calibration System	R. McKeown	J. Leung
1.4	Trig/DAQ	C. White	X. Li
1.5	Offline	C. Tull	J. Cao
1.6	Conventional Construction	—*	H.Y. Zhang
1.7	Installation & Test	R. Brown	H.L. Zhuang
1.8	System Integration	R. Brown	H.L. Zhuang

Table 18.1. The Daya Bay Subsystem Managers. * Chris Laughton of FNAL has been providing valuable consultation services to the Daya Bay Collaboration on civil construction issues.

18.2 Cost and Schedule Development Plans and Tools

The Project has undertaken the development of a detailed cost estimate and schedule over the past several months and continuing through CD-2. Under the guidance and support of both Project Offices, the subsystem managers will oversee the collection of cost estimates in the framework of a detailed WBS (down to the most appropriate level — probably 5 or 6).

The cost estimates will be gathered from the best available information, from vendor quotes based on detailed engineering specifications to engineering estimates based on design concepts. The information gathered, besides including labor and material base costs, will also include WBS dictionary entries, basis of estimate information as well as a detailed contingency/risk analysis on these base costs. This information will be 'rolled up' and presented in a variety of output reports at any level of WBS detail.

Subsystem schedules will be developed concurrently with the costs and integrated into a system schedule to help create a budget/funding profile that will allow the Project to meet its milestones. Preliminary cost, schedule and fiscal year budget information will be reviewed and iterated over the coming year, leading to a baselined project plan for the Daya Bay experiment after a successful DOE CD-2 review.

18.3 Technical Reviews

In addition to the various agency review processes, the Project will hold internal reviews at appropriate points in the development of the Project and its subsystems. Early in the subsystem development process, requirements reviews will be held to ensure the system scientific requirements flow down correctly to define subsystem technical specifications. Additionally, subsystem design reviews will take place at specific points in the development of the subsystem technical elements. Lastly, prior to initiating large procurement activities, production readiness reviews will be held. Each of these reviews will have uniquely assembled committees, utilizing relevant expertise, both internal and external to the Collaboration as necessary, to ensure the subsystem designs are optimal.

18.4 Change Control

The Change Control process is documented in the P-PEP.

19 Schedule, Scope and Cost Range

In this chapter, the overall project plan is described. This includes an overview of the project schedule, and the concept for the international division of scope and cost. The planned U.S. scope and cost range is outlined. This is a joint project with an international collaboration, and the cost accounting approaches differ substantially from country to country. Project cost accounting in the Peoples Republic of China is quite different from the approach taken in the U.S. For example, in China essentially all labor costs (Physicist, Engineer and technician) do not appear in the estimate. The primary cost items in China are materials and equipment. The price of labor for items such as tunnel mining is very much less than the price in the U.S. As a result, it is very difficult to review the cost of a Chinese scope element by applying typical U.S. costing standards. For this reason, while the total project schedule and scope are discussed, the only cost estimate presented is that for the planned U.S. scope.

19.1 Project Schedule

Briefly, the first significant construction event of the Daya Bay experiment schedule begins with the initiation of civil construction on the tunnels in the spring of 2007. The Project's goal is to complete the civil construction of the tunnels, experimental halls and utility infrastructure before the middle of 2009.

There is an additional goal to complete the Daya Bay Near Hall (and Filling Hall) as early as possible — approximately 12 months earlier than the final (far) hall. The schedule for the detector elements is therefore driven by the completion of the first two antineutrino detectors and one third of the muon system hardware by the fall of 2008 in order to deploy these in this first experimental hall. This Daya Bay Near Hall will be used as an early opportunity to install, test and begin partial experiment operations — a chance to debug and gain insight into detector operations. This would occur in the early summer of 2009. The next hall to follow would be the Mid Hall, if the fast results option is adopted. This hall and its detectors will most likely be available for installation tasks 3–4 months after the Daya Bay Near Hall (early in calendar 2009). This would then allow us an opportunity to install and begin measurements of θ_{13} by late summer of 2009.

The remainder of the detectors will be installed and commissioned in the Ling Ao Near and Far Halls by early summer of calendar 2010 so that the full complement of near and far detectors can begin data taking. A more complete view of the project schedule is shown in Fig. 19.1 below.

19.2 Project Scope

The project's entire technical scope has been described in the previous chapters. The total Daya Bay project includes the civil construction of the experimental facility at the Daya Bay nuclear reactor complex as well as the construction of the detector elements (antineutrino detectors, muon system, calibration system, DAQ/Trigger/Online and offline). Crucial to all of these activities are the project integration elements: Installation and System Test, System Integration and Project Management.

19.2.1 U.S. Project Scope Range

The U.S. Project scope will not be finalized until a formal MOU is developed and signed between the U.S., China and other countries. Most likely this will be done at the Laboratory to Laboratory level. Therefore, the scope and possible range of U.S. costs shown in Table 19.1 are based on the current status of discussions within the Collaboration. The major elements of U.S. scope deliverables include:

1. Parts of the Antineutrino Detector:
    (a) Design and 50% of the fabrication costs of the Acrylic Vessels,
    (b) Critical expertise, materials and processing equipment for the production of Gadolinium loaded Liquid Scintillator
    (c) PMTs (w/bases, cables and high-voltage)

   (d) PMT support structure
   (e) AD safety systems

2. Significant portions of the Muon System:
   (a) Water Cherenkov PMTs (w/ bases and HV)
   (b) PMT support structure
   (c) Water Pool liner, N_2 cover gas system
   (d) high-voltage and gas mixing/control system for Resistive Plate Chambers (RPC)
   (e) key elements of the Muon safety systems

3. Major portion of the Calibration system:
   (a) automated deployment system
   (b) monitoring system.

4. Front-end, DAQ and trigger electronics design (as well as portions of online software).

5. Off-line software and simulations effort (jointly with China)

6. Transporter system for moving the assembled, and then filled, antineutrino detectors as well as Electric Vehicles for moving personnel within the tunnels

7. Installation and test planning and equipment

8. Design integration activities

9. US Project management

19.2.2 U.S. Project Cost Range

The U.S. Cost associated with the above scope is shown in Table 19.1. The projected funding profile is shown in Table 19.2. The TEC cost range for the proposed U.S. scope, in FY07 U.S. dollars, is $24M to $26.6M. This equates to a range of from $25.5–28.2M of then-year dollars. The total includes such items as System (or design) Integration and Project Management. Installation and test is included, but the U.S. contribution will primarily be used for installation/system test planning and somewhat limited travel and execution funds. It is possible to cap the U.S. contribution in Installation and Test as China can supply the vast majority of the technical resources necessary for assembly and installation. Finally, the total includes contingency at the level of $\sim$30% of the total U.S. base cost. Contingency is currently estimated at L3 or below of the WBS. It is based on the level of design maturity and the level of risk associated with the element, the level of cost basis and the level of risk associated with the element. The contingency percents can be seen in the table along side the element base costs.

The cost estimates for most elements have been developed in some detail with a rudimentary basis of estimate, etc., but are still evolving somewhat. We will continue to refine the cost estimates, cost basis and resource loaded schedule in the near future as the design and U.S. scope matures. We will utilize an Excel-based cost estimating tool, previously developed and utilized in other projects, to capture and build our cost book. We'll also utilize MS Project for building our resource loaded schedule, escalating to now-year dollars and capturing performance for earned value management once we're baselined.

WBS	Description	Subtotal	% Contingency	Contingency	Total
1.1	**Antineutrino Detector**	8,456	36%	3,050	11,506
1.2	**Muon System**	3,700	22%	806	4,507
1.3	**Calibration System**	1,940	22%	429	2,369
1.4	**Electronics**	213	12%	27	239
1.5	**Offline**	1,365	19%	253	1,618
1.6	**Conventional Construction**	—	—	—	—
1.7	**Installation**	1,961	19%	374	2,335
1.8	**Integration**	1,028	20%	203	1,231
1.9	**Project Management**	1,766	8%	133	1,899
	Management Reserve	—	—	854	854
	Subtotal TEC	20,428	30%	6,128	26,557
1.10	**Preliminary Design & Development (OPC)**	3,571	5%	179	3,749
	Total Project Cost (TPC)	23,999	26%	6,307	30,306

Table 19.1. U.S. Daya Bay Project cost estimate with contingency in FY07 k$.

	FY07	FY08	FY09	FY10	Total
OPC	1,700	1,700	—	200	3,600
TEC	—	7,000	11,000	10,000	28,000
TPC	1,700	8,700	11,000	10,200	31,600

Table 19.2. Projected U.S. Daya Bay funding profile in at-year k$.

ID	Task Name	Start	Finish
1	Conceptual Dsgn & R&D Activities	Fri 3/17/06	Tue 3/27/07
2	CD-1 Approval	Fri 5/11/07	Fri 5/11/07
3	Preliminary Dsgn & R&D Activities	Wed 3/28/07	Tue 10/2/07
4	Begin Civil/Tunnel Construction	Mon 7/2/07	Mon 7/2/07
5	CD-2/3a Approval	Thu 11/15/07	Thu 11/15/07
6	Prototyping	Fri 8/4/06	Thu 4/26/07
7	System Test (prototype elements)	Fri 3/2/07	Thu 8/30/07
8	Finalize Detail Dsgn & Prep for Construction	Wed 10/3/07	Tue 3/18/08
9	Procure materials for Gd loaded LS	Fri 11/16/07	Thu 3/13/08
10	Ship elements and produce Gd Loaded LS	Fri 3/14/08	Thu 8/28/08
11	Deliver Gd Loaded LS to Site	Fri 8/29/08	Fri 8/29/08
12	Contract & Procure PMT's & Bases (200 per mo)	Fri 11/16/07	Thu 1/1/09
13	CD-3b Approval	Thu 3/20/08	Thu 3/20/08
14	**PMT Deliveries 1-4 to China**	**Wed 3/19/08**	**Fri 10/31/08**
19	Fab & ship AD Steel Vessels (China)	Mon 10/1/07	Tue 9/30/08
20	Fab & ship AD Acrylic Vessels (Taiwan)	Mon 10/29/07	Fri 9/26/08
21	Surf Assy Bldg Beneficial Occupancy	Fri 4/18/08	Fri 4/18/08
22	1st Pair of Steel & Acrylic Vessels at SAB	Mon 6/9/08	Mon 6/9/08
23	Fab & Assemble Calibration Syst Elements	Thu 3/20/08	Wed 12/24/08
24	Construct Muon Syst Elem for D-B & L-A Cavern	Thu 3/20/08	Wed 1/21/09
25	Ship Muon Syst Elem for D-B Near Hall	Thu 7/10/08	Wed 10/1/08
26	Assemble 1st AD Pair in SAB	Fri 6/27/08	Thu 10/30/08
27	DB Near & Filling Hall Beneficial Occupancy	Mon 9/1/08	Mon 9/1/08
28	Test First 6 Calibration Boxes	Thu 8/7/08	Wed 10/1/08
29	Ship Calib Sys Elems for 1st AD Pair	Fri 10/31/08	Thu 11/27/08
30	Fill 1st AD Pair in Filling Hall	Fri 10/31/08	Thu 12/25/08
31	Assemble Muon elements and install AD's in DB Nea	Mon 9/1/08	Fri 1/16/09
32	System Test (in-situ in D-B Near Hall)	Mon 12/15/08	Fri 5/1/09
33	CD-4a Daya Bay Near Site Ready to Take Data	Mon 11/30/09	Mon 11/30/09
34	Assemble remaining AD Pairs in SAB	Fri 10/31/08	Thu 10/1/09
35	Fill 2nd AD Pair in Filling Hall	Fri 1/23/09	Thu 3/5/09
36	L-A Hall Beneficial Occupancy	Wed 4/1/09	Wed 4/1/09
37	Assemble Veto & AD Elems in L-A Cavern	Thu 4/2/09	Wed 7/22/09
38	System Test (in-situ in L-A)	Thu 7/23/09	Wed 10/14/09
39	L-A Site Ready to Take Data	Wed 10/14/09	Wed 10/14/09
40	Construct Veto Syst Elem for Far Cav	Thu 1/22/09	Wed 8/5/09
41	Crate & Ship Veto Elements	Thu 6/11/09	Wed 9/30/09
42	Far Hall Beneficial Occupancy	Wed 7/1/09	Wed 7/1/09
43	Assemble Veto & AD Elems in Far Caverns	Thu 8/20/09	Wed 1/6/10
44	System Test (in-situ Far Caverns)	Thu 12/24/09	Wed 3/31/10
45	CD4b - Far Site Ready to Take Data	Wed 9/1/10	Wed 9/1/10

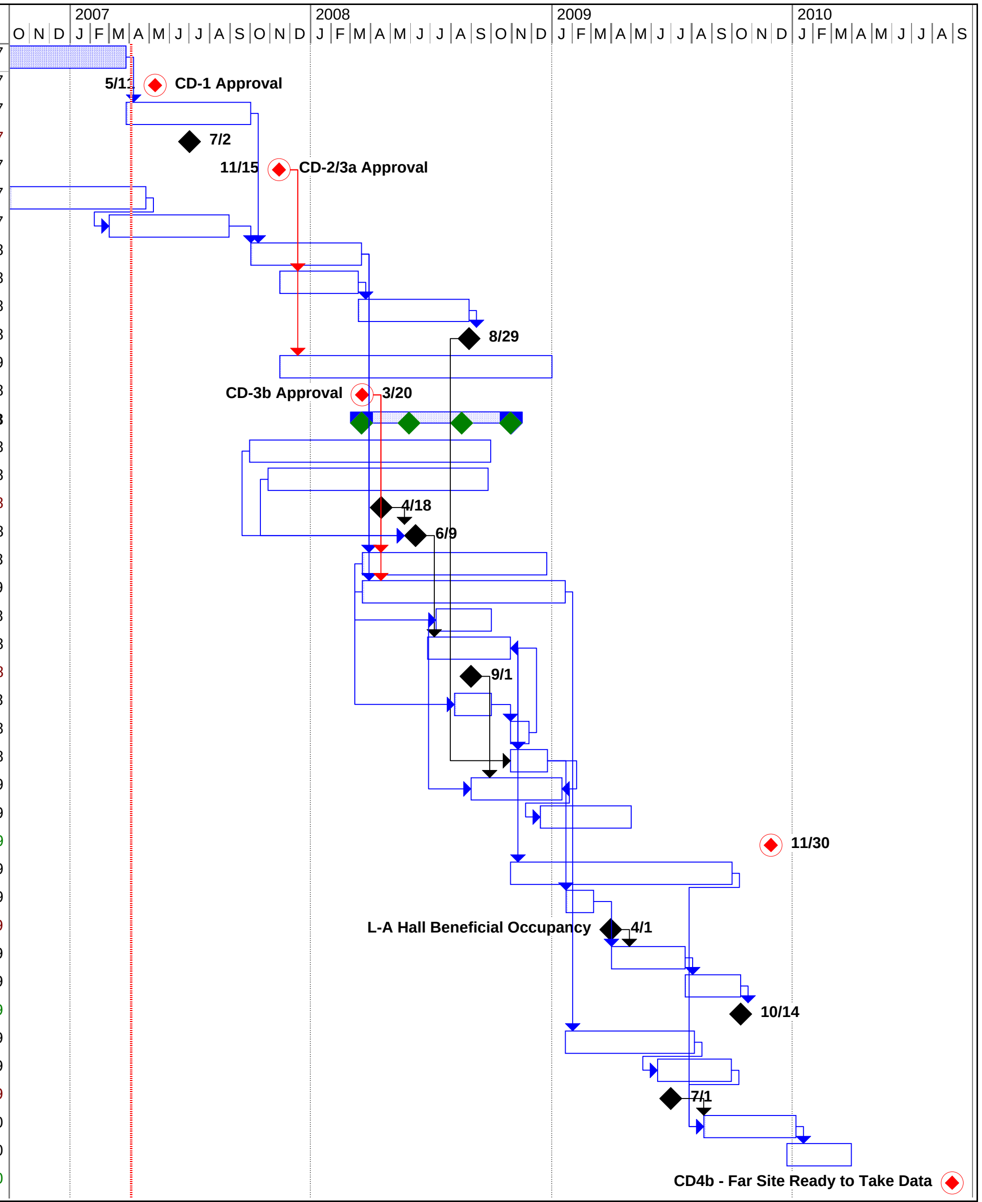

Page 1

Fig. 19.1. Daya Bay Project Summary Schedule.

A Acknowledgements

This work was supported in part by the the Chinese Academy of Sciences, the National Natural Science Foundation of China (Project numbers 10225524, 10475086, 10535050 and 10575056), the Ministry of Science and Technology of China, the Guangdong provincial goverment, the Shenzhen Municipal government, the China Guangdong Nuclear Power Group, the Research Grants Council of the Hong Kong Special Administrative Region of China (Project numbers 400805 and 400606), the United States Department of Energy (Contracts DE-AC02-98CH10886, DE-AS02-98CH1-886, and DE-FG02-91ER40671 and Grant DE-FG02-88ER40397), the U.S. National Science Foundation (Grants PHY-0555674 and NSF03-54951), the University of Houston (GEAR Grant number 38991), the University of Wisconsin and the Ministry of Education, Youth and Sports of the Czech Republic (Project numbers MSM0021620859 and LC527).

B Acronyms

AC	alternating current
Access	database program from Microsoft Corporation
AD	Daya Bay antineutrino detector
ADC	analog to digital converter
APS	American Physical Society
BES	Beijing Spectrometer at the Beijing Electron Positron Collider
BINE	Beijing Institute of Nuclear Energy
BNL	Brookhaven National Laboratory
Bugey 3	Reactor antineutrino experiment in France
CAS	Chinese Academy of Sciences
CDR	conceptual design report
CC	charged-current neutrino interactions
CCD	charge coupled device
CCG	central clock generator
CD-1	Critical Decision #1 — Site Selection (CDR)
CD-2	Critical Decision #2 — Cost/Schedule/Scope well defined (TDR)
CD-3a	Critical Decision #3a — Long lead procurements
CD-3b	Critical Decision #3b — Start of Construction
CD-4a	Critical Decision #4a — Initiate early operations
CD-4b	Critical Decision #4b — begin full experiment operations
CERN	European Organization for Nuclear Research
CGNPC	China Guandong Nuclear Power Group (Daya Bay owner)
C.L.	confidence level
CP	charge, parity symmetry
CPT	charge, parity, time reversal symmetry
CSE	Computing Science Engineering
CVS	code versioning system
DAC	digital to analog converter
DAQ	data acquisition
DB	Daya Bay
DC	direct current
DCS	detector control system
DOE	U.S. Department of Energy
ES	elastic neutrino scattering
ES&H	environment, safety & health
FADC	flash ADC
FEC	front-end card
FEE	front-end electronics
FET	field effect transistor
FPGA	field programmable gate array
FY	fiscal year
FWHM	full width at half maximum
Gallex	Gallium Experiment
Gd-LS	Gd loaded liquid scintillator
GEANT	detector description and simulation tool

GNO	Gallium Neutrino Observatory
GOC	global operation clock
GPS	Global Positioning System
$GW_{\rm th}$	reactor's thermal power in GigaWatts
H/C	ratio of hydrogen to carbon
H/Gd	ratio of hydrogen to gadolinium
HOTLink	bus for clock distribution
HV	high voltage
HVPS	high voltage power supplies
IBD	inverse beta decay
IFC	International Finance Committee
IGG	Institute of Geology and Geophysics
IHEP	Institute for High Energy Physics
ILL	Institut Laue-Langevin
ISO	International Standards Organization
IRNC	International Research Network Connections
JINR	Joint Institutes for Nuclear Research
JTAG	electronic standard for testing & downloading FPGA's
KamLAND	Kamioka Liquid Scintillator Antineutrino Detector
K2K	KEK to Kamiokanda neutrino oscillation experiment
KARMEN	Karlsruhe Rutherford Medium Energy Neutrino experiment
KEK	High Energy Accelerator Research Organization in Japan
Kr2Det	Two Detector Reactor Neutrino Oscillation experiment at Krasnoyarsk
L/E	distance divided by energy
L3C	L3 cosmic ray experiment
LA	Ling Ao
LAB	Linear Alkyl Benzene
LabVIEW	Laboratory Virtual Instrument Engineering Workbench
LBNL	Lawrence Berkeley National Laboratory
LEC	Local Emergency Coordinator
LED	light emitting diode
LENS	Low Energy Solar Neutrino Spectrometer
LIGO	Laser Interferometric Gravity Observatory
LMA	Large Mixing Angle solution
Ln	lanthanides
LOG	Laboratory Oversight Group
LS	liquid scintillator
LSND	Liquid Scintillator Neutrino Detector
LVDS	low voltage differential
MBLT	Multiplexed Block Transfer
m.w.e.	meters of water equivalent
MC	Monte Carlo
MIE	Major Item of Equipment
MINOS	Main Injector Neutrino Oscillation experiment
MoST	Ministry of Science and Technology of China
MOU	Memorandum of Understanding
MSB	1,4-bis[2-methylstyrl]benzene
MSPS	mega-sample per second

NC	neutral current neutrino interactions
NHIT	counter for number of hits
NSFC	Natural Science Foundation of China
NPP	nuclear power plant
NTP	Network Time Protocol
NuSAG	Neutrino Science Assessment Group
NWW	North-West by West
ODH	oxygen deficiency hazard
OPC	Other Project Costs (Project costs not in TEC)
OPERA	Oscillation Project with Emulsion-tRacking Apparatus
p.e.	photo-electrons
P-HAD	Preliminary Hazards Assessment Document
P-PEP	Preliminary Project Execution Plan
PAP	Project Advisory Panel
PC	pseudocumene
PC	personal computer
PMT	photomultiplier tube
PPS	Pulse Per Second
PRD	Pearl River Delta (elevation above sea level)
PVC	Poly Vinyl Chloride
PWR	pressurized water reactors
QA	quality assurance
QC	quality control
QE	quantum efficiency
QM	quality management
REE	rare earth elements
R&D	research and development
RPC	resistive plate chamber
RPVC	rigid polyvinyl chloride
RQD	Rock Quality Designation
RS	Richter scale
SAGE	Soviet American Gallium solar neutrino Experiment
SBMS	Standards Based Management System
SCADA	supervisory, control, and data acquisition
s.p.e.	single photo-electron
SNO	Sudbury Neutrino Observatory
SNO+	proposed solar and geo-neutrino experiment using liquid scintillator in the existing SNO detector
SS	stainless steel
SAB	surface assembly building
TDC	time to digital converter
TEC	Total Estimate to Complete (total cost of project funded by MIE)
TPC	Total Project Cost (total cost of project including OPC)
TSY	Fourth Survey and Design Institute of China Railways
UCT	Universal Coordinated Time
UV	ultraviolet light
VME	Versa Module Europa
WBS	work-breakdown structure
YREC	Yellow River Engineering Consulting Co. Ltd.